EXPERIMENTAL INVESTIGATION OF
THE EFFECT OF CAVITATION ON
THE ROTORDYNAMIC FORCES ON
A WHIRLING CENTRIFUGAL PUMP IMPELLER

Thesis by

Ronald John Franz

Division of Engineering and Applied Science

In Partial Fulfillment

of the Requirements for the Degree of

Doctor of Philosophy

California Institute of Technology

Pasadena, California

1989

(Submitted January 5, 1989)

Acknowledgements

Abstract

The interaction of a rotating impeller and the working fluid introduce forces on the rotor. These fluid–induced forces can cause self–excited whirl, where the rotor moves away from and whirls along a trajectory eccentric to its undeflected position. When designing a turbomachine, particularly one which is to operate at high speed, it is important to be able to predict the fluid–induced forces, both steady and unsteady, acting on the various components of the machine. The fluid–induced rotordynamic forces acting upon the impeller and therefore on the bearings was investigated for a centrifugal impeller in a spiral volute in the presence of cavitation.

An experiment in forced vibration was made to study the fluid–induced rotordynamic force on an impeller whirling around its machine axis of rotation in water. The whirl trajectory of the rotor is prescribed to be a circular orbit of a fixed radius. A dynamometer mounted behind the rotor and rotating with it measures the force on the impeller. The force measured is a combination of a steady radial force due to volute asymmetries and an unsteady force due to the eccentric motion of the rotor. These measurements have been carried out over a full range of whirl/impeller speed ratios at different flow coefficients for various turbomachines. A destabilizing force was observed over a region of positive whirl ratio. Cavitation corresponding to a three percent head loss did not have a significant effect upon this destabilizing force. However, a lesser degree of cavitation at the design point for the impeller-volute combination tested increased this destabilizing force for a particular set of whirl ratios.

Table of Contents

Nomenclature

$[A]$ hydrodynamic force matrix, non-dimensionalized by $\frac{1}{2}\rho u_2^2 A_2/r_2$

A_1, A_2 impeller inlet area (πr_1^2), outlet area $(2\pi r_2 b_2)$

$[B]$ hydrodynamic moment matrix, non-dimensionalized by $\frac{1}{2}\rho u_2^2 A_2$

b_2 impeller discharge width

$[C]$ hydrodynamic damping matrix, non-dimensionalized by $\frac{1}{2}\rho u_2^2 A_2/(\omega r_2)$

$\mathbf{F}$ instantaneous lateral force on the impeller

F_1, F_2 components of the instantaneous lateral force on the impeller in the rotating dynamometer reference frame

F_x, F_y components of the instantaneous lateral force on the impeller in the stationary volute frame, non-dimensionalized by $\frac{1}{2}\rho u_2^2 A_2$

F_{ox}, F_{oy} values of F_x and F_y if the impeller was located at the origin of the volute frame (volute center), non-dimensionalized by $\frac{1}{2}\rho u_2^2 A_2$

F_n, F_t components of the lateral force on the impeller which are normal to and tangential to the whirl orbit, averaged over the orbit, non-dimensionalized by $\frac{1}{2}\rho u_2^2 A_2 \varepsilon/r_2$

g gravitational constant

I/J ratio of whirl/impeller shaft speeds

$[K]$ hydrodynamic stiffness matrix, non-dimensionalized by $\frac{1}{2}\rho u_2^2 A_2/r_2$

$[M]$ hydrodynamic mass matrix, non-dimensionalized by $\frac{1}{2}\rho u_2^2 A_2/(\omega^2 r_2)$

$\mathbf{M}$ instantaneous lateral moment on the impeller

m mass of the "impeller," includes the mounting spindle and the front plate of the dynamometer

M_1, M_2	components of the instantaneous lateral moment on the impeller in the rotating dynamometer reference frame
M_x, M_y	components of the instantaneous lateral moment on the impeller in the stationary volute frame, non-dimensionalized by $\frac{1}{2}\rho u_2^2 A_2 r_2$
M_{ox}, M_{oy}	values of M_x and M_y if the impeller was located at the origin of the volute frame (volute center), non-dimensionalized by $\frac{1}{2}\rho u_2^2 A_2 r_2$
M_n, M_t	components of the lateral moment on the impeller which are normal to and tangential to the whirl orbit, averaged over the orbit, non-dimensionalized by $\frac{1}{2}\rho u_2^2 A_2 \varepsilon$
p_1, p_{t1}	upstream static, total pressure
p_2, p_{t2}	downstream static, total pressure
p_I	static pressure at impeller inlet, $p_{t1} - \frac{1}{2}\rho\left(\frac{Q}{A_1}\right)^2$
p_v	vapor pressure of water
Q	flow rate
r_1, r_2	impeller inlet, discharge radius
t	time
u_1, u_2	tip speed at impeller inlet, ωr_1, at discharge, ωr_2
X_L, Y_L	axes of the stationary laboratory reference frame
X_V, Y_V	axes of the stationary volute reference frame
x, y	instantaneous coordinates of the impeller center in a stationary frame, non-dimensionalized by r_2
z	coordinate of the machine axis, pointing upstream in the direction of impeller rotation from the plane bisecting the impeller discharge area, non-dimensionalized by r_2
z_o	lever arm computed from the steady moment and force, Eqn. (8.4a), non-dimensionalized by r_2

z_ε lever arm computed from the unsteady moment and force, Eqn. (8.4b), non-dimensionalized by r_2

ε radius of the circular whirl orbit (0.0495 inch)

θ angular position of the impeller on the whirl orbit, measured from the volute tongue in the direction of impeller rotation

ρ density of water

σ cavitation number, $\dfrac{p_I - p_v}{\frac{1}{2}\rho u_1^2}$

σ^2 variance

ϕ flow coefficient, $\dfrac{Q}{u_2 A_2}$

φ_V angle of the volute tongue measured from the stationary laboratory axis, X_L.

ψ total head coefficient, $\dfrac{p_{t2} - p_{t1}}{\rho u_2^2}$

ω radian frequency of the impeller (shaft) rotation

Ω radian frequency of the whirl motion $= I\omega/J$

Abbreviations

DPTF   Dynamic Pump Test Facility

HPOTP   High Pressure Oxygen Turbopump

RFTF   Rotor Force Test Facility

SSME   Space Shuttle Main Engine

List of Figures

List of Tables

Chapter 1

Introduction

1.1 Self-Excited Whirl

The dynamic analysis of a turbomachine encompasses the response of the rotating impeller-shaft system. The presence of the working fluid influences the dynamic behavior of the rotor. Elements of the machine which influence its vibration characteristics include mass imbalance of the rotor-shaft system, unequal transverse moments of inertia, and asymmetric lateral stiffness of the support structure. The displacement of the rotor-shaft system away from the machine centerline within the working fluid causes asymmetric variation of pressure and fluid momentum between small clearance surfaces, in seals and in hydrodynamic bearings, and between the rotor and its housing. Verhoeven and Gopalakrishnan (1988) provide a literature review of the dynamic response analysis of rotors, including different mechanisms of rotor instability. This thesis focuses on the fluid-induced forces from the interaction between the rotor and its housing. These fluid-induced forces depend upon the position of the rotor and the operating condition of the turbomachine.

The effect of these various forces is reflected in the vibration or motion of the rotor-shaft system away from its stationary equilibrium position. The orientation and location of the rotor-shaft system can be described as a whirling motion of the deflected shaft centerline about the machine centerline. For synchronous vibration typical of a mass unbalance, the lateral vibration of the rotor-shaft system is a whirl at the shaft rotation frequency. The deflection curve of the shaft is stationary in the rotating shaft frame. In asynchronous vibration the rotor whirls at a frequency different from shaft frequency, subjecting the shaft to fluctuating stresses that are unsteady in both the frame of shaft rotation and the stationary frame. Ehrich and Childs (1984) discuss several mechanisms of self-excited whirl in turbomachines, where the vibration is at or near a frequency of natural vibration of the rotor-shaft

system. A biennial series of workshops on "Rotordynamic Instability Problems in High-Performance Turbomachinery," * held at Texas A&M University present field experience and the results of research that relate to the present effort.

This thesis focuses on the the fluid-induced rotordynamic forces arising from the interaction of the rotor and its housing which can result in self-excited whirl. Fig. 1.1 is a schematic of a centrifugal pump impeller undergoing whirl, and Fig. 1.2 indicates the forces acting on a whirling impeller. Assuming small displacements of the impeller, the hydrodynamic force on the impeller rotating at a frequency ω, can be expressed as,

$$\mathbf{F}(t) = \mathbf{F_o} + [\mathbf{A}]\,\mathbf{x}(t) \tag{1.1}$$

The lateral force, $\mathbf{F}(t)$, can be considered as the sum of two forces: a steady force, $\mathbf{F_o}$, which the impeller would experience if located at the volute center, arising from asymmetries in the flow around the impeller in the volute, and an unsteady force due to the eccentric motion of the impeller, represented by a force matrix $[\mathbf{A}]$; $\mathbf{x}(t)$ is the displacement vector of the impeller from the volute center. The fluid-induced rotordynamic force matrix $[\mathbf{A}]$ in general will be a function of the frequency of lateral vibration, nondimensionalized by shaft frequency, Ω/ω, and of the operating condition of the turbomachine. Frequently the unsteady force is expanded in terms of the time derivatives of $\mathbf{x}(t)$: position, velocity and acceleration, with the coefficient matrices being the stiffness, damping and mass matrices.

$$\mathbf{F}(t) = \mathbf{F_o} - [\mathbf{K}]\,\mathbf{x}(t) - [\mathbf{C}]\,\dot{\mathbf{x}}(t) - [\mathbf{M}]\,\ddot{\mathbf{x}}(t) \tag{1.2}$$

To measure the forces on an impeller undergoing self-excited whirl, an experiment in forced vibration was carried out. The imposed whirl trajectory was a circular orbit of fixed radius and radian frequency Ω. The force matrix $[\mathbf{A}(\Omega/\omega)]$ can then be expanded as a quadratic to obtain the elements of the stiffness, damping and

---

* The proceedings of these workshops are published as NASA Conference Publications: NASA CP 2133 (1980), CP 2250 (1982), CP 2338 (1984), CP 2443 (1986), CP 3026 (1988).

mass matrices. The unsteady force can also be resolved into components normal to and tangential to the whirl motion. The normal force is perpendicular to the whirl motion, directed radially outward when positive. The tangential force is positive when in the direction of shaft rotation. A positive normal force tends to increase the displacement of the impeller. Whenever the tangential force is in the same direction as the whirl velocity it encourages the whirl motion and is thus destabilizing.

In the next two sections, past measurements of fluid-induced forces on impellers will be reviewed. First, measurements without an imposed whirl trajectory will be discussed. Then, measurements of the unsteady force on impellers undergoing a whirling motion will be covered.

1.2 Measurements of the Impeller Force without Whirl

The steady force caused by the asymmetric flow within a volute was measured by Agostinelli et al. (1960) from the reaction of a cylindrical bearing support structure. They tested centrifugal pumps of various specific speeds with single volute, double volute, concentric, and mixed concentric-volute casings. Iversen et al. (1960) used bearing reactions detected by a "strain-beam spider" attached between the bearing cap and the test bedplate to measure the steady force for an impeller-volute configuration. They also integrated volute pressure tap measurements to evaluate the force.

Domm and Hergt (1970) measured the reaction of the bearing support structure through strain-gaged tie rods for an impeller centered and also at an eccentric location within a vaneless volute. Hergt and Krieger (1969–70) measured the force on a centrifugal impeller centered and at various eccentric locations in a vaned diffuser. The measured force was directed radially outward with a small tangential component. Sufficient data was taken to indicate the location of the hydraulic center of the diffuser where the steady force would vanish for each flow rate tested. The data was not presented in terms of a stiffness matrix. Nonstationary forces were also observed, particularly at flow coefficients below optimum.

Uchida et al. (1971) measured the bearing reaction from a cantilevered cylindrical support structure to detect the force on a centrifugal impeller in a volute. The interchangeable tongue of the volute had a significant effect upon the force on the impeller. The dynamic force contained shaft and blade passage frequencies and also random fluctuations. For flow rates above best efficiency, the impeller force was measured in the presence of cavitation.

Kanki, Kawata and Kawakami (1981) used strain gages on the shaft neck to measure the force of a centrifugal impeller in a double volute and in a vaned diffuser. The impeller was positioned centered and also off-center from the casing centerline. The hydraulic force acted in the general direction of the impeller displacement. The unsteady impeller force was larger than the static component at low flow rates for both the volute and the diffuser. The unsteady force had frequency components at a low frequency ($\frac{1}{10}-\frac{1}{5}$ shaft frequency), at blade passage and at harmonics of shaft frequency. Pressure measurements were taken at the impeller tip and in the casing. Kawata, Kanki and Kawakami (1984) measured the force on a centrifugal impeller in a vaned diffuser under cavitating conditions. The magnitude of the dynamic force increased with decreasing flow rate under non-cavitating conditions. With breakdown of pump performance the dynamic force increased. For flow rates at and below 70% of rated flow, the dynamic force eventually decreased with further loss of head.

From the measurements of the steady force on an impeller positioned at various locations within its casing, the location at which the steady force would vanish can be inferred. The measurements had indicated that the force was in the general direction of the impeller displacement and also contained various frequency components. However the measurements were not presented in terms of a stiffness matrix. The nonzero force measured tends to deflect the rotor. With various unsteady forces acting on the impeller, the conditions under which these fluid-induced forces can cause the impeller to undergo lateral vibration needs to be investigated.

1.3 Measurements of the Unsteady Force Matrix

At Sulzer Brothers Ltd. in Switzerland, Bolleter et al. (1987) translated an impeller inside a vaned diffuser along a single axis. The motion was imposed by a "rocking arm" excited by a transient frequency sweep. The deflections of the impeller in the lateral plane were measured by two eddy current probes. The rotating force measuring section at the base of the impeller was instrumented with six full bridges of strain gages, each sensitive to one of the six degrees of freedom. The geometry of the test section was typical of a single stage of a boiler feed pump.

At the University of Tokyo, Ohashi and Shoji (1987), using a circular whirl orbit at fixed frequency, tested two-dimensional impellers to measure the force on the impeller blades in order to compare with their theory, which is mentioned in the next section. Employing a rebuilt eccentric whirl mechanism, Ohashi et al. (1986) tested a centrifugal impeller in a vaned diffuser. The force was measured using bearing reaction load cells positioned on an outer race of bearings that only whirled. For all of the measurements, the diffuser chamber has two symmetrically located discharge pipes and a mesh screen at the chamber periphery to provide for an axisymmetric diffuser flow. The tangential force was observed to be destabilizing over a small range of forward whirl, $\Omega/\omega > 0$, only for partial flow. Ohashi et al. (1988) compare measurements for a centrifugal impeller in a vaned and in a vaneless diffuser, both with a large clearance around the front shroud of the impeller. For the vaneless diffuser a spacer was inserted into the annular gap between the casing and the impeller front shroud. The decreased clearance around the shroud emphasized the effect of the eccentric impeller on the flow outside the shroud. The tangential force was larger and destabilizing over a wider range of forward whirl, also for design flow. Radial grooves were cut into the spacer facing the front shroud to reduce the rotational velocity of the fluid within the clearance. These swirl breaks reduced the magnitude and whirl ratio range of the destabilizing tangential force.

Brennen et al. (1980) describe the development of the Rotor Force Test Facility at the California Institute of Technology. Chamieh (1983) and Chamieh et al.

(1985) used a stationary external balance to measure the hydrodynamic stiffness of a centrifugal impeller. Using a rotating internal balance, mounted between the impeller and the drive shaft, Jery et al. (1985) and Jery (1987) measured the forces on a centrifugal impeller, designated Impeller X, whirling in a circular orbit inside various vaneless and vaned volutes. Adkins (1986) and Adkins and Brennen (1988) observed that the pressure distribution around the front shroud of Impeller X had a significant contribution to the hydrodynamic stiffness. He also reported measurements taken with the annular region surrounding the shroud exposed to the housing reservoir. This data was compared with measurements taken without the enlarged annular region and with a two dimensional version of the impeller, Impeller Z, (Franz and Arndt (1986b) and Franz et al. (1987)) demonstrating that the large shroud clearances reduce the magnitude of the rotordynamic forces for reverse whirl and for the region of destabilizing forward whirl. Bolleter et al. (1987), who had a smaller gap between the impeller shroud and the casing, measured much larger forces. Data presented in various reports (Franz and Arndt (1986a) and Arndt and Franz (1986)) are gathered and included in Brennen et al. (1988) to demonstrate the dependence of the rotordynamic forces upon whirl ratio and flow coefficient for an axial inducer and for one half of the double-suction impeller of the High Pressure Oxygen Turbopump (HPOTP) of the Space Shuttle Main Engine (SSME).

Forced vibration experiments using the Rotor Force Test Facility to measure the rotordynamic forces have been carried out on various turbomachines: centrifugal impellers, axial inducers, and a centrifugal impeller with an inducer. Housings used include a spiral volute, vaned diffusers and the volute housing chamber itself. Typically there is a region of whirl in the same direction as shaft rotation, forward whirl, for which the average tangential force, F_t, is destabilizing. At low flow coefficients the tangential force on the impeller, depending upon the volute used, may become a strong function of the whirl ratio, to the extent that the region of destabilizing forward whirl may become disjoint, e.g., F_t resemble a cubic. It has

even been observed that at sufficiently low flow coefficients the force on a centrifugal impeller in a seventeen vaned diffuser was destabilizing over a region of reverse whirl. For the HPOTP (a centrifugal impeller with an inducer), the appearance of the cubic character of the curve of F_t was independent of volute. The occurrence of flow reversal upstream of the inducer appears to coincide with the transition in the shape of the tangential force curve to a cubic.

1.4 Models of a Whirling Impeller

The problem of an impeller whirling inside a volute or a vaned diffuser has been treated theoretically by assuming the flow to be two-dimensional, incompressible, and inviscid. Colding-Jørgensen (1980) modeled the volute by distributed vortices. The impeller was replaced by a point source-vortex located at an eccentric position within a volute and had a specified velocity. He calculated stiffness and damping coefficients.

Shoji and Ohashi (1987) used potential theory for an impeller whirling in a vaned or a vaneless diffuser. The whirl path is assumed to be a circular orbit, with radian frequency constant and with the ratio of whirl radius to impeller outlet radius small. The impeller and/or diffuser vanes, logarithmic spirals of zero thickness, were replaced by distributed vortices. The interaction of the impeller blade and diffuser guide vanes was neglected by assuming the diffuser vane vortex distribution to be steady. The theory did not predict the destabilizing tangential force measured on a two-dimensional impeller at partial flow (Ohashi and Shoji, 1987).

Tsujimoto et al. (1988b) similarly used a vortex distribution to model the volute, including the unsteady vortex distribution. However the impeller was treated as an "actuator disk," with the impeller flow perfectly guided by the vanes. The vorticity at the impeller outlet was used to match the impeller model with the volute flow. He included a favorable comparison with the measurements made on the two-dimensional version of Impeller X, Impeller Z. Tsujimoto et al. (1988a) treated the case of a vaned diffuser open to a space of constant pressure. The total

pressure losses in the impeller and the vaned diffuser were included.

Adkins (1986) and Adkins and Brennen (1988) used a one-dimensional bulk flow description for the volute, employing measured geometry. The flow inside the impeller is along a spiral path with the inclination angle derived from the performance, "H–Q," curve thus permitting the flow to deviate from the blade angle. The impeller flow is described by a velocity magnitude function which is linearized with respect to the impeller eccentricity vector. The pressure and velocity at the impeller discharge are matched to the volute inlet to mate the impeller and volute models. The model did reasonably well near design flow. Limitations in the numerical technique used is believed to have prevented calculation of the force matrix for $|\Omega/\omega| > .2$.

1.5 Using the Rotordynamic Forces in Numerical Calculations

The analysis of the vibration of a turbomachine requires models for the structure and the fluid interaction in order to calculate the critical speeds or dynamic response. The formulation of the vibration problem for the structure is generally in terms of mass, damping and stiffness matrices. Fluid-induced interactions from bearings and seals are similarly modelled. Childs (1978) and Childs and Moyer (1985) discuss rotordynamic models for the hydrogen and the oxygen turbopumps of the Space Shuttle Main Engine, respectively. Black (1974) treats a boiler feed pump. He models the impeller-diffuser interaction using a stiffness and a damping matrix determined by the angle of incidence. The impeller-diffuser interaction is also typically modeled by stiffness, damping and mass matrices. Expanding the unsteady force, $[A]x(t)$, in terms of the time derivatives of the position vector up to the second order yields these matrices as coefficient matrices. For the forced vibration experiments conducted at Caltech using a circular whirl orbit, the mass-damping-stiffness model implies that the matrix $[A(\Omega/\omega)]$ is parabolic in Ω/ω. Depending upon the turbomachine and the operating condition, the curve $[A(\Omega/\omega)]$ may resemble a cubic. Consequently the mass-damping-stiffness

model may not be sufficient to describe the rotordynamic forces from the impeller-housing interaction.

As an example, Williams and Childs (1988) deal with the non-quadratic dependence of the unsteady force matrix upon whirl ratio for the model of flow leakage back through the impeller front shroud region of Childs (1986). A quadratic fit is used to obtain mass, damping and stiffness matrices. In addition, stiffness terms dependent upon whirl ratio are introduced into the rotordynamic calculation to account for the non-quadratic dependence.

1.6 Designing with Self-Excited Whirl

Options to deal with self-excited whirl include increasing the natural frequency of lateral vibration and adding damping to counteract the destabilizing tangential force. Stiffening the rotor-shaft-bearing system will increase the natural frequency whirl ratio beyond the destabilizing region. Reducing the circumferential velocity of the fluid in the shroud-casing gap by using swirl breaks decreases the contribution from the forces acting on the impeller shroud. Another method is to inject fluid in a direction opposite that of the impeller rotation, (e.g. Brown and Hart (1986), and with active control, Muszynska et al. (1988)).

The vibration of a whirling impeller is transmitted to the structure through the bearings. Damping can be added by employing squeeze film dampers on the bearings, (Botman 1976 and McLean and Hahn 1984). The vibration of the shaft at the bearing can be counteracted by using magnetic bearings under active control, (Allaire et al. 1986).

1.7 Present Investigation

Measurements of rotordynamic forces have been made on a variety of impellers over a range of flow rates. However all these operating conditions have been in the absence of cavitation. Some phenomenon associated with cavitation include erosion

and noise, (Knapp, 1970). The presence of the gas phase in the flow within the impeller increases the compliance of the fluid within the machine, and reduces the pressure gradient that the fluid can support. The unsteady pressure rise is also affected by cavitation. The frequency dependence of the transfer function matrix, relating upstream and downstream mass flow and pressure fluctuations, of inducers is altered by cavitation, Ng (1976) and Ng and Brennen (1978). For a centrifugal impeller the transfer function matrix had been measured by Stirnemann and Eberl (1985) with some cavitation at design flow.

Using the Rotor Force Test Facility at Caltech, the region of flow conditions for which rotordynamic forces have been measured has been extended for a centrifugal impeller in a spiral volute by operating in the presence of cavitation.
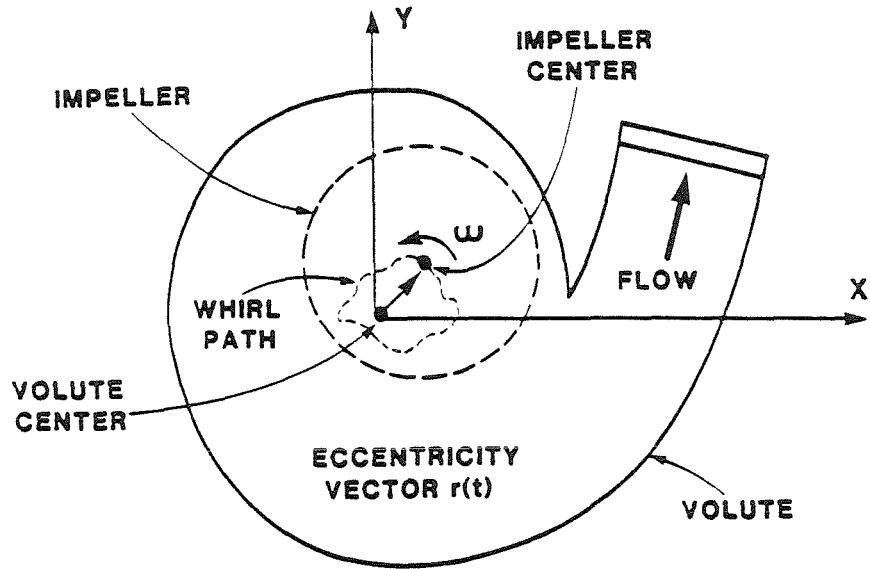
Fig. 1.1   Schematic of a centrifugal pump with a whirling impeller.
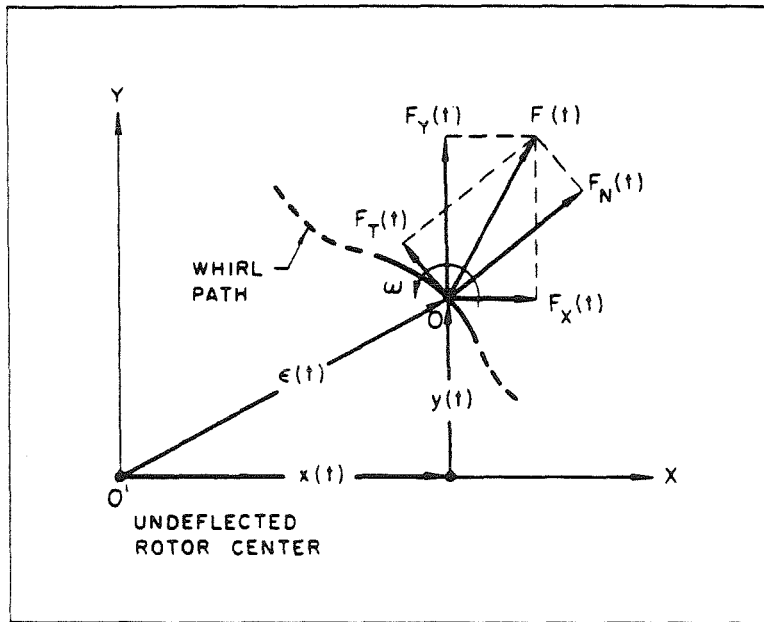
Fig. 1.2   Diagram of the forces acting on a whirling impeller in the plane of vibration.

Chapter 2

Description of the Facility

The Rotor Force Test Facility (RFTF) at the California Institute of Technology was used in the present investigation of the rotordynamic force on a cavitating pump impeller. The facility, a water recirculating pump loop closed to the atmosphere, has been modified over time. The RFTF is a modification of the original facility, the Dynamic Pump Test Facility (DPTF), which was built to measure transfer functions of cavitating inducers. The DPTF is described in detail by Ng (1976) and by Braisted (1979). For the measurement of rotordynamic forces the DPTF was modified and renamed the RFTF. Fig 2.1 is a layout of the pump loop. The flow fluctuators had been dismantled and the test section rebuilt. A cast housing acts as a "container," permitting volutes of various designs to be contained within the housing without supporting the full pressure loading. An eccentric drive mechanism moves the impeller on a circular orbit of constant radius. Chamieh (1983) and more recently Jery (1987) describe the conversion of the facility into the RFTF. Chamieh slowly whirled the impeller at 3 RPM and used an externally mounted stationary force balance to measure the steady and quasi-steady forces experienced by the impeller. To measure unsteady forces Jery mounted a dynamometer between the impeller and the drive shaft. A more powerful whirl motor was installed which increased the range of whirl frequencies. Both the whirl and the main shaft motors were synchronized with the data acquisition system.

2.1 Eccentric Drive Mechanism

The assembly drawing of the test section, Fig. 2.2, shows the eccentric drive mechanism. The main shaft (part #10 of Fig. 2.2) rotates in a double bearing system (8,9,12,13). The inner bearing pair (13) is eccentric to the inner bearing carrier (9). Rotation of the sprocket (11) attached to the inner bearing carrier moves the main

shaft in a circular orbit of radius ε (.0495 inch). The whirling motion of the impeller is imposed by a 2 HP motor driving the eccentric drive mechanism via a timing belt. The 2 HP dc motor from Sabina Electric and Engineering of Orange, CA, has a rated speed of 1750 RPM.

The main shaft within the eccentric drive mechanism is connected by a Thomas coupling (20) to a shaft through the slip ring assembly which extends beyond a 2:1 stepup gear box to an optical encoder. The main drive motor, a 20 HP dc motor also from Sabina, has rated speed of 1750 RPM, enabling a maximum main shaft speed of 3500 RPM. Using optical encoders to provide feedback, each motor was closed-loop controlled to be synchronized with data acquisition, (see chapter 3). Fig. 2.3 is a photograph of the Rotor Force Test Facility. The eccentric drive mechanism and both motors are shown in Fig. 2.4.

2.2 Instrumentation

The force measuring device is a rotating dynamometer mounted between the impeller and the main drive shaft. The dynamometer, also referred to as the internal balance, consists of two parallel plates connected by four parallel bars which are strain gaged to measure the six components of force and moment. Chapter 4 discusses calibration of the dynamometer using an arrangement of cables, pulleys and weights. Drawings are given in Appendix A. Jery (1987) contains further information on the design of the internal balance. Wires from the dynamometer go through the hollow shaft (part #10 of Fig. 2.2) and flexible coupling (20) to the slip ring assembly and then to a rack of Vishay model 2310 signal conditioning amplifiers.

Mounted on the shaft of the flexible coupling are four strain gages forming a Wheatstone bridge to measure torque. They have a gage resistance of 350 ohms and a nominal gage factor of 2. The output signal is amplified prior to the slip ring assembly.

The flow rate through the pump loop was measured by a turbine flow meter.

The flow was throttled by a "silent valve" which was comprised of a block of elastomer containing about 200 longitudinal holes that was squeezed axially by a hydraulic cylinder. The oil pressure to the hydraulic cylinder was controlled by a servo-valve under feedback control from the turbine flow meter.

Two Statham pressure transducers were used to measure the static pressure after a honeycomb screen at the end of the upstream and downstream flow smoothing sections. For observation, the static pressure in the pipe immediately upstream of the impeller and in the cavity surrounding the internal balance were measured by dial gauges. In addition a Heise pressure gauge was connected to the downstream smoothing chamber. The datum pressure of the pump loop was determined by the absolute pressure of the air inside an inner tube in the reservoir. With the use of a vacuum pump or a high pressure air line the system pressure could be changed, therefore the cavitation number of the pump could be controlled. Also in the reservoir was a heat exchanger connected to the building's chilled water system. Not shown in Fig. 2.1 is an auxiliary pump on the floor placed upstream of the silent throttle valve with sufficient piping to enable the water to be pumped in either direction through the loop. During the present tests, valves were closed to isolate the auxiliary circuit.

2.3 Water Treatment

A deaeration system was used to lower the air content of the water. Extra valves and piping were added to connect the pump loop to the deaeration circuit. From the highest point of each section of the pump loop, bleed lines were connected to a water accumulator of the vacuum system. After filling the pump loop, trapped air was bled out. Air was also removed while cavitating the impeller. A Van Slyke Blood Gas Analyzer was used to measure the dissolved air content. The pump loop water is a mixture of distilled and de-ionized water. To prevent corrosion the water was treated chemically by maintaining a concentration of about 700 ppm sodium chromate (Na_2CrO_4) and a minimum pH of 8 through addition of potassium

hydroxide (KOH).

2.4 Impellers and Volutes Tested

A five bladed, cast bronze impeller, donated by the Byron-Jackson Company of Commerce, CA was used. Its specific speed was .57. Fig. 2.5 is a drawing of the impeller, designated Impeller X. The impeller was tested in a spiral volute of trapezoidal cross section, Volute A. It was designed and constructed of fiberglass by Chamieh (1983) using procedures described in Lazarkiewicz and Troskolanski (1965) to be "well-matched" with Impeller X. The cross sectional area varies linearly with distance from the tongue, with the largest area being 3.22 in^2. Fig. 2.6 shows the overall geometry of the volute. Cross sections in increments of 45 degrees are given in Fig. 2.7. Fig. 2.8 is an assembly drawing of Impeller X and Volute A installed in the test section. To reduce leakage flow from the impeller discharge along the front shroud to the inlet, rings were installed inside the volute in addition to the front face seal. Impeller X was used in the bulk of the data presented, including all of the measurements in the presence of cavitation. Fig. 2.9 is a photograph of Impeller X. Fig. 2.10 shows Impeller X and Volute A installed in the test section.

Also used was one half of the double-suction impeller of the High Pressure Oxygen Turbopump (HPOTP) of the Space Shuttle Main Engine (SSME), provided by the George C. Marshall Space Flight Center and the Rocketdyne Division of Rockwell International. The impeller, designated Impeller R, has a centrifugal section with eight blades and an axial inducer section with four blades. Four of the centrifugal blades are partial blades. They have a shorter chord length than the other four full blades. The impeller was modified prior to installation. The principal change was a slight reduction in the outlet diameter. It was installed in Volute E, which has seventeen circular arc vanes and an elliptical cross section. The volute was donated by Rocketdyne Division, Rockwell International, Canoga Park, CA. Data taken with Impeller R is presented in Chapter 5 where a mechanical resonance that was detected in the rotating frame measurements is discussed.

The impeller dimensions used to non-dimensionalize the data are summarized below.

Table 2.1 Impeller Dimensions

Impeller	r_1 (inch)	r_2 (inch)	b_2 (inch)	# of blades
X	1.954	3.188	.62	5
R	2.425	3.3	.57	4 inducer/8 impeller
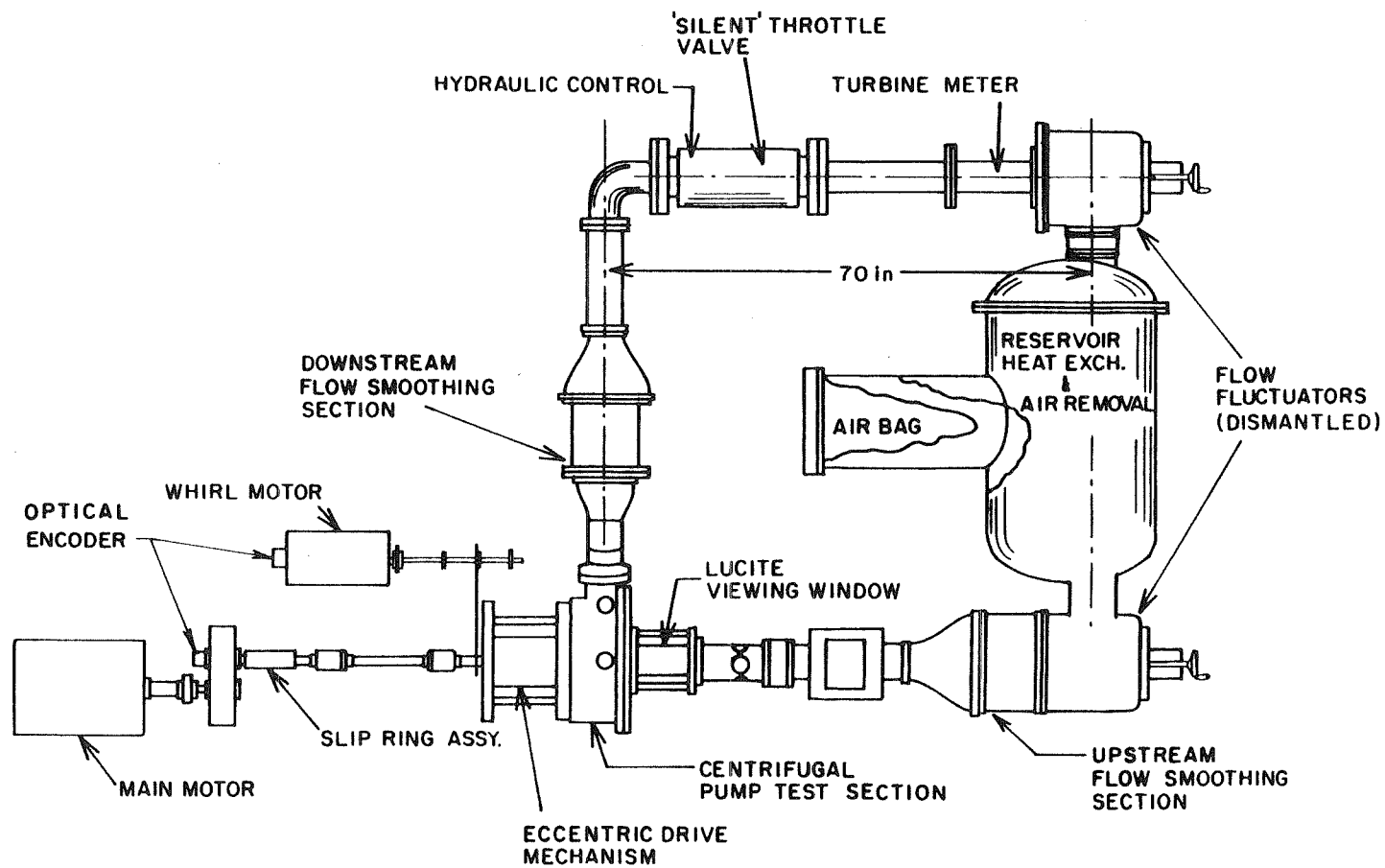
Fig. 2.1   Layout of the Rotor Force Test Facility.

FLOW IN

FLOW OUT

PLAN VIEW
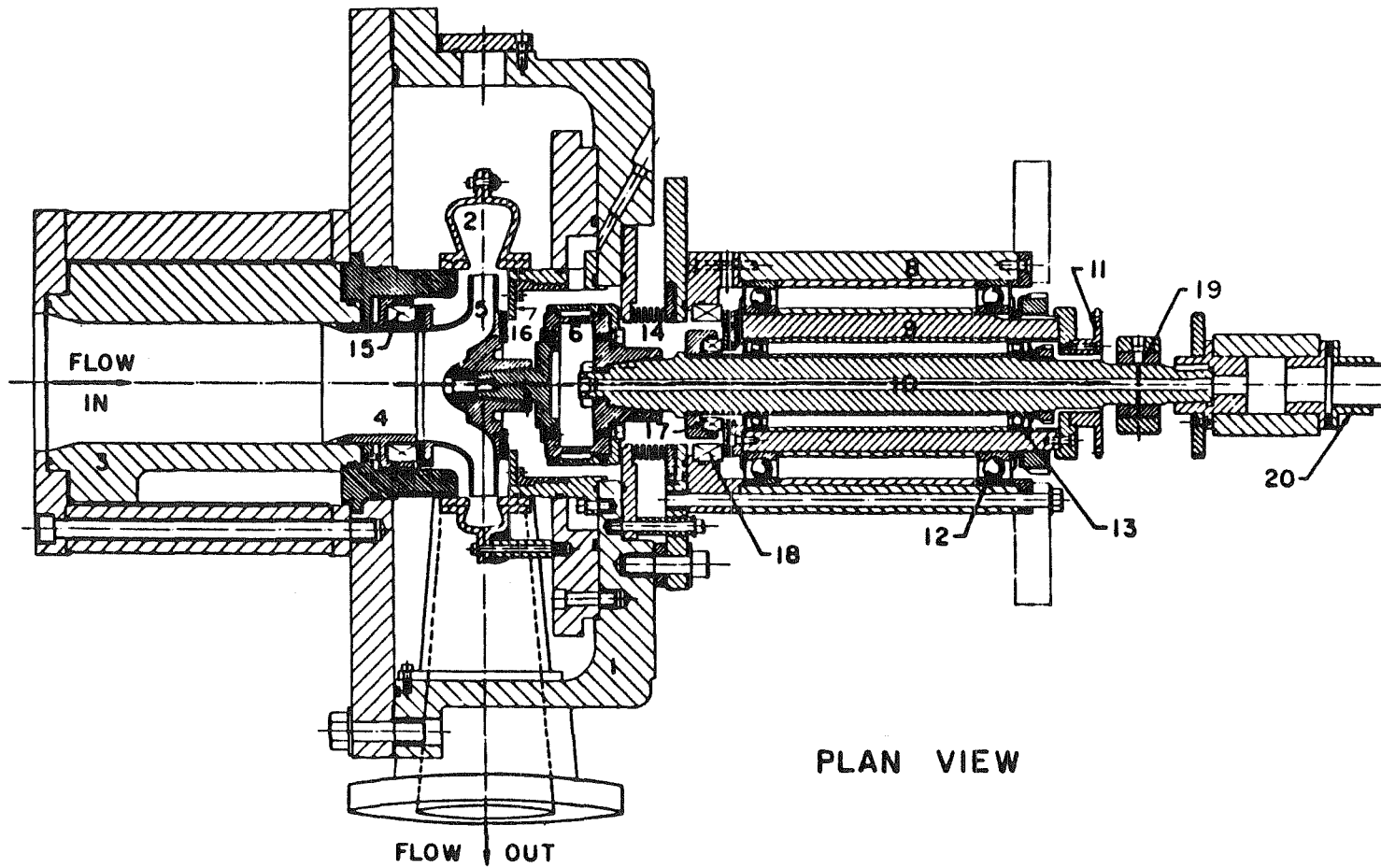
Fig. 2.2 Assembly drawing of the test section and the eccentric drive mechanism. Pump housing, (1); volute (2); inlet connection (3); inlet bell (4); impeller (5); rotating dynamometer (6); eccentric drive mechanism: outer and inner bearing carriers (8 and 9), main shaft (10), orbiting motion sprocket (11); outer and inner bearing sets (12 and 13); bellows (14); impeller front face seal (15); impeller back seal (16); eccentric drive inner and outer face seals (17 and 18); air bearing stator (19); flexible coupling (20).
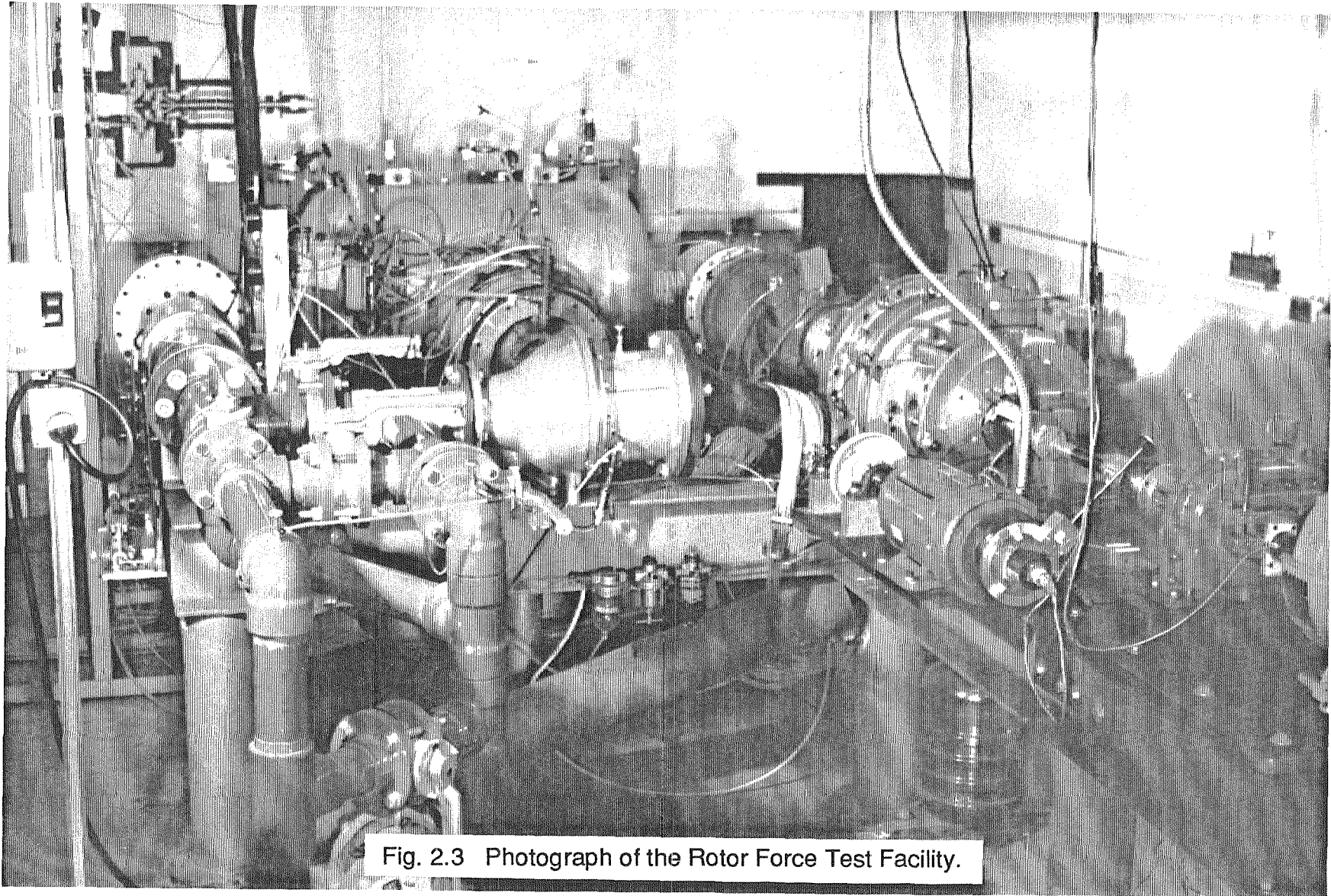
Fig. 2.3 Photograph of the Rotor Force Test Facility.
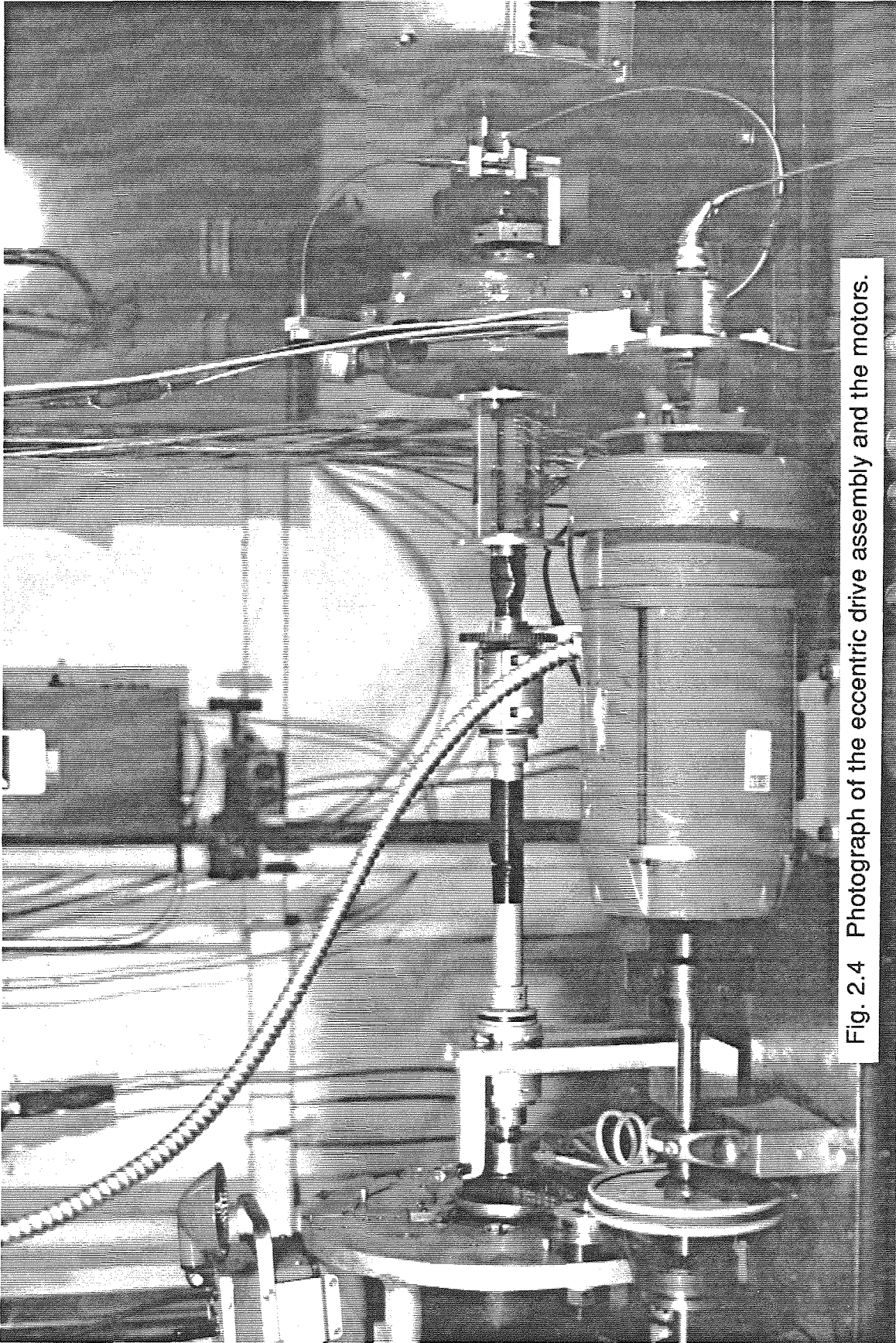
Fig. 2.4 Photograph of the eccentric drive assembly and the motors.
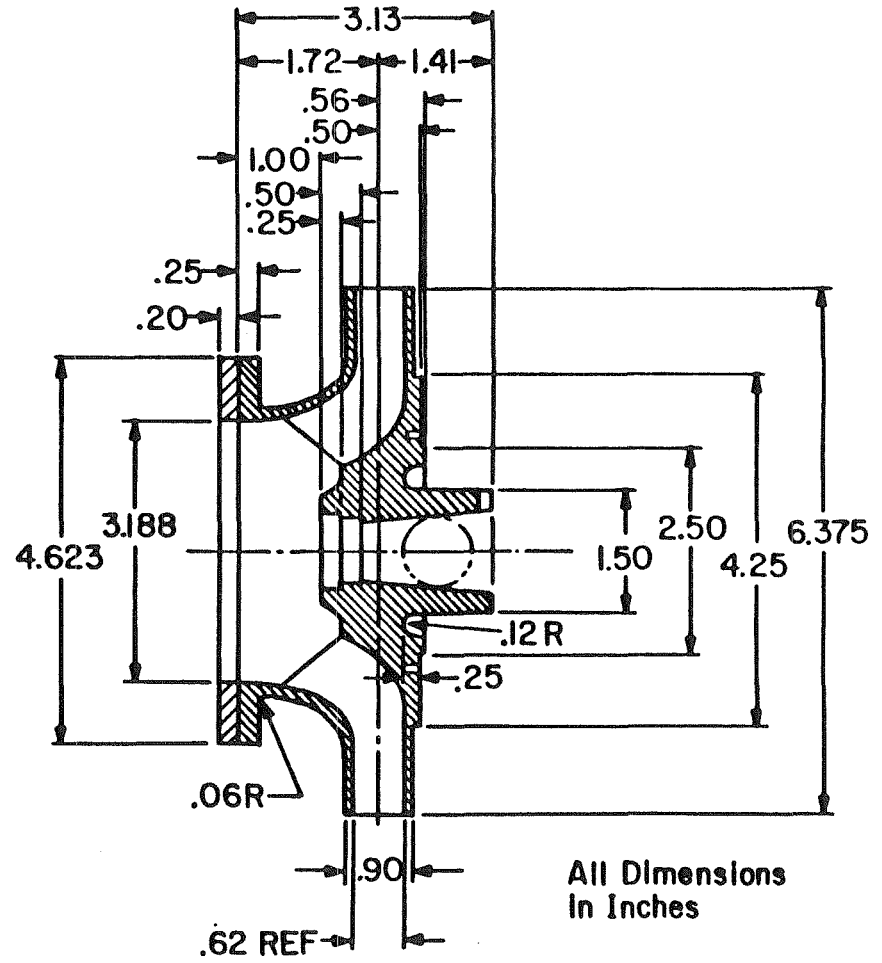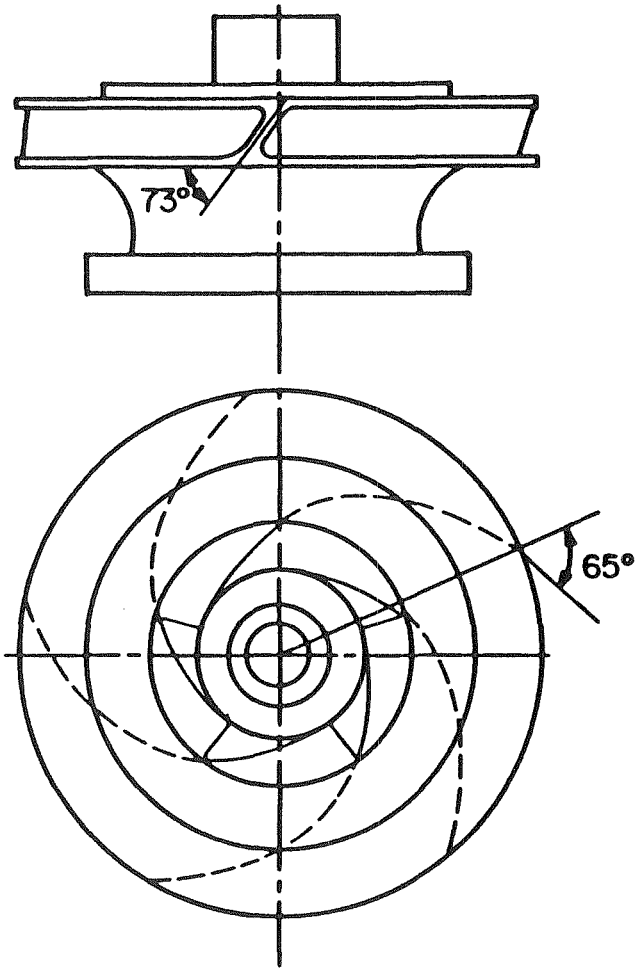
Fig. 2.5   Drawing of Impeller X.
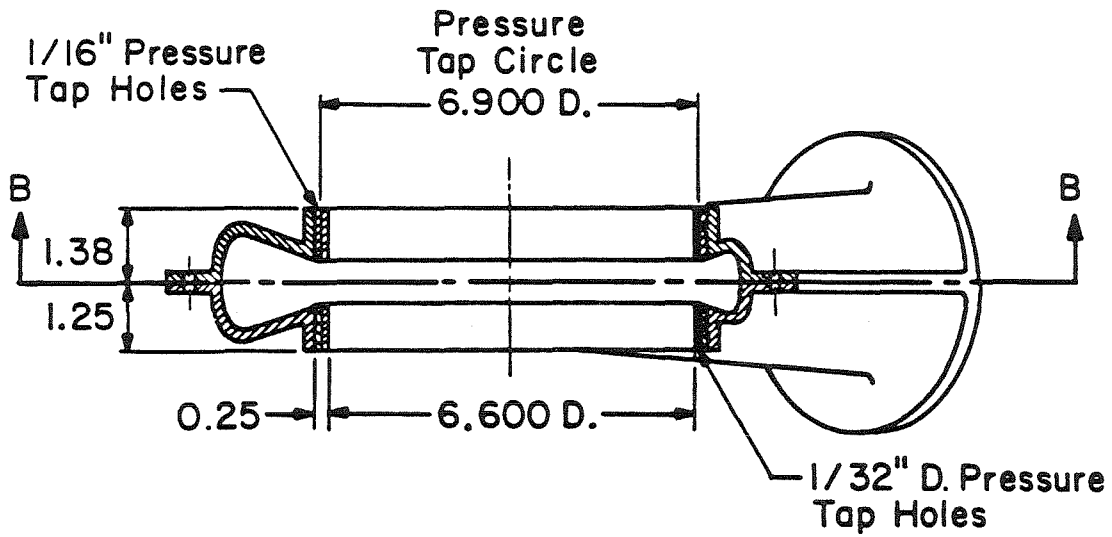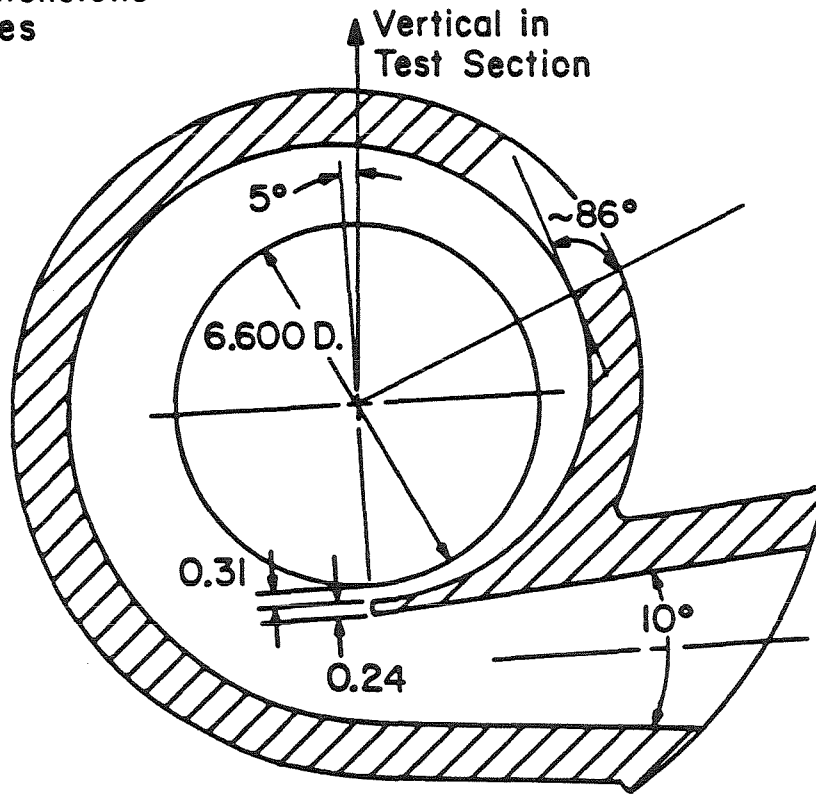
Fig. 2.6   Drawing of the overall geometry of Volute A.
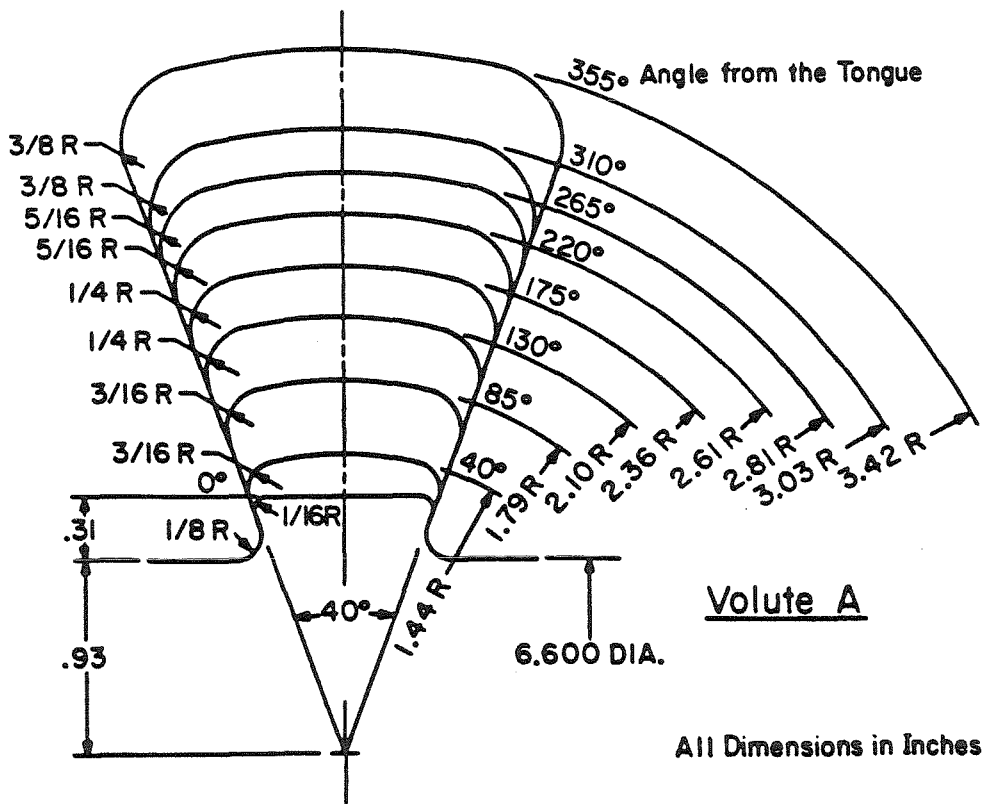
Fig. 2.7   Cross sections of Volute A in increments of 45°.

ϕ 3.0
(76.2 mm)
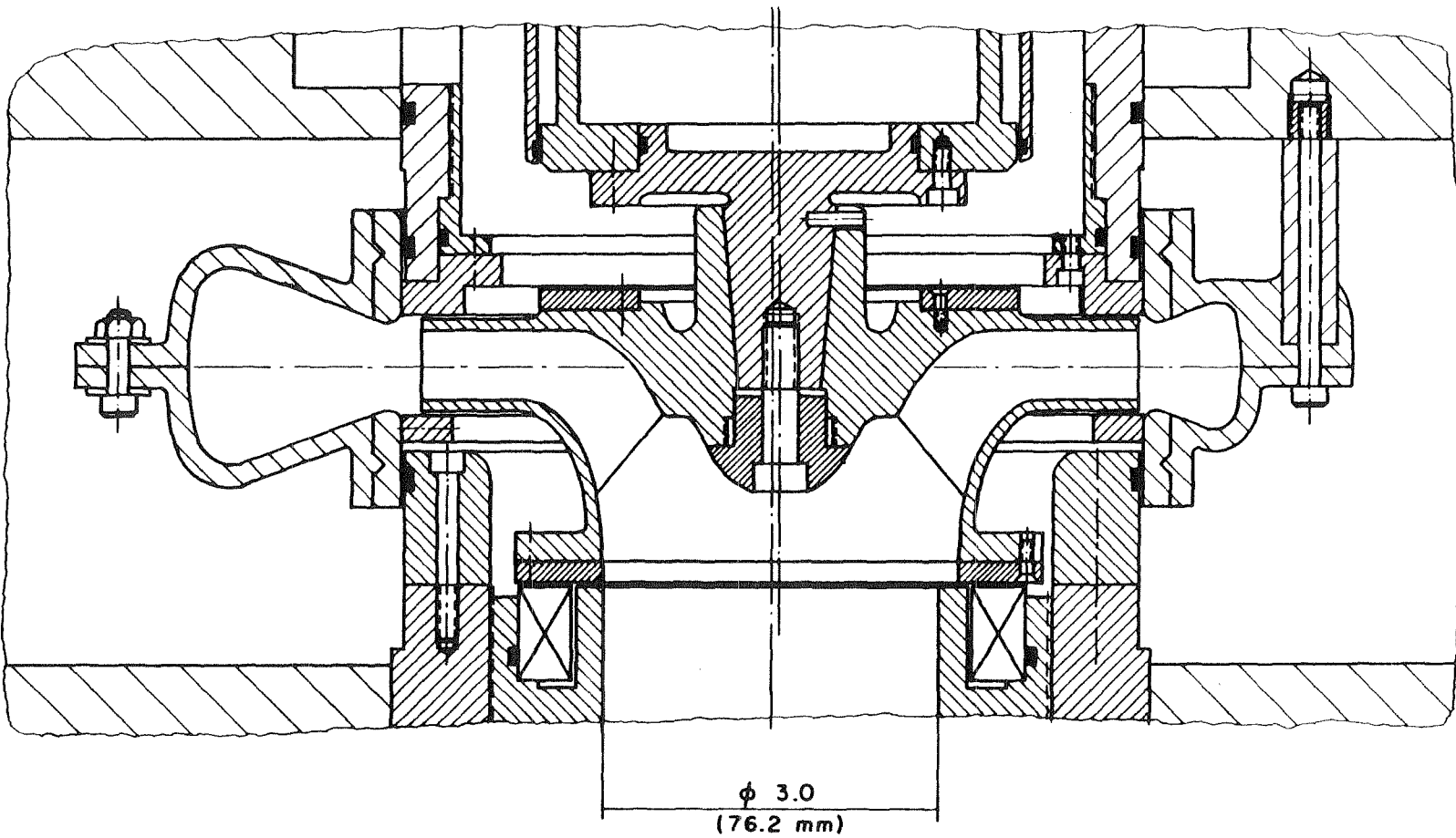
Fig. 2.8 Assembly drawing of Impeller X and Volute A installed in the test section.
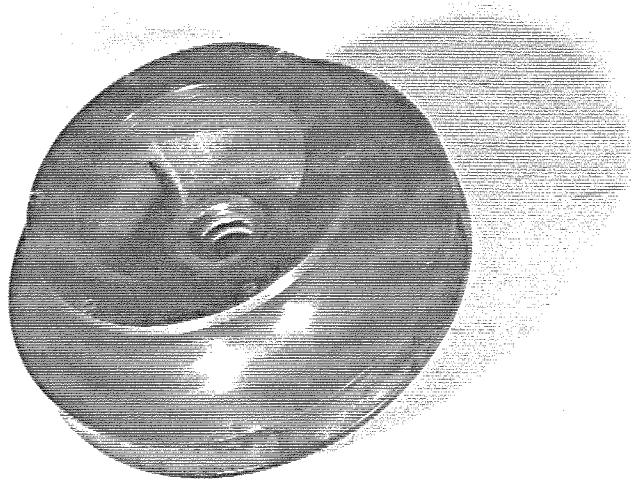
Fig. 2.9   Photograph of Impeller X.
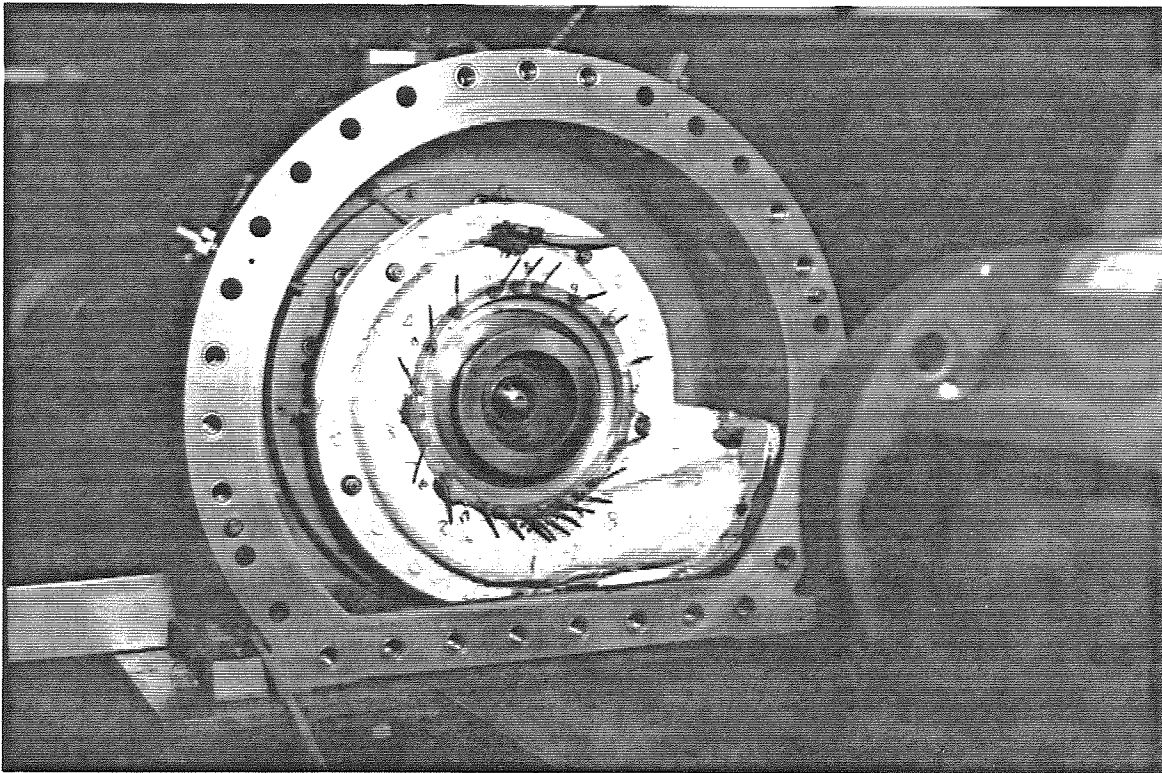
Fig. 2.10   Photograph of Impeller X and Volute A installed in the test section.

Chapter 3

Data Acquisition and Processing

The force on the impeller is measured by the Wheatstone bridges of the dynamometer mounted on the drive shaft behind the impeller. The signals from the bridges go from the rotating dynamometer to slip rings then through cables across the ceiling to a rack of signal conditioning amplifiers. The amplifier outputs are sampled by an analog-to-digital (A/D) converter and stored in the memory of a desktop personal computer. This chapter will explain how this data acquisition is accomplished. The data acquisition system has four elements, the data taker (A/D converter and computer), two motor closed-loop control systems, and a frequency multiplier/divider which synchronizes the previous three elements.

3.1 Processing of Hydrodynamic Forces

Before discussing the system, the objective of subsequent processing will be considered. The hydrodynamic force on a rotating impeller which is translating along a circular orbit of a small radius can be expressed in the stationary frame as

$$\begin{pmatrix} F_x(t) \\ F_y(t) \end{pmatrix} = \begin{pmatrix} F_{ox} \\ F_{oy} \end{pmatrix} + \begin{bmatrix} A_{xx} & A_{xy} \\ A_{yx} & A_{yy} \end{bmatrix} \begin{pmatrix} \varepsilon \cos \Omega t \\ \varepsilon \sin \Omega t \end{pmatrix} \tag{3.1}$$

where Ω is the frequency of the imposed whirl orbit. Referring to Fig. 3.1, the lateral forces in the laboratory frame, F_x and F_y, are related to the lateral forces detected by the dynamometer in the rotating frame, F_1 and F_2, by a rotation through the angle $-\omega t$, where ω is the frequency of main shaft rotation.

$$F_x(t) = F_1(t) \cos(\omega t) - F_2(t) \sin(\omega t)$$

$$F_y(t) = F_1(t) \sin(\omega t) + F_2(t) \cos(\omega t) \tag{3.2}$$

Taking the angle from the volute tongue, φ_V, to be zero, $\mathbf{F}_o$ and $[\mathbf{A}]$ will first be written in the laboratory frame with the x-axis vertically upward and then rotated into the volute frame. Combine Eqns. (3.1) and (3.2) to yield

$$F_1(t)\cos(\omega t) - F_2(t)\sin(\omega t) = F_{ox} + A_{xx}\varepsilon\cos(\Omega t) + A_{xy}\varepsilon\sin(\Omega t)$$

$$F_1(t)\sin(\omega t) + F_2(t)\cos(\omega t) = F_{oy} + A_{yx}\varepsilon\cos(\Omega t) + A_{yy}\varepsilon\sin(\Omega t)$$

$$(3.3)$$

The components of the steady force are obtained by averaging each equation over time.

$$F_{ox} = \frac{1}{T}\int_0^T \left\{ F_1(t)\cos(\omega t) - F_2\sin(\omega t) \right\} dt$$

$$F_{oy} = \frac{1}{T}\int_0^T \left\{ F_1(t)\sin(\omega t) + F_2\cos(\omega t) \right\} dt$$

$$(3.4)$$

The time interval T is given below. Obtain the Fourier cos and sin coefficients at Ω to get the elements of the hydrodynamic force matrix by the following integrations, $\frac{2}{T}\int_0^T \{ \quad \}\cos(\Omega t)\, dt$:

$$A_{xx}\varepsilon = \frac{2}{T}\int_0^T \left\{ F_1(t)\cos(\omega t)\cos(\Omega t) - F_2(t)\sin(\omega t)\cos(\Omega t) \right\} dt$$

$$= \frac{2}{T}\int_0^T \frac{1}{2}\left\{ F_1(t)\cos(\omega - \Omega)t + F_1(t)\cos(\omega + \Omega)t \right.$$

$$\left. - F_2(t)\sin(\omega + \Omega)t - F_2(t)\sin(\omega - \Omega)t \right\} dt$$

$$(3.5)$$

$$A_{yx}\varepsilon = \frac{2}{T}\int_0^T \left\{ F_1(t)\sin(\omega t)\cos(\Omega t) + F_2(t)\cos(\omega t)\cos(\Omega t) \right\} dt$$

$$= \frac{2}{T}\int_0^T \frac{1}{2}\left\{ F_1(t)\sin(\omega + \Omega)t + F_1(t)\sin(\omega - \Omega)t \right.$$

$$\left. + F_2(t)\cos(\omega - \Omega)t + F_2(t)\cos(\omega + \Omega)t \right\} dt$$

$\frac{2}{T}\int_0^T \{ \quad \}\sin(\Omega t)\, dt$:

$$A_{xy}\varepsilon = \frac{2}{T} \int_0^T \left\{ F_1(t) \cos(\omega t) \sin(\Omega t) - F_2(t) \sin(\omega t) \sin(\Omega t) \right\} dt$$

$$= \frac{2}{T} \int_0^T \frac{1}{2} \left\{ F_1(t) \sin(\omega + \Omega)t - F_1(t) \sin(\omega - \Omega)t \right.$$

$$\left. - F_2(t) \cos(\omega - \Omega)t + F_2(t) \cos(\omega + \Omega)t \right\} dt$$

$$A_{yy}\varepsilon = \frac{2}{T} \int_0^T \left\{ F_1(t) \sin(\omega t) \sin(\Omega t) + F_2(t) \cos(\omega t) \sin(\Omega t) \right\} dt \qquad (3.6)$$

$$= \frac{2}{T} \int_0^T \frac{1}{2} \left\{ F_1(t) \cos(\omega - \Omega)t - F_1(t) \cos(\omega + \Omega)t \right.$$

$$\left. + F_2(t) \sin(\omega + \Omega)t - F_2(t) \sin(\omega - \Omega)t \right\} dt$$

In order to compute the components of the steady force $\mathbf{F_o}$ and the hydrodynamic force matrix [A], the orientation of the impeller and its location along its circular orbit must be imparted to the data acquisition system. Using a frequency multiplier/divider to provide command signals and a closed-loop control for each motor, the orientation and position of the dynamometer were synchronized with data acquisition, see Fig. 3.2. Non-cavitating tests on an inducer were curtailed because of failure of the whirl motor closed-loop control to maintain phase. Also the power supply of the original data taker, which performed an A/D conversion and stored the sum over a specified number of cycles, was damaged. The data taker and both motor closed-loop controls were replaced, though the basic philosophy was not changed. Because the original data taker stored only the cumulative value of each of the sampled 1024 data points per cycle of the reference frequency, the motor closed-loop control system enabled ensemble averaging over successive cycles of the reference frequency during which the impeller orientation and position on the whirl orbit would repeat. Over one cycle of the reference frequency there are an integral number of rotations of the main shaft and whirl motors. The modified data acquisition system will be presented.

Given an input TTL signal and two thumb wheel selected integers, I and J, the

frequency multiplier/divider outputs the following pulse signals:

output		application	frequency
N	clock	main motor command	$1024*\omega$
NI/J	clock	whirl motor command	$1024*\Omega$
N/J	clock	A/D conversion start	$1024*\omega/J$
N/J	index	synchronizing reset (time=0)	ω/J

where the clock frequency=1024*index frequency. This frequency multiple was used because the feedback for the motor control is provided by an optical encoder which outputs two signals: an index pulse at every revolution (phase control) and a clock (speed control) of 1024 pulses per revolution. The ratio of the whirl to main motor speed, Ω/ω, is I/J. The N/J index output synchronizes data acquisition. It starts the data taking process and synchronizes phase control of the motors. The motor control will be described at the end of the chapter. A Wavetek model 171 synthesizer/function generator provided the input TTL signal.

Taking the N/J index as the reference frequency, each term of the above equations is a component in the Fourier series expansion of $F_1(t)$ and $F_2(t)$. Summing over NCYC cycles of the reference frequency, $T=NCYC*J/\omega$. For example, the last term of $A_{yy}\varepsilon$ becomes,

$$
\begin{aligned}
\frac{2}{T}\frac{1}{2}\int_0^T -F_2(t)\sin(\omega-\Omega)t\ dt &= -\frac{1}{2}\frac{2}{T}\int_0^T F_2(t)\sin\left(\frac{J-I}{J}\omega t\right)dt \\
&= -\frac{1}{2}F_{2S}^{J-I}
\end{aligned}
\tag{3.7}
$$

where the subscript refers to the sin or cos component and the superscript denotes the harmonic number of the fundamental frequency ω/J. Rewriting Eqns. (3.4)–(3.6),

$$F_{ox} = \frac{1}{2}(F_{1C}^J - F_{2S}^J)$$

$$F_{oy} = \frac{1}{2}(F_{1S}^J + F_{2C}^J)$$

$$A_{xx} = \frac{1}{2\varepsilon}(F_{1C}^{J-I} - F_{2S}^{J-I} + F_{1C}^{J+I} - F_{2S}^{J+I})$$

$$A_{xy} = \frac{1}{2\varepsilon}(-F_{1S}^{J-I} - F_{2C}^{J-I} + F_{1S}^{J+I} + F_{2C}^{J+I})$$

$$A_{yx} = \frac{1}{2\varepsilon}(F_{1S}^{J-I} + F_{2C}^{J-I} + F_{1S}^{J+I} + F_{2C}^{J+I})$$

$$A_{yy} = \frac{1}{2\varepsilon}(F_{1C}^{J-I} - F_{2S}^{J-I} - F_{1C}^{J+I} + F_{2S}^{J+I})$$

$$(3.8)$$

The unsteady force, $[A]\varepsilon(t)$, due to the eccentric motion of the impeller can be resolved into its components, F_n and F_t, normal to and tangential to the whirl orbit, averaged over the orbit. The normal force is considered positive radially outward. The tangential force is considered positive when in the direction of shaft rotation. For the imposed circular whirl orbit,

$$F_n = \frac{1}{2}(A_{xx} + A_{yy})\varepsilon$$

$$F_t = \frac{1}{2}(-A_{xy} + A_{yx})\varepsilon$$

$$(3.9)$$

The hydrodynamic steady force, $\mathbf{F_o}$, and force matrix, $[\mathbf{A}]$, are presented in the volute frame of reference. The expressions above are rotated through an angle φ_V until the x-axis passes through the volute tongue. Appendix B contains a complete derivation.

The lateral hydrodynamic moment experienced by a whirling impeller can be expressed in the stationary frame in the same way as the force $\mathbf{F}(t)$,

$$\mathbf{M}(t) = \mathbf{M_o} + [\mathbf{B}]\varepsilon(t) \qquad (3.10)$$

The moment is measured in the plane bisecting the impeller discharge area. The expressions for $\mathbf{M_o}$ and $[\mathbf{B}]$ in terms of the lateral moments M_1 and M_2 are similar to the above equations.

The forces and moments are non-dimensionalized by the product of the dynamic head using the impeller outlet tip velocity and the impeller discharge area. The impeller outlet radius, r_2, is used as the non-dimensionalizing length for the whirl orbit radius, ε, and for the moments. The force and moment components normal to and tangential to the whirl orbit are non-dimensionalized by the additional factor ε/r_2 so that they are numerically equal to the average of the appropriate matrix elements. The Nomenclature gives the details.

For data taken without whirl, the $\Omega/\omega = 0$ point, the impeller is placed at four locations on its eccentric orbit, each 90 degrees apart, corresponding to the location nearest the volute tongue, farthest, and the two intermediary locations. The steady force is computed from the average of the main shaft component. The matrix [A] at $\Omega/\omega = 0$, the stiffness matrix, is computed by subtracting the appropriate force components of diametrically opposite whirl orbit locations.

To experimentally extract the fluid-induced forces at a given whirl ratio and operating condition, two identical tests are performed, one in air and the other in water, in other words a "dry" run and a "wet" run. The forces from the former experiment are subtracted from the latter to yield the fluid-induced forces. The buoyancy force on the rotor is subtracted separately.

3.2 Data Taker

The 12-bit A/D converter of the data taker can sample up to sixteen channels. The first channel is sampled at the N/J index pulse (time=0). Subsequent samples are taken by following the N/J clock signal. The 1024 samples per data taking cycle are divided among six bridges of the dynamometer at 128 points/bridge/cycle leaving four channels at 64 points/channel/cycle. The highest frequency of a Fourier transform of the bridge signal would be the 64th harmonic, $64*\omega/J$ Hz. The four remaining channels were usually connected to the upstream and downstream pressure transducers, the flow meter, and the shaft torque bridge or to accelerometers. Generally 256 cycles of data were taken to average, the

instantaneous data (8*64kbytes) were occasionally stored for subsequent processing. The data taker circuit drawings are given in Appendix C.

In the event it was desired to Fourier transform a set of data up to a higher frequency, an integrated hardware and software package, the Computerscope ISC-16 system from RC Electronics, Santa Barbara, CA, capable of sampling up to 1 MHz, was used. The Fast Fourier Transform used was written by Hall (1982).

3.3 Motor Control

The two motor closed-loop controls bring the speed and phase of each motor into alignment with the impeller orientation and location on the whirl orbit expected by the data taker. The closed-loop control uses the optical encoder mounted on each shaft as feedback. The motor control system is described in Appendix D.

The actual orientation of the impeller and its location on the whirl orbit was set by manually rotating the optical encoders on the main and whirl shafts, respectively, within their fixtures. The main shaft encoder was set so that at the leading edge of the data taking reference pulse frequency, N/J index, (time=0) the rotating force component F_1 pointed vertically upward. The whirl encoder was set so that the impeller was at the top of its orbit at time=0 of the reference frequency. These orientations were monitored by using the N/J index to externally trigger a stroboscope. Markings on the main shaft and on the eccentric drive mechanism were compared with stationary marks when the stroboscope flashed. This established the proper orientation and location of the impeller required for synchronizing the data acquisition system.

An oscilloscope was used to monitor the phase of each motor. The main shaft encoder index oscillated within ±1 degree of the internally derived command index at 2000 RPM, where the bulk of the data were taken. The instantaneous phase error of the whirl motor was generally ±1 degree. The up/down DAC of each motor was connected to a strip chart recorder. For each data run a record indicative of the closed-loop control performance was obtained. A sudden loss of phase between the

command and encoder indices would cause a ripple in the output of the up/down DAC, as the closed-loop control seeks to reestablish phase. Such an occurrence could usually be heard by the operator.
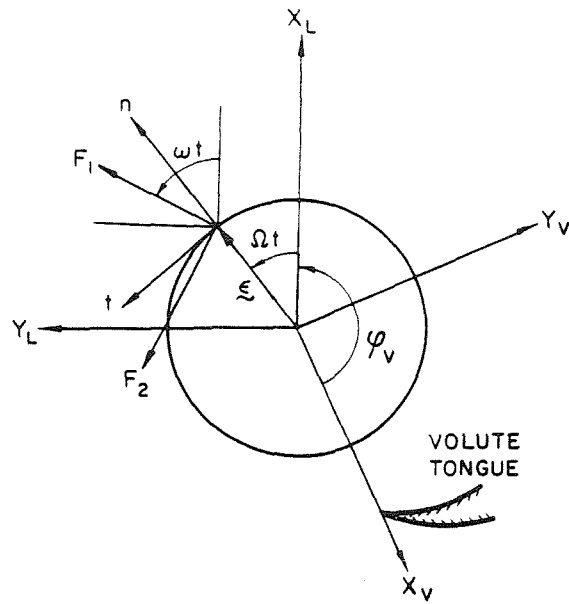
Fig. 3.1 Schematic representation of the lateral forces in the rotating dynamometer frame, F_1 and F_2, on an impeller whirling in a circular orbit. X_L and Y_L represent the stationary laboratory frame, X_V and Y_V the stationary volute frame, and n and t the polar coordinate frame, normal to and tangential to the circular whirl orbit.
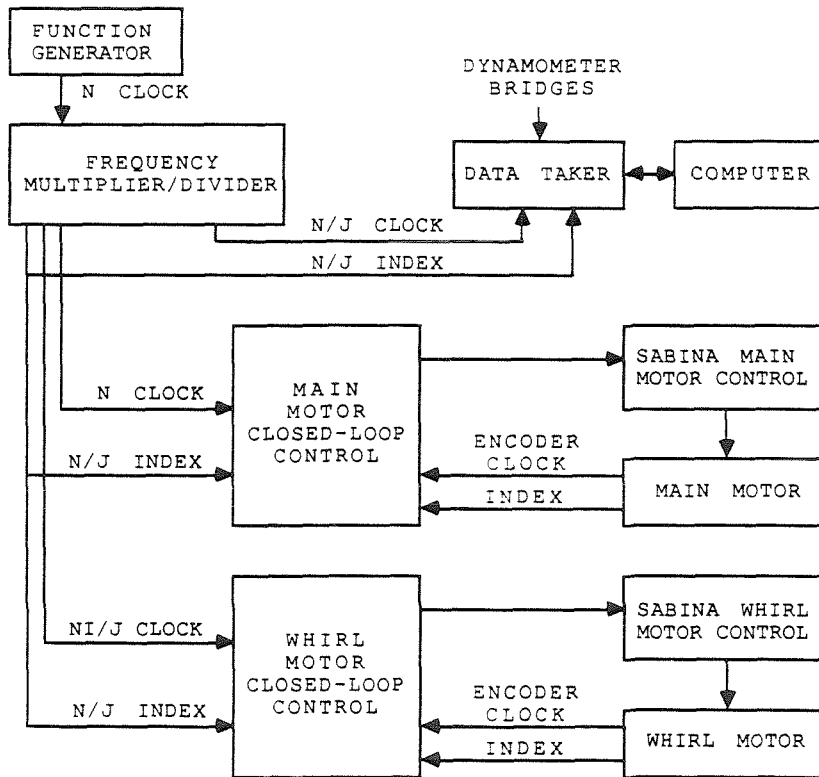
Fig. 3.2 Block diagram of the data acquisition system showing the motor control system and the data taker.

Chapter 4

The Rotating Dynamometer

The dynamometer is mounted between the impeller and the main drive shaft. The dynamometer, also referred to as the internal balance, consists of two parallel plates connected by four parallel bars of square cross section, forming a single monolithic stainless steel structure. The bars are instrumented to measure the six components of force and moment with thirty-six strain gages, forming nine Wheatstone bridges. One bridge is primarily sensitive to thrust, each of the other eight is sensitive to two of the remaining five generalized force components. Three of the bridges are redundant. Appendix A contains drawings showing the placement of the gages. Jery (1987) contains further information on the design of the dynamometer.

4.1 Static Calibration

Calibration of the dynamometer consisted of static force loadings *in situ* and dynamic tests. For each of the six generalized force components, a set of individual loadings in both positive and negative force directions was applied to the dynamometer using a rig of pulleys, cables and weights. The origin of the calibration coordinate frame is the point on the axis of the impeller which is in the plane bisecting the discharge area of Impeller X. The force components defined by calibration nearly coincided with the orientation of primary sensitivity to lateral forces of the Wheatstone bridges formed from the strain gages mounted on the four bars of the dynamometer. The response of the bridges are linear. Correlation coefficients for primary and interaction force loadings are typically 1.000 and .9 respectively. The matrix of the slopes of the bridge voltages vs applied generalized forces is inverted to obtain the calibration matrix.

The static calibration described above had been supplemented earlier by

additional tests described by Jery (1987). These included measurements of drift in time under constant loads, hysteresis loading cycles, larger loads and mixed force loadings.

4.2 Dynamic Behavior

Besides the static calibration, the dynamic response of the dynamometer must be addressed. By rotating the main shaft in air, the dynamometer will sense gravity as a periodic force. In the laboratory reference frame, Fig. 3.1, with the volute tongue angle, φ_V, set to zero,

$$F_x = -mg$$
$$F_y = 0 \tag{4.1}$$

where m is the mass of the impeller and the mounting spindle and g is the gravitational constant. In the rotating frame, the force on the dynamometer is

$$F_1(t) = -mg \cos(\omega t)$$
$$F_2(t) = mg \sin(\omega t) \tag{4.2}$$

For Impeller X the magnitude and phase error of this radial force is presented in Fig. 4.1. For the components, F_1 and F_2, the magnitude is within 1% and the phase error is less than 1 degree. This set of data was taken after remachining the sleeves separating the bearing pairs of Fig. 2.2, see the next chapter.

The weight of Impeller R was measured the same way. It weighs 75% more than Impeller X. The response of the dynamometer in the rotating frame exhibits a resonance near 2950 RPM. Fig. 5.1, which shows F_1 and F_2 for Impeller R before the sleeves were remachined, is in the next chapter where the resonance will be discussed. When resolved into the stationary frame, the resonance disappears. The dynamic response of the dynamometer to the periodic force of gravity is flat.

By rotating and whirling the impeller in air, the dynamometer measures as periodic the gravity and the centrifugal forces from whirling the impeller in a circular

orbit of radius ε. In the dynamometer frame

$$F_1(t) = -mg\cos(\omega t) + m\Omega^2\varepsilon\cos(\omega - \Omega)t$$

$$F_2(t) = mg\sin(\omega t) - m\Omega^2\varepsilon\sin(\omega - \Omega)t$$

$$(4.3)$$

The phase angle of the gravity and centrifugal forces is used to check the orientation of the optical encoders on the main and whirl shafts, respectively. This verifies that at the start of taking data, F_1 points vertically upward and the impeller is at the top of the circular whirl orbit.

In the laboratory frame the steady force $\mathbf{F_o}$ due to gravity is presented in Fig. 4.2 for Impeller X at 2000 RPM. The centrifugal force is presented in Fig. 4.3 as the elements of the "dry" hydrodynamic force matrix $[\mathbf{A}]$. The centrifugal force, which is normal to the whirl orbit, is presented in Fig. 4.4 as the impeller mass, $F_n/(\Omega^2\varepsilon)$. The data, resembling a parabola instead of a constant value, reflects the finite stiffness of the dynamometer-shaft system. As an example, the plotted value of F_n for Ω=1000 RPM (i.e. $\Omega/\omega = .5$ at 2000 RPM) is 2% greater than the value corresponding to an infinitely rigid shaft. The corresponding unsteady dry moment, $M_t/(\Omega^2\varepsilon)$, is included in the figure. Dry whirl tests with $-.6 < \Omega/\omega < 0.6$ were also done at 3000 RPM, increasing the frequency that the dynamometer measures F_n up to 1.6*3000 RPM. Data at 2000 RPM are presented herein because the wet tests were done at 2000 RPM. The rotor-dynamometer-shaft system is modelled as a massless shaft supported by two bearings with an overhung "disk." The gyroscopic effect of deflecting the rotating impeller is included. The details are in Appendix B. The model is presented in Fig. 4.4 as the dotted curve. Results from using this model to process the data for the hydrodynamic forces and moments are also given in Appendix B.

The spectral content of the dynamometer bridges under different tests is presented in Figs. 4.5–7. The instantaneous data were taken using the Computerscope ISC-16 hardware-software package. The response to a lateral impulse load applied to a stationary Impeller X, a hammer test, is shown in Fig. 4.5. Bridge 1 is sensitive to the lateral force F_1 and to torque. The peak at 145 Hz corresponds to the

natural frequency of the dynamometer with Impeller X mounted. For Impeller X rotating and whirling at $\Omega/\omega=.1$ in air, Fig.4.6a–b shows the spectra for bridges 1 and 6. Bridge 6 is sensitive to the lateral force F_2 and lateral moment M_1. Peaks at main shaft, ω, and the main-whirl difference frequency, $\omega - \Omega$, and multiples of line frequency, 60 Hz, are present. The driving frequency of the dc motor (60 Hz) imposes a fluctuating torque. At $\Omega/\omega=.1$ with Impeller X in Volute A at design flow without cavitation, Fig.4.7a–b show the spectra for the same two bridges. Notice that a peak at the sum frequency, $\omega + \Omega$, is now present. This frequency distinguishes the elements of the force matrix [A] from the corresponding unsteady force components F_n and F_t.

Fig. 4.1 The weight of Impeller X in the rotating dynamometer frame, F_1 and F_2, and in the stationary laboratory frame, $\mathbf{F_o}$. Plotted are (a) the magnitude and (b) the phase error from rotating the shaft at various speeds in air.

Fig. 4.2   The weight of Impeller X as the components of the steady force, F_{ox} and F_{oy}, in the stationary volute frame from rotating the shaft at 2000 RPM and whirling in air.
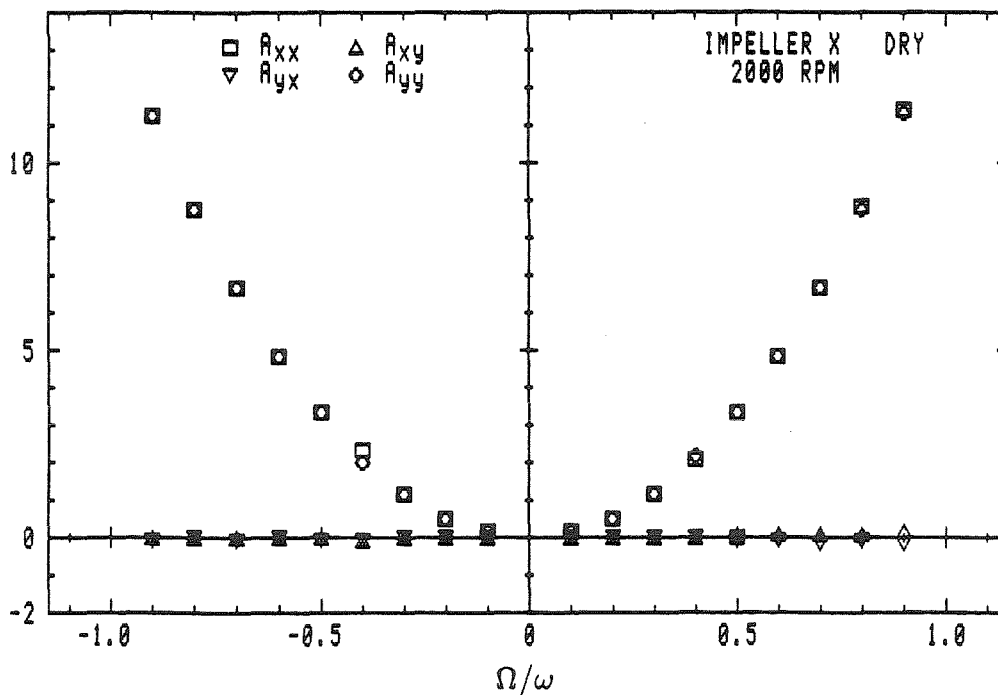
Fig. 4.3   The elements of the rotordynamic force matrix [A] sensed by the dynamometer when rotating the shaft at 2000 RPM and whirling in air.
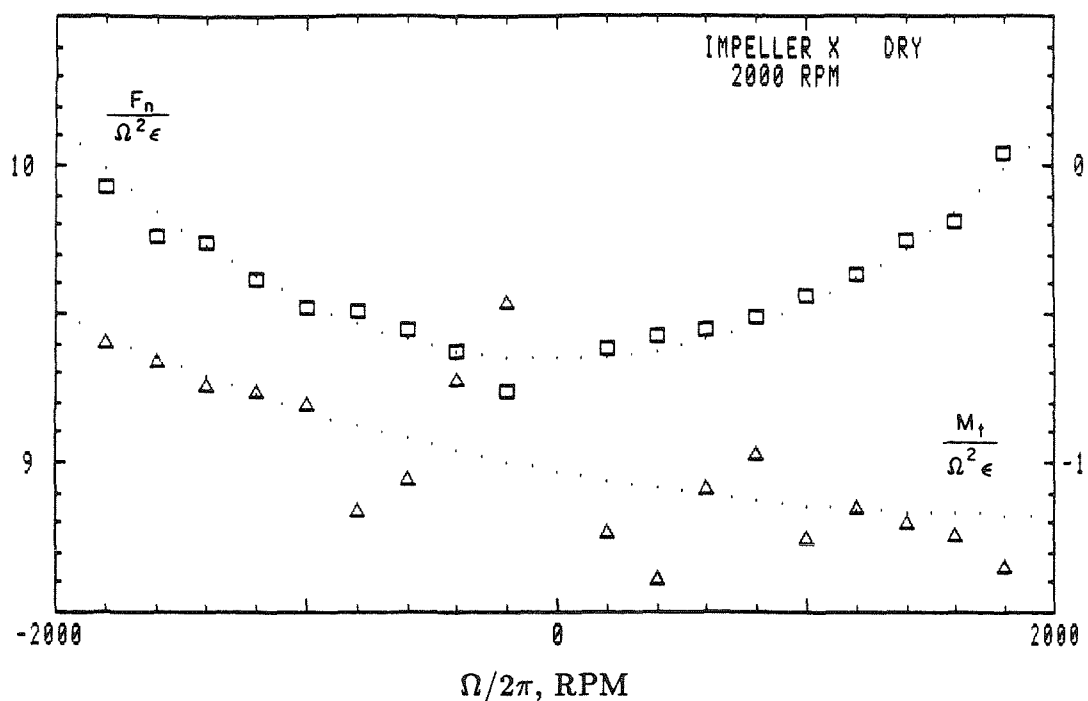
Fig. 4.4 The mass derived from the centrifugal force sensed by the whirling dynamometer, $m = F_n/(\Omega^2\varepsilon)$, and $M_t/(\Omega^2\varepsilon)$ as a function of the whirl frequency, Ω. The dotted curves represent the model from Appendix B.
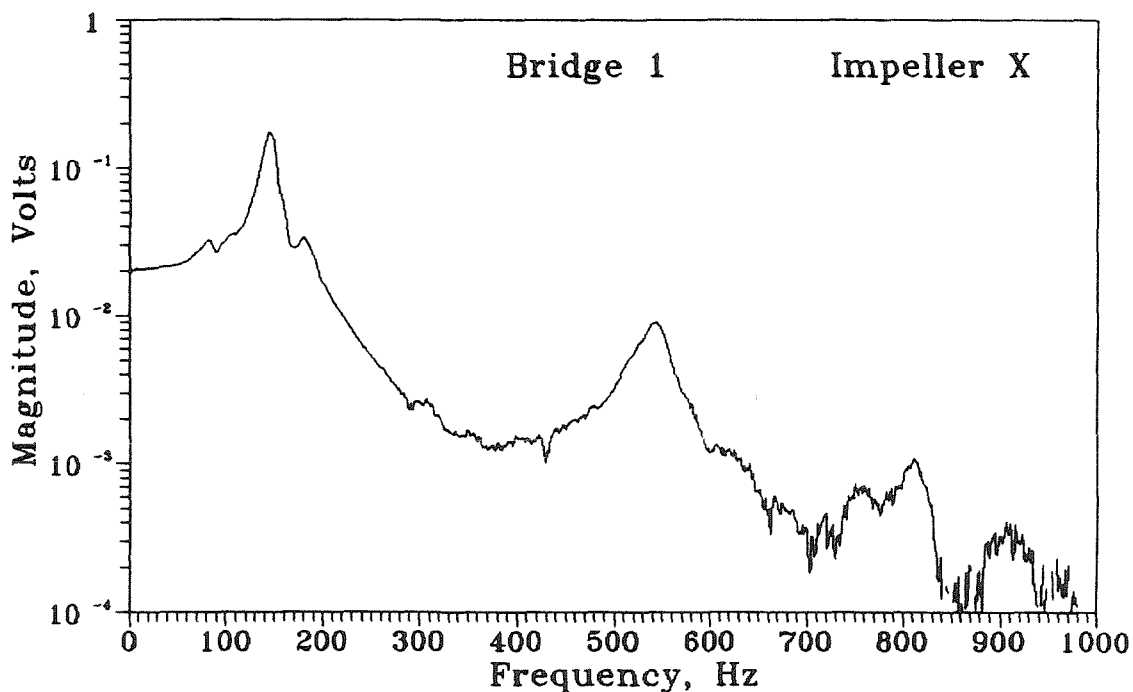
Fig. 4.5 Magnitude spectra of bridge 1 showing the response of the dynamometer-shaft system to a lateral impulse (hammer test) applied to Impeller X in the F_1 direction. The damped natural frequency is at 145 Hz.
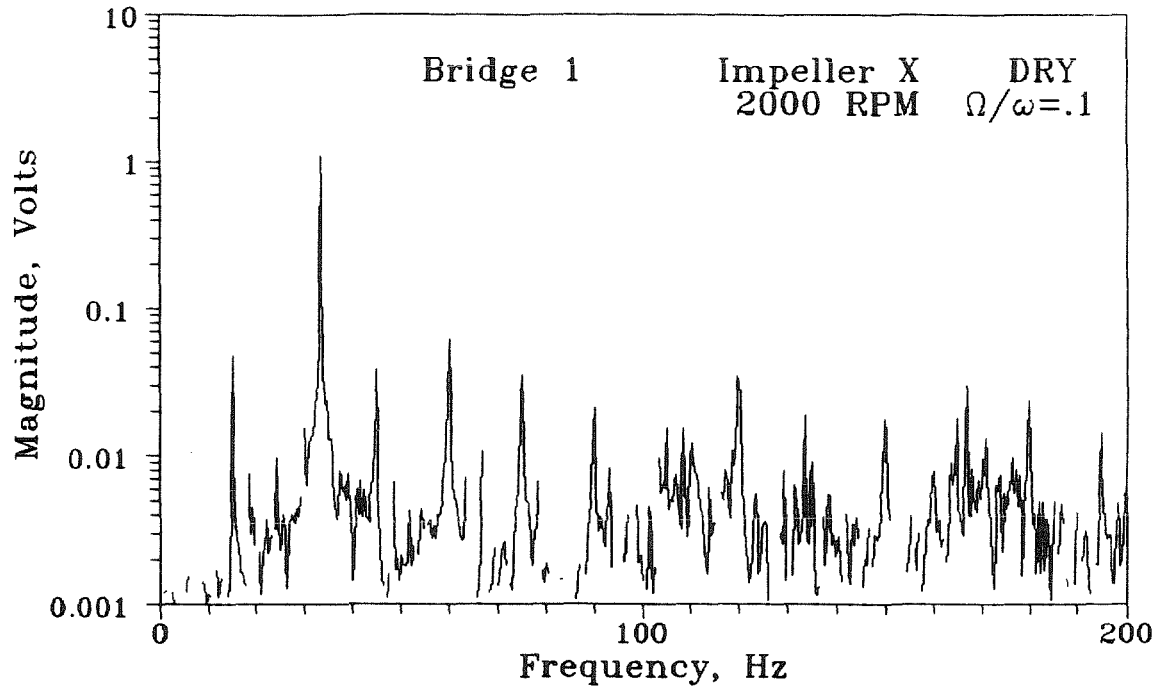
(a)
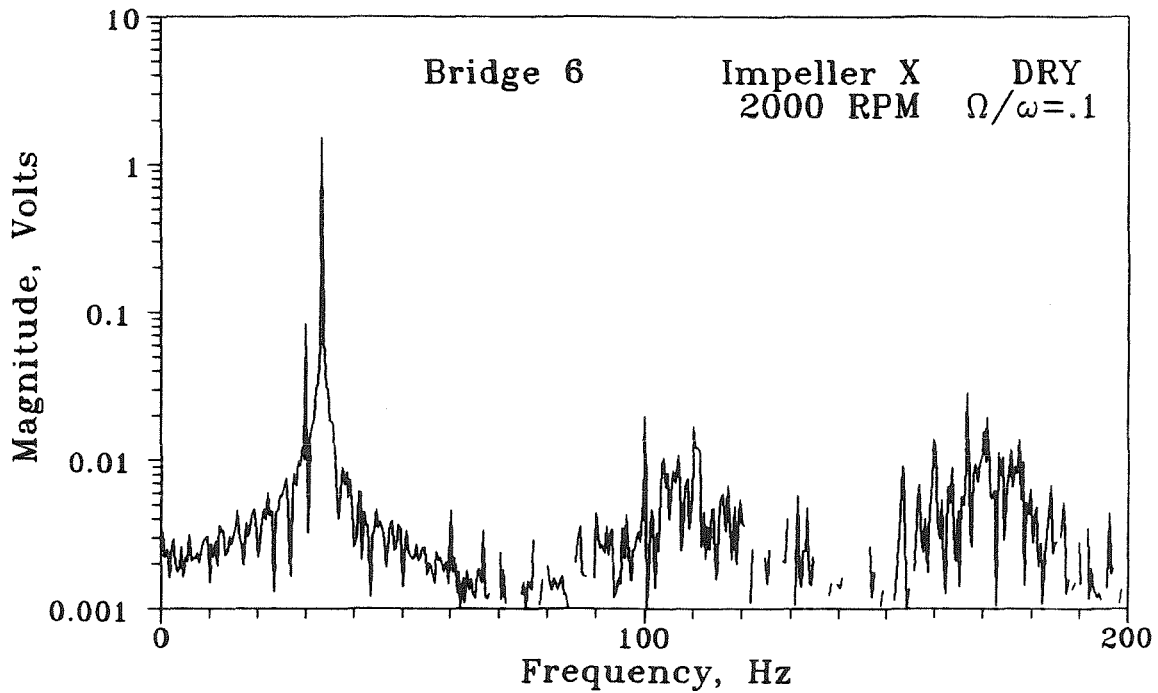
(b)

Fig. 4.6   Magnitude spectra of (a) bridge 1 and (b) bridge 6 of the dynamometer with Impeller X whirling and rotating in air at 2000 RPM with $\Omega/\omega=.1$.
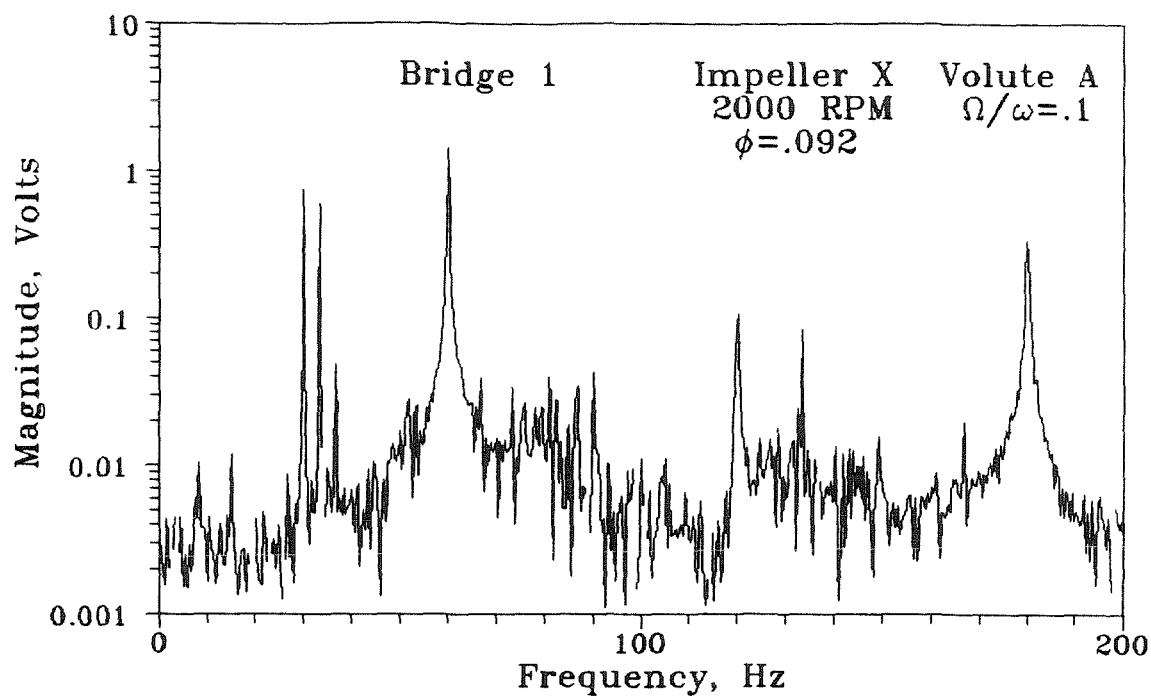
(a)
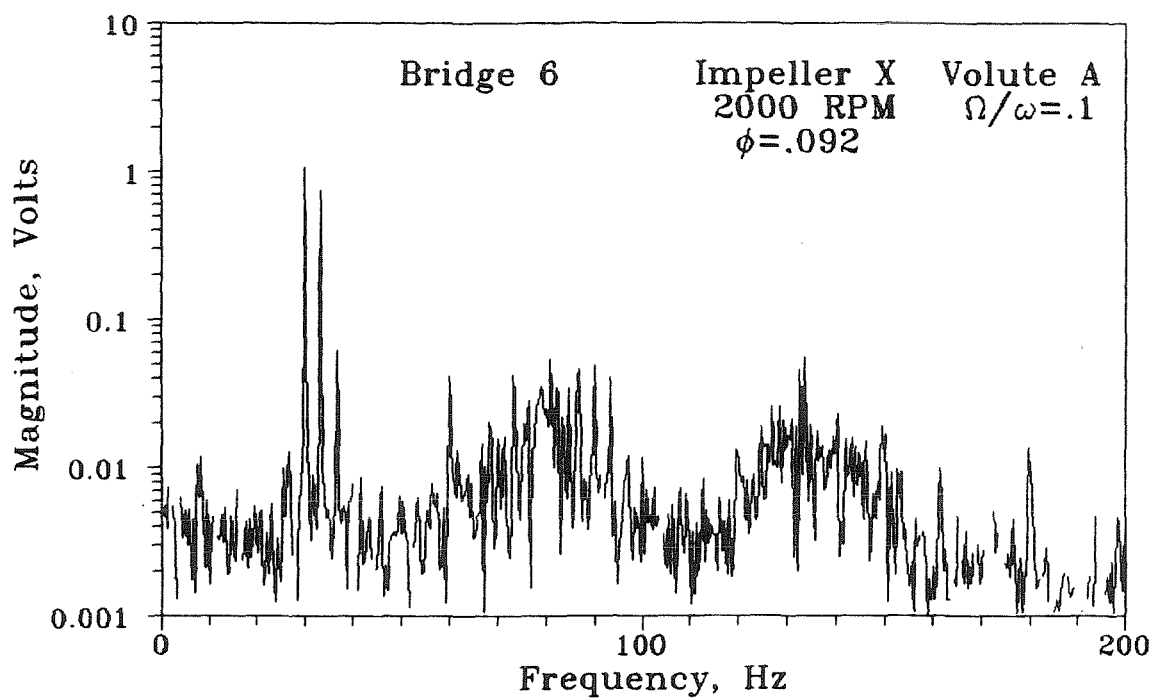
(b)

Fig. 4.7   Magnitude spectra of (a) bridge 1 and (b) bridge 6 of the dynamometer with Impeller X in Volute A at 2000 RPM for non–cavitating design flow at a whirl ratio of Ω/ω=.1.

Chapter 5

Resonance in the Dynamometer

In order to extract the hydrodynamic forces from the measurements in water, the dynamic behavior of the dynamometer must be known through the frequencies of interest. Rotating the shaft in air without whirl subjects the dynamometer in its rotating frame to the periodic force of gravity. The response in magnitude and phase error of the lateral forces F_1 and F_2 should be flat, (refer to Eqn. (4.2)). This chapter examines tests for which the magnitude and phase error depend upon shaft frequency. For all the measurements taken without whirl, the impeller was placed at the top of the whirl orbit. Measurements of the weight of Impeller R by rotating the shaft in air are displayed in Fig. 5.1. The magnitude and phase error of the rotating force components F_1 and F_2 are shown. Also included is the corresponding steady force in the stationary laboratory frame, Eqn. (4.1). For Impeller R the dynamometer exhibits a resonance near 2950 RPM in the rotating frame measurements, the steady force in the stationary frame is unaffected.

An unsuccessful attempt was made to find this frequency in other "dry" data. Accelerometers were placed in various positions on the facility in the hope of gaining information. A Fast Fourier Transform of instantaneous data from the measuring device generally had a frequency component at shaft frequency. Gravity acts as a forcing function to the rotating dynamometer while the accelerometer detects a mass unbalance. The accelerometer data will be discussed after reviewing the dynamometer data.

To examine the hydrodynamic effect upon the observed resonance, Impeller X and Impeller R were installed in Volutes A and E, respectively. With a fixed whirl ratio, each impeller was rotated at various shaft speeds. The resonant frequency for Impeller R had decreased and the peak broadened. The main shaft frequency Fourier components of F_1 and F_2 are presented in Fig. 5.2 showing their contribution

to the components of the steady force F_o, Eqn. (3.8ab). The gravitational and buoyancy forces are subtracted out. Fig. 5.3a–b show the non-dimensionalized F_n and F_t and the appropriate Fourier component of F_1 and F_2. The dry run subtracted was "ideal," $F_n = m\Omega^2\varepsilon$ and $F_t = 0$. When the force components are transformed out of the rotating dynamometer frame the resonance disappears. Figs. 5.4–5 present the same data for Impeller X in Volute A.

The eccentric drive mechanism was disassembled and examined. The parallelism of the sleeves separating the inner and outer bearing pairs of the eccentric drive mechanism was not to the tolerance suggested by the manufacturer. The eccentric drive mechanism was reassembled after machining the sleeve ends. Two accelerometers were placed on the drive shaft side of the eccentric drive mechanism on the plate of Fig. 2.2 outlined by dotted lines. They were positioned to sense a positive acceleration directed radially outward in a horizontal and in a vertical direction, along the X_L and Y_L axes of the laboratory frame, $\varphi_V = 0$. Impellers R and X were rotated at various speeds in air. Dynamometer measurements of the weight of Impeller R are given in Fig. 5.6. Notice that the direction of the deviation of F_1 and F_2 have switched after reassembly. At 2950 RPM the magnitude deviation is approximately 0.8 lbf and the phase error 3°. Stiffening the eccentric drive mechanism reduced the amplitude of the deviation. For Impeller X they have been presented earlier in Fig. 4.1. Fig. 5.7a–b present the magnitude and phase of the accelerometer outputs at shaft frequency. The rapid climb above 3000 RPM suggests a mass unbalance or a resonance in the eccentric drive assembly. The unequal accelerometer outputs indicates an unequal stiffness in the horizontal and vertical directions. Dimentberg (1961) analyzed a shaft system with mass unbalance and unequal stiffness. It exhibited reverse precession, i.e. reverse synchronous whirl. The phase difference of nearly 180° in Fig. 5.7b supports this conclusion. An unsymmetric lateral stiffness will be observed in the rotating frame as a time dependent stiffness.

In the laboratory frame the force of gravity is stationary, $F = -mg$. In the

rotating dynamometer frame $F = -mge^{-i\omega t}$, using a complex representation of the force components. Unequal stiffness introduces an additional complex conjugate response, $-mgf(\omega)e^{i\omega t}$, where $f(\omega)$ is some function of stiffness. Rotating back into the laboratory frame, the additional response becomes $-mg\,f(\omega)e^{i2\omega t}$. Fig. 5.8a,b show the magnitude of the accelerometer outputs at twice shaft frequency for Impellers R and X, respectively. The peaks above the background correspond with the peculiarities of the dynamometer response in the rotating frame.

From the figures presented, the resonance encountered in the force components F_1 and F_2 in the rotating dynamometer frame disappears when the forces are transformed into the stationary laboratory frame. Consequently, the resonance encountered does not affect the hydrodynamic forces that are presented in subsequent chapters. This chapter was intended to provide some documentation on the dynamic behavior of the apparatus.
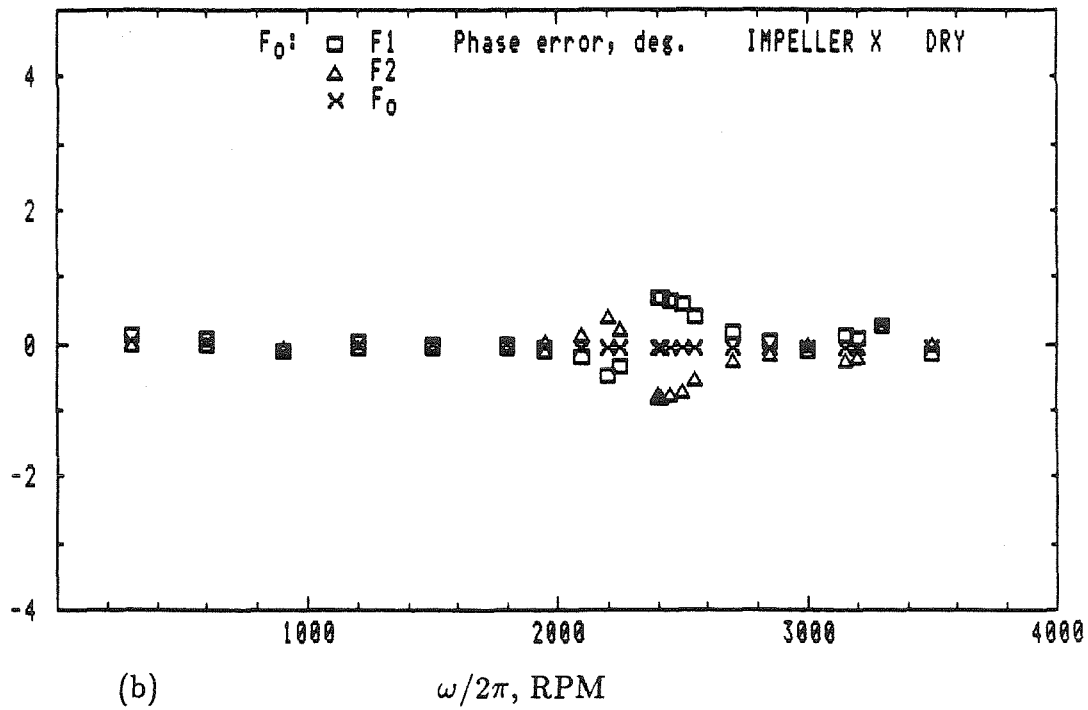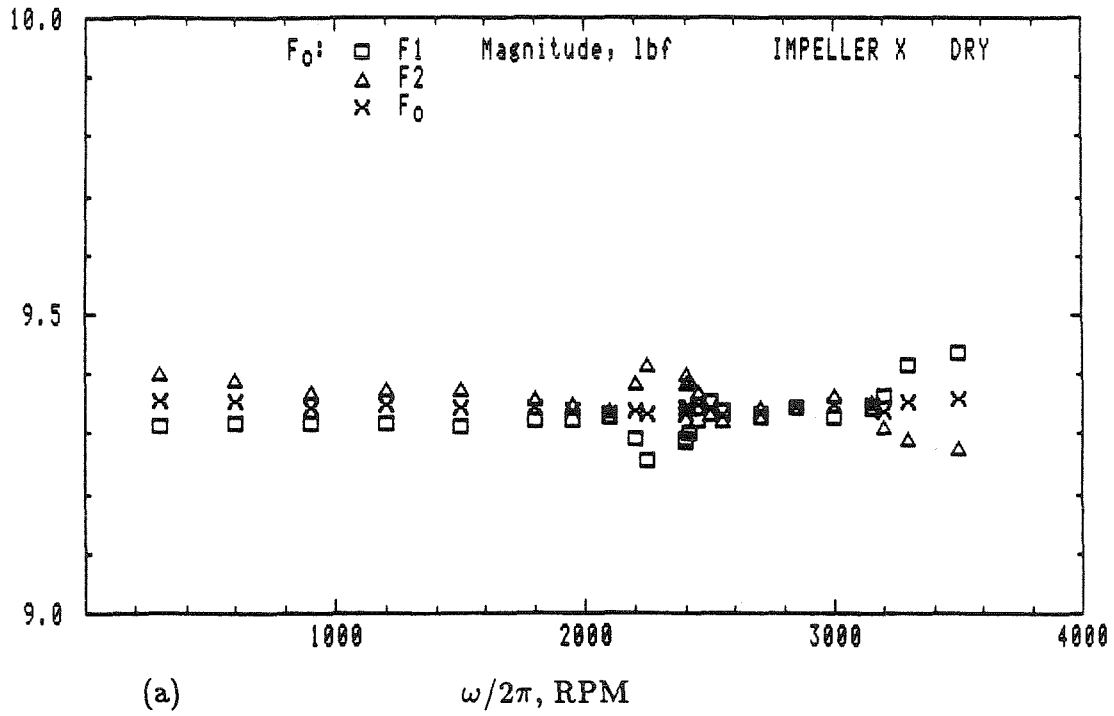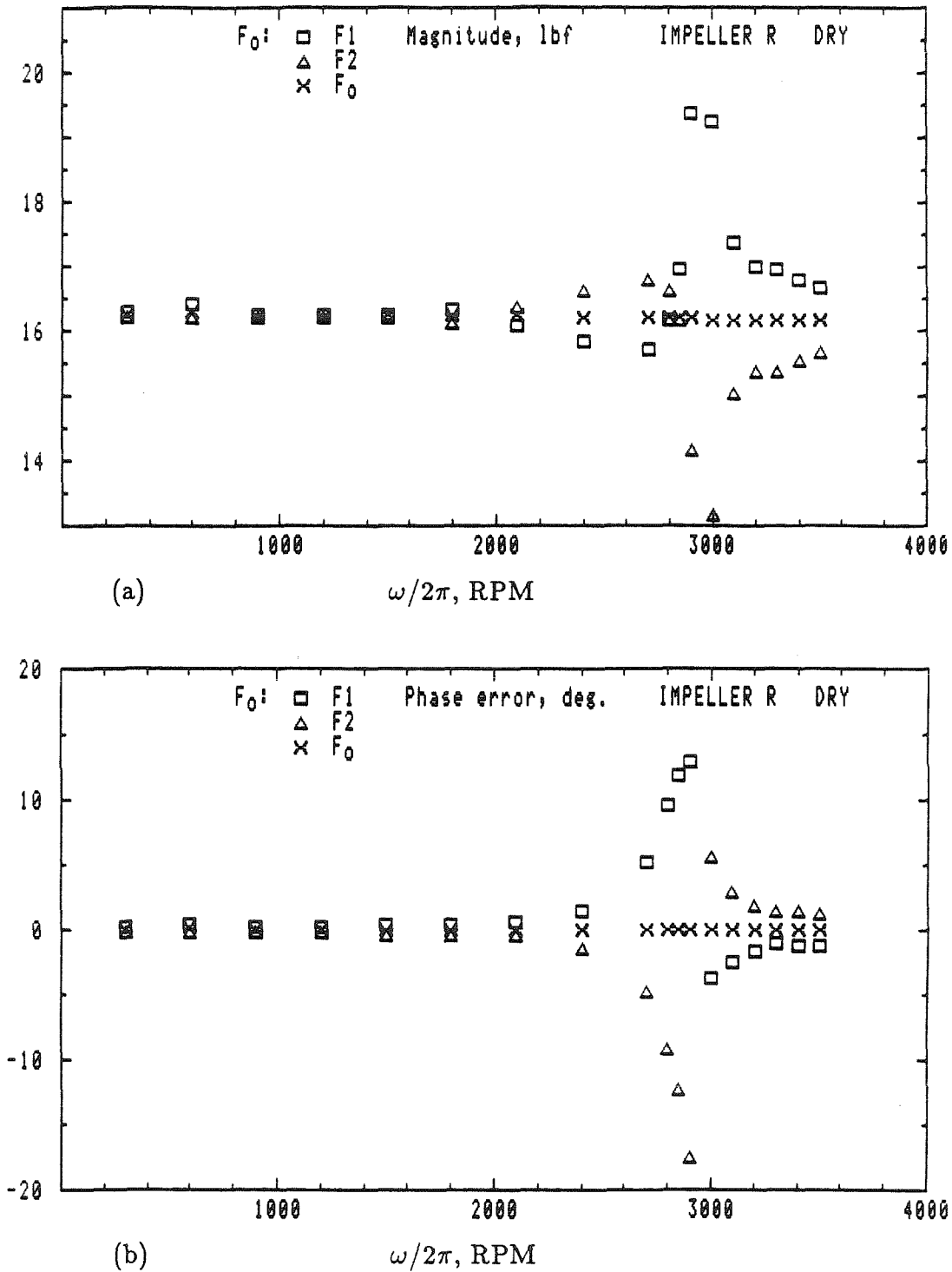
Fig. 5.1 The weight of Impeller R in the rotating dynamometer frame, F_1 and F_2, and in the stationary laboratory frame, $\mathbf{F_o}$. Plotted are (a) the magnitude and (b) the phase error from rotating the shaft at various speeds in air, before machining the bearing sleeves.
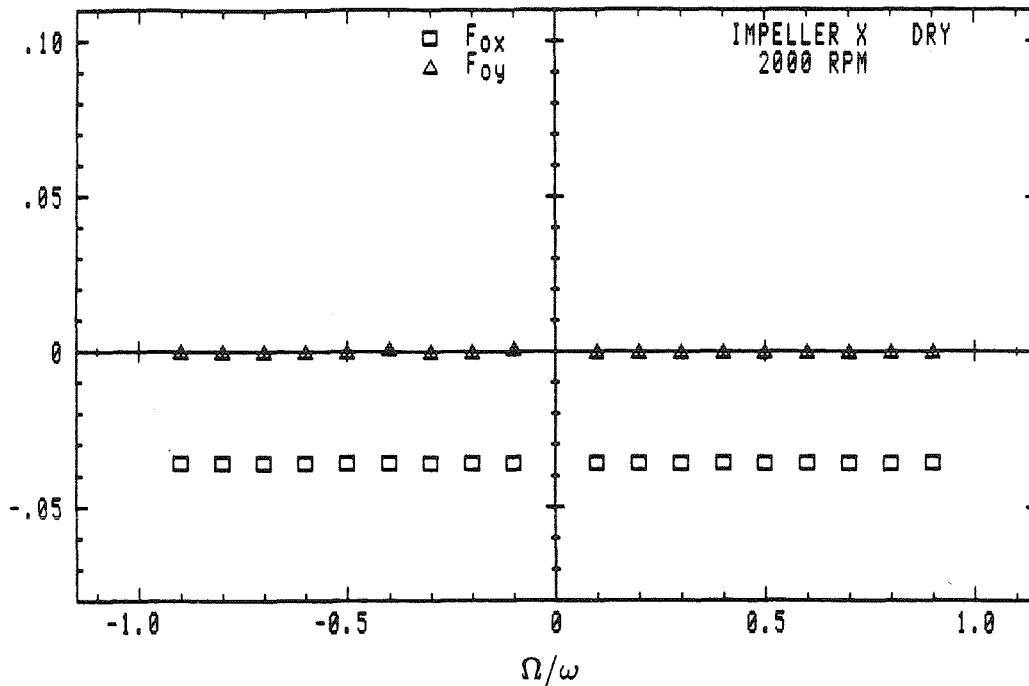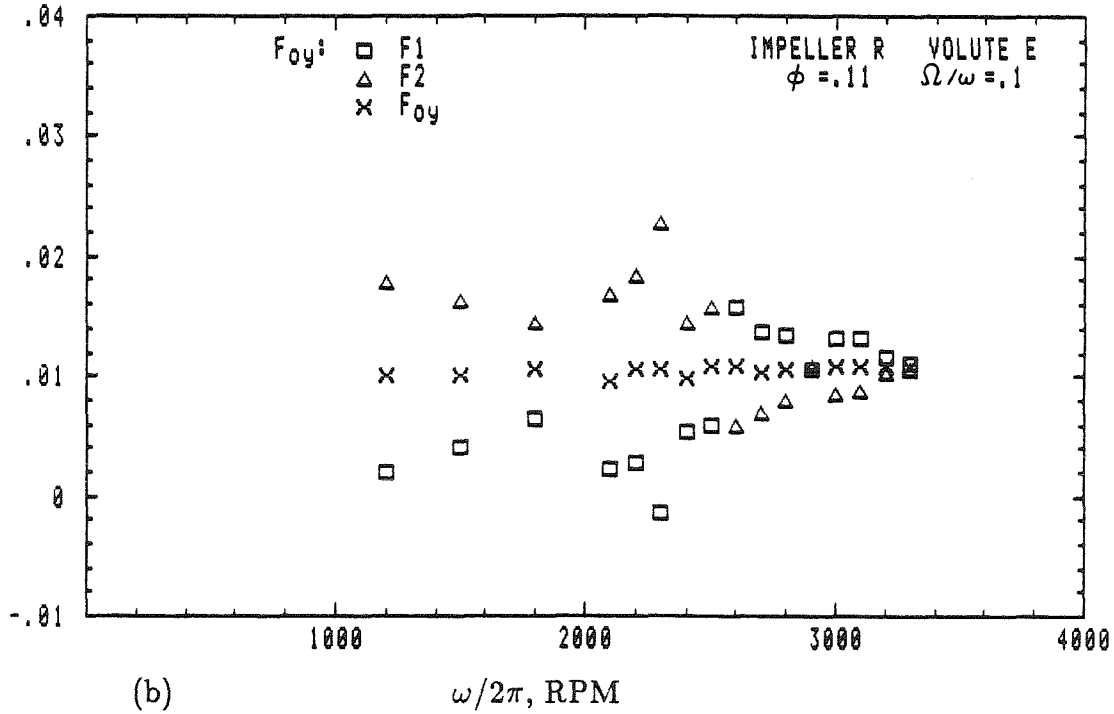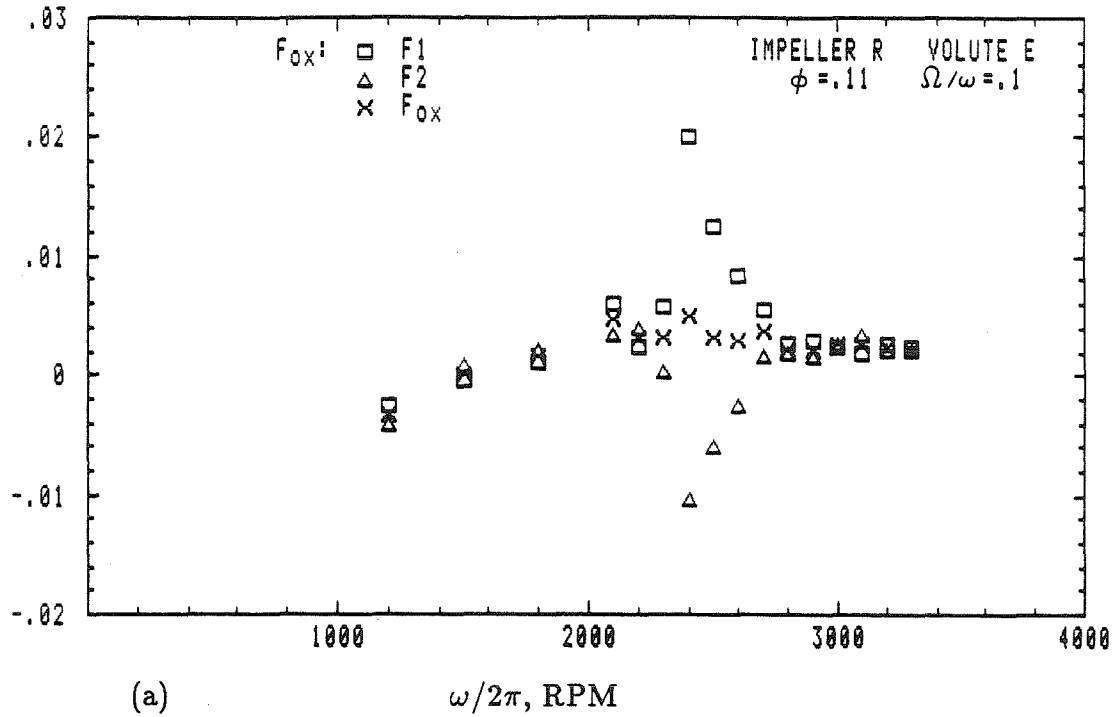
Fig. 5.2 The components of the steady force, (a) F_{ox} and (b) F_{oy}, with the appropriate contributions from F_1 and F_2 of Impeller R in Volute E for various shaft speeds at a flow coefficient of $\phi=.11$ and a whirl ratio of $\Omega/\omega=.1$.
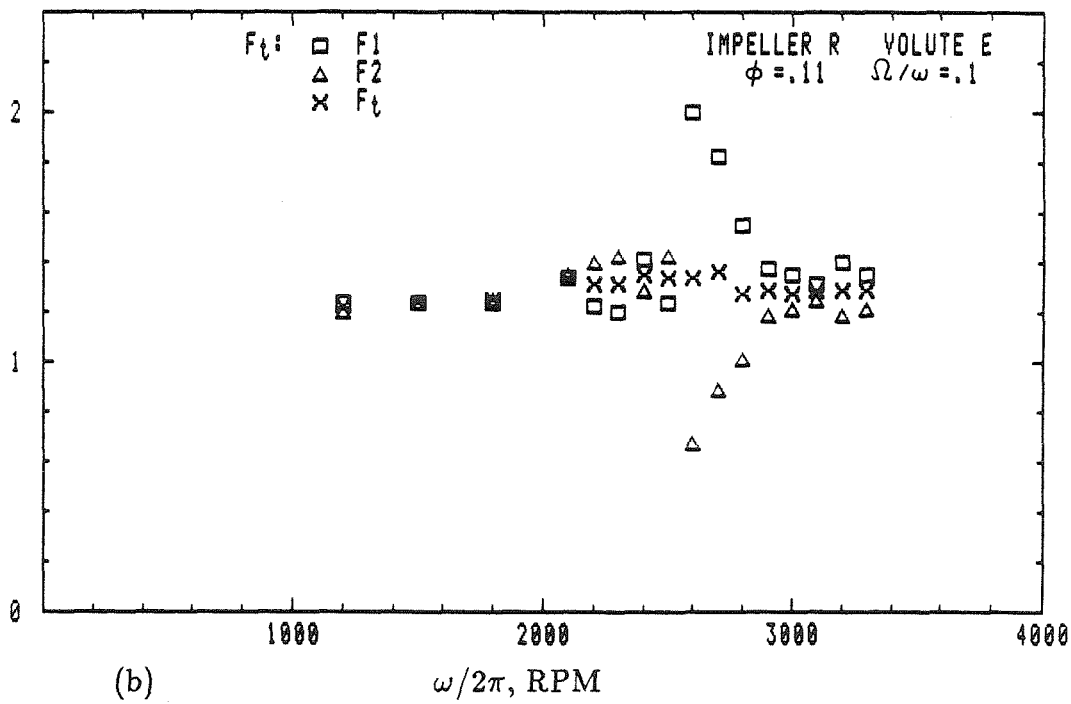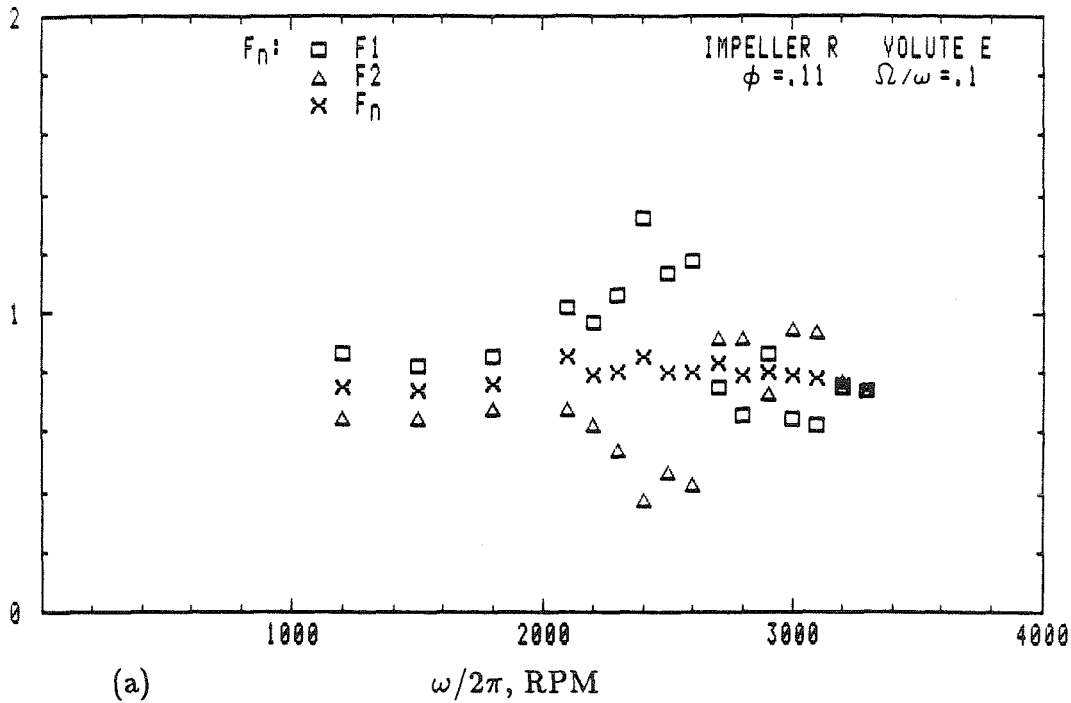
Fig. 5.3 The components of the unsteady force, (a) F_n and (b) F_t, with the appropriate contributions from F_1 and F_2 of Impeller R in Volute E for various shaft speeds at a flow coefficient of $\phi=.11$ and a whirl ratio of $\Omega/\omega=.1$.
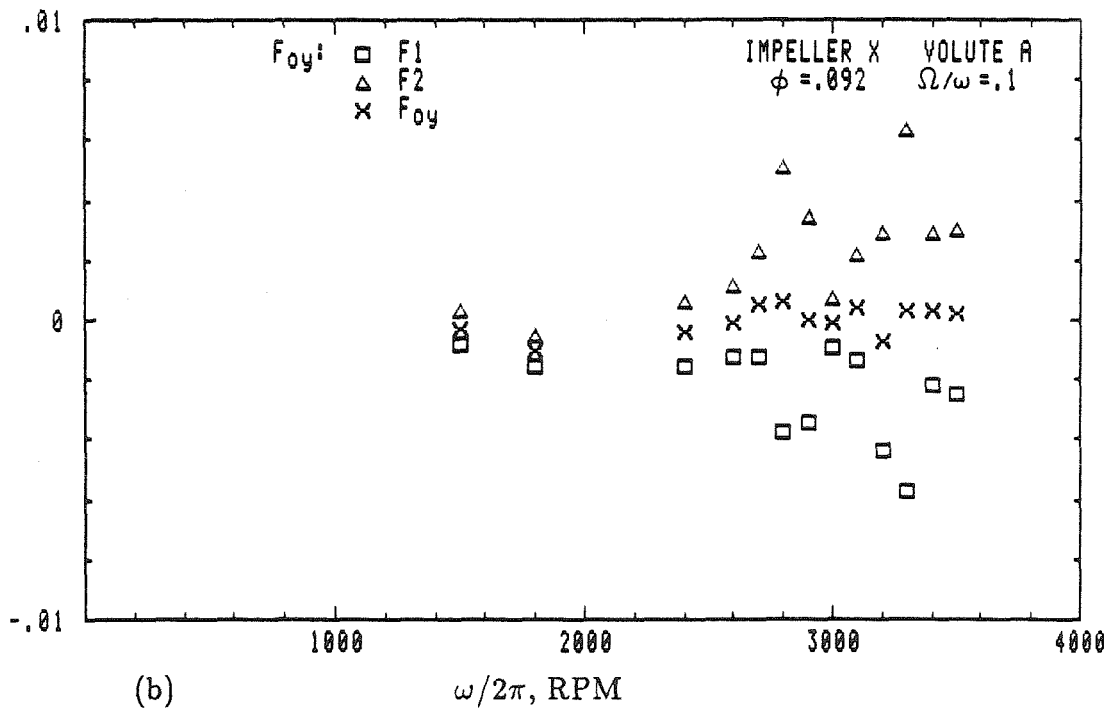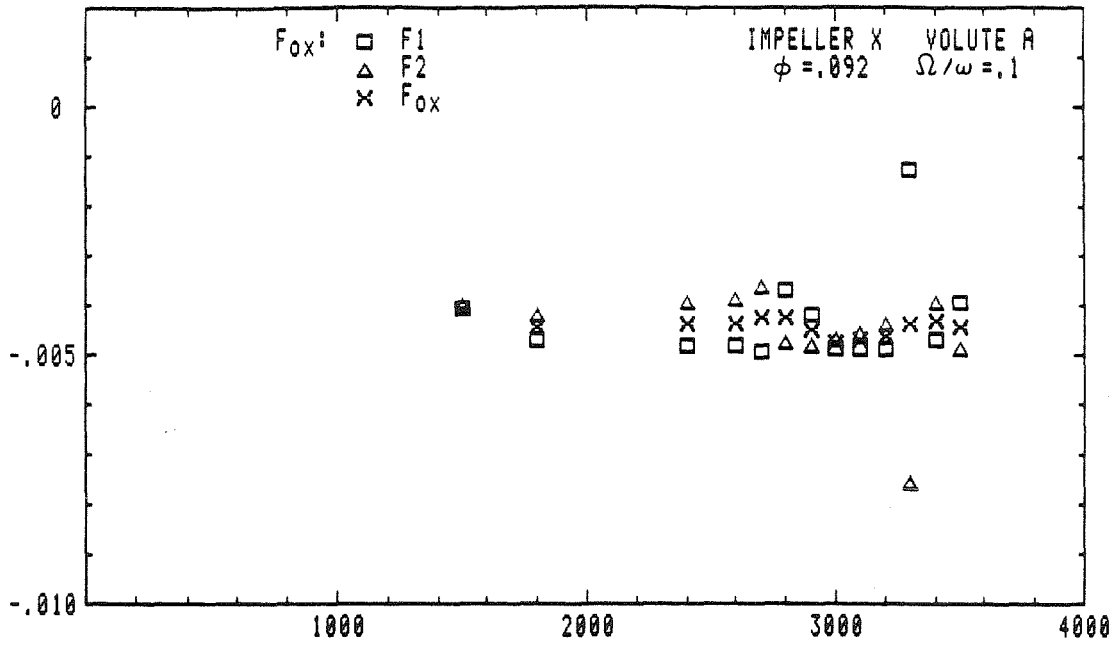
Fig. 5.4 The components of the steady force, (a) F_{ox} and (b) F_{oy}, with the appropriate contributions from F_1 and F_2 of Impeller X in Volute A for various shaft speeds at a flow coefficient of $\phi=.092$ and a whirl ratio of $\Omega/\omega=.1$.
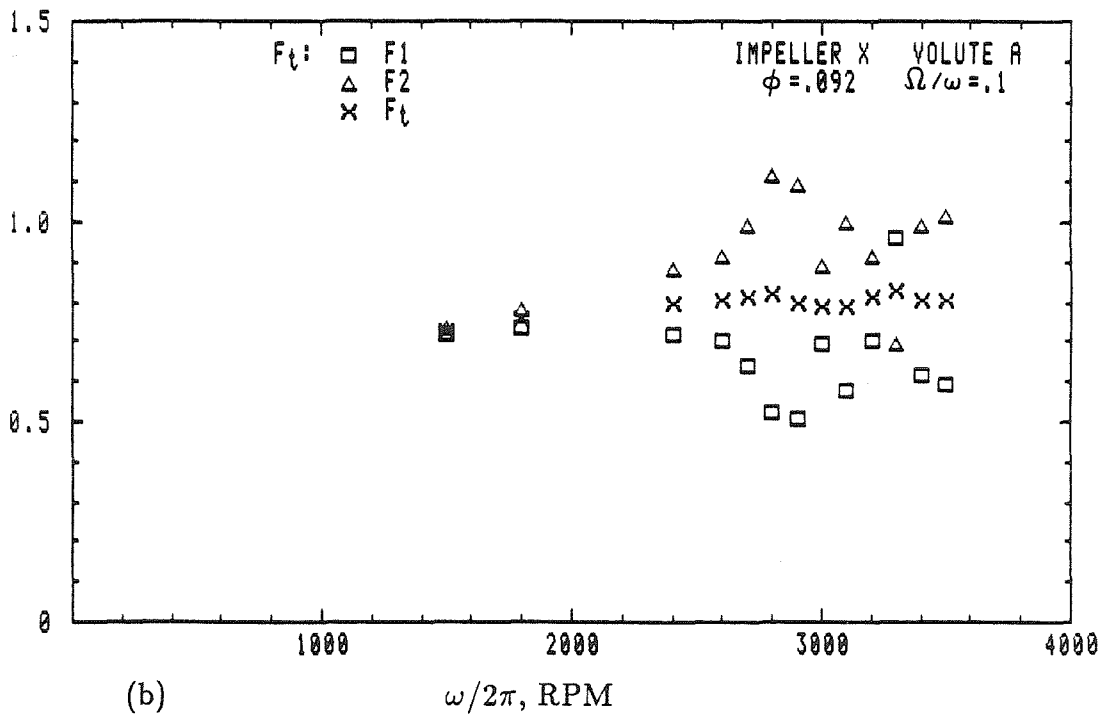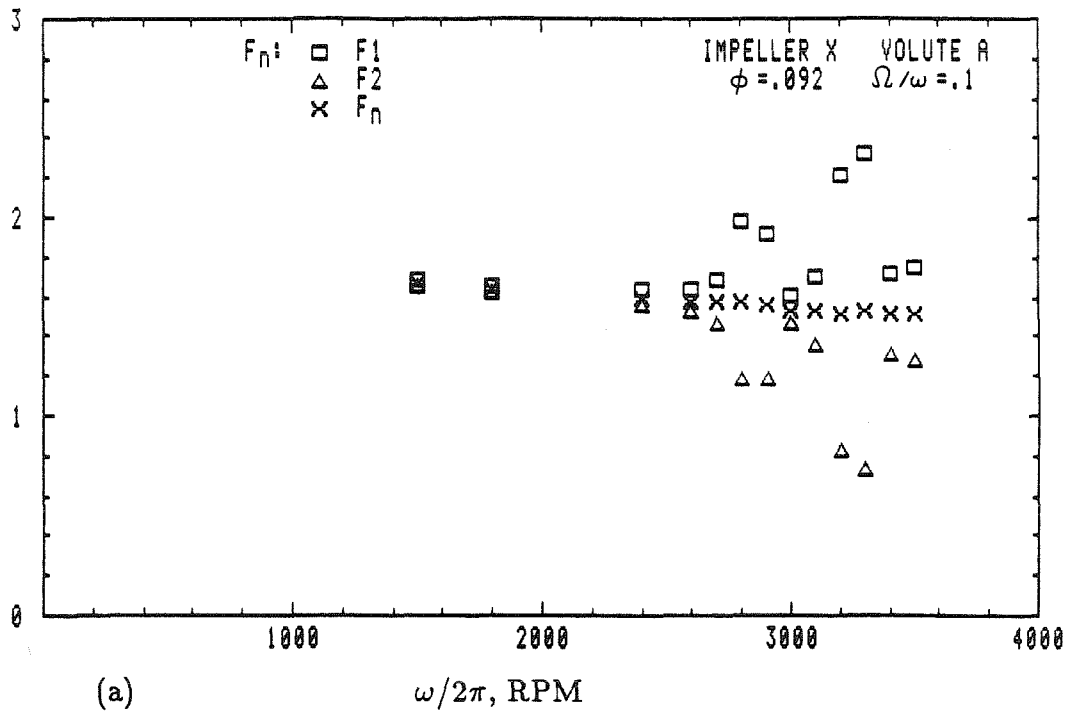
Fig. 5.5 The components of the unsteady force, (a) F_n and (b) F_t, with the appropriate contributions from F_1 and F_2 of Impeller X in Volute A for various shaft speeds at a flow coefficient of ϕ=.092 and a whirl ratio of Ω/ω=.1.
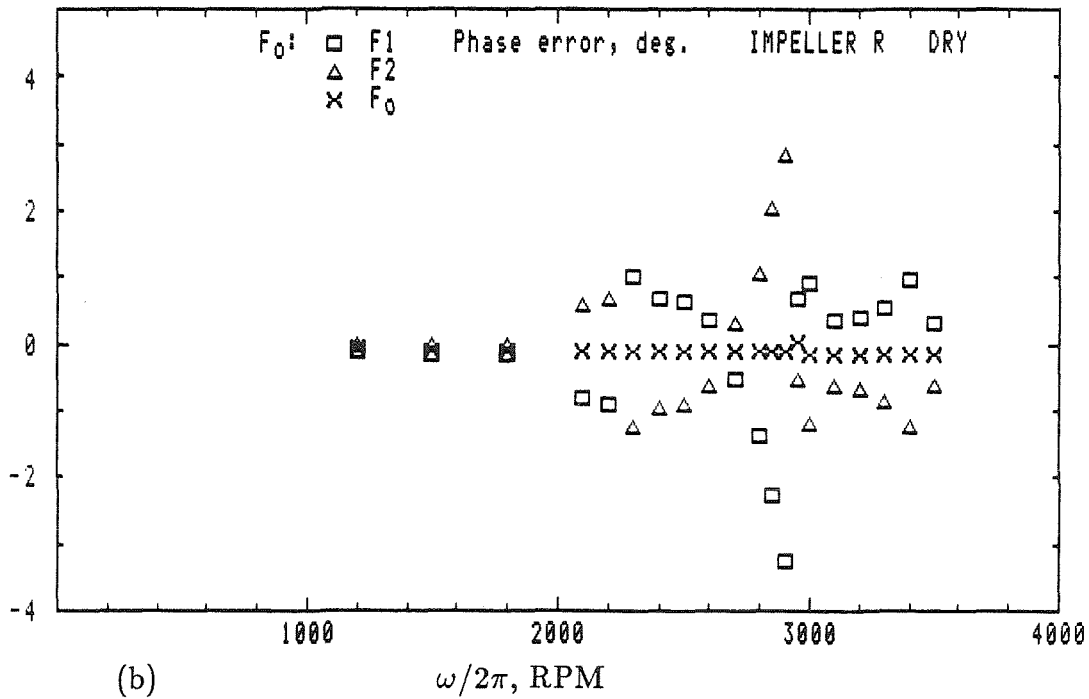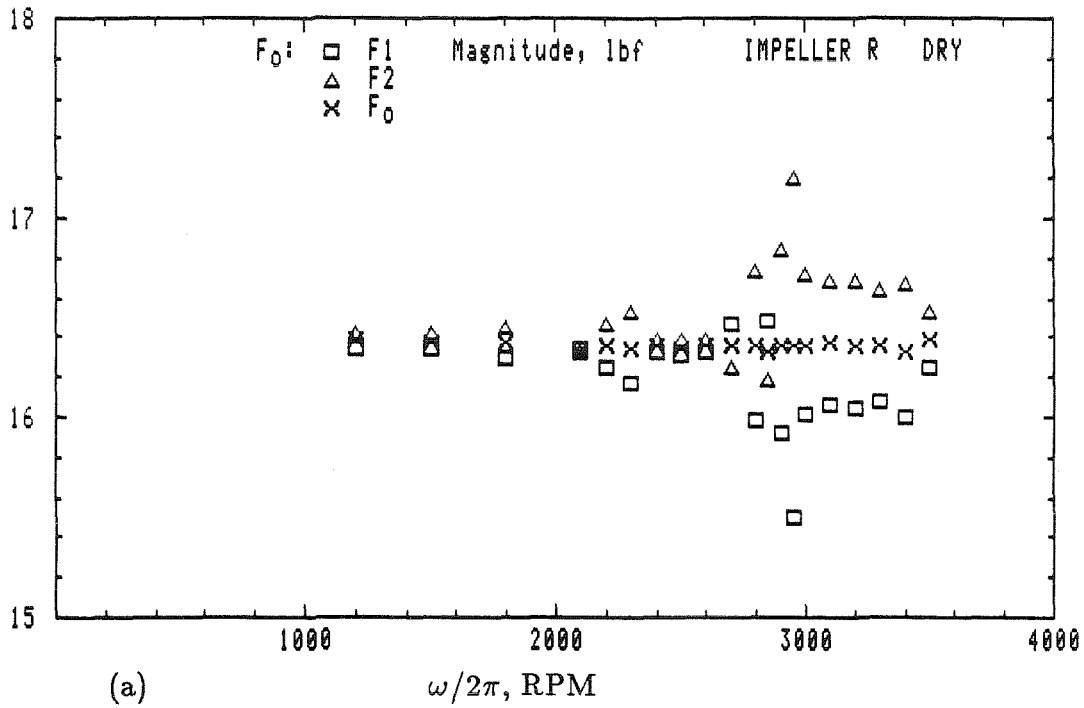
Fig. 5.6 The weight of Impeller R in the rotating dynamometer frame, F_1 and F_2, and in the stationary laboratory frame, $\mathbf{F_o}$. Plotted are (a) the magnitude and (b) the phase error from rotating the shaft at various speeds in air, after machining the bearing sleeves.
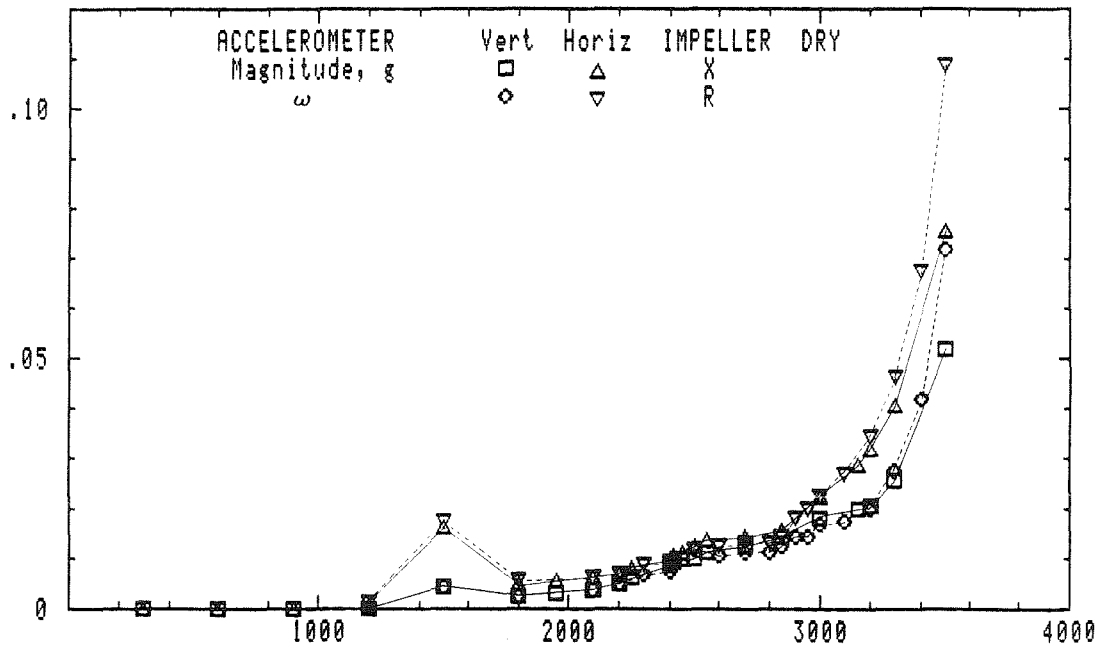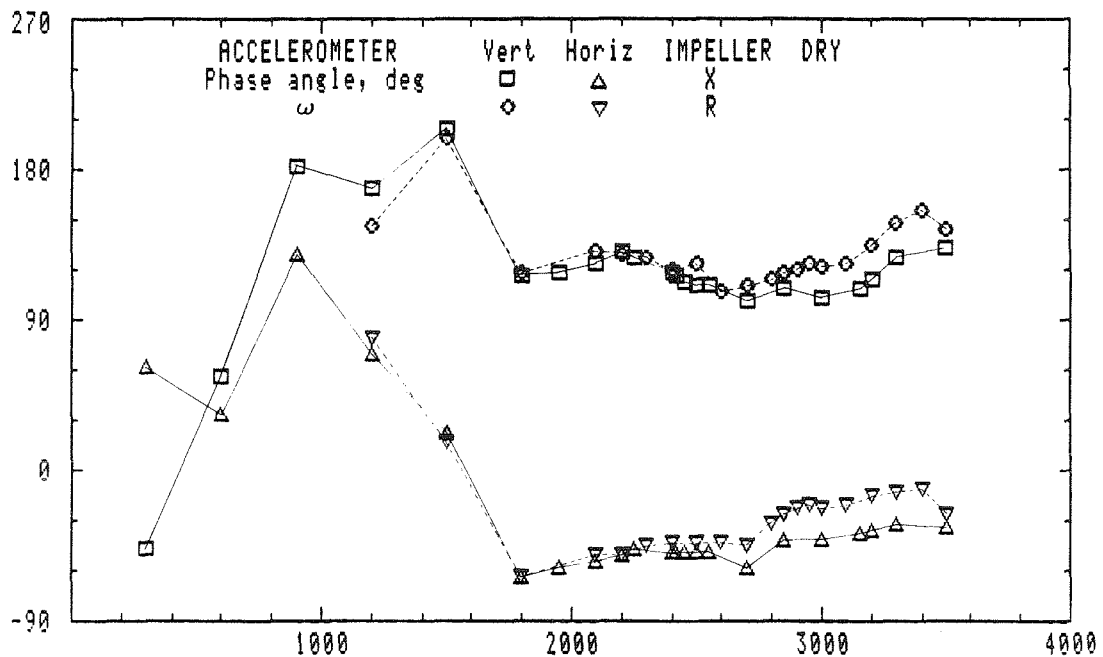
Fig. 5.7 (a) the magnitude and (b) the phase at main shaft frequency, ω, of the accelerometers placed on the eccentric drive mechanism for Impeller X and Impeller R rotating at various speeds in air, after machining the bearing sleeves.
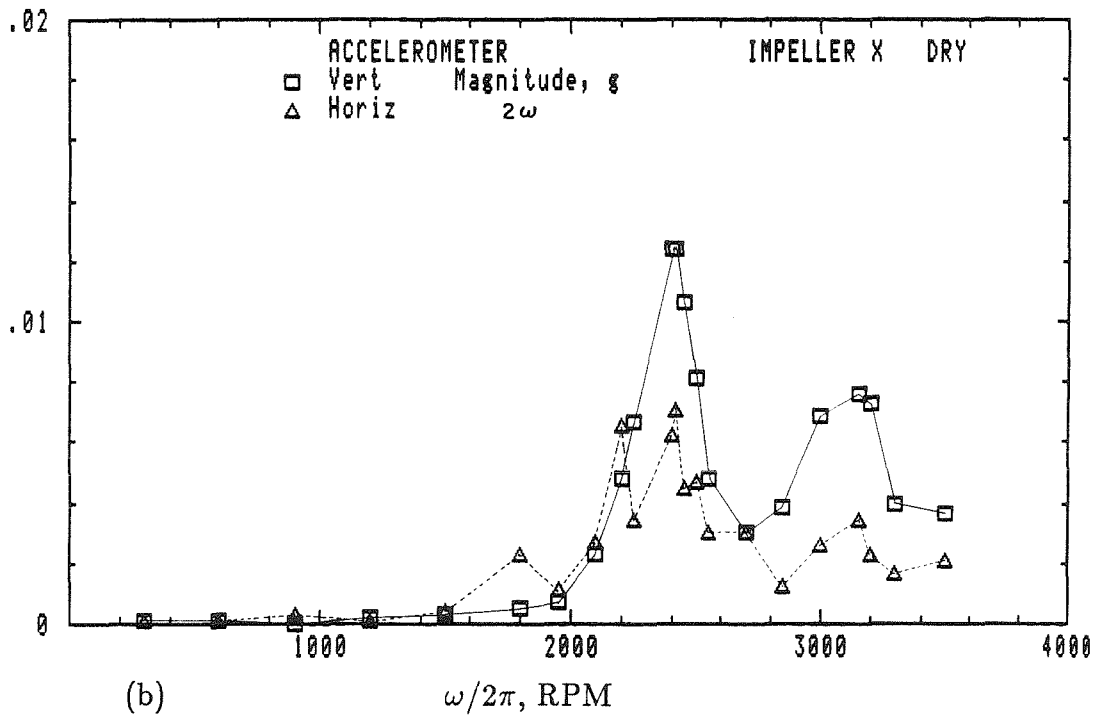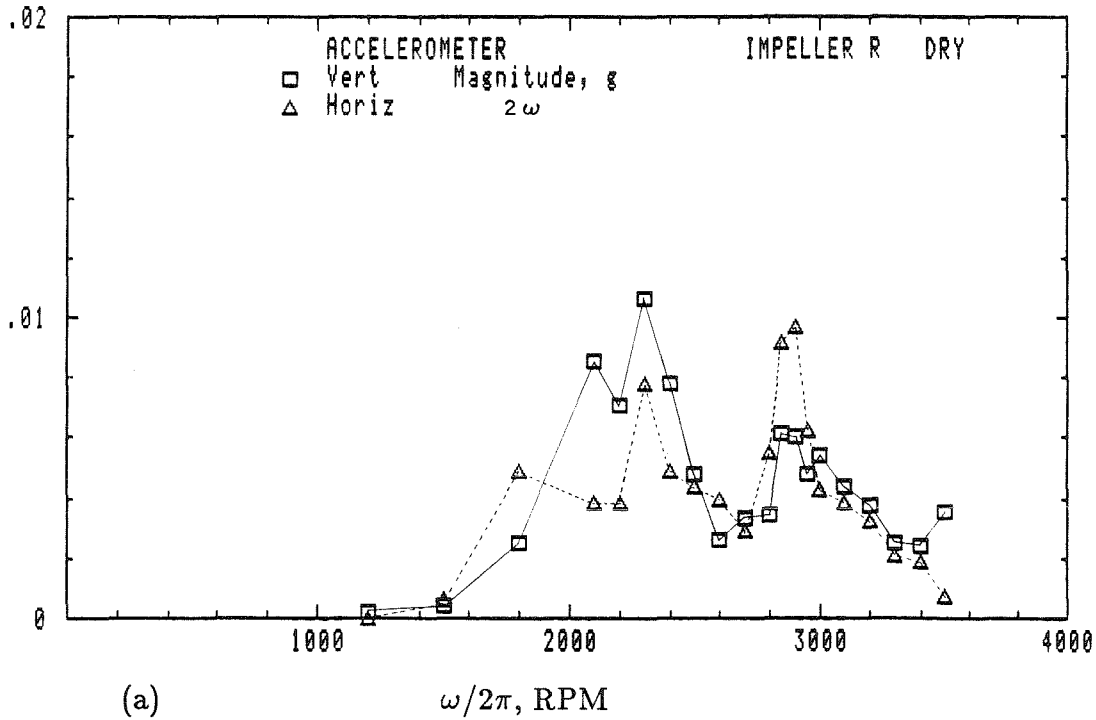
Fig. 5.8 The magnitude at twice main shaft frequency, 2ω, of the accelerometers placed on the eccentric drive mechanism for (a) Impeller R and (b) Impeller X rotating at various shaft speeds in air, after machining the bearing sleeves.

Chapter 6

Test Procedure

6.1 Operating Point

Each measurement of the forced vibration experiment to study the fluid-induced rotordynamic impeller forces is carried out at a specific operating point of the pump. The flow condition is described by the flow rate and main shaft speed. The total pressure rise is determined from the upstream and downstream pressures. The forced vibration is described by the whirl speed and the orbit radius, which is fixed. These quantities are non-dimensionalized to form the following parameters.

$$\text{flow coefficient} \quad \phi \quad = \quad \frac{Q}{u_2 A_2}$$

$$\text{cavitation number} \quad \sigma \quad = \quad \frac{p_I - p_v}{\frac{1}{2}\rho u_1^2}$$

$$\text{head coefficient} \quad \psi \quad = \quad \frac{p_{t2} - p_{t1}}{\rho u_2^2}$$

$$\text{whirl ratio} \quad \Omega/\omega$$

The frequency selected on the Wavetek synthesizer/function generator is the clock frequency $(1024*\omega)$ of the main shaft. The whirl ratio is the selected integer ratio, I/J, of the frequency multiplier/divider. The flow rate of the recirculating water loop is adjusted by a servo-control system which governs the silent throttle valve and uses the turbine flow meter to monitor the flow rate. The datum pressure of the pump loop is changed by either the vacuum pump or by supplying high pressure air to a bladder inside the reservoir. This pressure determines the operating point on the cavitating performance curve $(\psi - \sigma)$ for a given flow coefficient. The temperature of the water was measured by a thermometer in the reservoir. Digital readout voltmeters monitored the upstream and downstream pressure transducers and the turbine flow meter with a frequency-to-voltage converter. The A/D converter salvaged from the original data taker was used to sample both pressure

transducers. Using this data a computer calculated the cavitation number and head coefficient to enable the operator to continually monitor the performance operating point.

6.2 Measurements Performed

Measurements in the presence of cavitation were made for Impeller X, a five bladed centrifugal impeller, installed in the spiral Volute A at a main shaft speed of 2000 RPM with a water temperature of 120°F. Dry runs were first performed with Impeller X rotating and whirling in air. The volute, volute mounting plate and back face seal mounting fixture were removed. A water jet sprayed the back cavity eccentric drive inner face seal. Besides measuring the force experienced by the dynamometer due to the mass of the mounted impeller, the dry runs check the dynamic behavior of the dynamometer and verify the orientation of the optical encoders on the whirl and main drive shafts. This ensures the dynamometer orientation and whirl orbit location that is expected by the data acquisition system at time=0.

Then Impeller X was installed in Volute A, with a front face seal clearance of .005 inch. Rings were installed in the volute to reduce leakage flow. The front and back shroud rings had an axial clearance of .010 and .005 inch, respectively. The front ring at the impeller exit provided a restriction to the flow entering the large gap surrounding the shroud of the eccentric impeller. These rings were first installed by Adkins (1986, 1988) who had taken pressure measurements circumferentially around the volute entrance and in the annular region surrounding the shroud with the impeller at fixed positions on its whirl orbit. With the rings in place the pressure distribution was more sinusoidal. After the loop was filled, deaeration of the water continued. From the deaeration tank, water was continually pumped up to the pump loop, drained into the storage tank, and then pumped back into the deaeration tank. The water had a dissolved air content of 4 ppm during the tests.

The wet tests began with measuring the non-cavitating performance curve

$(\psi - \phi)$. With a fixed whirl ratio of $\Omega/\omega = .1$, measurements were taken over a range of flow coefficients under non-cavitating conditions with an upstream pressure of 10 psig. The steady force had a minimum at design, $\phi = .092$. Measurements were taken at the design flow coefficient, one above design ($\phi = .120$) and one below ($\phi = .060$) over the whirl ratio range $-.3 \leq \Omega/\omega \leq 0.6$ in increments of 0.1 at two cavitation numbers: one non-cavitating and the other corresponding to a head loss of 3%. By $\Omega/\omega = .6$ the tangential force had become stabilizing again, (see Figs. 7.9a–7.11a of the next chapter), consequently tests at higher whirl ratios were not necessary. For two whirl ratios in the region of destabilizing whirl, $\Omega/\omega=.1$ and .3, measurements were taken from non-cavitating conditions through breakdown of the head rise across the pump for the three flow coefficients. An operating constraint was to maintain the pressure in the back seal region above atmosphere to prevent air from leaking into the pump loop. At $\phi = .120$ a head loss of 15% was achieved, (see Fig. 7.5). Each set of the breakdown measurements was done in a single sitting.

After each measurement, the data were processed and plotted by hand. The corresponding dry runs were subtracted to eliminate the force of gravity and the centrifugal force on the whirling impeller. The buoyancy force was also subtracted, leaving only the fluid-induced rotordynamic force on the whirling impeller. This force is presented in the next chapter for the above tests in terms of the steady force $\mathbf{F_o}$ and the unsteady force due to the eccentric motion. The unsteady force is represented by the hydrodynamic force matrix $[\mathbf{A}]$, or by the average force normal to and tangential to the whirl orbit, F_n and F_t. In addition, the fluid-induced moment on the impeller is similarly presented.

Chapter 7

Presentation of Data

The hydrodynamic forces and moments on a centrifugal impeller in a spiral volute with the shroud-casing geometry shown in the assembly drawing of Fig. 2.8 were measured in the presence of cavitation. The lateral moment is presented in the plane bisecting the impeller discharge area.

7.1 Variation with Flow Coefficient

The force on the impeller depends upon its location on the whirl orbit. The impeller is whirled to average this dependency in order to obtain steady quantities, i.e. $\mathbf{F_o}$ and ψ, from a single test. With a whirl ratio of $\Omega/\omega = .1$, Figs. 7.1–3 show measurements taken over a range of flow coefficients under non-cavitating conditions. The fully wetted performance curve is shown in Fig. 7.1. The dependence of the magnitude and direction of the steady force $\mathbf{F_o}$ and the steady moment $\mathbf{M_o}$ upon flow coefficient is shown in Fig. 7.2. The angle of the force and moment vectors are measured from the volute tongue in the direction of main shaft rotation. The minimum of the steady force and greatest angular change occur at design, $\phi = .092$. $\mathbf{M_o}$ changes in a similar fashion. Fig. 7.3 gives the components of $\mathbf{F_o}$ and $\mathbf{M_o}$ in the volute reference frame. The dependence of the steady force upon flow coefficient is similar to previous results for a centrifugal impeller in a volute.

7.2 Variation with Whirl Ratio

The effect of cavitation upon the hydrodynamic forces was examined by testing three flow coefficients: $\phi = .120$, .092 (design) and .060. To demonstrate that the steady force is independent of whirl ratio, Fig. 7.4 shows the components under non-cavitating conditions for these flow coefficients.

With $\Omega/\omega = .1$ the pump loop datum pressure was lowered through breakdown in head rise across the pump for the three flow coefficients. Fig. 7.5 shows the cavitation performance curves. The forces from these tests will be examined later. The operating constraint of keeping the pressure of the back seal cavity above atmosphere permitted a breakdown in head rise across the pump of approximately 15%, 20% and 25% for $\phi = .120$, .092 and .060 respectively.

For the bulk of the data presented in this chapter, the unsteady force will be represented by its components normal to and tangential to the whirl orbit, averaged over the orbit, F_n and F_t. Fig. 7.6 shows for non-cavitating design flow, the elements of the hydrodynamic force matrix $[A]$ formed as F_n and F_t and as the difference between F_n or F_t and the corresponding matrix element. Because the scale is magnified, it should be viewed in conjunction with Fig. 7.10a. Recall from Eqn. (3.8) that the elements of $[A]$ have components in the rotating dynamometer frame at the difference and sum frequencies of the whirl and shaft frequencies: $\omega - \Omega$ and $\omega + \Omega$. One can think of the dynamometer as integrating two pressure fluctuations around the impeller, one travelling with the whirling impeller and the other going the opposite direction.

If $A_{xx} = A_{yy}$ and $A_{xy} = -A_{yx}$ then the matrix $[A]$ is independent of rotation, Eqn. (B.16). Fig. 7.7 shows $\frac{1}{2}(A_{xx} - A_{yy})$ and $\frac{1}{2}(A_{xy} + A_{yx})$ for the three flow coefficients and two operating points. The change in operating point from non-cavitating to 3% head loss had less effect than the change in flow coefficient. Because $\frac{1}{2}(A_{xx} - A_{yy})$ and $\frac{1}{2}(A_{xy} + A_{yx})$ are not zero, $[A]$ is not independent of rotation. However, since the values are small the presence of the volute tongue does not have a significant effect upon $[A]$. Similarly the hydrodynamic moment matrix $[B]$ is presented in Fig. 7.8 as M_n, M_t, $\frac{1}{2}(B_{xx} - B_{yy})$, and $\frac{1}{2}(B_{yx} + B_{xy})$ for design flow without cavitation. For $\Omega/\omega \leq 0.3$, M_n is small, comparable in magnitude to $\frac{1}{2}(B_{xx} - B_{yy})$ and $\frac{1}{2}(B_{yx} + B_{xy})$. For forward whirl where F_t is stabilizing M_n is larger. The elements of $[B]$ have a larger uncertainty than those of $[A]$.

The normal and tangential forces as a function of whirl ratio are plotted in

Figs. 7.9–11a for the three flow coefficients tested. The curves drawn on the figures of the unsteady forces are a quadratic fit to $F_n(\Omega/\omega)$ and $F_t(\Omega/\omega)$. Since $M_n(\Omega/\omega)$ and $M_t(\Omega/\omega)$ do not resemble parabolas, these symbols are connected by straight lines. Each plot has two flow conditions: one without cavitation, $\sigma \approx 4.3$, and the other at 3% head loss. At 3% head loss, F_n is slightly smaller and the magnitude of F_t is smaller for positive Ω/ω. At $\Omega/\omega = -.3$, for $\phi = .120$ F_t is smaller though for $\phi = .092$ (design) and $\phi = .060$ F_t is larger than for the non-cavitating case. Over a range of forward whirl F_t is in the same direction as the whirl motion, and is thus destabilizing. There is a slight decrease in the range of whirl ratio that F_t is destabilizing with cavitation at 3% head loss. The zero-crossing whirl ratio of F_t separates the destabilizing from the stabilizing whirl ratio region. Where $F_n > 0$ the hydrodynamic force tends to increase the radius of the whirl motion. For forward whirl there is a region over which $F_n < 0$, and tends to decrease the whirl radius. Based on past experiments, F_n will be positive again at higher whirl ratios reflecting its parabolic character. At design, $\phi = .092$, the zero-crossing whirl ratios for F_n and F_t are nearly the same. F_t is destabilizing over the same range of whirl ratio as F_n tends to increase the whirl orbit radius. For $\phi = .060$ F_t is positive up to a higher Ω/ω whereas for $\phi = .120$ the destabilizing region is smaller than the region over which F_n would increase the whirl radius. The region of destabilizing whirl ratio decreases with increasing flow coefficient.

For the above mentioned operating conditions, the corresponding unsteady moment components normal to and tangential to the whirl orbit, M_n and M_t, are presented in Figs. 7.9b–11b. A positive M_t would tend to tilt the impeller outward. M_n with the same sign as the whirl velocity would tend to tilt the impeller inlet away from the whirl direction. M_t is positive. The tilt away from the undeflected shaft axis would decrease the natural frequency of the rotor system operating in water. This is consistent with the decrease from the negative stiffness and the added mass (zero crossing value and the Ω^2 term of F_n) of the hydrodynamic force. The magnitude increases with increasing positive whirl ratio. The values are larger for

lower flow coefficients. With cavitation there is greater variation for reverse whirl. M_t is in the same direction as the whirl velocity, except in the region where the value is small, for small whirl ratios. With an expanded scale M_t would resemble a cubic function of Ω/ω.

7.3 Two Whirl Ratios through Breakdown

The effect of cavitation on the steady force and moment through breakdown of the head rise across the pump is displayed in Figs. 7.12–15. The dependence of the magnitude and direction of $\mathbf{F_o}$ and $\mathbf{M_o}$ upon cavitation number and upon head coefficient is shown in Fig. 7.12a,b, respectively. For off-design, $\phi = .120$ and $\phi = .060$, the magnitude of $\mathbf{F_o}$ decreases with breakdown. For design the magnitude of $\mathbf{F_o}$ decreases with decreasing cavitation number until breakdown, where it increases above the non-cavitating value. This is difficult to see because of the scale of the plot. In Fig. 7.14 the components of $\mathbf{F_o}$ for design flow are shown with a magnified scale. The direction of $\mathbf{F_o}$ rotates away from the tongue in the direction of impeller shaft rotation for each flow coefficient through breakdown. The steady moment showed similar tendencies.

The components of $\mathbf{F_o}$ and $\mathbf{M_o}$ in the volute frame are shown in Figs. 7.13-15 plotted against cavitation number and head coefficient for the three flow coefficients. Cavitation had more effect upon the steady force component parallel to the line between the volute center and the volute tongue, F_{ox}. Data taken in preliminary tests at 3000 RPM, prior to stiffening the eccentric drive mechanism by remachining the bearing sleeves, are presented in Figs. 7.16–17. The setup was slightly different, so these figures should not be directly compared with the other data presented. The steady force components are given for various flow coefficients at the operating points: non-cavitating, 3% head loss and 10% head loss. The steady force component in the direction of the volute tongue, F_{ox}, was more affected by cavitation. With increasing head loss, the curve F_{ox} as a function of ϕ appears to rotate about design flow, Fig. 7.16b. For a centrifugal impeller in a volute pump

tested at several flow coefficients above best efficiency, Uchida et al. (1971) has also observed that the steady force component in the tongue direction increases with developing cavitation. Fig. 7.17 shows the components of $\mathbf{M_o}$. Similarly M_{oy} was more affected by cavitation.

For two whirl ratios, $\Omega/\omega = 0.1$ and 0.3, the effect of cavitation upon the unsteady force components F_n and F_t and the unsteady moment components M_n and M_t is shown in Figs. 7.18–21 through breakdown in pump performance. For the above design flow coefficient, $\phi = .120$, the force and moment components decrease with head loss. For $\Omega/\omega=.3$, F_t becomes slightly more negative, increasing the stability margin.

At design flow, $\phi = .092$, for $\Omega/\omega = .1$ F_n and F_t decrease with head loss, however for a head loss greater than 10% there is a slight rise in F_t. M_t follows F_n, while M_n changes sign after head has begun decreasing. $\Omega/\omega = .3$ exhibits similar behavior except in the region between peak head rise and 1% head loss, where F_n goes through a trough and F_t a peak. Through this swing the unsteady force vector increases slightly in magnitude and rotates in a direction to increase the destabilizing tangential force, then rotates back. M_n and M_t increase in this region before decreasing with head loss. With both components increasing, the magnitude of the unsteady moment increases and swings only a few degrees in the direction to increase M_n. Fig. 7.22a shows that this perturbation is reflected in the steady force calculated from the $\Omega/\omega = .3$ data, which swings in the direction of main shaft rotation. For this operating region the flow was sufficiently disturbed so that the linearization of $\mathbf{F}(t)$, Eqn. (1.1), which represents the unsteady force by $[\mathbf{A}]\varepsilon(t)$, is invalid, because $\mathbf{F_o}$ was perturbed for $\Omega/\omega=.3$. $\mathbf{M_o}$ was also perturbed, Fig. 7.22b. However, the moment vector swings in the direction opposite to its eventual direction with further breakdown.

For below design flow, $\phi = .060$, F_n and F_t decrease with developing cavitation. For $\Omega/\omega=.1$ F_n increases approaching the knee of the performance curve, before decreasing with breakdown, while F_t increases with loss. For $\Omega/\omega=.3$ F_n decreases

with breakdown though momentarily increasing with head loss. F_t, doing the opposite, increases with breakdown. The changes in M_t reflect the changes in head. For $\Omega/\omega=.1$ M_n decreases in magnitude with breakdown before beginning to increase with 15% head loss. For $\Omega/\omega=.3$ M_n increases with developing cavitation and changes sign near the cavitation number where head begins to drop.

7.4 Variance of the Measurements

Data were taken over 256 cycles of the reference frequency ω/J at which the orientation of the dynamometer and its location on the whirl orbit geometrically repeat. For each cycle $\mathbf{F_o}$ and $[\mathbf{A}]$ were computed. The variances over the 256 cycles, including the tests performed in air, were calculated for $\Omega/\omega=-.1$, 0.1, 0.3 and 0.5, from the whirl ratio sets and for selected runs of the breakdown sets. The standard deviations were typically less than 0.00078 for F_{ox} and F_{oy}, 0.04 for F_n and 0.047 for F_t. For $\Omega/\omega=.5$ the standard deviations were occasionally larger than the mentioned values. For the breakdown sets of $\Omega/\omega = .3$, frequently the small values of F_t were not significantly larger than the associated standard deviations.

During the course of the experiment, the rotordynamic forces were of primary interest. The moments were obtained during subsequent processing of the data. Fewer sets of instantaneous data were available to compute the variance of $\mathbf{M_o}$ and $[\mathbf{B}]$ over 256 cycles. Evaluation of the available data indicates that the standard deviations were typically less than 0.0014 for M_{ox} and M_{oy}, and 0.11 for M_n and M_t.

7.5 Rotordynamic Force Matrices

The mass-damping-stiffness model of the unsteady hydrodynamic force gives,

$$\mathbf{F}(t) = \mathbf{F_o} - [\mathbf{K}]\,\mathbf{x}(t) - [\mathbf{C}]\,\dot{\mathbf{x}}(t) - [\mathbf{M}]\,\ddot{\mathbf{x}}(t) \qquad (7.1)$$

For the imposed circular whirl orbit, the model implies that the matrix $[\mathbf{A}(\Omega/\omega)]$ is quadratic in Ω/ω. With the non-dimensionalization of $[\mathbf{K}]$, $[\mathbf{C}]$ and $[\mathbf{M}]$ given in

the Nomenclature,

$$\begin{bmatrix} A_{xx} & A_{xy} \\ A_{yx} & A_{yy} \end{bmatrix} = \begin{bmatrix} -K_{xx} - C_{xy}\frac{\Omega}{\omega} + M_{xx}\left(\frac{\Omega}{\omega}\right)^2 & -K_{xy} + C_{xx}\frac{\Omega}{\omega} + M_{xy}\left(\frac{\Omega}{\omega}\right)^2 \\ -K_{yx} - C_{yy}\frac{\Omega}{\omega} + M_{yx}\left(\frac{\Omega}{\omega}\right)^2 & -K_{yy} + C_{yx}\frac{\Omega}{\omega} + M_{yy}\left(\frac{\Omega}{\omega}\right)^2 \end{bmatrix} \quad (7.2)$$

Since $[\mathbf{A}(\Omega/\omega)]$ does resemble a parabola for the impeller-volute combination presented, the coefficient matrices from a least squares fit are given in Table 7.1. For the set of Ω/ω tested, the curves A_{xy} and A_{yx} do not quite resemble a parabola for every flow condition. Fig. 7.11a shows that F_t can flatten over the destabilizing whirl ratio range for $\phi{=}.060$.

Using "root-sum-square" for the propagation of uncertainty, the variance of the coefficients of the quadratic fit can be calculated, Bevington (1969). The variance of a function f of n independent variables x_i, $i{=}1$, n, is

$$\sigma_f^2 = \sum_{i,j=1}^{n} \frac{\partial f}{\partial x_i} \frac{\partial f}{\partial x_j} \sigma_{x_i x_j}^2 \quad (7.3)$$

If x_i and x_j are uncorrelated then

$$\sigma_f^2 = \sum_{i=1}^{n} \left(\frac{\partial f}{\partial x_i}\right)^2 \sigma_{x_i}^2 \quad (7.4)$$

Because the variance of the elements of $[\mathbf{A}]$ were not available for every whirl ratio, the quadratic coefficients were calculated without including the errors. This is equivalent to assuming the same variance for every whirl ratio. An "average variance",

$$\frac{1}{\sigma_{avg}^2} = \frac{1}{N_w} \sum_{i=1}^{N_w} \frac{1}{\sigma_i^2} \quad (7.5)$$

was used to obtain the variance for the coefficient matrices. N_w is the number of whirl ratios for which the variance of the elements of $[\mathbf{A}]$ were available. These were similar to those obtained from calculating the coefficient variances using the variances of $[\mathbf{A}(\Omega/\omega)]$ that were available for a complete set of whirl ratios. The standard deviation in the coefficients is approximately 0.02, 0.08, and 0.2 for the

stiffness, damping and mass matrices, respectively. For $\phi=.060$, they are larger, in particular 0.1 for the damping matrix.

Over the whirl ratio range tested, the unsteady moments due to the imposed lateral displacement do not in general resemble a quadratic in Ω/ω. Consequently, the coefficients of a quadratic fit are not presented. A complete rotordynamic analysis would require forces and moments for the deflection as well as lateral rotation of the rotor about its undeflected position within the volute.

The coefficient matrices presented are for two operating points: non-cavitating and cavitating with 3% head loss. Cavitation at 3% head loss did not make the rotordynamic behavior of the impeller worse. The range of destabilizing whirl ratio was slightly reduced. A monotonic change in the coefficients between the two operating points cannot be assumed. At design flow [A] changes differently for $\Omega/\omega=.1$ and .3 with less cavitation.
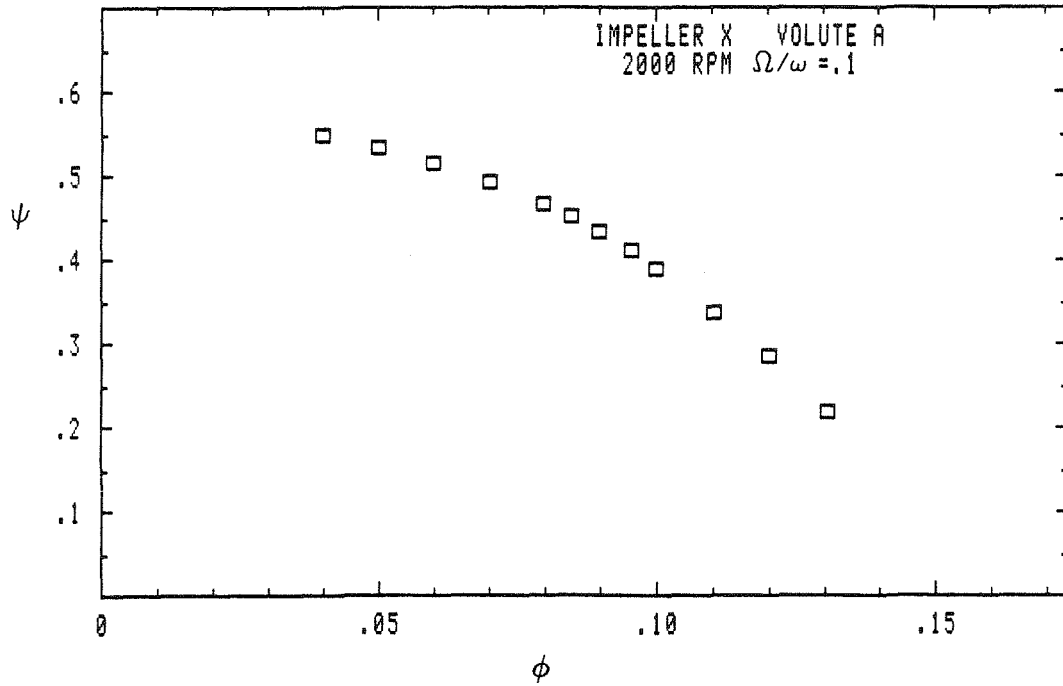
Fig. 7.1 Noncavitating performance curve of Impeller X in Volute A at 2000 RPM.
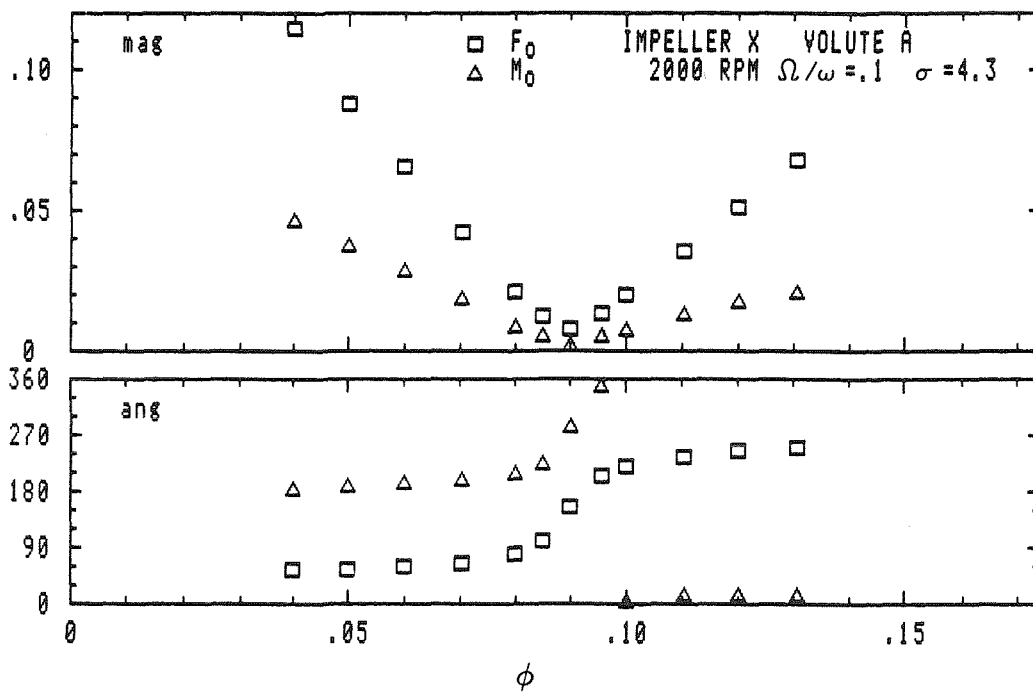
Fig. 7.2 The magnitude and direction of the steady force F_o and moment M_o on Impeller X in Volute A at 2000 RPM as a function of flow coefficient.
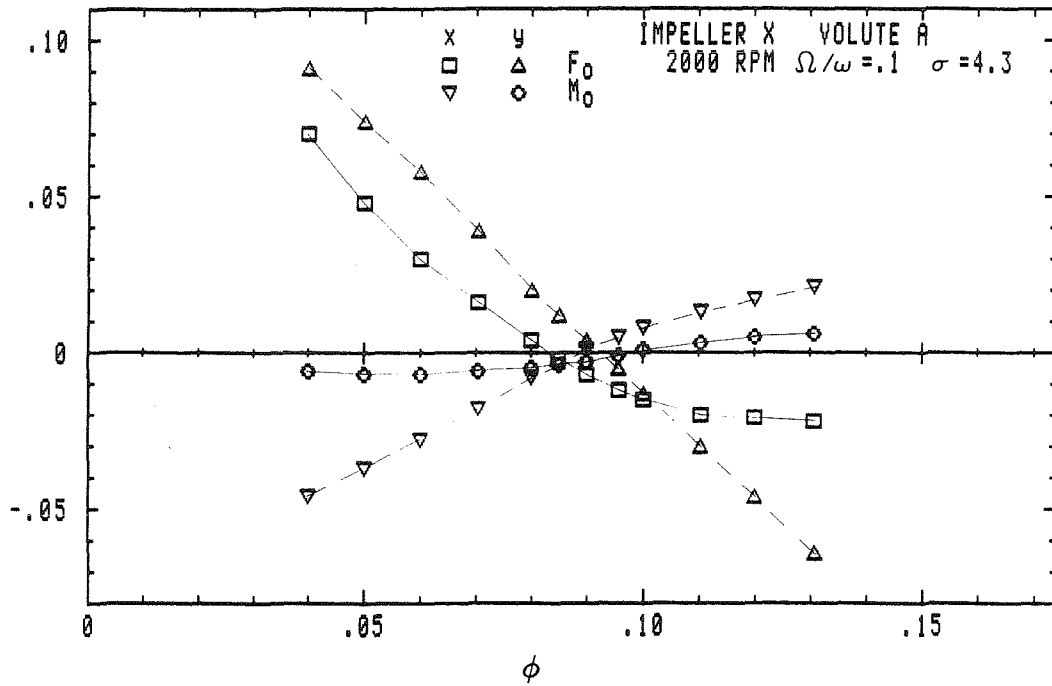
Fig. 7.3 The components of the steady force, F_{ox} and F_{oy}, and moment, M_{ox} and M_{oy}, on Impeller X in Volute A at 2000 RPM as a function of flow coefficient.
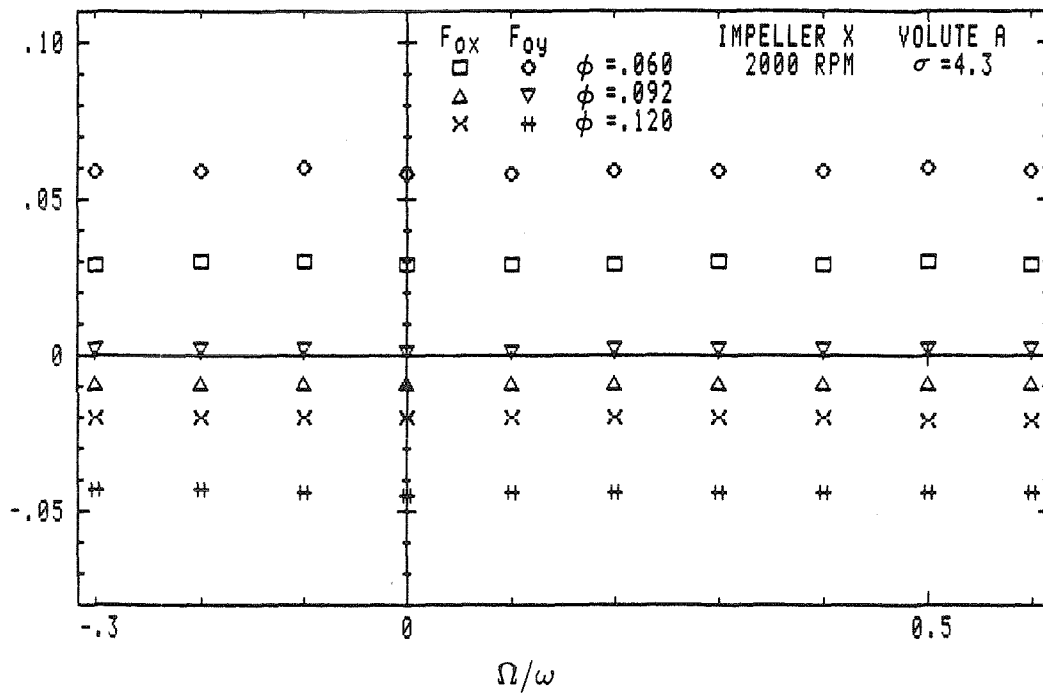
Fig. 7.4 The components of the steady force, F_{ox} and F_{oy}, on Impeller X in Volute A at 2000 RPM for the three flow coefficients: ϕ=.060, .092 (design) and .120, as a function of whirl ratio.
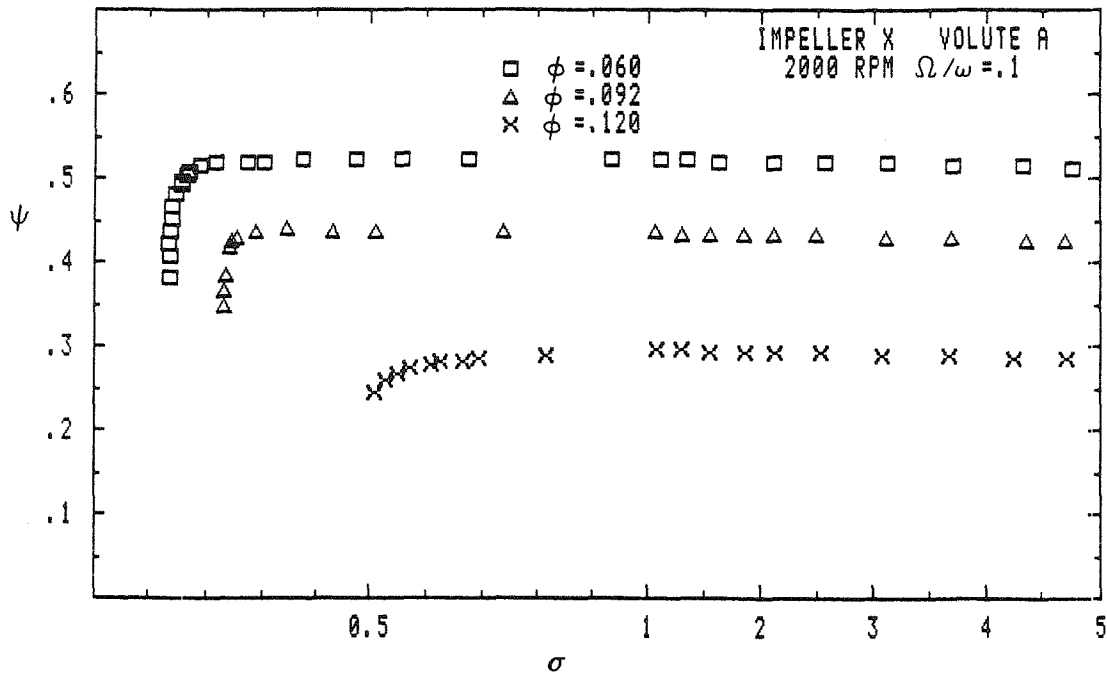
Fig. 7.5 Cavitation performance curve for Impeller X in Volute A at 2000 RPM with Ω/ω=.1 for the three flow coefficients: ϕ=.060, .092 (design) and .120.
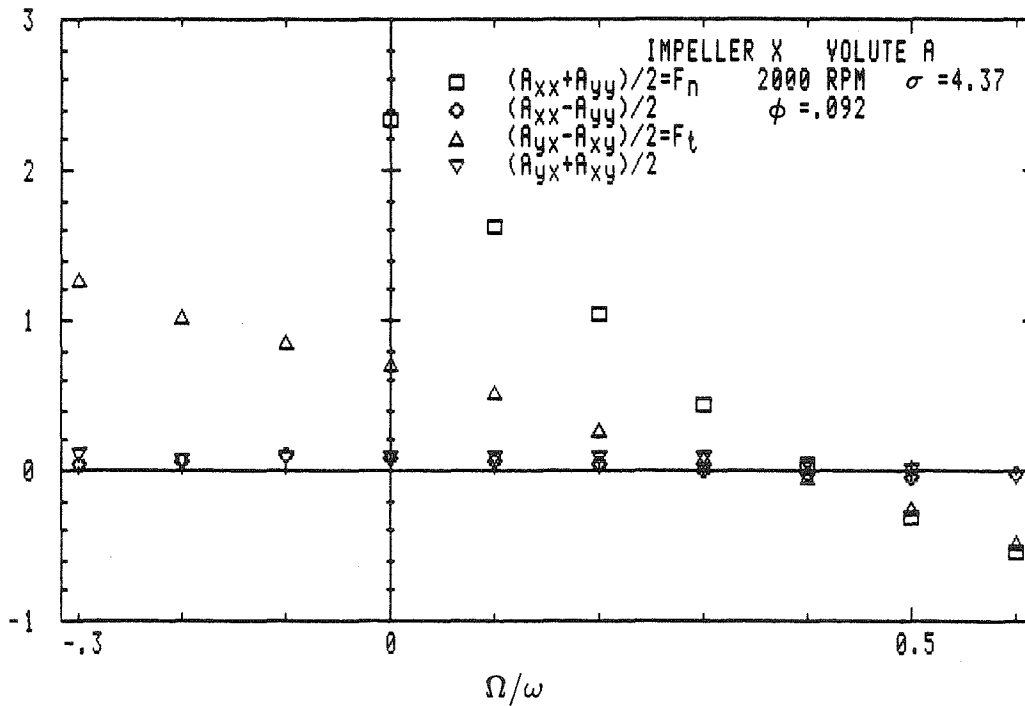
Fig. 7.6 The elements of the hydrodynamic force matrix [A] expressed as the force normal to and tangential to the whirl orbit in the same direction and opposite to the azimuthal unit vector for Impeller X in Volute A at 2000 RPM at design flow, $\phi = .092$, under non–cavitating conditions.
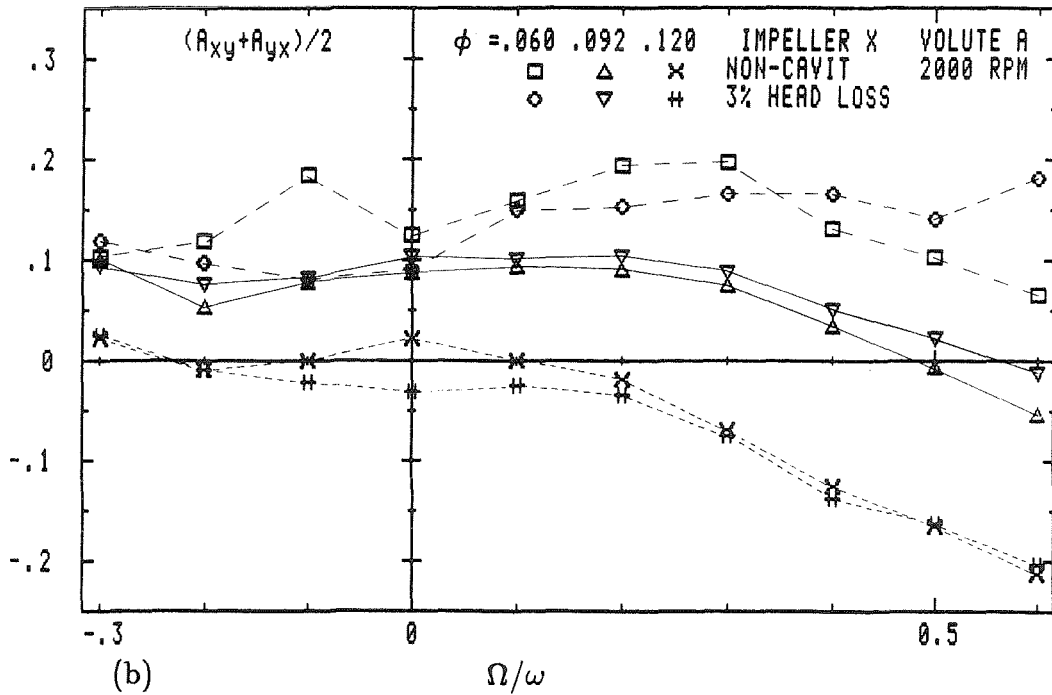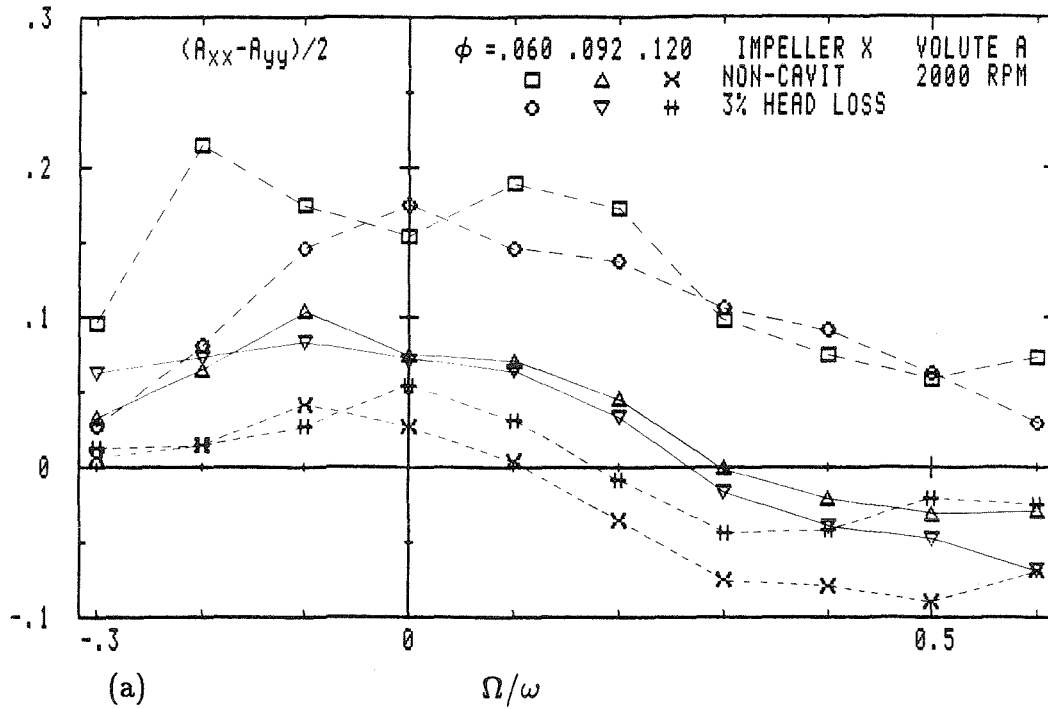
Fig. 7.7 (a) $\frac{1}{2}(A_{xx}-Ayy)$ and (b) $\frac{1}{2}(A_{xy}+A_{yx})$ of the hydrodynamic force matrix of Impeller X in Volute A at 2000 RPM for the three flow coefficients: ϕ=.060, .092 (design) and .120, as a function of whirl ratio for flow without cavitation and with a head loss of 3%.
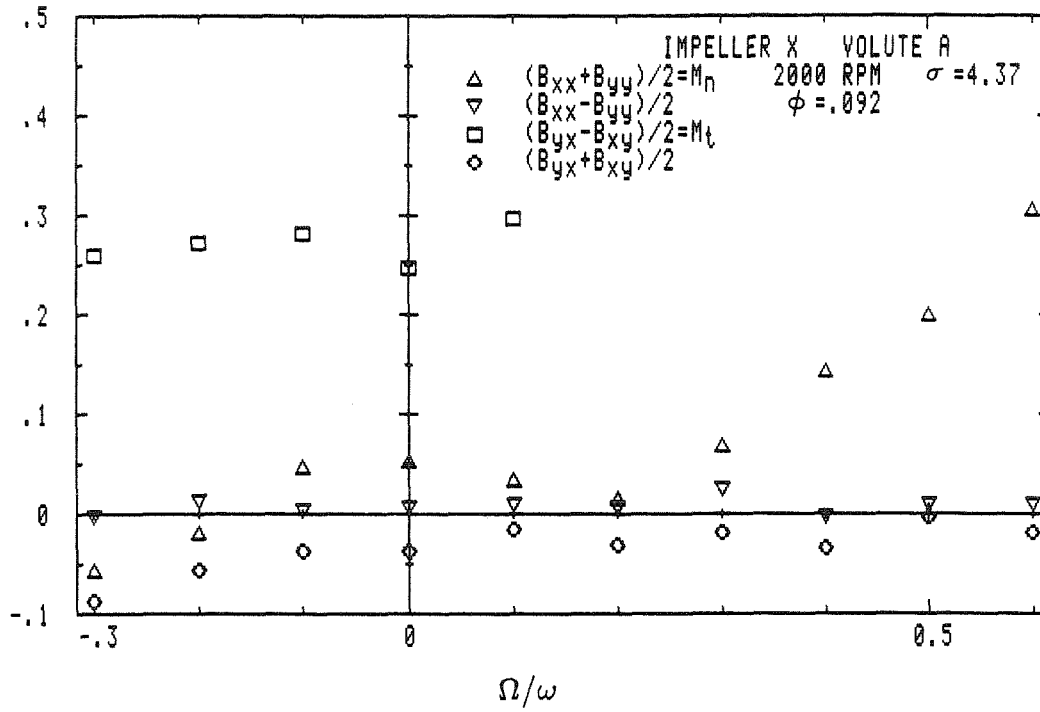
Fig. 7.8   The elements of the hydrodynamic moment matrix [B] expressed as the moment normal to and tangential to the whirl orbit in the same direction and opposite to the azimuthal unit vector for Impeller X in Volute A at 2000 RPM at design flow, $\phi = .092$, under non–cavitating conditions.
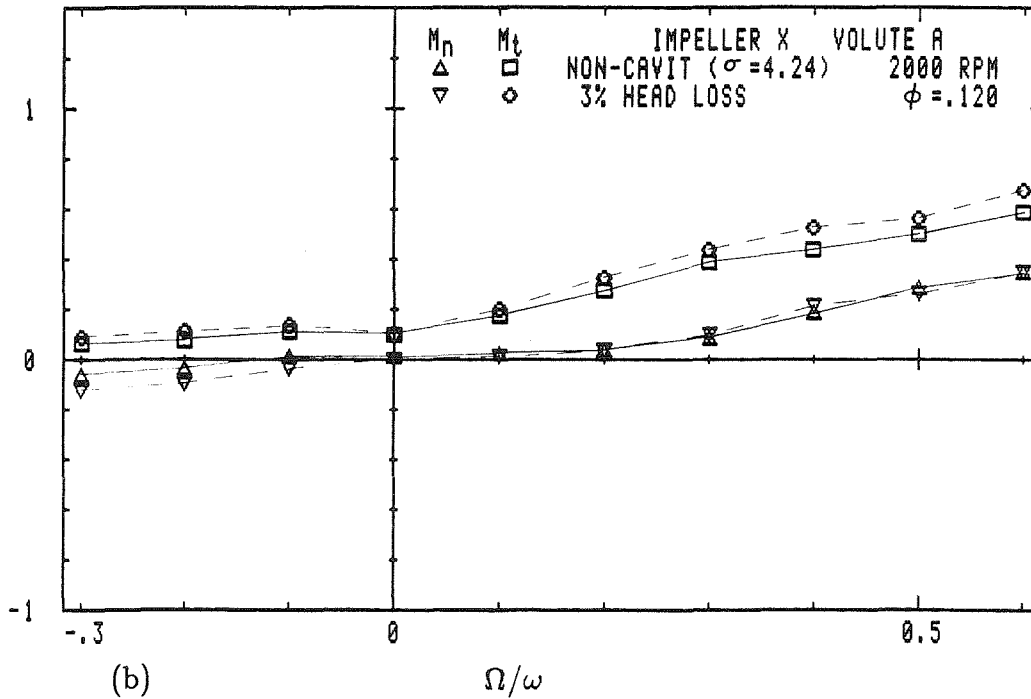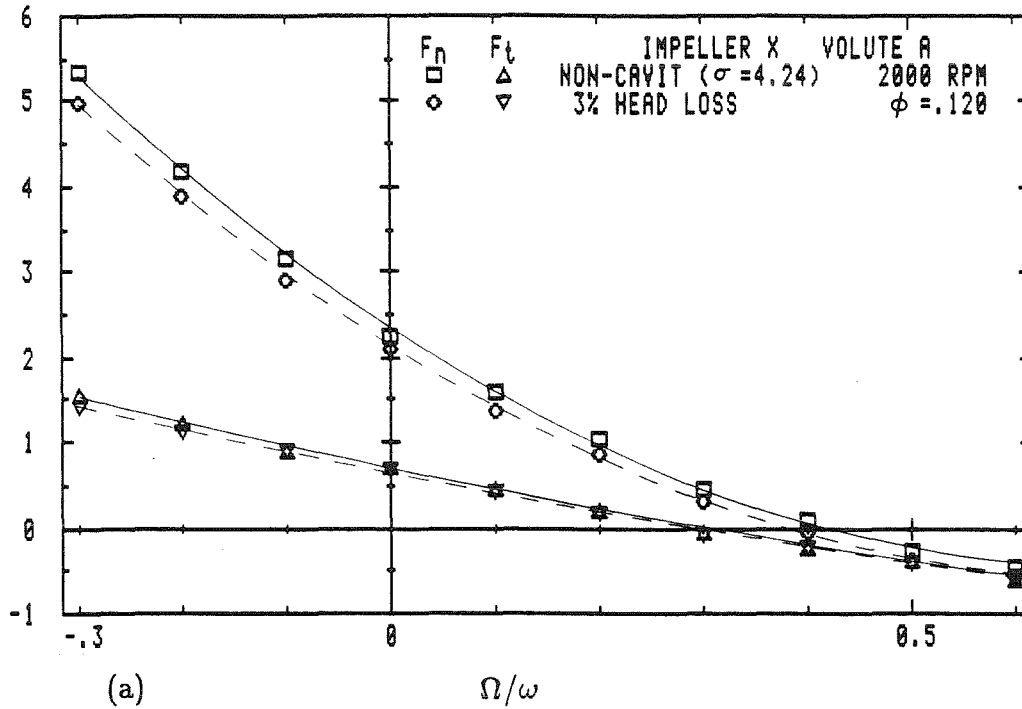
Fig. 7.9 (a) the average normal and tangential force, F_n and F_t, and (b) the average normal and tangential moment, M_n and M_t, on Impeller X in Volute A at 2000 RPM at a flow coefficient of $\phi = .120$ as a function of whirl ratio for flow without cavitation and with a head loss of 3%.
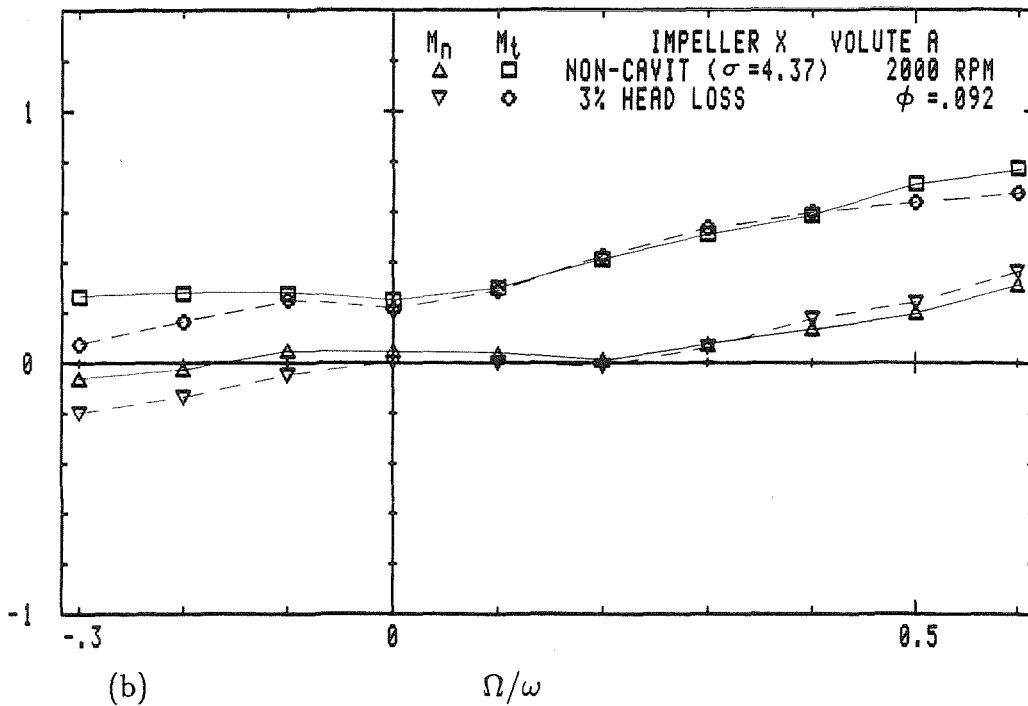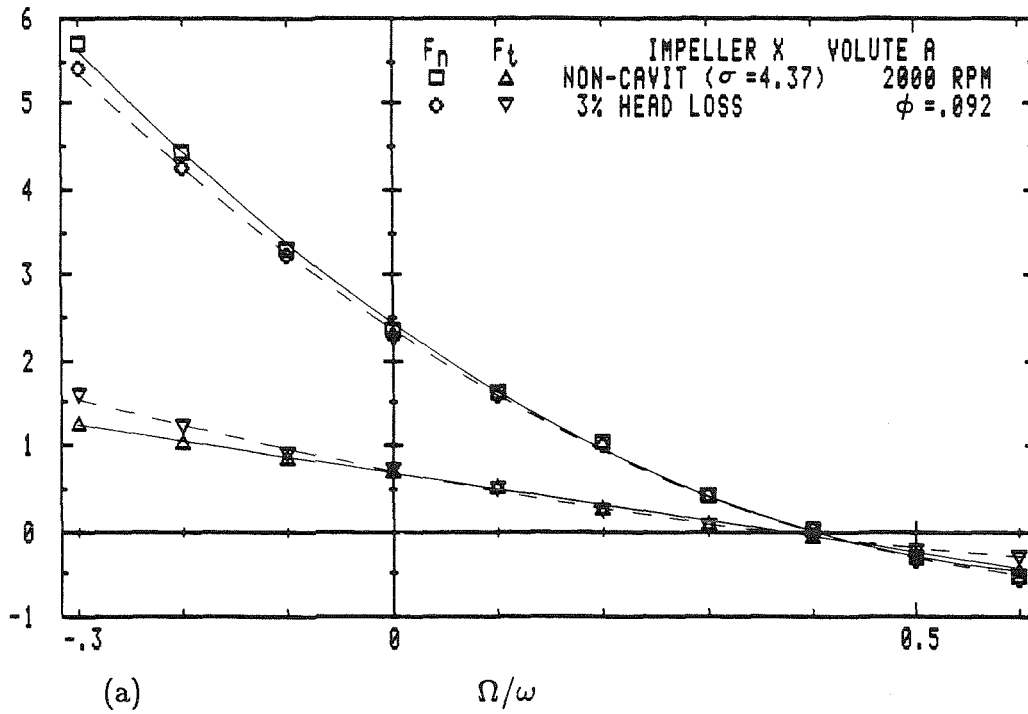
Fig. 7.10   (a) the average normal and tangential force, F_n and F_t, and (b) the average normal and tangential moment, M_n and M_t, on Impeller X in Volute A at 2000 RPM at design flow ($\phi = .092$) as a function of whirl ratio for flow without cavitation and with a head loss of 3%.
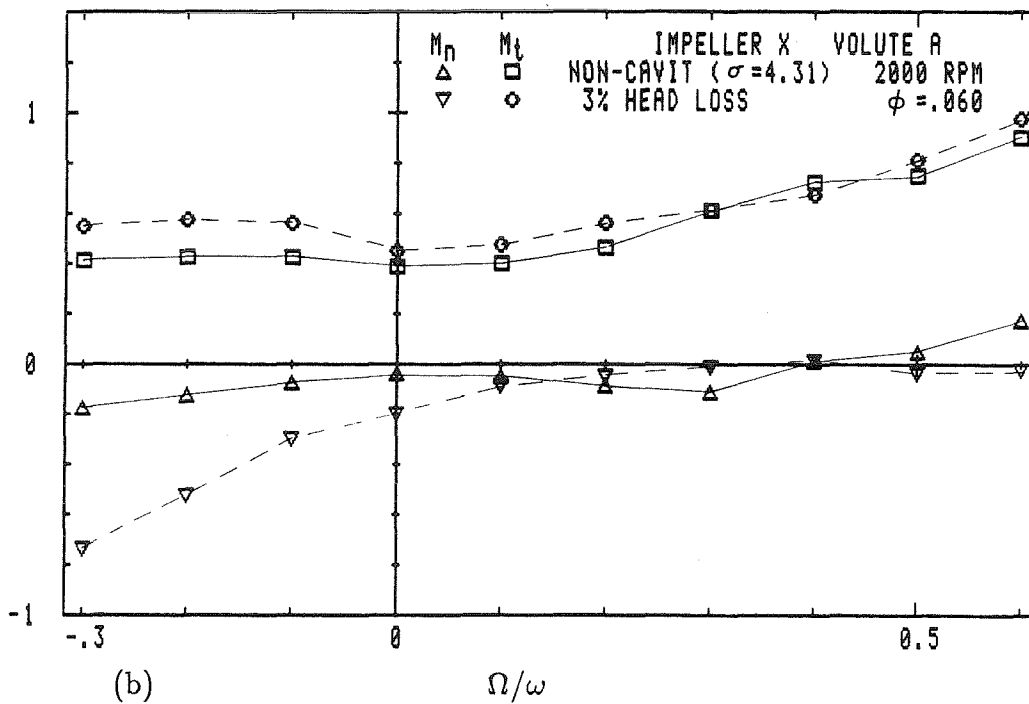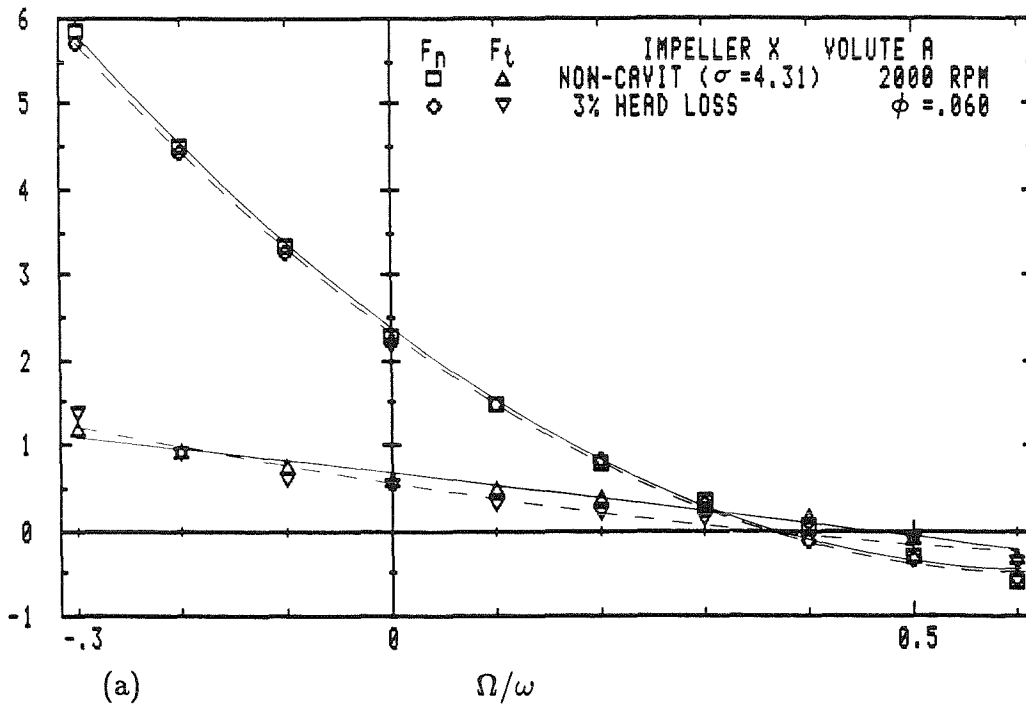
Fig. 7.11 (a) the average normal and tangential force, F_n and F_t, and (b) the average normal and tangential moment, M_n and M_t, on Impeller X in Volute A at 2000 RPM at a flow coefficient of $\phi = .060$ as a function of whirl ratio for flow without cavitation and with a head loss of 3%.
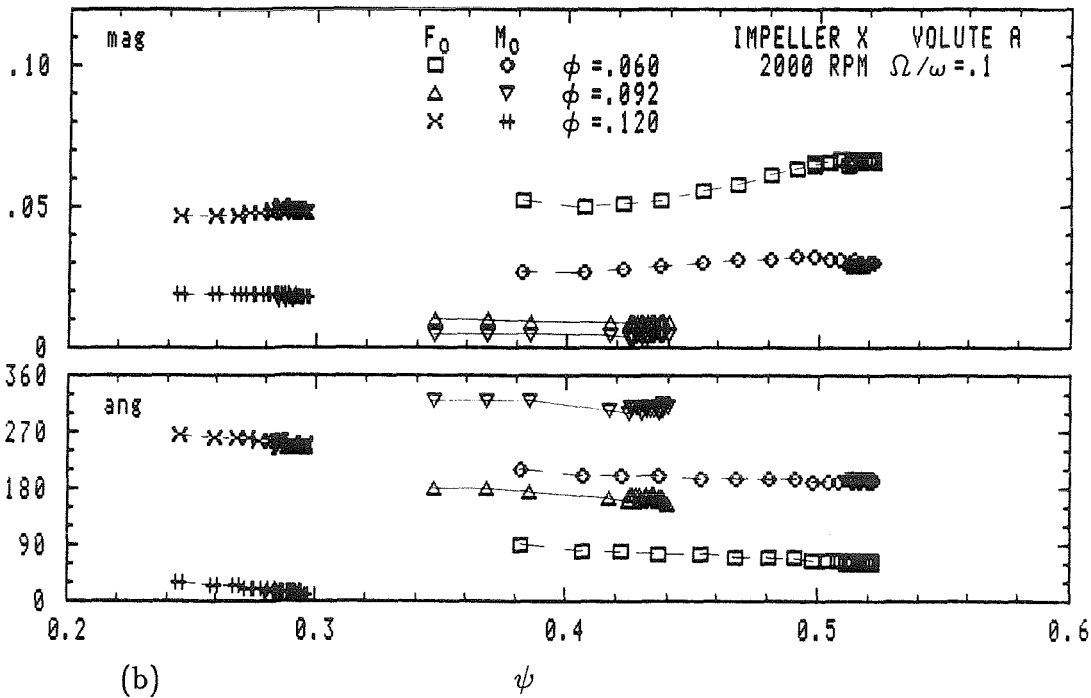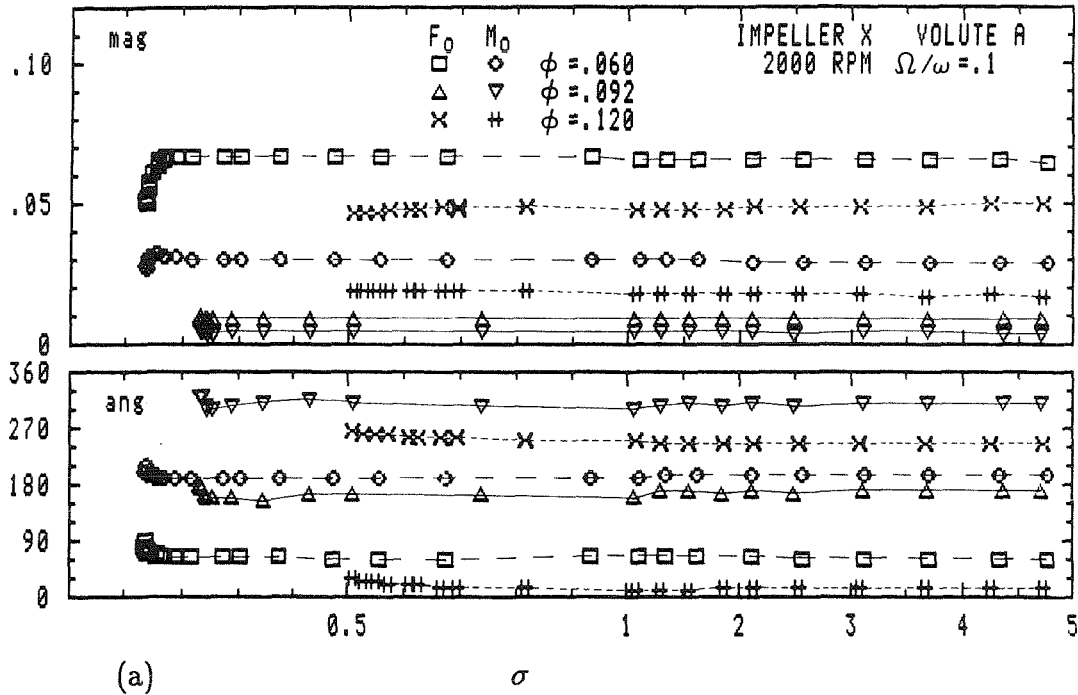
Fig. 7.12 The magnitude and direction of the steady force $\mathbf{F_o}$ and moment $\mathbf{M_o}$ on Impeller X in Volute A at 2000 RPM with $\Omega/\omega = .1$ for the three flow coefficients: $\phi = .060$, .092 (design) and .120, as a function of (a) the cavitation number and (b) the head coefficient.
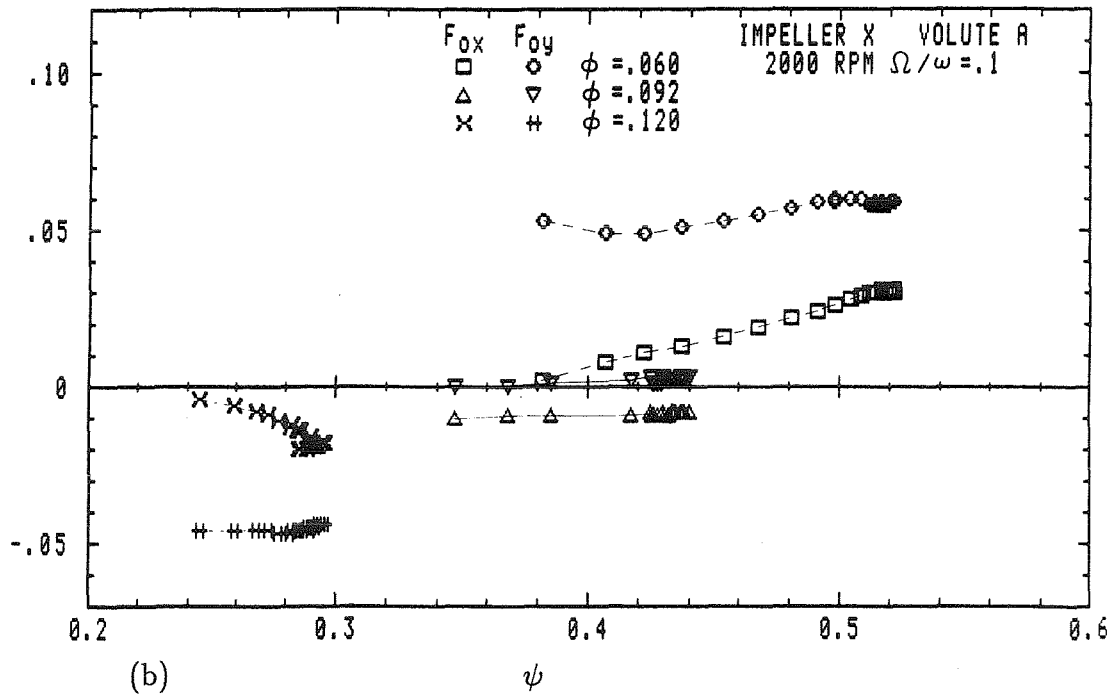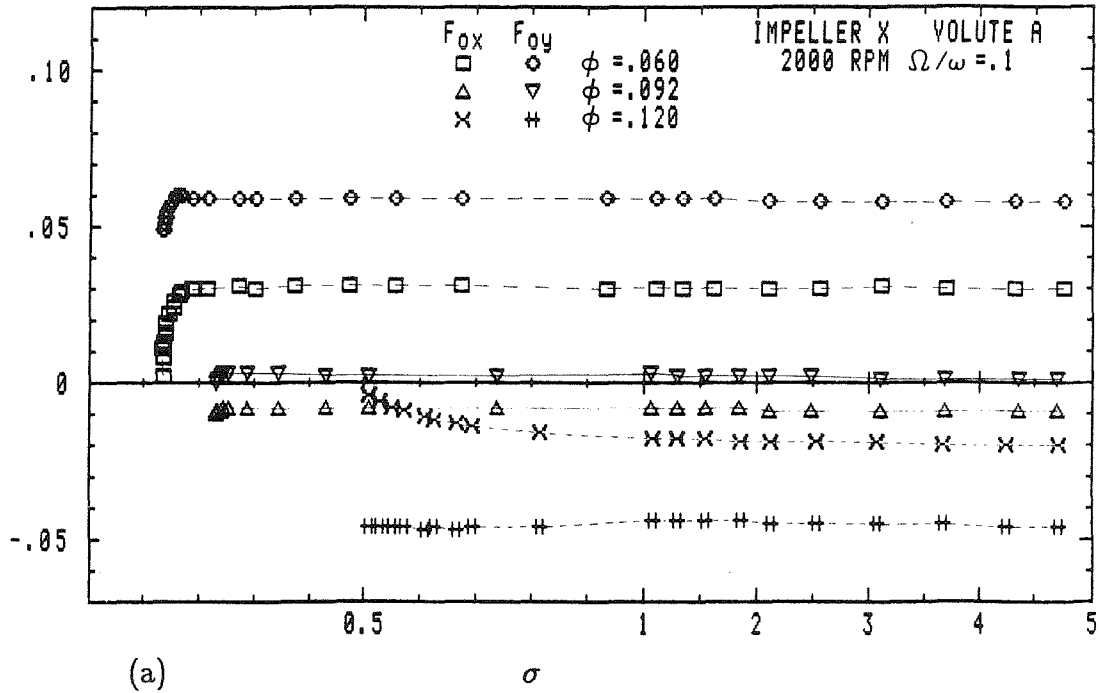
Fig. 7.13 The components of the steady force, F_{ox} and F_{oy}, on Impeller X in Volute A at 2000 RPM with Ω/ω =.1 for the three flow coefficients: ϕ=.060, .092 (design) and .120, as a function of (a) the cavitation number and (b) the head coefficient.
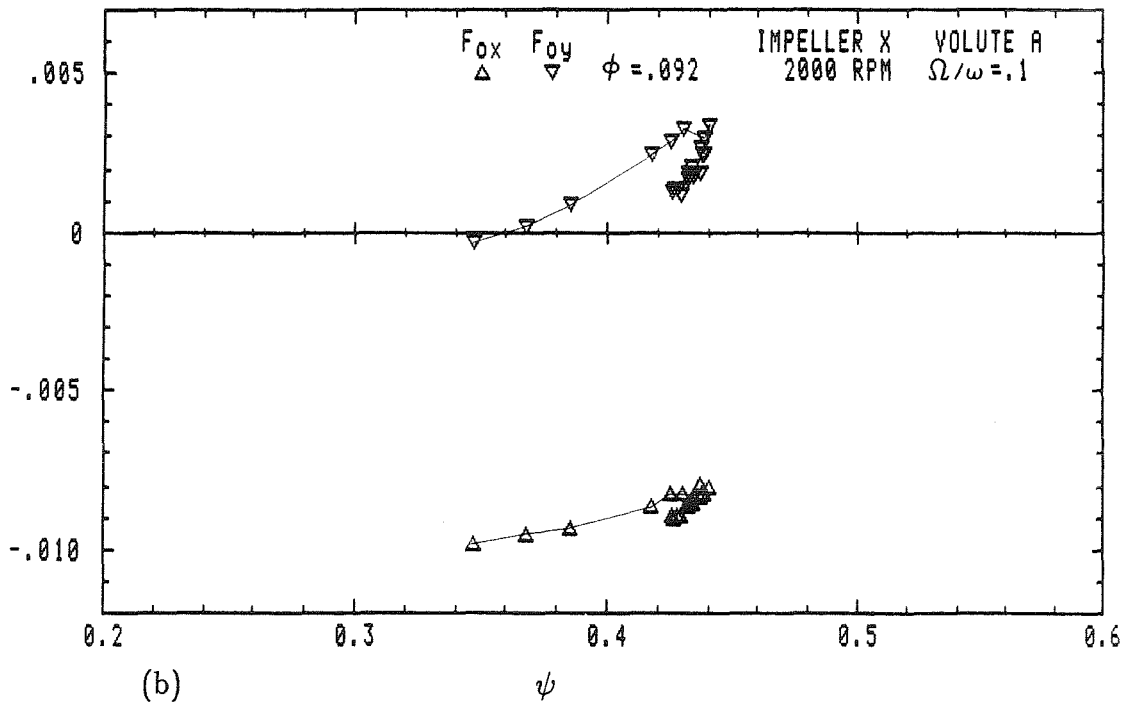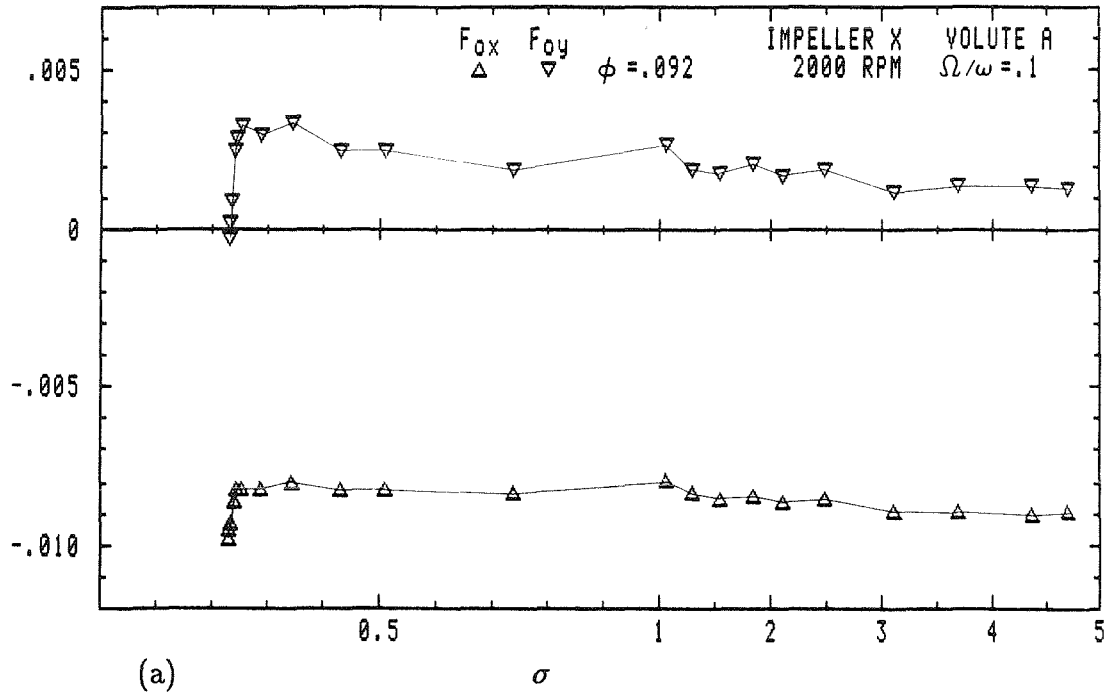
Fig. 7.14   The components of the steady force, F_{ox} and F_{oy}, on Impeller X in Volute A at 2000 RPM with Ω/ω =.1 for design flow (ϕ=.092) as a function of (a) the cavitation number and (b) the head coefficient.
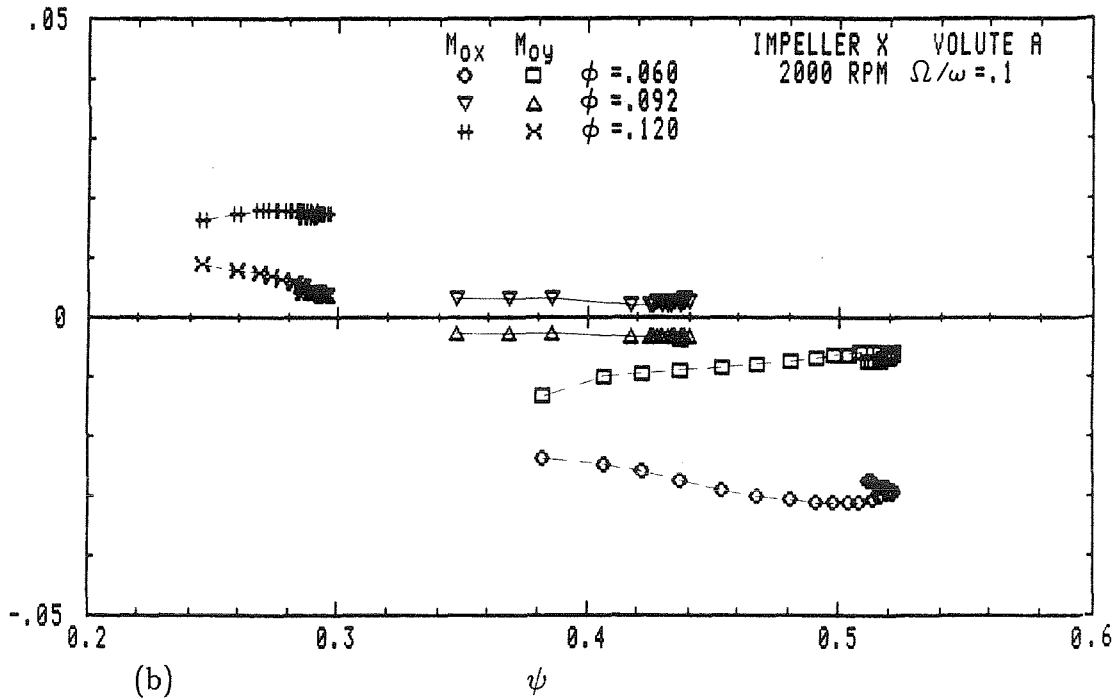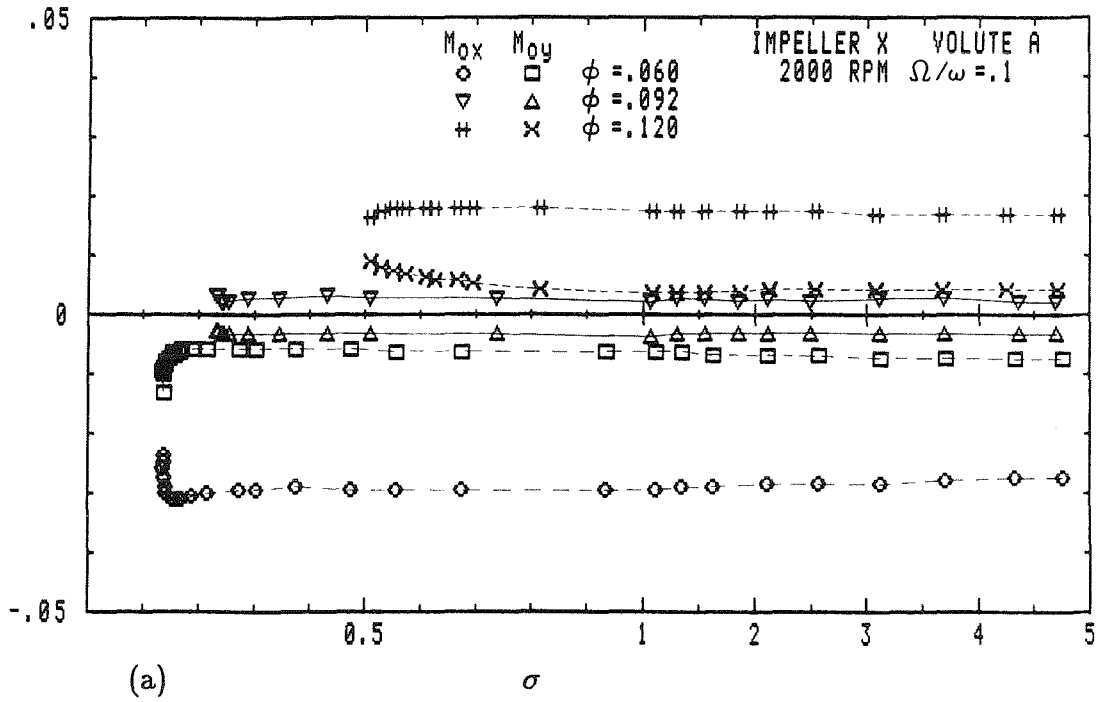
Fig. 7.15   The components of the steady moment, M_{ox} and M_{oy}, on Impeller X in Volute A at 2000 RPM with $\Omega/\omega =.1$ for the three flow coefficients: ϕ=.060, .092 (design) and .120, as a function of (a) the cavitation number and (b) the head coefficient.
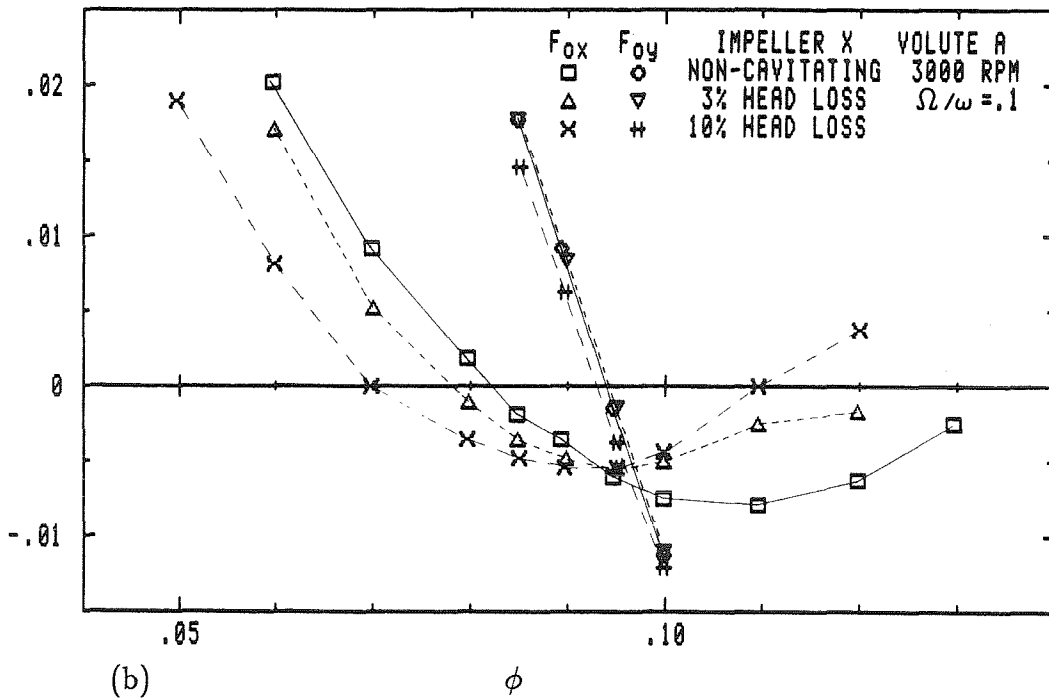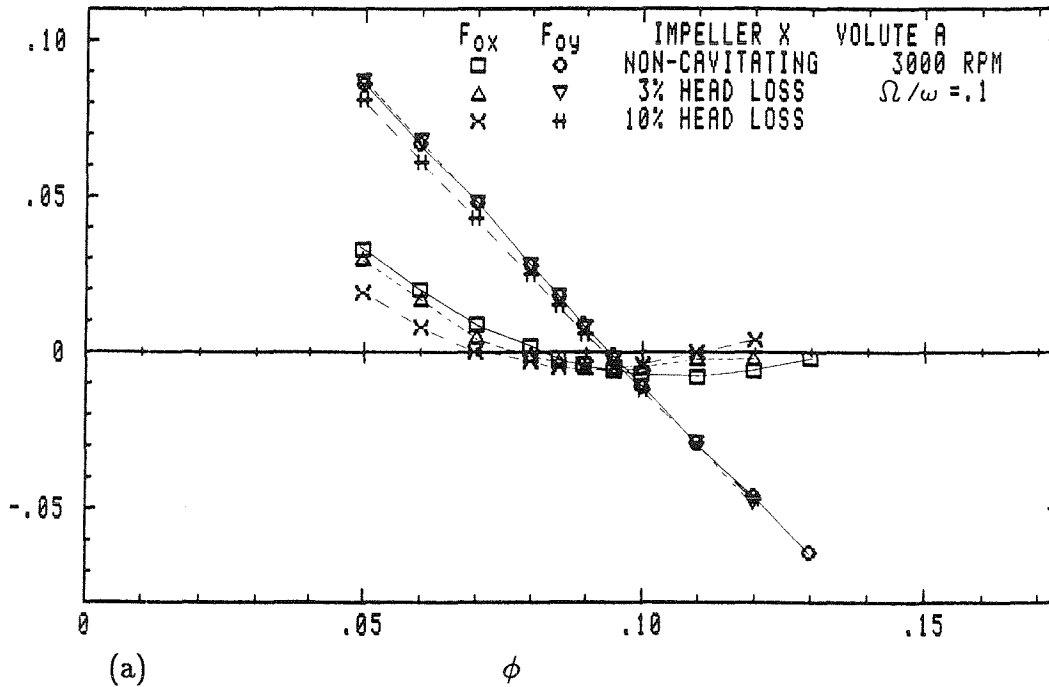
Fig. 7.16   The components of the steady force, F_{ox} and F_{oy}, on Impeller X in Volute A at 3000 RPM with Ω/ω =.1 for the three operating conditions: non-cavitating, 3% head loss and 10% head loss as a function of the flow coefficient (a), and focusing upon design (b).
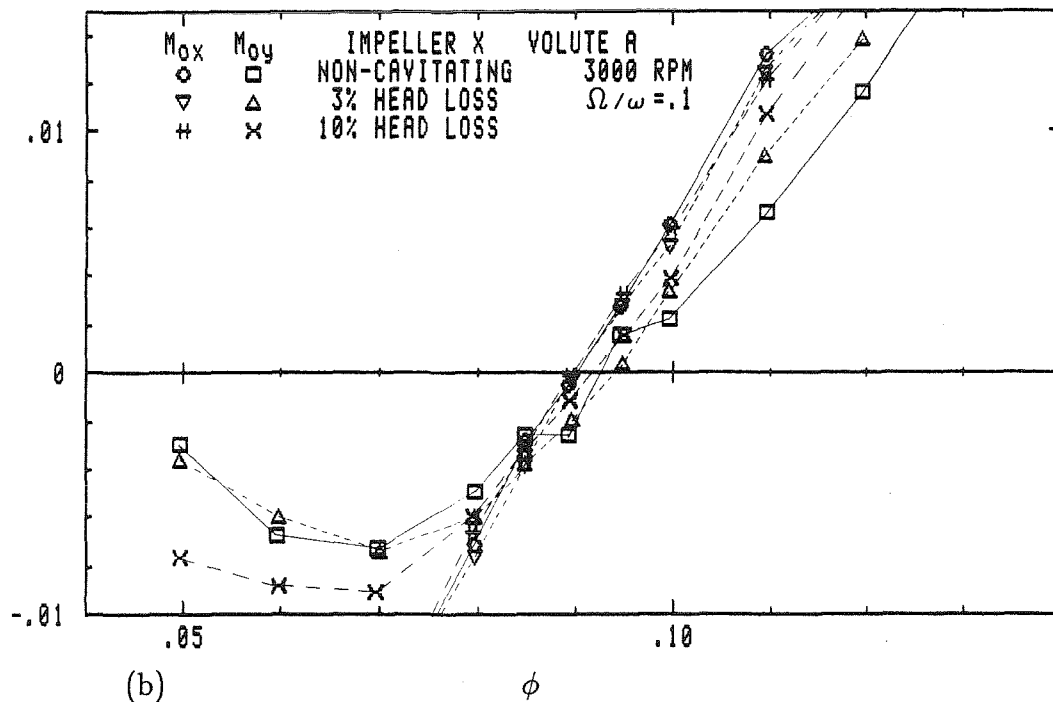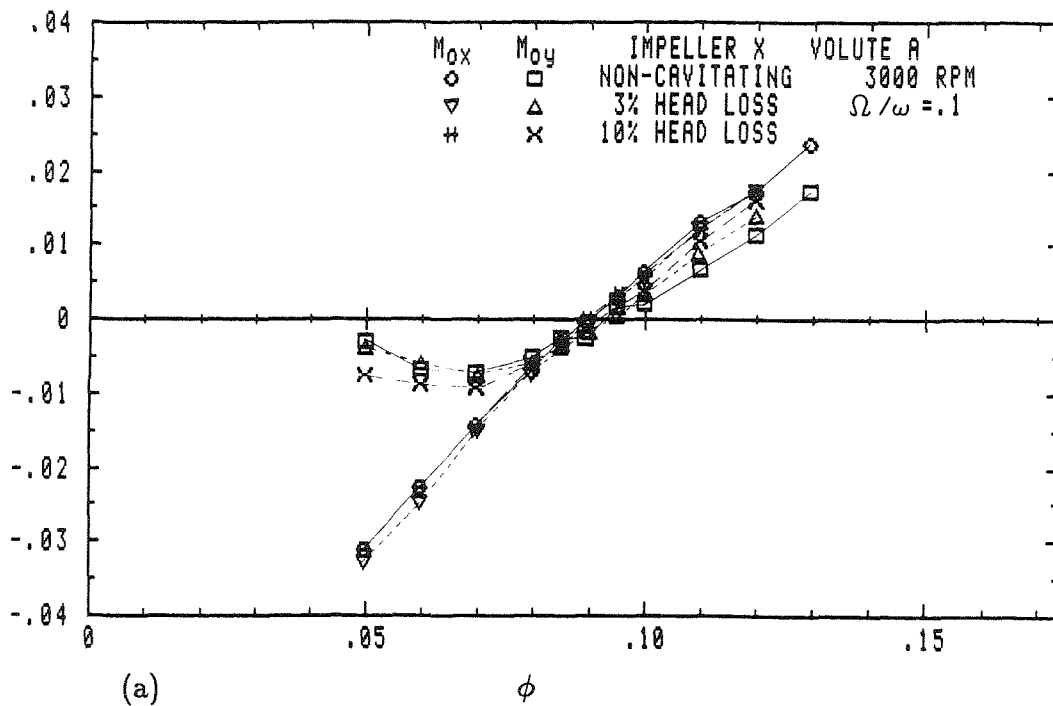
Fig. 7.17   The components of the steady moment, M_{ox} and M_{oy}, on Impeller X in Volute A at 3000 RPM with Ω/ω =.1 for the three operating conditions: non-cavitating, 3% head loss and 10% head loss as a function of the flow coefficient (a), and focusing upon design (b).
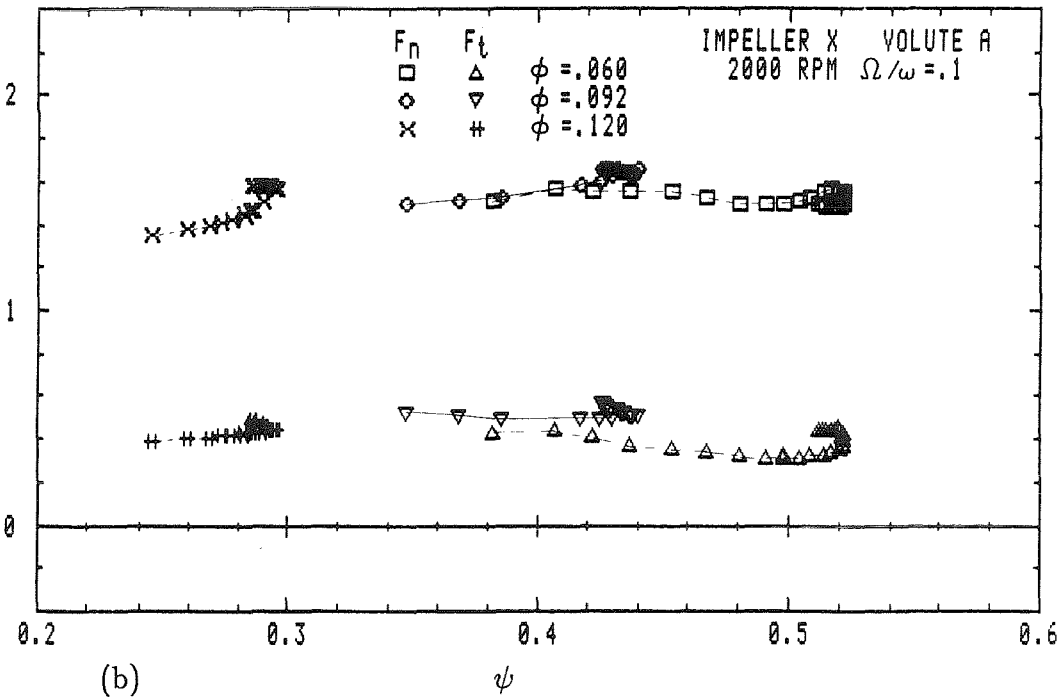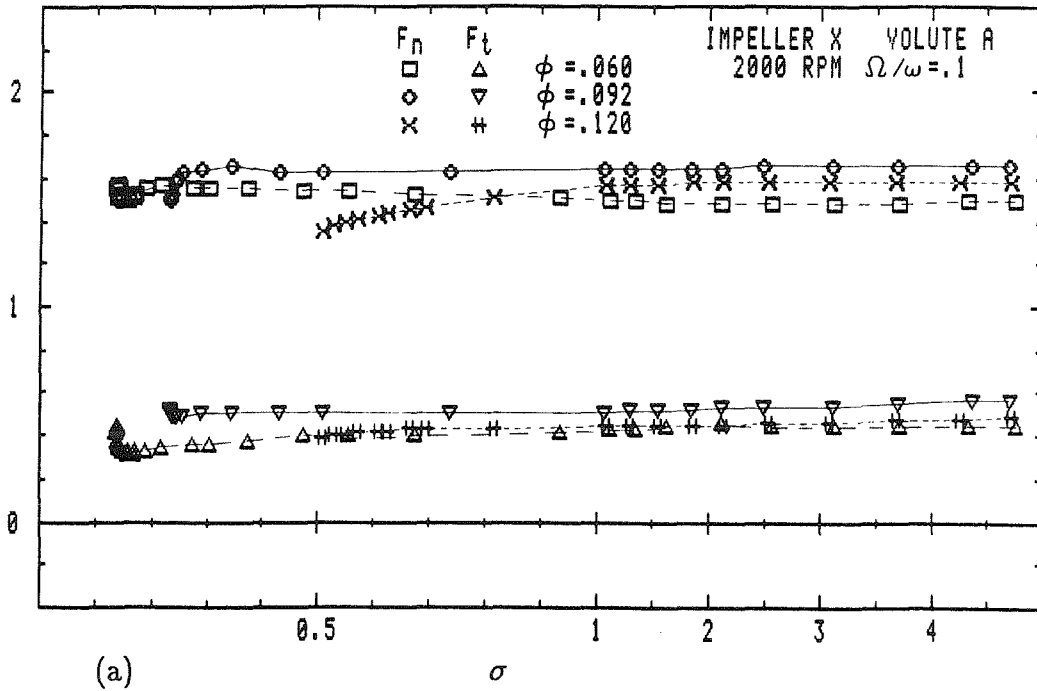
Fig. 7.18 The average normal and tangential force, F_n and F_t, on Impeller X in Volute A at 2000 RPM with $\Omega/\omega=.1$ for the three flow coefficients: $\phi=.060$, .092 (design) and .120, as a function of (a) the cavitation number and (b) the head coefficient.
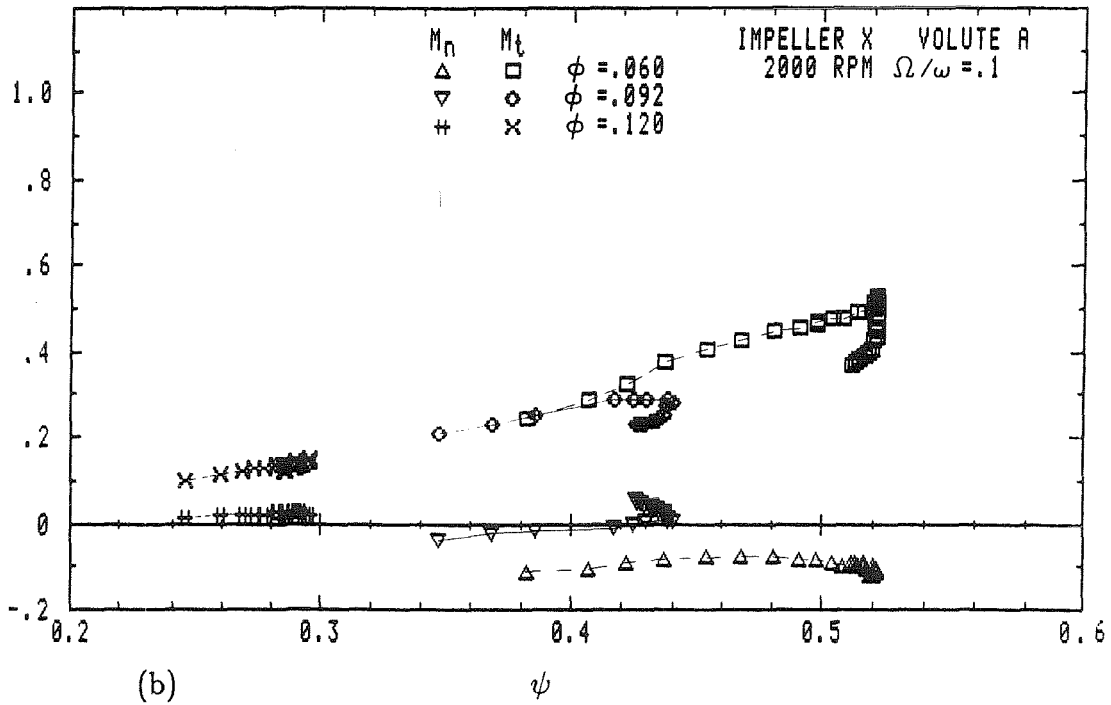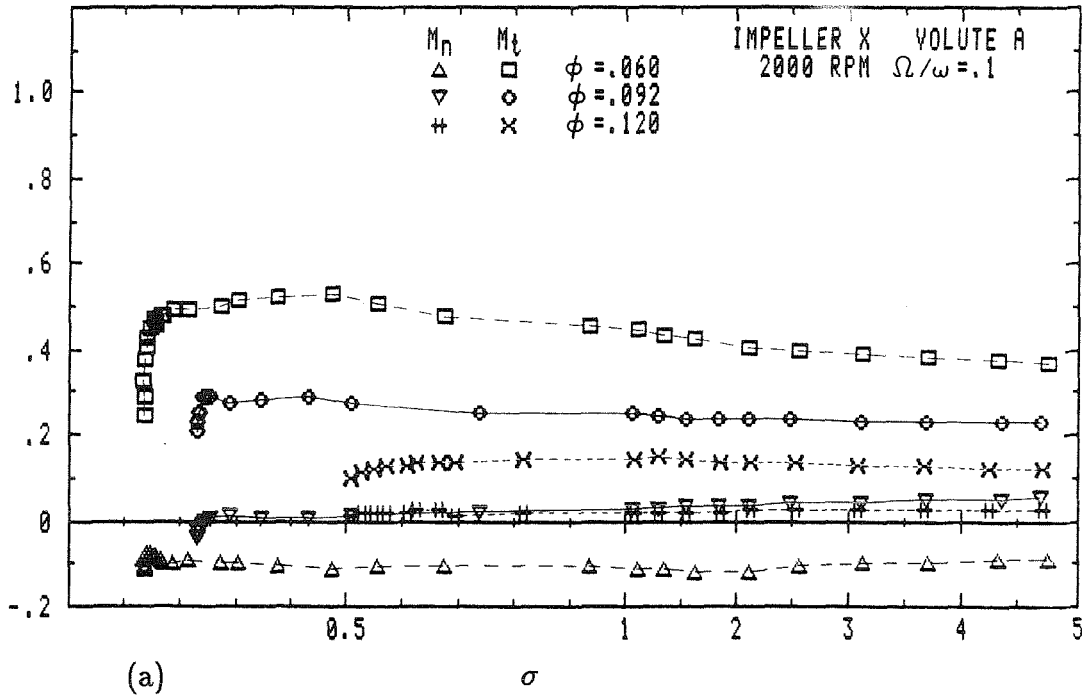
Fig. 7.19   The average normal and tangential moment, M_n and M_t, on Impeller X in Volute A at 2000 RPM with $\Omega/\omega=.1$ for the three flow coefficients: $\phi=.060$, .092 (design) and .120, as a function of (a) the cavitation number and (b) the head coefficient.
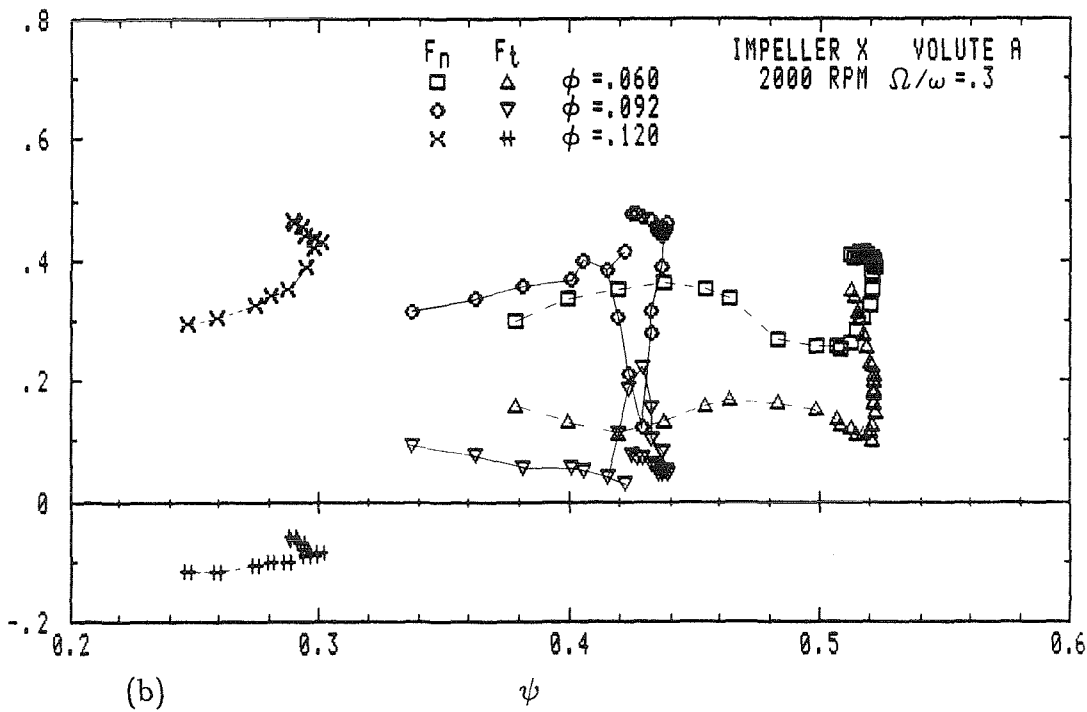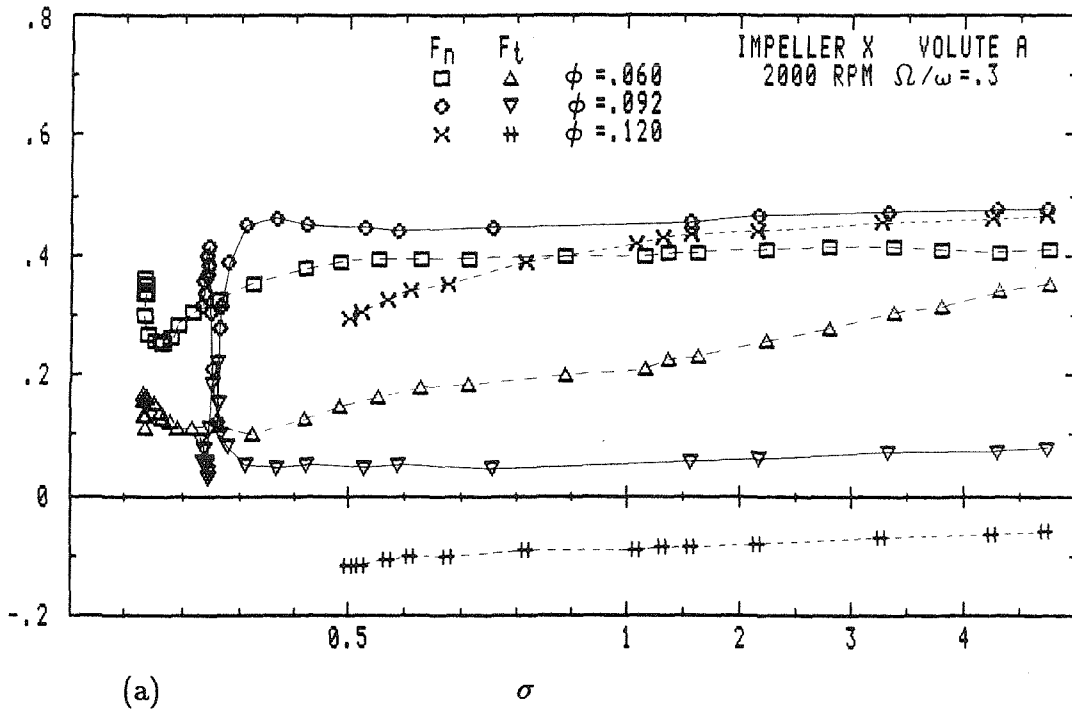
Fig. 7.20 The average normal and tangential force, F_n and F_t, on Impeller X in Volute A at 2000 RPM with $\Omega/\omega=.3$ for the three flow coefficients: $\phi=.060$, .092 (design) and .120, as a function of (a) the cavitation number and (b) the head coefficient.
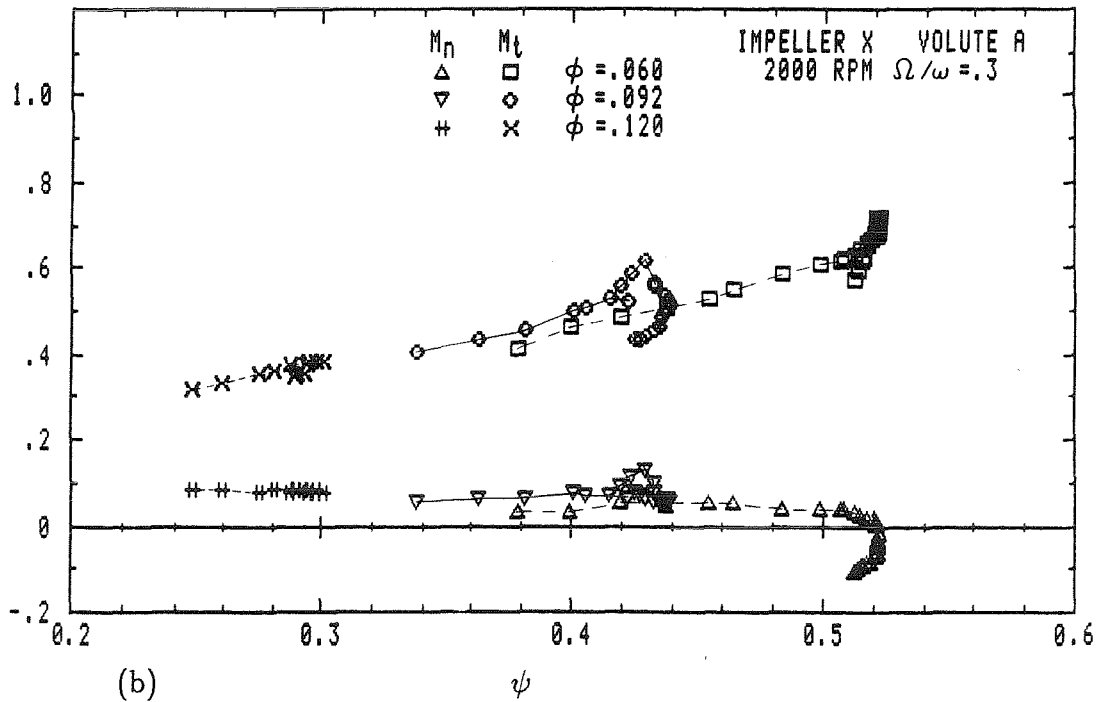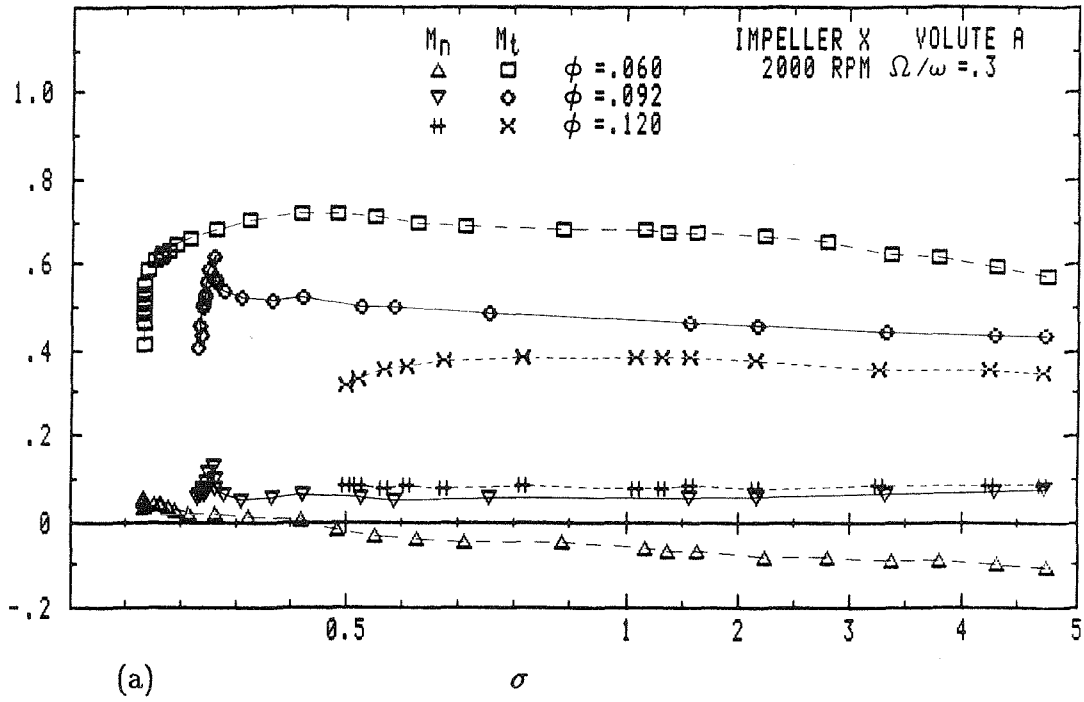
Fig. 7.21 The average normal and tangential moment, M_n and M_t, on Impeller X in Volute A at 2000 RPM with Ω/ω=.3 for the three flow coefficients: ϕ=.060, .092 (design) and .120, as a function of (a) the cavitation number and (b) the head coefficient.
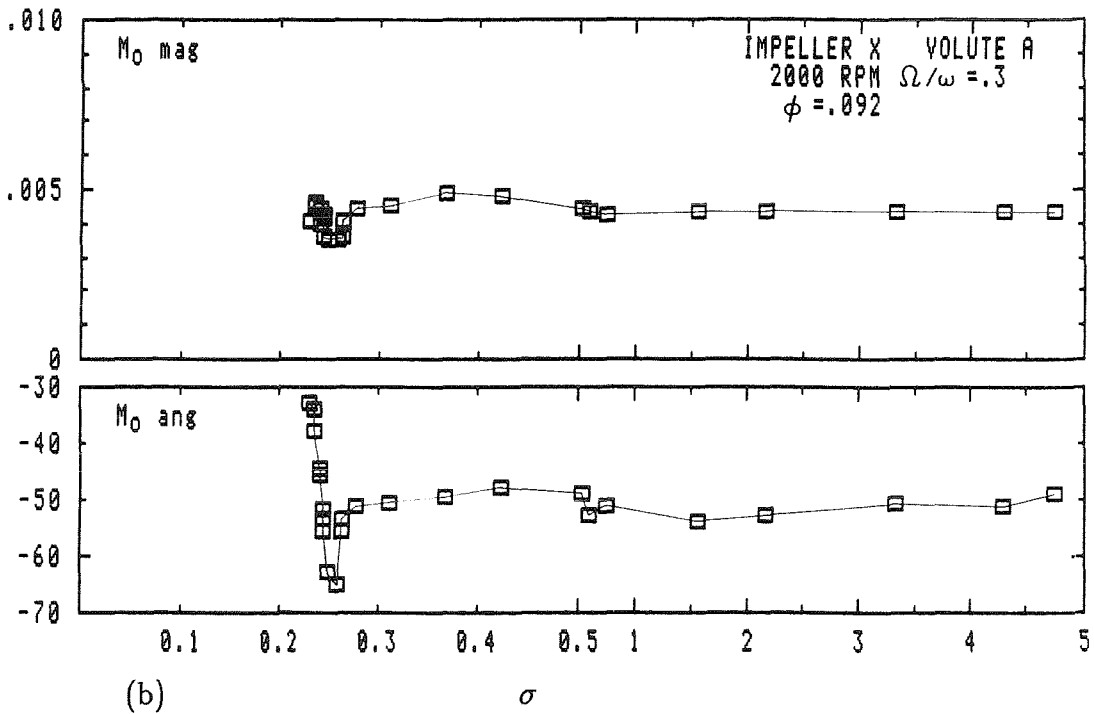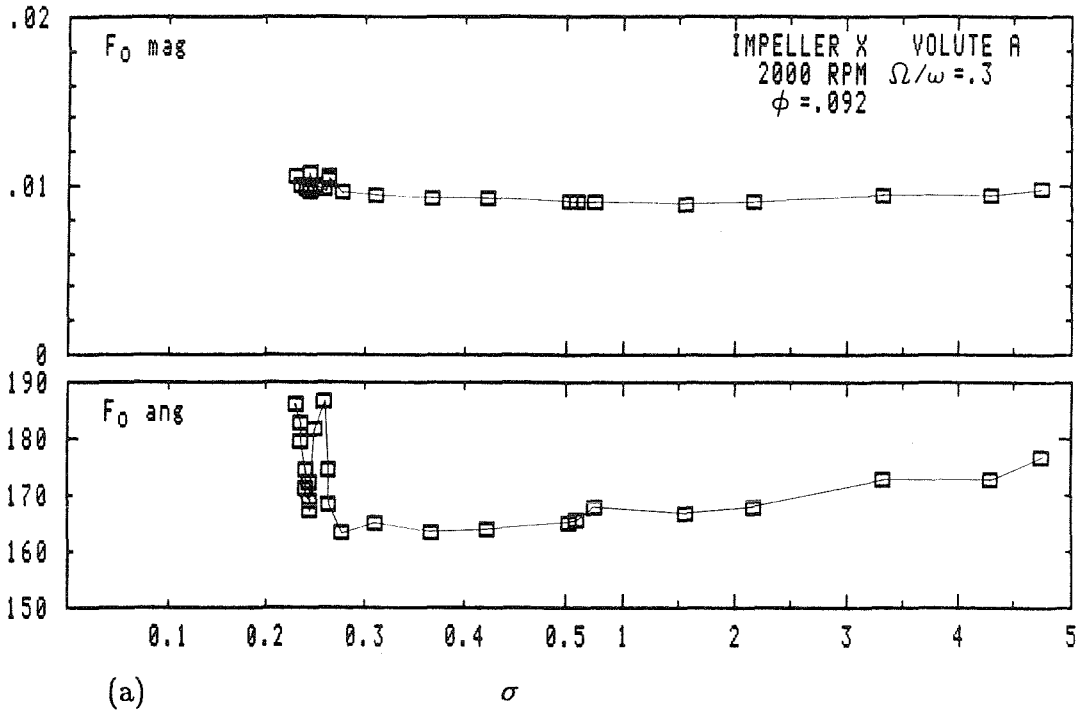
Fig. 7.22 The magnitude and direction of (a) the steady force $\mathbf{F_o}$ and (b) the steady moment $\mathbf{M_o}$ on Impeller X in Volute A at 2000 RPM with $\Omega/\omega = .3$ at design flow ($\phi = .092$) as a function of the cavitation number.

Table 7.1 Stiffness, Damping and Mass Matrices

flow condition	K_{xx} K_{yx}	K_{xy} K_{yy}	C_{xx} C_{yx}	C_{xy} C_{yy}	M_{xx} M_{yx}	M_{xy} M_{yy}
$\phi=.120$	-2.34	.68	2.46	8.19	5.7	-1.2
non-cavit	-.70	-2.34	-7.96	2.70	.3	5.9
$\phi=.120$	-2.15	.65	2.27	7.80	5.4	-.9
3% head loss	-.62	-2.12	-7.70	2.58	.4	5.6
$\phi=.092$	-2.51	.58	1.88	8.76	6.1	-.4
non-cavit	-.78	-2.38	-8.66	1.92	-.3	6.6
$\phi=.092$	-2.42	.60	2.47	8.39	5.6	-1.6
3% head loss	-.81	-2.30	-8.16	2.46	.9	6.0
$\phi=.060$	-2.54	.50	1.6	9.2	7.1	-.3
non-cavit	-.84	-2.20	-9.2	1.3	-.6	7.8
$\phi=.060$	-2.46	.43	2.0	8.9	6.7	-.9
3% head loss	-.67	-2.17	-9.2	1.8	1.0	7.9

Chapter 8

Discussion

The rotating dynamometer measures the integrated force on the whirling impeller. The measured force is from the pressure and shear stress acting on the surface of the impeller body.

$$\mathbf{F} = -\int_B \mathbf{n} \cdot \sigma \, dS \qquad (8.1)$$

where B is the surface of the impeller including the blades, n is the unit normal vector pointing into the body, and σ is the stress tensor. Applying a control volume to the momentum equation replaces the contribution from the internal hub and shroud walls and from the blade surfaces by the stress and momentum flux through the impeller inlet and outlet and the unsteady momentum of the fluid within the machine.

$$\mathbf{F} = -\int_V \left[\frac{\partial \rho \mathbf{u}}{\partial t} - \rho \mathbf{f}\right] dV - \int_\Sigma \mathbf{n} \cdot (\rho \mathbf{u}\mathbf{u} - \sigma) \, dS \qquad (8.2)$$

where f is the body force per unit mass, u the velocity, Σ the circumscribing exterior surface of the impeller, and V the volume of the fluid within the impeller. The theoretical work mentioned in the introduction for whirling two-dimensional impellers generally used the control volume method. For the present, attention will be focused on the impeller blades, Eqn. (8.1).

8.1 Whirling with Cavitation

With sufficiently low upstream pressure, cavities will form on the impeller blade surfaces and bubbles will appear in the flow stream. Kasai and Takamatu (1964) describe observations made of the development of cavitation within centrifugal pumps. Kikuyama et al. (1986) have made pressure measurements at the leading

edge of an impeller blade in the presence of cavitation that was also visually observed. For the present investigation of the rotor forces, the phenomenon of cavitation could not be physically observed. Its presence was inferred from pump performance loss and from its influence upon the dynamometer measurements.

The operating point reflects the pressure distribution on the pressure and suction surfaces of the impeller blades. Without cavitation, the pressure upstream of the machine serves as a datum pressure. With a sufficiently low upstream pressure, cavities form on the impeller blade surfaces and change the pressure distribution across the blade. Pulling a greater vacuum on the pump loop extends the length of cavity, and so for the conditions tested herein, the head rise produced by the rotating impeller decreased.

The forced vibration of whirling adds an additional component, $\Omega \times \varepsilon$, to the peripheral velocity of the rotating impeller when transferring from the absolute frame to the relative frame of the impeller. The local incidence angle varies circumferentially around the impeller. With the changing incidence angle the force on the blade will vary. Considering this simple description, when the impeller whirls on a small whirl radius orbit the local incidence angle varies about a mean corresponding to a centered impeller for a specific flow coefficient. The unsteady forces are associated with the slope of the blade force with respect to the changing incidence angle. The presence of cavitation on the blade will affect the slope of the blade force. An integral over the whirl orbit of the sum over the blades of the radial and azimuthal components of the fluctuating blade force gives the components of the unsteady force in the direction normal to and tangential to the whirl orbit.

Considering only the dependence of the blade force upon the incidence angle is not sufficient. The average of the blade forces over time corresponds to the steady force F_o, which depends upon the asymmetries introduced by the volute to the flow. Also, the unsteady force is not independent of volute, see previous work using the RFTF such as Jery et al. (1985), Jery (1987) or Brennen et al. (1988). The measurements of Ohashi et al. (1988) on an impeller in a symmetric

diffuser chamber (see the Introduction) did not have a destabilizing tangential force at design flow. Tsujimoto (1988b) comments that his theory does not predict a destabilizing tangential force without a volute or when neglecting the unsteady vortex distribution on the volute. Consequently, integrating a perturbation of the force on the impeller blades due to the imposed whirl motion in order to obtain the unsteady rotor force requires the inclusion of the changing flow exit angle.

8.2 Lever Arms

The measurements presented in the previous chapter are in the calibration plane of the dynamometer which coincides with the plane bisecting the discharge area of Impeller X. A force that is not acting through the origin of this plane would contribute to the measured moment. The lateral moment data will be examined in an attempt to compute a line of action for the lateral force. An implicit assumption is that the axial thrust F_3 acts along the impeller centerline. The relation $\mathbf{r} \times \mathbf{F} = \mathbf{M}$ is used to search for a location in which the lateral moment vanishes.

$$yF_z - zF_y = M_x$$
$$zF_x - xF_z = M_y \qquad (8.3)$$
$$xF_y - yF_x = M_z$$

With the assumption that axial thrust acts along the impeller centerline, there is no contribution by F_3, i.e. F_z, to the lateral moment. Also assuming that the lateral force acts through the impeller centerline, the contribution to M_z vanishes.

The following lever arms are considered for the steady force and for the unsteady force

$$z_o = \frac{M_{oy}}{F_{ox}}, \quad -\frac{M_{ox}}{F_{oy}}$$
$$z_\varepsilon = \frac{M_t}{F_n}, \quad -\frac{M_n}{F_t} \qquad (8.4)$$

With the non-dimensionalization given previously for the forces and moments, the computed lever arm is non-dimensionalized by the impeller discharge radius, r_2.

Fig. 7.12 of the previous chapter shows that the steady force and moment are not perpendicular. Also the unsteady force and moment due to whirl are not 90° apart.

Recall that the dynamometer measures the integrated force and moment experienced by the impeller. In terms of Eqn. (8.1), the contributions are from the exterior shroud and from internal surfaces such as the blades. Alternatively using the control volume formulation, one can consider the total force as separated into the contribution from the shrouds and from the impeller-volute interaction, which would include the integral over the impeller inlet and outlet surfaces and the integral over the internal fluid volume. Similarly the moment integral,

$$\mathbf{M} = -\int_B \mathbf{r} \times \mathbf{n} \cdot \sigma \; dS \tag{8.6}$$

can be separated into the contribution from the exterior shroud and from the internal surfaces or the impeller-volute interaction.

In order to simplify the discussion, attention will be focused on the integrals over the shroud and over the impeller blades.

$$\mathbf{M} = -\int_{\text{shroud}} \mathbf{r} \times \mathbf{n} \cdot \sigma \; dS - \int_{\text{blade}} \mathbf{r} \times \mathbf{n} \cdot \sigma \; dS$$
$$= -\mathbf{R}_{\text{shroud}} \times \mathbf{F}_{\text{shroud}} - \mathbf{R}_{\text{blade}} \times \mathbf{F}_{\text{blade}} \tag{8.7}$$

Since the unsteady rotor forces which can encourage self-excited whirl are of primary interest, attention will be focused on the unsteady moments. The unsteady lateral force is expected to contribute to the moment as

$$M_n = -z_{\text{shroud}} \; F_{t,\text{shroud}} - z_{\text{blade}} \; F_{t,\text{blade}}$$
$$M_t = z_{\text{shroud}} \; F_{n,\text{shroud}} + z_{\text{blade}} \; F_{n,\text{blade}} \tag{8.8}$$

where the z axis points upstream from the plane mid-span of the impeller discharge. Unless the forces $\mathbf{F}_{\text{shroud}}$ and $\mathbf{F}_{\text{blade}}$ are parallel, the introduced moment will not be perpendicular to the force. The impeller-volute contribution may be discussed in terms of the force on the impeller blades because cavitation occurring within the machine would affect the contribution from the internal surfaces first.

In Figs. 8.1–5 the lever arms computed from Eqn. (8.4) are presented for the unsteady lateral forces and moments. Because the measurements are integrated over the entire impeller, the contribution from each force element of the preceding paragraph is impossible to quantify.

The lever arms as a function of whirl ratio are given in Figs. 8.1–3 for the three flow coefficients tested at the non-cavitating and 3% head loss operating points. The lever arms are disturbed over the range where F_n and F_t cross zero. For reverse whirl, the lever arms M_t/F_n and $-M_n/F_t$ are closer. Recall from the Introduction the comparison of the two-dimensional version, Impeller Z, with Impeller X. For reverse whirl the forces on Impeller Z are smaller, indicating a significant contribution to the forces on Impeller X from the front shroud. Further away from the calibration plane, the shroud force would have a greater contribution to the lateral moment. Consequently, with the larger forces for reverse whirl, the computed lever arms are more reasonable. On Fig. 8.2 the error bars represent ± 1 standard deviation calculated using "root-sum-square" for the propagation of uncertainty. The error is dependent upon the magnitude of the denominator, F_n or F_t.

The unsteady lever arms are given for $\Omega/\omega{=}.1$ and .3 through breakdown in Figs. 8.4–5. For non-cavitating flow (the $\sigma \approx 4.3$ point) the standard deviation of M_t/F_n for $\Omega/\omega{=}.1$ is approximately 0.03, 0.04 for $\phi{=}.060$. For $-M_n/F_t$ it is 0.1. For $\Omega/\omega{=}.3$ the standard deviation of M_t/F_n is 0.3, 0.2, and 0.1 for $\phi{=}.060$, .092, and .120, respectively. For $-M_n/F_t$ it is 0.2, 0.5, and 1.2. A simple description of the effect of cavitation on the lever arms is that cavitation will affect the contribution to the integrated forces and moments from the impeller blades before the contribution from the external shroud surfaces, which would have a larger lever arm.

The framework of Eqns. (8.7, 8) does not take into account the contribution from force elements acting in the axial direction. An example is the contribution from the external shroud. The pressure distribution giving rise to the unsteady

lateral force also has a projected force element in the axial direction, $pn_z \, dS$. An integral over the moment of the axial pressure force element, $\mathbf{r} \times pn_z \, dS$, would contribute to the lateral moment.

Fig. 8.6 shows z_o computed from the steady moment and force for $\Omega/\omega = .1$ under cavitation. For off-design, $z_o = M_{oy}/F_{ox}$ is more affected by cavitation. Recall from Figs. 7.13, 16 that cavitation had a greater affect on F_{ox} than F_{oy}. For design the scatter of $-M_{ox}/F_{oy}$ reflects the small values of F_{oy}. The lever arms were presented in this chapter as an alternative to the moments themselves.

8.3 Concluding Remarks

The results presented herein on the effect of cavitation on the rotordynamic forces are for a single turbomachine: a centrifugal impeller in a spiral volute. Surprisingly, the effect was not significant for most of the flow conditions and whirl ratios tested. The existence of an operating region with cavitation for which the destabilizing tangential force had increased indicates further study is needed.

A model to describe the cavitating flow conditions in which these measurements were made does not yet exist. An impeller whirling inside a volute in fully wetted flow has been treated theoretically, see section 1.4. Cavitation within a centrifugal impeller without whirl has been treated. For example, leading edge sheet cavitation within centrifugal impeller passages with steady flow has been modelled theoretically by mapping methods, Tsujimoto et al. (1986). For bubbly flow, requiring a different treatment, Furuya uses a two-fluid model with non-condensible (1985a) or condensible gas (1985b) with empirical loss data to calculate the performance of centrifugal pumps with large void fraction.

Past measurements using the Rotor Force Test Facility have been made on various turbomachines in fully wetted flow. These had shown that for the impeller-volute combination presented, the unsteady forces did not exhibit an unusual dependence upon flow coefficient or whirl ratio. In fully wetted flow tests a centrifugal impeller with an inducer (one half of the double-suction impeller of

the HPOTP) had exhibited a change in the dependence of F_t upon whirl ratio. The curve resembled a cubic for low flow coefficients where flow reversal was observed upstream of the inducer. Further experiment is necessary to observe how operation in the presence of cavitation will alter the rotordynamic forces experienced by such an impeller.
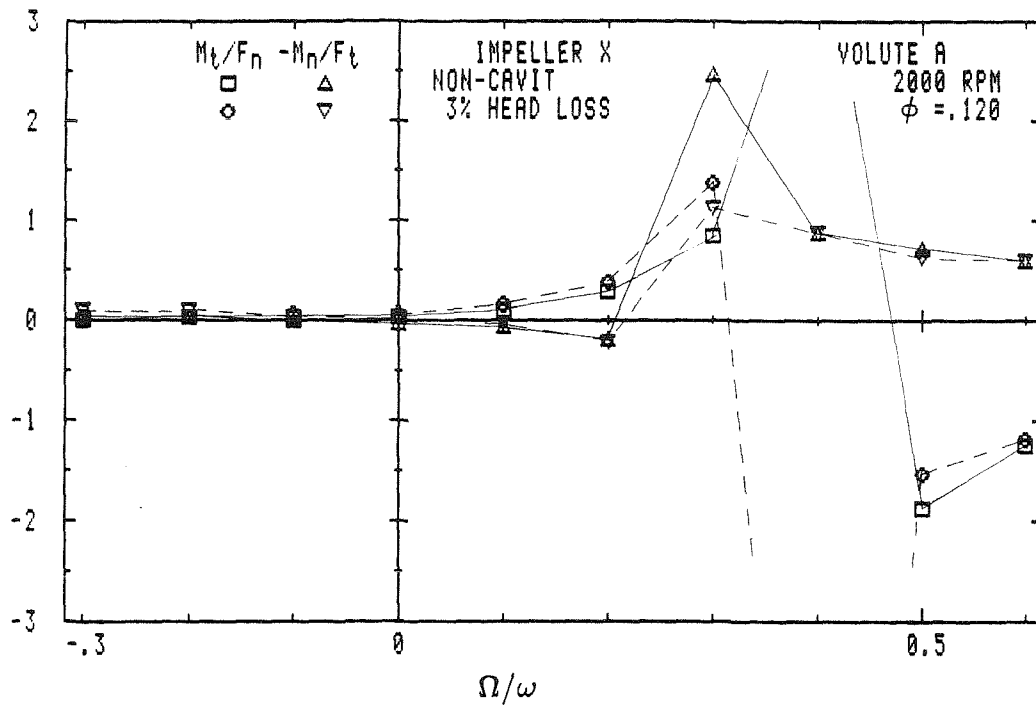
Fig. 8.1 The lever arm, z_ε, computed from the components of the unsteady moment and force on Impeller X in Volute A at 2000 RPM at a flow coefficient of $\phi = .120$ as a function of whirl ratio for flow without cavitation and with a head loss of 3%.
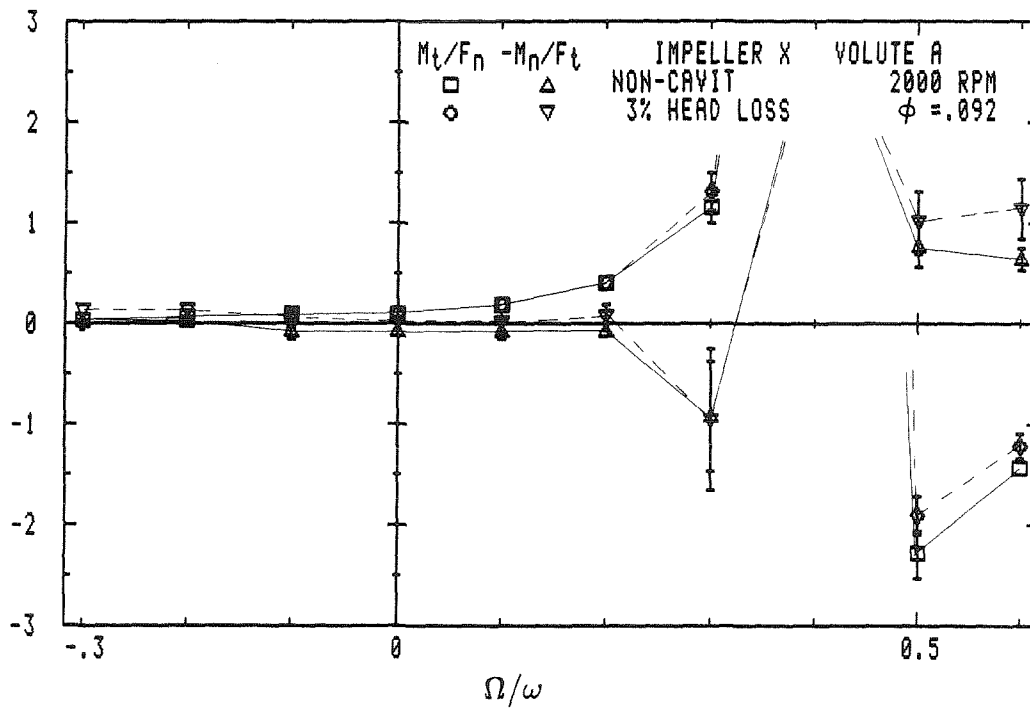
Fig. 8.2 The lever arm, z_ε, computed from the components of the unsteady moment and force on Impeller X in Volute A at 2000 RPM at design flow ($\phi = .092$) as a function of whirl ratio for flow without cavitation and with a head loss of 3%.
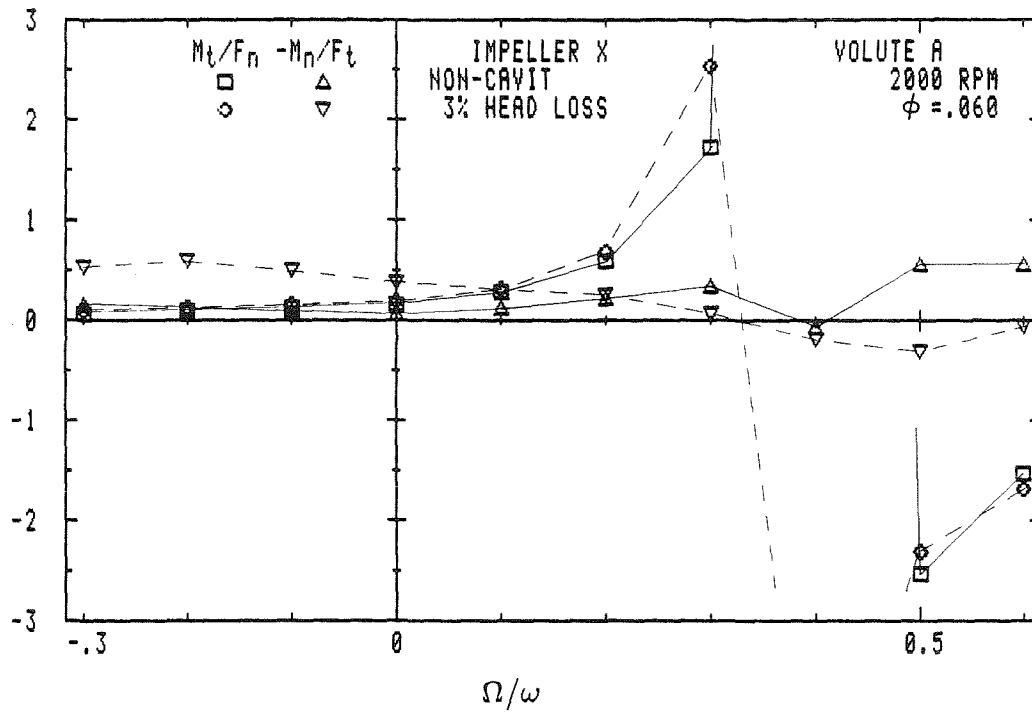
Fig. 8.3 The lever arm, z_ε, computed from the components of the unsteady moment and force on Impeller X in Volute A at 2000 RPM at a flow coefficient of $\phi = .060$ as a function of whirl ratio for flow without cavitation and with a head loss of 3%.

(a)

σ

(b)

ψ
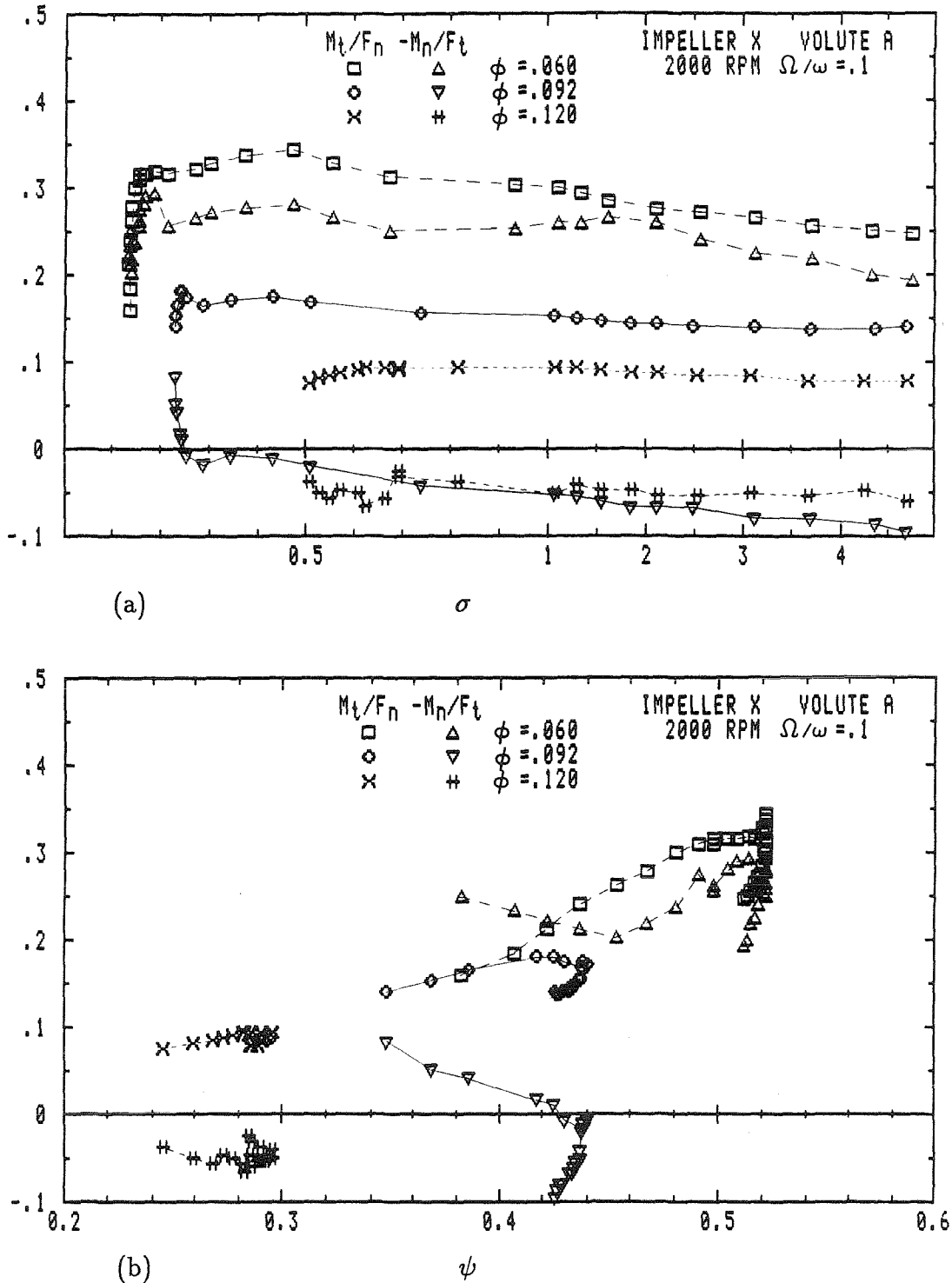
Fig. 8.4 The lever arm, z_ε, computed from the components of the unsteady moment and force on Impeller X in Volute A at 2000 RPM with $\Omega/\omega=.1$ for the three flow coefficients: $\phi=.060$, .092 (design) and .120, as a function of (a) the cavitation number and (b) the head coefficient.
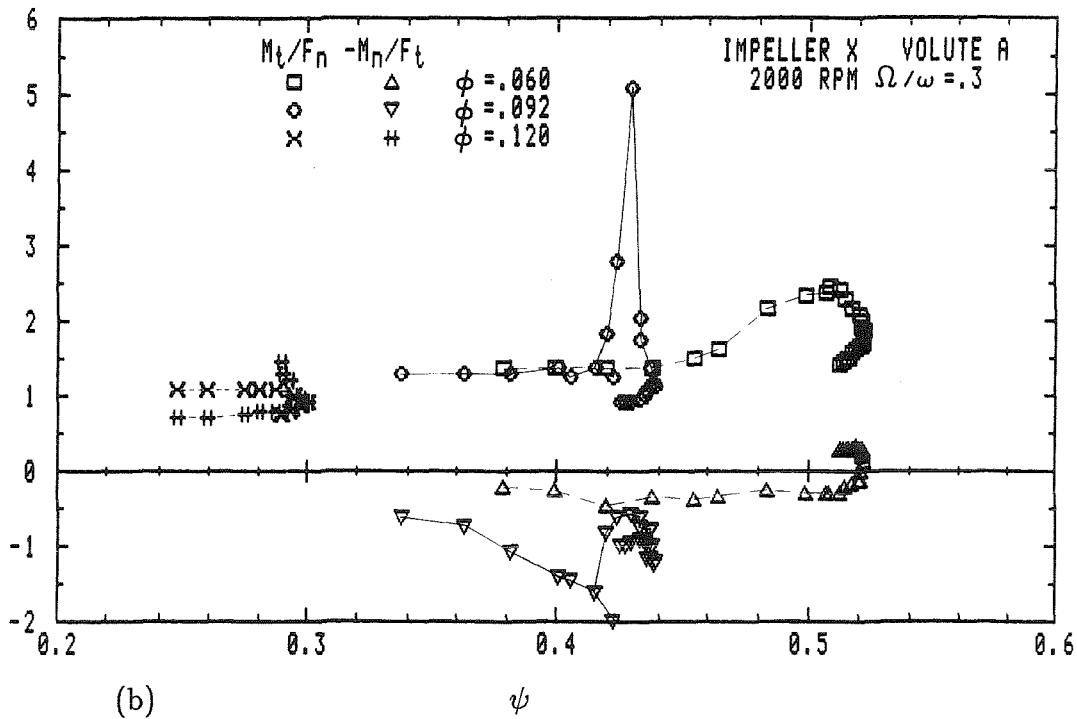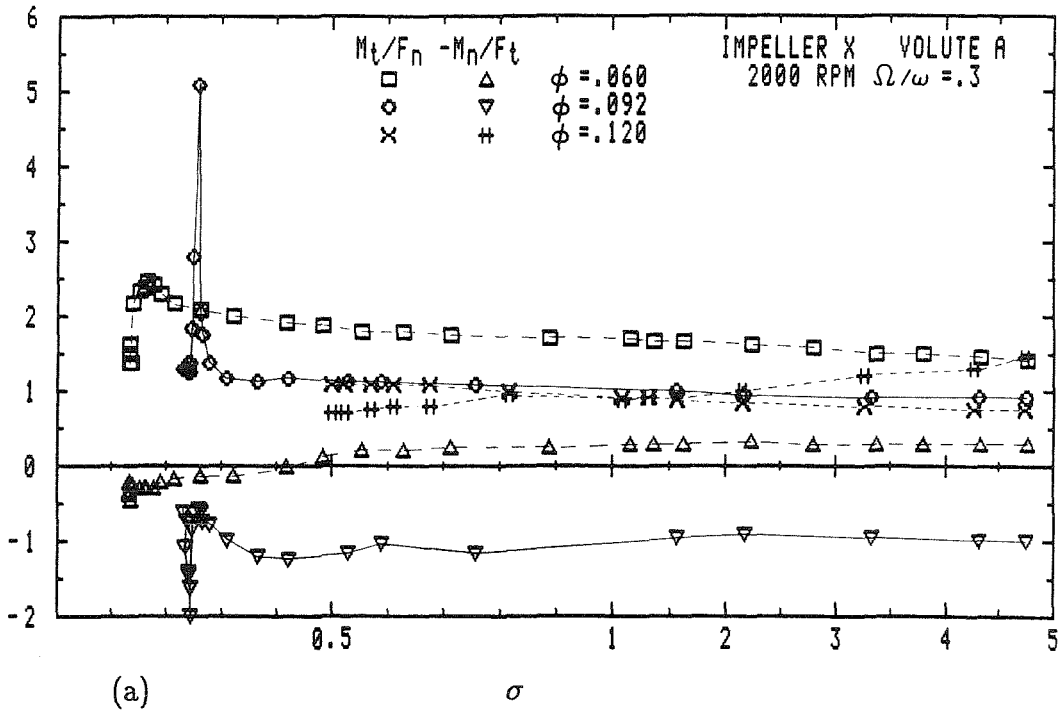
Fig. 8.5 The lever arm, z_s, computed from the components of the unsteady moment and force on Impeller X in Volute A at 2000 RPM with Ω/ω=.3 for the three flow coefficients: ϕ=.060, .092 (design) and .120, as a function of (a) the cavitation number and (b) the head coefficient.
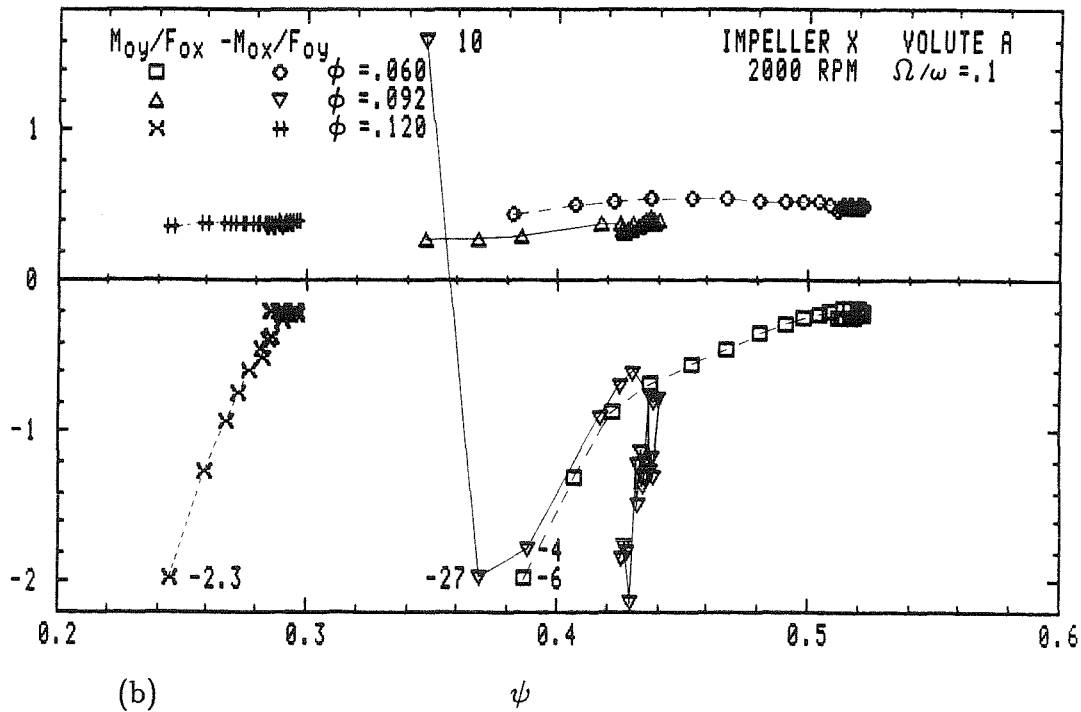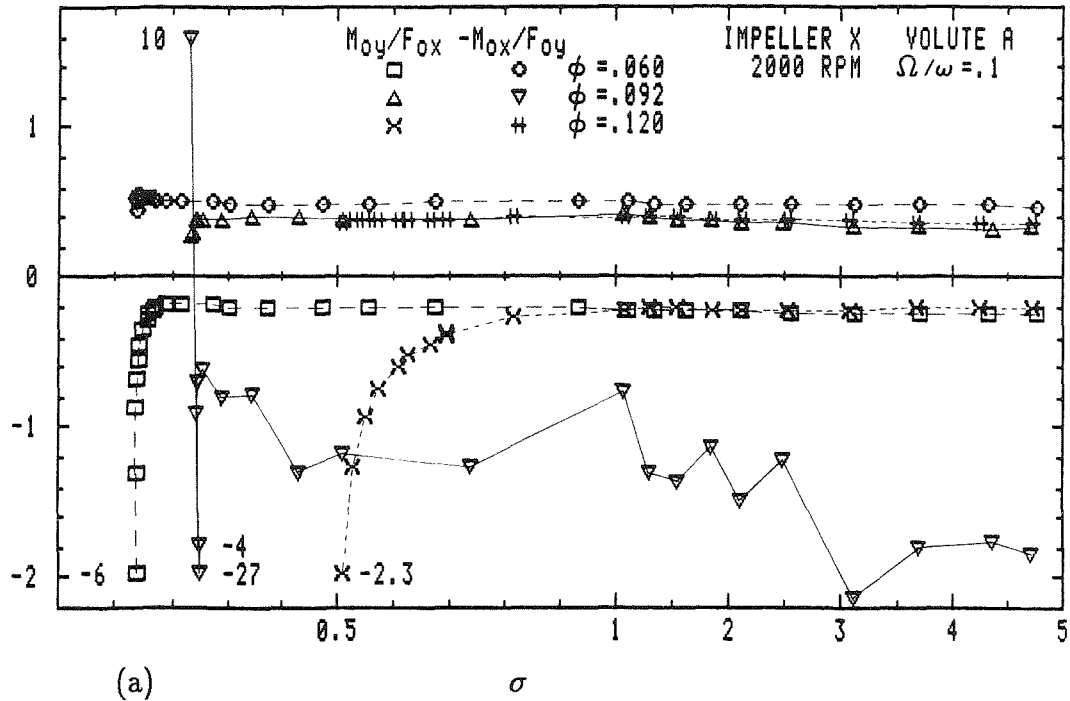
Fig. 8.6 The lever arm, z_o, computed from the components of the steady moment and force on Impeller X in Volute A at 2000 RPM with Ω/ω=.1 for the three flow coefficients: ϕ=.060, .092 (design) and .120, as a function of (a) the cavitation number and (b) the head coefficient.

Chapter 9

Summary and Conclusion

In summary, rotordynamic forces were measured in the presence of cavitation for a centrifugal impeller in a spiral volute, designed to be "well-matched." Measurements using this five-bladed impeller in a variety of volutes have already been made (Jery 1985 and 1987) under non-cavitating operating conditions. In the present investigation three flow coefficients were tested, $\phi = .060, .092$ (design), and .120. A set of whirl ratios, Ω/ω, were taken under non-cavitating conditions and operating at three percent head loss over the range $-0.3 \leq \Omega/\omega \leq 0.6$, in increments of 0.1. The range of forward whirl over which the tangential force is destabilizing was bracketed by these tests. In the presence of cavitation at 3% head loss there was little difference in the average normal and tangential force, F_n and F_t, for forward whirl, slightly more for the larger values of reverse whirl. The range of whirl ratio that the tangential force is destabilizing had decreased slightly with cavitation.

For each flow coefficient data was taken at two whirl ratios, $\Omega/\omega =.1$ and .3, with decreasing cavitation number through breakdown. The percentage of head loss obtained for the three flow coefficients was for $\phi = .060$, 25%, for $\phi = .092$, 20%, and for $\phi = .120$, 15%. The magnitude of the steady force, $\mathbf{F_o}$, for off-design flow decreases with breakdown and its direction changes in the direction of main shaft rotation. For design flow the magnitude decreased then began to increase approaching the knee of the performance curve. It varied less than 10% from flow without cavitation to 20% head loss, though its direction changed. At 3% head loss the destabilizing unsteady forces had decreased. Through breakdown in head the destabilizing forces did not exceed their non-cavitating values except for one set of data. For design flow, between peak head rise and 1% head loss for $\Omega/\omega =.3$, the flow was sufficiently disturbed to perturb both the unsteady and the steady forces.

Passing through the knee of the performance curve, the unsteady force vector moved in a direction to increase the destabilizing tangential force, then moved back with greater head loss. The corresponding change in the steady force vector was first in the direction of impeller rotation. For this set of tests cavitation had a noticeable effect upon the unsteady rotordynamic forces. The destabilizing tangential force had increased above its non-cavitating value over a range of operating conditions.

Measurements of the rotordynamic forces on impellers and inducers that have been made using the rotating dynamometer of the Rotor Force Test Facility at Caltech are integrated measurements. The contribution to the total force from the varying clearance between the impeller front shroud and the casing wall during whirl is not distinguished from the contribution from the unsteady flow field between the whirling impeller and the volute.

To conclude, cavitation did not have a significant effect upon the hydrodynamic forces on a centrifugal impeller in a spiral volute. However, the data taken at design flow for $\Omega/\omega=.3$ indicates the existence of a range of flow coefficients and whirl ratios for which operation with some cavitation would increase the destabilizing tangential force, though the normal force, which tends to increase the amplitude of the lateral vibration, is smaller.

Further work is necessary to quantify the contribution of the shroud flow to the impeller force measurements. Childs (1986) has theoretically examined the forces from the annulus between the impeller shroud and the pump housing. His model is not appropriate for the rather large annular gap for the tested Impeller X. The theoretical model of Tsujimoto et al. (1988b) for the impeller-volute interaction has compared favorably with two-dimensional impellers. Both a model and additional measurements are needed to understand the effect of cavitation upon the rotordynamic forces.

References

Adkins, D. R., 1986, "Analyses of Hydrodynamic Forces on Centrifugal Pump Impellers," Ph.D. Thesis, Division of Engineering and Applied Science, California Institute of Technology, Pasadena, CA.

Adkins, D. R., and Brennen, C. E., 1988, "Analyses of Hydrodynamic Radial Forces on Centrifugal Pump Impellers," ASME *Journal of Fluids Engineering*, **110**(1), 20–28.

Agostinelli, A., Nobles, D., and Mockridge, C. R., 1960, "An Experimental Investigation of Radial Thrust in Centrifugal Pumps," ASME *Journal of Engineering for Power*, **82**(2), 120–126.

Allaire, P. E., Humphris, R. R., Kelm, R. D., 1986, "Dynamics of a Flexible Rotor in Magnetic Bearings," Proceedings of the Fourth Workshop on Rotordynamic Instability Problems in High–Performance Turbomachinery, Texas A & M University, College Station, Texas, NASA CP 2443, pp. 419–430.

Arndt, N., and Franz, R., 1986, "Observations of Hydrodynamic Forces on Several Inducers including the SSME LPOTP," Division of Engineering and Applied Science, California Institute of Technology, Pasadena, CA, Report No. E249.3.

Bevington, P. R., 1969, *Data Reduction and Error Analysis for the Physical Sciences*, McGraw-Hill Inc., New York, chapter 8.

Black, H. F., 1974, "Calculation of Forced Whirling and Stability of Centrifugal Pump Rotor Systems," ASME *Journal of Engineering for Industry*, **96**(3), 1076–1084.

Bolleter, U., Wyss, A., Welte, I., and Stürchler, R., 1987, "Measurement of Hydrodynamic Interaction Matrices of Boiler Feed Pump Impellers," ASME *Journal of Vibration, Acoustics, Stress, and Reliability in Design*, 109(2), 144–151.

Botman, M., 1976, "Experiments on Oil-Film Dampers for Turbomachinery," ASME *Journal of Engineering for Power*, 98(3), 393–400.

Braisted, D. M., 1979, "Cavitation Induced Instabilities Associated with Turbomachines," Ph.D. Thesis, Division of Engineering and Applied Science, California Institute of Technology, Pasadena, CA.

Brennen, C., 1978, "Bubbly Flow Model for the Dynamic Characteristics of Cavitating Pumps," *Journal of Fluid Mechanics*, 89, part 2, 223–240.

Brennen, C. E., Acosta, A. J., and Caughey, T. K., 1980, "A Test Program to Measure Fluid Mechanical Whirl–Excitation Forces in Centrifugal Pumps," Proceedings of the First Workshop on Rotordynamic Instability Problems in High–Performance Turbomachinery, Texas A & M University, College Station, Texas, NASA CP 2133, pp. 229–235.

Brennen, C. E., Franz, R., and Arndt, N., 1988, "Effects of Cavitation on Rotordynamic Force Matrices," Third Conference on Advanced Earth–to–Orbit Propulsion Technology, Huntsville, Alabama, May, 1988.

Brown, R. D., and Hart, J. A., 1986, "A Novel Form of Damper for Turbomachinery," Proceedings of the Fourth Workshop on Rotordynamic Instability Problems in High–Performance Turbomachinery, Texas A&M University, College Station, Texas, NASA CP 2443, pp. 325–347.

Chamieh, D. S., 1983, "Forces on a Whirling Centrifugal Pump–Impeller," Ph.D. Thesis, Division of Engineering and Applied Science, California Institute of Technology, Pasadena, CA.

Chamieh, D. S., Acosta, A. J., Brennen, C. E., and Caughey, T. K., 1985, "Experimental Measurements of Hydrodynamic Radial Forces and Stiffness Matrices for a Centrifugal Pump–Impeller," ASME *Journal of Fluids Engineering*, **107**(3), 307–315.

Childs, D. W., 1978, "The Space Shuttle Main Engine High–Pressure Fuel Turbopump Rotordynamic Instability Problem," ASME *Journal of Engineering for Power*, **100**(1), 48–57.

Childs, D. W., and Moyer, D. S., 1985, "Vibration Characteristics of the HPOTP (High Pressure Oxygen Turbopump) of the SSME (Space Shuttle Main Engine)," ASME *Journal of Engineering for Gas Turbines and Power*, **107**(1), 152–159.

Childs, D. W., 1986, "Force and Moment Rotordynamic Coefficients for Pump–Impeller Shroud Surfaces," Proceedings of the Fourth Workshop on Rotordynamic Instability Problems in High–Performance Turbomachinery, Texas A & M University, College Station, Texas, NASA CP 2443, pp. 503–529.

Colding–Jørgensen, J., 1980, "Effect of Fluid Forces on Rotor Stability of Centrifugal Compressors and Pumps," Proceedings of the First Workshop on Rotordynamic Instability Problems in High–Performance Turbomachinery, Texas A & M University, College Station, Texas, NASA CP 2133, pp. 249–265.

Dimentberg, F. M., 1961, *Flexural Vibrations of Rotating Shafts*, translated from Russian by Production Engineering Research Association, Butterworths, London, chapter 4.

Domm, U., and Hergt, P., 1970, "Radial Forces on Impeller of Volute Casing Pumps," *Flow Research on Blading* (L. S. Dzung, ed.), Elsevier Pub. Co., The Netherlands, pp. 305–321.

Ehrich, F. F., and Childs, D. W., 1984, "Self–Excited Vibration in High Performance Turbomachinery," *Mechanical Engineering*, **106**(5), 66-79.

Franz, R., and Arndt, N., 1986a, "Measurements of Hydrodynamic Forces on the Impeller of the HPOTP of the SSME," Division of Engineering and Applied Science, California Institute of Technology, Pasadena, CA, Report No. E249.2.

Franz, R., and Arndt, N., 1986b, "Measurements of Hydrodynamic Forces on a Two–Dimensional Impeller and a Modified Centrifugal Pump," Division of Engineering and Applied Science, California Institute of Technology, Pasadena, CA, Report No. E249.4.

Franz, R., Arndt, N., Caughey, T.K., Brennen, C.E., and Acosta, A.J., 1987, "Rotordynamic Forces on Centrifugal Pump Impellers," Proceedings of the Eighth Conference on Fluid Machinery, Akadémiai Kiadó, Budapest, Hungary, Vol. 1, pp. 252–258.

Furuya, O., 1985a, "An Analytical Model for Prediction of Two–Phase (Noncondensable) Flow Pump Performance," ASME *Journal of Fluids Engineering*, **107**(1), 139–147.

Furuya, O., and Maekawa, S., 1985b, "An Analytic Model for Prediction of Two–Phase Flow Pump Performance–Condensable Flow Case," 1985 Cavitation and Multiphase Phase Forum, pp. 74–77.

Hall, J. F., 1982, "An FFT Algorithm for Structural Dynamics," *Earthquake Engineering and Structural Dynamics*, **10**(6), 797–811.

Hergt, P., and Krieger, P., 1969–70, "Radial Forces in Centrifugal Pumps with Guide Vanes," *Advance Class Boiler Feed Pumps, Proceedings of the Institute of Mechanical Engineers*, **184**, Part 3N, 101–107.

Iversen, H. W., Rolling, R. E., and Carlson, J. J., 1960, "Volute Pressure Distribution, Radial Force on the Impeller, and Volute Mixing Losses of a Radial Flow Centrifugal Pump," ASME *Journal of Engineering for Power*, **82**(2), 136–144.

Jery, B., Brennen, C. E., Caughey, T. K., and Acosta, A. J., 1985, "Forces on Centrifugal Pump Impellers," Second International Pump Symposium, Houston, Texas, April 29–May 2, 1985.

Jery, B., 1987, "Experimental Study of Unsteady Hydrodynamic Force Matrices on Whirling Centrifugal Pump Impellers," Ph.D. Thesis, Division of Engineering and Applied Science, California Institute of Technology, Pasadena, CA.

Kanki, H., Kawata, Y., and Kawakami, T., 1981, "Experimental Research on the Hydraulic Excitation Force on the Pump Shaft," ASME Paper No. 81–DET–71.

Kasai, T., and Takamatu, Y., 1964, "Flow in a Radial Impeller with Cavitation," *Bulletin of the Japan Society of Mechanical Engineers*, **7**(27), 543–552.

Kawata, Y., Kanki, H., and Kawakami, T., 1984, "The Dynamic Radial Force on the Cavitating Centrifugal Impeller," The 12th IAHR Symposium on Hydraulic Machinery in the Energy–Related Industries, Stirling, Scotland, August 27–30, 1984, pp. 305–315.

Kikuyama, K., Murakami, M., Asakura, E., and Hasegawa, Y., 1986, "Effect of Inlet Flow Pattern on Cavitation Inception of Centrifugal Pumps," *Bulletin of the Japan Society of Mechanical Engineers*, **29**(254), 2522–2528.

Knapp, R. T., Daily, J. W., and Hammitt, F. G., 1970, *Cavitation*, McGraw-Hill Inc., New York.

Lazarkiewicz, S., and Troskolanski, A. T., 1965, *Impeller Pumps*, Pergamon Press, translated by D. K. Rutter (Polish Ed. Title: *Pompy Wirowe*).

McLean, L. J., and Hahn, E. J., 1984, "Squeeze-Film Dampers for Turbomachinery Stabilization," Proceedings of the Third Workshop on Rotordynamic Instability Problems in High–Performance Turbomachinery, Texas A & M University, College Station, Texas, NASA CP 2338, pp. 391–405.

Muszynska, A., Franklin, W. D., and Bently, D. E., 1988, "Rotor Active "Anti-Swirl" Control," ASME *Journal of Vibration, Acoustics, Stress, and Reliability in Design*, **110**(2), 143–150.

Ng, S. L., 1976, "Dynamic Response of Cavitating Turbomachines," Ph.D. Thesis, Division of Engineering and Applied Science, California Institute of Technology, Pasadena, CA.

Ng, S. L. and Brennen, C. E., 1978, "Experiments on the Dynamic Behavior of Cavitating Pumps," ASME *Journal of Fluids Engineering*, **100**(2), 166–176.

Ohashi, H., Hatanaka, R., and Sakurai, A., 1986, "Fluid Force Testing Machine for Whirling Centrifugal Impeller," International Conference on Rotordynamics, Tokyo, Japan, Sept. 14–17, 1986.

Ohashi, H., Shoji, H., 1987, "Lateral Fluid Forces on a Whirling Centrifugal Impeller (2nd Report: Experiment in Vaneless Diffuser)," ASME *Journal of Fluids Engineering*, **109**(2), 100–106.

Ohashi, H., Sakurai, A., and Nishihama, J., 1988, "Influence of Impeller and Diffuser Geometries on the Lateral Fluid Forces of Whirling Centrifugal Impeller," Proceedings of the Fifth Workshop on Rotordynamic Instability Problems in High-Performance Turbomachinery, Texas A & M University, College Station, Texas, NASA CP 3026, pp. 285–306.

Shoji, H., and Ohashi, H., 1987, "Lateral Fluid Forces on a Whirling Centrifugal Impeller (1st Report: Theory)," ASME *Journal of Fluids Engineering*, 109(2), 94–99.

Stirnemann, A., Eberl, J., Bolleter, U., and Pace, S., 1987, "Experimental Determination of the Dynamic Transfer Matrix for a Pump," ASME *Journal of Fluids Engineering*, 109(3), 218–225.

Thornton, D. L., 1940, *Mechanics Applied to Vibrations and Balancing*, John Wiley & Sons, New York, p. 416 foldout.

Tsujimoto, Y., Acosta, A. J., and Brennen, C. E., 1986, "Analyses of the Characteristics of a Centrifugal Impeller with Leading Edge Cavitation by Mapping Methods," (in Japanese), *Transactions of the Japan Society of Mechanical Engineers*, 52(480,B), 2954–2962.

Tsujimoto, Y., Acosta, A. J., and Yoshida, Y., 1988a, "A Theoretical Study of Fluid Forces on a Centrifugal Impeller Rotating and Whirling in a Vaned Diffuser," Proceedings of the Fifth Workshop on Rotordynamic Instability Problems in High-Performance Turbomachinery, Texas A & M University, College Station, Texas, NASA CP 3026, pp. 307–322.

Tsujimoto, Y., Acosta, A. J., and Brennen, C. E., 1988b, "Theoretical Study of Fluid Forces on a Centrifugal Impeller Rotating and Whirling in a Volute," ASME *Journal of Vibration, Acoustics, Stress, and Reliability in Design*, 110(3), 263–269.

Uchida, N., Imaichi, K., and Shirai, T., 1971, "Radial Force on the Impeller of a Centrifugal Pump," *Bulletin of the Japan Society of Mechanical Engineers*, 14(76), 1106–1117.

Verhoeven, J. J., and Gopalakrishnan S., 1988, "Rotor Dynamic Behavior of Centrifugal Pumps," *The Shock and Vibration Digest*, 20(1), 3–12.

Williams, J. P., and Childs, D. W., 1988, "Influence of Impeller Shroud Forces on Turbopump Rotor Dynamics," Proceedings of the Fifth Workshop on Rotordynamic Instability Problems in High–Performance Turbomachinery, Texas A & M University, College Station, Texas, NASA CP 3026, pp. 323–339.

Appendix A

The Dynamometer

The dynamometer, also referred to as the internal balance, is mounted behind the impeller on the drive shaft. Machined out of 17–4 PH stainless steel, it consists of two parallel plates connected by four bars. Fig. A.1 is a drawing of the dynamometer. Fig. A.2 shows it with the impeller mounting spindle and the protective sleeve assembled.

The four bars were wired with thirty-six semi-conductor strain gages into nine Wheatstone bridges. Fig. A.3 shows their placement on the four bars. The one bridge primarily sensitive to thrust used four gages placed at mid-length on the external face of each bar. The thrust gages had a gage resistance of 250 ohms and a nominal gage factor of about 60 (two positive and the other two negative). The other eight bridges, sensitive to two of the remaining five generalized forces, employed gages placed at quarter and three-quarter length on the bars. They had a gage resistance of 350 ohms and a nominal gage factor of 130. Fig. A.4 diagrams the thirty-six strain gages wired to form the nine bridges and the forces that they are sensitive to. The excitation voltage was five volts for each bridge. Figs. A.1–4 were taken from Jery (1987) where further information on the design, construction and calibration of the dynamometer can be found.
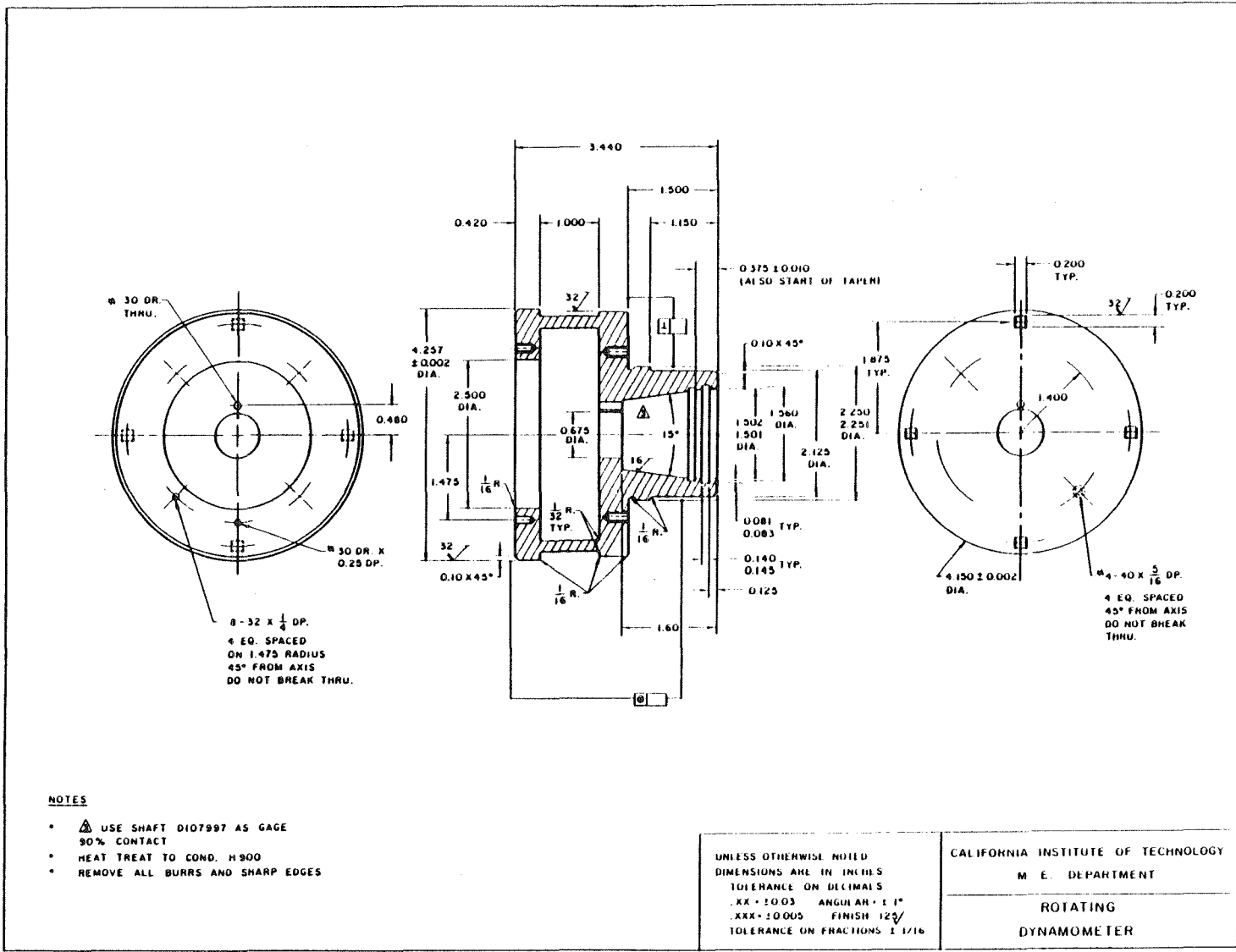
Fig. A.1   Drawing of the dynamometer.
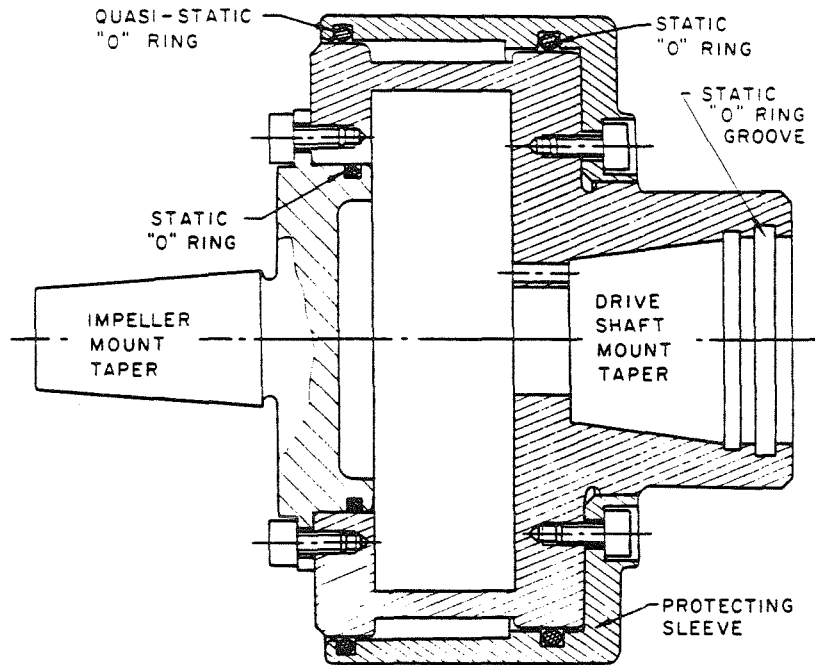
Fig. A.2 Assembly drawing of dynamometer with impeller mounting spindle, protective sleeve and various o-rings.
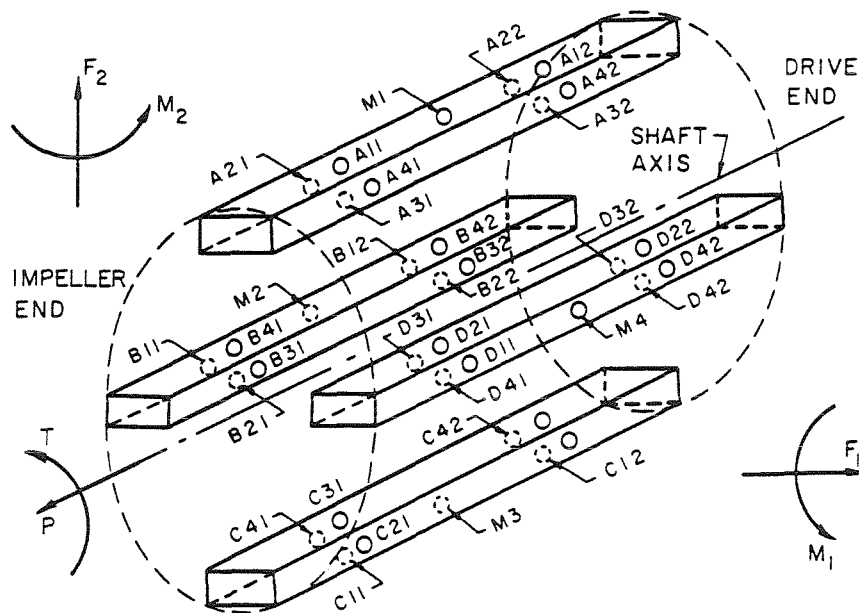
Fig. A.3 Sketch indicating the placement of the strain gages on the four bars of the dynamometer. The forces and moments shown are defined as acting on the impeller.
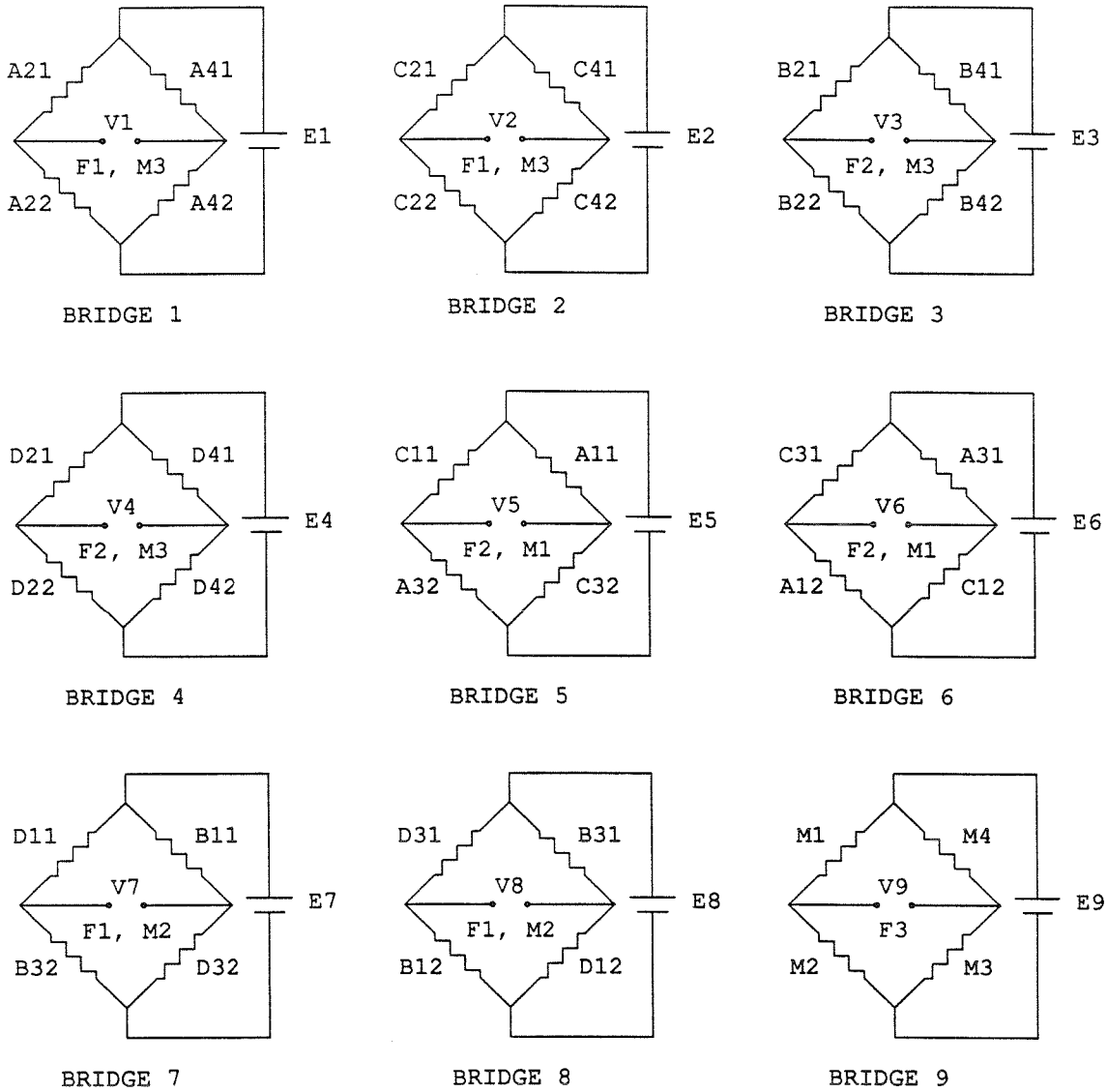
Fig. A.4 Arrangement of the 36 semi-conductor strain gages as nine Wheatstone bridges.

Appendix B

Derivation of Processing Equations

The hydrodynamic force on a rotating impeller which is translating along a circular orbit of a small radius can be expressed in the stationary frame as

$$\begin{pmatrix} F_x(t) \\ F_y(t) \end{pmatrix} = \begin{pmatrix} F_{ox} \\ F_{oy} \end{pmatrix} + \begin{bmatrix} A_{xx} & A_{xy} \\ A_{yx} & A_{yy} \end{bmatrix} \begin{pmatrix} \varepsilon \cos \Omega t \\ \varepsilon \sin \Omega t \end{pmatrix} \qquad (B.1)$$

where Ω is the frequency of the imposed whirl orbit. Boldface will be used to denote vectors and matrices with their components in italic. The equations used to process the forces measured with the rotating dynamometer are first derived assuming the dynamometer-shaft system has infinite stiffness. Then a model is used to account for the finite stiffness of the elastic dynamometer-shaft system.

B.1 Rigid

The data acquisition system discussed in Chapter 3 provides for control of the speed and phase of each motor. The ratio of the whirl/main shaft speeds is Ω/ω=I/J. At the reference frequency ω/J, the orientation of the impeller and its location on the whirl orbit geometrically repeat, because there are an integral number of rotations of the main shaft and whirl motors during each reference cycle. Data were taken over NCYC cycles of the reference frequency. The components of the steady force are obtained by averaging Eqn. (B.1) over the time $T = \text{NCYC}*\text{J}/\omega$. Performing the operation $\frac{1}{T} \int_0^T \{\quad\} dt$:

$$\begin{aligned} F_{ox} &= \frac{1}{T} \int_0^T \left\{ F_x(t) \right\} dt \\ &= F_x^0 \\ F_{oy} &= F_y^0 \end{aligned} \qquad (B.2)$$

To get the elements of the hydrodynamic force matrix $[\mathbf{A}]$ evaluate the Fourier cos and sin coefficients of Eqn. (B.1). Perform the following integrations,

$\frac{2}{T} \int_0^T \{ \ \} \cos(\Omega t) \, dt$:

$$
\begin{aligned}
A_{xx}\varepsilon &= \frac{2}{T} \int_0^T \left\{ F_x(t) \cos(\Omega t) \right\} dt \\
&= F_{xC}^{\Omega} \\
A_{yx}\varepsilon &= F_{yC}^{\Omega}
\end{aligned}
\tag{B.3}
$$

$\frac{2}{T} \int_0^T \{ \ \} \sin(\Omega t) \, dt$:

$$
\begin{aligned}
A_{xy}\varepsilon &= \frac{2}{T} \int_0^T \left\{ F_x(t) \sin(\Omega t) \right\} dt \\
&= F_{xS}^{\Omega} \\
A_{yy}\varepsilon &= F_{yS}^{\Omega}
\end{aligned}
\tag{B.4}
$$

The superscript and subscript denotes the frequency of the cos or sin, respectively, Fourier coefficient.

Referring to Fig. B.1 the lateral forces in the laboratory frame, F_x and F_y, are related to the lateral forces detected by the dynamometer in the rotating frame, F_1 and F_2, by a rotation through the angle $-\omega t$, where ω is the frequency of main shaft rotation,

$$
\begin{aligned}
F_x(t) &= F_1(t) \cos(\omega t) - F_2(t) \sin(\omega t) \\
F_y(t) &= F_1(t) \sin(\omega t) + F_2(t) \cos(\omega t)
\end{aligned}
\tag{B.5}
$$

Taking the angle from the volute tongue, φ_V, to be zero, the hydrodynamic forces will first be written in the laboratory frame with the x-axis pointing vertically upward, and then rotated into the volute frame. Combine Eqns. (B.1) and (B.5) to yield

$$
\begin{aligned}
F_1(t) \cos(\omega t) - F_2(t) \sin(\omega t) &= F_{ox} + \varepsilon A_{xx} \cos(\Omega t) + \varepsilon A_{xy} \sin(\Omega t) \\
F_1(t) \sin(\omega t) + F_2(t) \cos(\omega t) &= F_{oy} + \varepsilon A_{yx} \cos(\Omega t) + \varepsilon A_{yy} \sin(\Omega t)
\end{aligned}
\tag{B.6}
$$

Examine the integrals represented by F_x^0 (Eqn. B.2) and F_{xC}^Ω (Eqn. B.3).

$$F_x^0 = \frac{1}{T} \int_0^T \left\{ F_1(t)\cos(\omega t) - F_2 \sin(\omega t) \right\} dt$$

$$F_{xC}^\Omega = \frac{2}{T} \int_0^T \left\{ F_1(t)\cos(\omega t)\cos(\Omega t) - F_2(t)\sin(\omega t)\cos(\Omega t) \right\} dt$$

$$= \frac{2}{T} \int_0^T \frac{1}{2} \left\{ F_1(t)\cos(\omega - \Omega)t + F_1(t)\cos(\omega + \Omega)t \right.$$

$$\left. - F_2(t)\sin(\omega + \Omega)t - F_2(t)\sin(\omega - \Omega)t \right\} dt \qquad (B.7)$$

Each term of the above equations is a component in the Fourier series expansion of $F_1(t)$ and $F_2(t)$, with fundamental frequency ω/J. For example the last term of F_{xC}^Ω becomes,

$$\frac{2}{T} \frac{1}{2} \int_0^T -F_2(t)\sin(\omega - \Omega)t \; dt = -\frac{1}{2} \frac{2}{T} \int_0^T F_2(t) \sin\left(\frac{J-I}{J}\omega t\right) dt$$

$$= -\frac{1}{2} F_{2S}^{J-I} \qquad (B.8)$$

where the superscript denotes the harmonic number of the fundamental frequency ω/J. Rewriting Eqns. (B.2–6),

$$F_x^0 = \frac{1}{2}(F_{1C}^J - F_{2S}^J)$$

$$F_y^0 = \frac{1}{2}(F_{1S}^J + F_{2C}^J)$$

$$F_{xC}^\Omega = \frac{1}{2}(F_{1C}^{J-I} - F_{2S}^{J-I} + F_{1C}^{J+I} - F_{2S}^{J+I})$$

$$F_{xS}^\Omega = \frac{1}{2}(-F_{1S}^{J-I} - F_{2C}^{J-I} + F_{1S}^{J+I} + F_{2C}^{J+I}) \qquad (B.9)$$

$$F_{yC}^\Omega = \frac{1}{2}(F_{1S}^{J-I} + F_{2C}^{J-I} + F_{1S}^{J+I} + F_{2C}^{J+I})$$

$$F_{yS}^\Omega = \frac{1}{2}(F_{1C}^{J-I} - F_{2S}^{J-I} - F_{1C}^{J+I} + F_{2S}^{J+I})$$

To obtain the hydrodynamic forces at a given whirl ratio and flow condition, two tests are done, one in water and the other in air. The forces measured from the test in air is subtracted from the test in water to account for the force of gravity and the centrifugal force of the whirling impeller. These two tests are also referred to as

a "wet" and a "dry" run. The buoyancy force on the rotor is subtracted separately. Use the subscripts "W" and "A" to denote the tests performed in water and in air, respectively. The steady hydrodynamic force and matrix elements are

$$F_{ox} = F^0_{xW} - F^0_{xA} - F_{buoyancy}$$

$$F_{oy} = F^0_{yW} - F^0_{yA}$$

$$A_{xx} = \frac{1}{\varepsilon}(F^\Omega_{xWC} - F^\Omega_{xAC})$$

$$A_{xy} = \frac{1}{\varepsilon}(F^\Omega_{xWS} - F^\Omega_{xAS}) \qquad (B.10)$$

$$A_{yx} = \frac{1}{\varepsilon}(F^\Omega_{yWC} - F^\Omega_{yAC})$$

$$A_{yy} = \frac{1}{\varepsilon}(F^\Omega_{yWS} - F^\Omega_{yAS})$$

The unsteady hydrodynamic force, $[\mathbf{A}]\varepsilon(t)$, due to the eccentric motion of the impeller can be resolved into its components normal to and tangential to the whirl orbit, averaged over the orbit, F_n and F_t. The normal force is considered positive outward. The tangential force is considered positive when in the direction of shaft rotation. For the imposed circular whirl orbit, the unit normal and tangential vectors are $\varepsilon(t)/\|\varepsilon(t)\|$ and $\dot{\varepsilon}(t)/\|\dot{\varepsilon}(t)\|$, respectively.

$$F_n = \frac{1}{T}\int_0^T \left\{ \frac{\varepsilon(t)\cdot \mathbf{F}(t)}{\|\varepsilon(t)\|} \right\}\, dt$$

$$= \frac{1}{T}\int_0^T \left\{ F_x\cos\Omega t + F_y\sin\Omega t \right\}\, dt$$

$$= \frac{1}{2}\left(F^\Omega_{xC} + F^\Omega_{yS} \right)$$

$$= \frac{1}{2}\left(A_{xx} + A_{yy} \right)\varepsilon$$

$$F_t = \frac{1}{T}\int_0^T \left\{ \frac{\dot{\varepsilon}(t)\cdot \mathbf{F}(t)}{\|\dot{\varepsilon}(t)\|} \right\}\, dt \qquad (B.11)$$

$$= \frac{1}{T}\int_0^T \left\{ -F_x\sin\Omega t + F_y\cos\Omega t \right\}\, dt$$

$$= \frac{1}{2}\left(-F^\Omega_{xS} + F^\Omega_{yC} \right)$$

$$= \frac{1}{2}\left(-A_{xy} + A_{yx} \right)\varepsilon$$

The hydrodynamic steady force, $\mathbf{F_o}$, and force matrix, $[\mathbf{A}]$, are presented in the volute frame of reference. Referring to Fig. B.1 the expressions above are rotated through an angle φ_V until the x-axis passes through the volute tongue. Let

$$[\mathbf{R}] = \begin{bmatrix} \cos\varphi_V & -\sin\varphi_V \\ \sin\varphi_V & \cos\varphi_V \end{bmatrix} \qquad (B.12)$$

Let a prime denote the above quantities in the laboratory frame with $\varphi_V = 0$. Unprimed quantities are in the volute frame. Then

$$\begin{pmatrix} F_{ox} \\ F_{oy} \end{pmatrix} = [\mathbf{R}] \begin{pmatrix} F'_{ox} \\ F'_{oy} \end{pmatrix} \qquad (B.13)$$

and

$$[\mathbf{A}] = [\mathbf{R}][\mathbf{A}'][\mathbf{R}]^{\mathbf{T}} \qquad (B.14)$$

Written out, the rotated components are

$$F_{ox} = \cos\varphi_V F'_{ox} - \sin\varphi_V F'_{oy}$$
$$F_{oy} = \sin\varphi_V F'_{ox} + \cos\varphi_V F'_{oy} \qquad (B.15)$$

$$A_{xx} = \cos^2\varphi_V A'_{xx} - \cos\varphi_V \sin\varphi_V (A'_{xy} + A'_{yx}) + \sin^2\varphi_V A'_{yy}$$

$$A_{xy} = \cos\varphi_V \sin\varphi_V (A'_{xx} - A'_{yy}) + \cos^2\varphi_V A'_{xy} - \sin^2\varphi_V A'_{yx}$$

$$A_{yx} = \cos\varphi_V \sin\varphi_V (A'_{xx} - A'_{yy}) - \sin^2\varphi_V A'_{xy} + \cos^2\varphi_V A'_{yx} \qquad (B.16)$$

$$A_{yy} = \sin^2\varphi_V A'_{xx} + \cos\varphi_V \sin\varphi_V (A'_{xy} + A'_{yx}) + \cos^2\varphi_V A'_{yy}$$

Note that if $A'_{xx}=A'_{yy}$ and $A'_{xy}=-A'_{yx}$ then the matrix is independent of rotation.

The lateral hydrodynamic moment experienced by the whirling impeller can be expressed in the stationary laboratory frame in the same way as $\mathbf{F}(t)$,

$$\begin{pmatrix} M_x(t) \\ M_y(t) \end{pmatrix} = \begin{pmatrix} M_{ox} \\ M_{oy} \end{pmatrix} + \begin{bmatrix} B_{xx} & B_{xy} \\ B_{yx} & B_{yy} \end{bmatrix} \begin{pmatrix} \varepsilon\cos(\Omega t) \\ \varepsilon\sin(\Omega t) \end{pmatrix} \qquad (B.17)$$

The expressions for $\mathbf{M_o}$ and $[\mathbf{B}]$ in terms of the lateral moments M_1 and M_2 are similar to the above equations. The average, cos and sin integrals in terms of the lateral moments in the rotating dynamometer frame, M_1 and M_2, are

$$M_x^0 = \frac{1}{2}(M_{1C}^J - M_{2S}^J)$$

$$M_y^0 = \frac{1}{2}(M_{2S}^J + M_{2C}^J)$$

$$M_{xC}^\Omega = \frac{1}{2}(M_{1C}^{J-I} - M_{2S}^{J-I} + M_{1C}^{J+I} - M_{2S}^{J+I})$$

$$M_{xS}^\Omega = \frac{1}{2}(-M_{1S}^{J-I} - M_{2C}^{J-I} + M_{1S}^{J+I} + M_{2C}^{J+I})$$

$$M_{yC}^\Omega = \frac{1}{2}(M_{1S}^{J-I} + M_{2C}^{J-I} + M_{1S}^{J+I} + M_{2C}^{J+I})$$

$$M_{yS}^\Omega = \frac{1}{2}(M_{1C}^{J-I} - M_{2S}^{J-I} - M_{1C}^{J+I} + M_{2S}^{J+I})$$

$$(B.18)$$

The fluid-induced moment is obtained by subtracting two tests with the same whirl ratio, one in water and the other in air. The buoyancy moment is subtracted separately.

$$M_{ox} = M_{xW}^0 - M_{xA}^0$$

$$M_{oy} = M_{yW}^0 - M_{yA}^0 - M_{buoyancy}$$

$$B_{xx} = \frac{1}{\varepsilon}(M_{xWC}^\Omega - M_{xDC}^\Omega)$$

$$B_{xy} = \frac{1}{\varepsilon}(M_{xWS}^\Omega - M_{xDS}^\Omega)$$

$$B_{yx} = \frac{1}{\varepsilon}(M_{yWC}^\Omega - M_{yDC}^\Omega)$$

$$B_{yy} = \frac{1}{\varepsilon}(M_{yWS}^\Omega - M_{yDS}^\Omega)$$

$$(B.19)$$

The moments are rotated into the volute frame using Eqns. (B.13–14). The resulting components are similar to Eqns. (B.15–16) for the forces. These lateral moments are in the calibration plane, the plane bisecting the discharge area of Impeller X.

The forces and moments are non-dimensionalized by the product of the dynamic head using the impeller outlet tip velocity and the impeller discharge area. The impeller outlet radius, r_2, is used as the non-dimensionalizing length for the whirl orbit radius, ε, and for the moments. The force and moment components normal to

and tangential to the whirl orbit are non-dimensionalized by the additional factor ε/r_2, so that they are numerically equal to the average of the appropriate matrix elements. The Nomenclature gives the details.

B.2 With Stiffness

The effect of the finite stiffness of the impeller-dynamometer-shaft system upon the measurements taken using the rotating dynamometer is evident from Fig. 4.4 where $F_n/(\Omega^2\varepsilon)$ and $M_t/(\Omega^2\varepsilon)$ are not independent of the whirl speed. This will be examined in terms of a simple model for the system. The shaft is treated as a massless beam supported by two bearings with the overhung rotor treated as a "disk." The "disk" includes the impeller, the mounting spindle and the front plate of the dynamometer. The gyroscopic effect of a lateral angular deflection of the rotating "disk" is included, indicated in Fig. B.2. The deflection and rotation of the shaft at the disk (x, y, φ_x, φ_y) are related to the applied force and moment through the coefficients of the deflection matrix.

$$x = d_{11}F_x + d_{12}M_y \qquad y = d_{11}F_y - d_{12}M_x$$
$$\varphi_y = d_{21}F_x + d_{22}M_y \qquad \varphi_x = -d_{21}F_y + d_{22}M_x \tag{B.20}$$

The elastic force of the shaft in terms of the deflection and rotation of the shaft at the disk uses the stiffness matrix, the inverse of the deflection matrix.

$$F_x = k_{11}x - k_{12}\varphi_y \qquad F_y = k_{11}y + k_{12}\varphi_x$$
$$M_y = -k_{21}x + k_{22}\varphi_y \qquad M_x = k_{21}y + k_{22}\varphi_x \tag{B.21}$$

With the dynamometer placed between the bearing and the impeller, forces applied at the impeller deform the bars of the dynamometer. Applying the calibration matrix to the voltages of Wheatstone bridges formed from strain gages on the bars returns the applied lateral force and moment in the plane of calibration.

First the equations of the forces and moments on the center on mass of the disk are written for the impeller rotating and whirling in air. The force on the impeller is

$$m\ddot{\mathbf{r}} + \mathbf{F}_{elastic} = m\mathbf{g} \qquad (B.22)$$

where m is the mass of the "disk", and $\mathbf{r}$ is the displacement of the impeller from a fixed point, the center of the whirl orbit (the center of the volute). Let $\mathbf{r} = \mathbf{x} + \varepsilon$, where $\mathbf{x}$ is the elastic deflection of the shaft at the impeller and ε is the displacement due to the imposed circular whirl orbit. Since the force measured by the dynamometer represents the elastic force of the dynamometer-shaft the subscript *elastic* will be deleted. First the following equations will be solved in terms of lateral forces and moments at the center of mass, then they will be transformed to the calibration plane.

$$m\ddot{x} + F_x = -mg + m\Omega^2\varepsilon\cos\Omega t$$

$$m\ddot{y} + F_y = m\Omega^2\varepsilon\sin\Omega t$$

$$I\ddot{\varphi}_x + \omega I_z\dot{\varphi}_y + M_x = 0 \qquad (B.23)$$

$$I\ddot{\varphi}_y - \omega I_z\dot{\varphi}_x + M_y = 0$$

where I and I_z are the transverse and polar moments of inertia of the "disk," respectively. Represent the variables in the lateral x-y plane by a complex variable. Let

$$z = x + iy \qquad F_z = F_x + iF_y$$

$$\varphi = -\varphi_y + i\varphi_x \qquad M_z = -M_y + iM_x \qquad (B.24)$$

Then

$$m\ddot{z} + F_z = -mg + m\Omega^2\varepsilon e^{i\Omega t}$$

$$I\ddot{\varphi} - i\omega I_z\dot{\varphi} + M_z = 0 \qquad (B.25)$$

The steady solution is $F_z^0 = -mg$ and $M_z^0 = 0$. For the unsteady part, let $F_z = F_z^\Omega e^{i\Omega t}$ and $M_z = M_z^\Omega e^{i\Omega t}$. Using Eqn. (B.20),

$$(1 - d_{11}m\Omega^2)F_z^\Omega \qquad d_{12}m\Omega^2 M_z^\Omega \qquad = m\Omega^2\varepsilon$$

$$d_{21}(I\Omega^2 - I_z\omega\Omega)F_z^\Omega \quad (1 + d_{22}(-I\Omega^2 + I_z\omega\Omega))M_z^\Omega \quad = 0 \qquad (B.26)$$

Solving the system of equations,

$$\begin{pmatrix} F_z^{\Omega} \\ M_z^{\Omega} \end{pmatrix} = \frac{1}{det} \begin{bmatrix} 1 + d_{22}(I_z\omega\Omega - I\Omega^2) & -d_{12}m\Omega^2 \\ d_{21}(I_z\omega\Omega - I\Omega^2) & 1 - d_{11}m\Omega^2 \end{bmatrix} \begin{pmatrix} m\Omega^2\varepsilon \\ 0 \end{pmatrix}$$

$$= \frac{m\Omega^2\varepsilon}{det} \begin{pmatrix} 1 + d_{22}(I\omega\Omega - I\Omega^2) \\ d_{21}(I_z\omega\Omega - I\Omega^2) \end{pmatrix} \qquad (B.27)$$

where $det = (1 - d_{11}m\Omega^2)\left(1 + d_{22}(I_z\omega\Omega - I\Omega^2)\right) + d_{12}d_{21}m\Omega^2(I_z\omega\Omega - I\Omega^2)$. Because the measurements from the dynamometer are in the calibration plane, the above solution must be transformed from the center of mass plane to the calibration plane. Let z_{cm} be the distance of the center of mass of the "disk" from the calibration plane.

$$\begin{pmatrix} F_z^{calib} \\ M_z^{calib} \end{pmatrix} = \begin{bmatrix} 1 & 0 \\ -z_{cm} & 1 \end{bmatrix} \begin{pmatrix} F_z^{cm} \\ M_z^{cm} \end{pmatrix}$$

$$\begin{pmatrix} F_z^{\Omega\ calib} \\ M_z^{\Omega\ calib} \end{pmatrix} = \frac{m\Omega^2\varepsilon}{det} \begin{pmatrix} 1 + d_{22}(I\omega\Omega - I\Omega^2) \\ -z_{cm} + (d_{21} - z_{cm}d_{22}(I_z\omega\Omega - I\Omega^2) \end{pmatrix} \qquad (B.28)$$

From the reciprocity relation of strain energy, $d_{12} = d_{21}$. $F_z^{\Omega\ calib}$ and $M_z^{\Omega\ calib}$ are related to F_n and M_t from rotating and whirling in air,

$$F_n = F_z^{\Omega\ calib}$$

$$M_t = -M_z^{\Omega\ calib} \qquad (B.29)$$

The values of m and z_{cm} were found from measurements of the steady force and moment from dry runs. The moments of inertia, I and I_z, were measured by hanging the impeller with the mounting spindle attached from a clamped cable, measuring the period of oscillation, and comparing with the period for objects with an easily calculated inertia. The inertia of the front plate of the dynamometer was then added.

The deflection coefficient matrix was calculated for the dynamometer-shaft system. The values obtained were $d_{11} = 3.6 \ 10^{-5}$ in/lb$_f$, $d_{12} = 5.9 \ 10^{-6}$ lbf^{-1}, and $d_{22} = 1.8 \ 10^{-6}$ (in lb$_f$)$^{-1}$. The curves of $F_n/(\Omega^2\varepsilon)$ and $M_t/(\Omega^2\varepsilon)$ calculated from Eqn. (B.29) were compared with the data plotted on Fig. 4.4. The curves

fell below the data, indicating that the model was too stiff. Values of d_{11}, d_{12} and d_{22} were selected and the calculated curves compared with Fig. 4.4. $F_n/(\Omega^2 \varepsilon)$ was strongly dependent upon d_{11}. The values of d_{12} and d_{22} were then chosen to fit $M_t/(\Omega^2 \varepsilon)$. A least squares fit was employed to assist in the selection of the values of d_{ij}. Since the least squares fit did not iterate to the same values of d_{ij}, regardless of the initial guess, the ratio of $d_{12}^2/(d_{11}d_{22})$ from the calculation was used in making the final selection. The values used were $m = 9.35$ lb$_m$, $z_{cm} = -.11$ inch, $I = 25$ lb$_m$ in^2, $I_z = 30$ lb$_m$ in^2, $d_{11} = 7.36 \ 10^{-5}$ in/lb$_f$, $d_{12} = 9.68 \ 10^{-6}$ (lb$_f$)$^{-1}$, and $d_{22} = 2.44 \ 10^{-6}$ (in lb$_f$)$^{-1}$. The model did reasonably well except for the whirl ratios near $\Omega/\omega = 1.0$.

Since the stiffness of the dynamometer-shaft system did not significantly affect the unsteady force from whirling and rotating in air, a significant affect upon the hydrodynamic forces was not anticipated. For example, the measured value of F_n at $\Omega/\omega = 0.5$ from the dry run deviates 2% from the value corresponding to an infinitely stiff shaft. The relative contributions of the centrifugal force from whirling the impeller and the hydrodynamic force to F_n measured from the wet runs is evident by comparing the non-dimensionalized "dry" F_n ($\frac{1}{2}(A_{xx} + A_{yy})$) of Fig. 4.3 with the hydrodynamic F_n of design flow, Fig. 7.10a. Except for the whirl ratios where the value is small, the greater contribution is from the fluid-induced force, particularly for reverse whirl. For the average tangential force, the "dry" F_t is nominally zero.

Since the hydrodynamic forces noticeably contributed to the forces experienced by the impeller in the wet runs, the equations used to calculate the hydrodynamic forces and moments were rederived, incorporating the above model for the stiffness of the dynamometer-shaft system. In addition to gravity and the centrifugal force from whirling the impeller, the hydrodynamic forces and moments present in the

wet tests are added as follows,

$$F_x : \quad F_{ox} + A_{xx}(x_W + \varepsilon \cos \Omega t) + A_{xy}(y_W + \varepsilon \sin \Omega t)$$

$$F_y : \quad F_{oy} + A_{yx}(x_W + \varepsilon \cos \Omega t) + A_{yy}(y_W + \varepsilon \sin \Omega t)$$

$$M_x : \quad M_{ox} + B_{xx}(x_W + \varepsilon \cos \Omega t) + B_{xy}(y_W + \varepsilon \sin \Omega t) \qquad (B.30)$$

$$M_y : \quad M_{oy} + B_{yx}(x_W + \varepsilon \cos \Omega t) + B_{yy}(y_W + \varepsilon \sin \Omega t)$$

The buoyancy force and moment included in F_{ox} and M_{oy} will be subtracted later.

Because the lateral hydrodynamic moments are presented in the plane mid-span of the discharge area of the impeller, the calibration plane for Impeller X, the moments need to be transformed to the center of mass plane of the "disk," using

$$M_x^{cm} = M_x^{calib} + z_{cm} F_y$$
$$M_y^{cm} = M_y^{calib} - z_{cm} F_x \qquad (B.31)$$

Influence coefficients give the deflection and rotation at a particular point on the shaft due to a unit applied load or moment at a second point. The dry run model used coincident influence coefficients, the deflection matrix of Eqn. (B.20), because gravity acts on the center of mass of the "disk" at which the equations were written. The center of mass is between the bearing and the discharge plane where the hydrodynamic forces and moments are assumed to act. Consequently the influence coefficients for the deflection and rotation for a force and moment applied at the same point (the center of mass) correspond to the deflection and rotation for the hydrodynamic force and moment as if they were applied at the center of mass according to Eqn. (B.31). Texts such as Thornton (1940) give influence coefficients for the deflection and rotation of a uniform shaft supported by two bearings to coincident and non-coincident forces and moments. For the particular case of Impeller X, the difference would be minor since the calibration plane is 8 inches from the bearing and $z_{cm} = -.11$ inch.

Let

$$\delta_x = x_W + \varepsilon \cos \Omega t$$
$$\delta_y = y_W + \varepsilon \sin \Omega t \qquad (B.32)$$

Subtracting a dry run from a wet run yields,

$$m(\ddot{x}_W - \ddot{x}_A) + F_{xW} - F_{xA} = F_{ox} + A_{xx}\delta_x + A_{xy}\delta_y$$

$$m(\ddot{y}_W - \ddot{y}_A) + F_{yW} - F_{yA} = F_{oy} + A_{yx}\delta_x + A_{yy}\delta_y$$

$$I(\ddot{\varphi}_{xW} - \ddot{\varphi}_{xA}) + \omega I_z(\dot{\varphi}_{yW} - \dot{\varphi}_{yA})$$

$$+M_{xW}^{cm} - M_{xA}^{cm} = M_{ox}^{cm} + B_{xx}^{cm}\delta_x + B_{xy}^{cm}\delta_y \qquad (B.33)$$

$$I(\ddot{\varphi}_{yW} - \ddot{\varphi}_{yA}) - \omega I_z(\dot{\varphi}_{xW} - \dot{\varphi}_{xA})$$

$$+M_{yW}^{cm} - M_{yA}^{cm} = M_{oy}^{cm} + B_{yx}^{cm}\delta_x + B_{yy}^{cm}\delta_y$$

To obtain the steady hydrodynamic force and moment, average each equation over time,

$$F_{ox} = F_{xW}^0 - F_{xA}^0 - A_{xx}\delta_x^0 - A_{xy}\delta_y^0$$

$$F_{oy} = F_{yW}^0 - F_{yA}^0 - A_{yx}\delta_x^0 - A_{yy}\delta_y^0$$

$$M_{ox}^{cm} = M_{xW}^{0\ cm} - M_{xA}^{0\ cm} - B_{xx}\delta_x^0 - B_{xy}^{cm}\delta_y^0 \qquad (B.34)$$

$$M_{oy}^{cm} = M_{yW}^{0\ cm} - M_{yA}^{0\ cm} - B_{yx}\delta_x^0 - B_{yy}^{cm}\delta_y^0$$

Transform the lateral moment back to the calibration plane using Eqn. (B.31),

$$M_{ox}^{cm} = M_{ox}^{calib} + z_{cm}F_{oy}$$

$$= M_{xW}^{0\ calib} - M_{xA}^{0\ calib} + z_{cm}(F_{yW}^0 - F_{yA}^0 \qquad (B.35)$$

$$- B_{xx}^{calib}\delta_x^0 - B_{xy}^{calib}\delta_y^0 - z_{cm}(A_{yx}\delta_x^0 + A_{yy}\delta_y^0)$$

Gives

$$M_{ox}^{calib} = M_{xW}^{0\ calib} - M_{xA}^{0\ calib} - B_{xx}^{calib}\delta_x^0 - B_{xy}^{calib}\delta_y^0$$

$$\qquad (B.36)$$

$$M_{oy}^{calib} = M_{yW}^{0\ calib} - M_{yA}^{0\ calib} - B_{yx}^{calib}\delta_x^0 - B_{yy}^{calib}\delta_y^0$$

where

$$\delta_x^0 = x_W^0$$

$$= d_{11}F_{xW}^0 + d_{12}M_{yW}^{0\ cm}$$

$$= (d_{11} - z_{cm}d_{12})F_{xW}^0 + d_{12}M_{yW}^{0\ calib} \qquad (B.37)$$

$$\delta_y^0 = (d_{11} - z_{cm}d_{12})F_{yW}^0 - d_{12}M_{xW}^{0\ calib}$$

Calculate the Fourier cos coefficients of Eqn. (B.33). The first inertial term becomes, integrating by parts,

$$\frac{2}{T} \int_0^T \{m\ddot{x}_W \ \cos \Omega t\} \ dt = -m\Omega^2 x_{WC}^\Omega \qquad (B.38)$$

because the forces and consequently the deflections are periodic.

$$-m\Omega^2(x_{WC}^\Omega - x_{AC}^\Omega) + F_{xWC}^\Omega - F_{xAC}^\Omega = A_{xx}\delta_{xC}^\Omega + A_{xy}\delta_{yC}^\Omega$$

$$-m\Omega^2(y_{WC}^\Omega - y_{AC}^\Omega) + F_{yWC}^\Omega - F_{yAC}^\Omega = A_{yx}\delta_{xC}^\Omega + A_{yy}\delta_{yC}^\Omega$$

$$-I\Omega^2(\varphi_{xWC}^\Omega - \varphi_{xAC}^\Omega) + I_z\omega\Omega(\varphi_{yWS}^\Omega - \varphi_{yAS}^\Omega)$$

$$+M_{xWC}^{\Omega \ cm} - M_{xAC}^{\Omega \ cm} = B_{xx}^{cm}\delta_{xC}^\Omega + B_{xy}^{cm}\delta_{yC}^\Omega \qquad (B.39)$$

$$-I\Omega^2(\varphi_{yWC}^\Omega - \varphi_{yAC}^\Omega) - I_z\omega\Omega(\varphi_{xWS}^\Omega - \varphi_{xAS}^\Omega)$$

$$+M_{yWC}^{\Omega \ cm} - M_{yAC}^{\Omega \ cm} = B_{yx}^{cm}\delta_{xC}^\Omega + B_{yy}^{cm}\delta_{yC}^\Omega$$

Calculating the Fourier sin coefficients gives

$$-m\Omega^2(x_{WS}^\Omega - x_{AS}^\Omega) + F_{xWS}^\Omega - F_{xAS}^\Omega = A_{xx}\delta_{xS}^\Omega + A_{xy}\delta_{yS}^\Omega$$

$$-m\Omega^2(y_{WS}^\Omega - y_{AS}^\Omega) + F_{yWS}^\Omega - F_{yAS}^\Omega = A_{yx}\delta_{xS}^\Omega + A_{yy}\delta_{yS}^\Omega$$

$$-I\Omega^2(\varphi_{xWS}^\Omega - \varphi_{xAS}^\Omega) - I_z\omega\Omega(\varphi_{yWC}^\Omega - \varphi_{yAC}^\Omega)$$

$$+M_{xWS}^{\Omega \ cm} - M_{xAS}^{\Omega \ cm} = B_{xx}^{cm}\delta_{xS}^\Omega + B_{xy}^{cm}\delta_{yS}^\Omega \qquad (B.40)$$

$$-I\Omega^2(\varphi_{yWS}^\Omega - \varphi_{yAS}^\Omega) + I_z\omega\Omega(\varphi_{xWC}^\Omega - \varphi_{xAC}^\Omega)$$

$$+M_{yWS}^{\Omega \ cm} - M_{yAS}^{\Omega \ cm} = B_{yx}^{cm}\delta_{xS}^\Omega + B_{yy}^{cm}\delta_{yS}^\Omega$$

The moments need to be transformed back to the calibration plane. Eqn. (B.39c) becomes

$$-I\Omega^2(\varphi_{xWC}^\Omega - \varphi_{xAC}^\Omega) + I_z\omega\Omega(\varphi_{yWS}^\Omega - \varphi_{yAS}^\Omega) + M_{xWC}^{\Omega \ calib} - M_{xAC}^{\Omega \ calib}$$

$$+ z_{cm}(F_{yWC}^\Omega - F_{yAC}^\Omega) = B_{xx}^{calib}\delta_{xC}^\Omega + B_{xy}^{calib}\delta_{yC}^\Omega + z_{cm}(A_{yx}\delta_{xC}^\Omega + A_{yy}\delta_{yC}^\Omega) \qquad (B.41)$$

Using Eqn. (B.39b),

$$-I\Omega^2(\varphi^\Omega_{xWC} - \varphi^\Omega_{xAC}) + I_z\omega\Omega(\varphi^\Omega_{yWS} - \varphi^\Omega_{yAS}) + M^{\Omega\ calib}_{xWC} - M^{\Omega\ calib}_{xAC}$$

$$+ m\Omega^2 z_{cm}(y^\Omega_{WC} - y^\Omega_{AC}) = B^{calib}_{xx}\delta^\Omega_{xC} + B^{calib}_{xy}\delta^\Omega_{yC} \tag{B.42}$$

Define the matrix

$$[\Delta] = \begin{bmatrix} \delta^\Omega_{xC} & \delta^\Omega_{yC} \\ \delta^\Omega_{xS} & \delta^\Omega_{yS} \end{bmatrix} \tag{B.43}$$

Combining Eqns. (B.39–40),

$$[\Delta]\begin{pmatrix} A_{xx} \\ A_{xy} \end{pmatrix} = \begin{pmatrix} F^\Omega_{xWC} - F^\Omega_{xAC} - m\Omega^2(x^\Omega_{WC} - x^\Omega_{AC}) \\ F^\Omega_{xWS} - F^\Omega_{xAS} - m\Omega^2(x^\Omega_{WS} - x^\Omega_{AS}) \end{pmatrix}$$

$$\tag{B.44}$$

$$[\Delta]\begin{pmatrix} A_{yx} \\ A_{yy} \end{pmatrix} = \begin{pmatrix} F^\Omega_{yWC} - F^\Omega_{yAC} - m\Omega^2(y^\Omega_{WC} - y^\Omega_{AC}) \\ F^\Omega_{yWS} - F^\Omega_{yAS} - m\Omega^2(y^\Omega_{WS} - y^\Omega_{AS}) \end{pmatrix}$$

$$[\Delta]\begin{pmatrix} B^{calib}_{xx} \\ \\ B^{calib}_{xy} \end{pmatrix} = \begin{pmatrix} M^{\Omega\ calib}_{xWC} - M^{\Omega\ calib}_{xAC} + m\Omega^2 z_{cm}(y^\Omega_{WC} - y^\Omega_{AC}) \\ -I\Omega^2(\varphi^\Omega_{xWC} - \varphi^\Omega_{xAC}) + I_z\omega\Omega(\varphi^\Omega_{yWS} - \varphi^\Omega_{yAS}) \\ \\ M^{\Omega\ calib}_{xWS} - M^{\Omega\ calib}_{xAS} + m\Omega^2 z_{cm}(y^\Omega_{WS} - y^\Omega_{AS}) \\ -I\Omega^2(\varphi^\Omega_{xWS} - \varphi^\Omega_{xAS}) - I_z\omega\Omega(\varphi^\Omega_{yWC} - \varphi^\Omega_{yAC}) \end{pmatrix}$$

$$\tag{B.45}$$

$$[\Delta]\begin{pmatrix} B^{calib}_{yx} \\ \\ B^{calib}_{yy} \end{pmatrix} = \begin{pmatrix} M^{\Omega\ calib}_{yWC} - M^{\Omega\ calib}_{yAC} - m\Omega^2 z_{cm}(x^\Omega_{WC} - x^\Omega_{AC}) \\ -I\Omega^2(\varphi^\Omega_{yWC} - \varphi^\Omega_{yAC}) - I_z\omega\Omega(\varphi^\Omega_{xWS} - \varphi^\Omega_{xAS}) \\ \\ M^{\Omega\ calib}_{yWS} - M^{\Omega\ calib}_{yAS} - m\Omega^2 z_{cm}(x^\Omega_{WS} - x^\Omega_{AS}) \\ -I\Omega^2(\varphi^\Omega_{yWS} - \varphi^\Omega_{yAS}) + I_z\omega\Omega(\varphi^\Omega_{xWC} - \varphi^\Omega_{xAC}) \end{pmatrix}$$

The components of the matrix $[\Delta]$ are

$$\begin{aligned} \delta^\Omega_{xC} &= \varepsilon + x^\Omega_{WC} &= \varepsilon + (d_{11} - z_{cm}d_{12})F^\Omega_{xWC} + d_{12}M^{\Omega\ calib}_{yWC} \\ \delta^\Omega_{xS} &= x^\Omega_{WS} &= (d_{11} - z_{cm}d_{12})F^\Omega_{xWS} + d_{12}M^{\Omega\ calib}_{yWS} \\ \delta^\Omega_{yC} &= y^\Omega_{WC} &= (d_{11} - z_{cm}d_{12})F^\Omega_{yWC} - d_{12}M^{\Omega\ calib}_{xWC} \\ \delta^\Omega_{yS} &= \varepsilon + y^\Omega_{WS} &= \varepsilon + (d_{11} - z_{cm}d_{12})F^\Omega_{yWS} - d_{12}M^{\Omega\ calib}_{xWS} \end{aligned} \tag{B.46}$$

Also

$$\varphi^{\Omega}_{xWC} = -(d_{21} - z_{cm}d_{22})F^{\Omega}_{yWC} + d_{22}M^{\Omega\ calib}_{xWC}$$

$$\varphi^{\Omega}_{xWS} = -(d_{21} - z_{cm}d_{22})F^{\Omega}_{yWS} + d_{22}M^{\Omega\ calib}_{xWS}$$

$$\varphi^{\Omega}_{yWC} = (d_{21} - z_{cm}d_{22})F^{\Omega}_{xWC} + d_{22}M^{\Omega\ calib}_{yWC}$$

$$\varphi^{\Omega}_{yWS} = (d_{21} - z_{cm}d_{22})F^{\Omega}_{xWS} + d_{22}M^{\Omega\ calib}_{yWS}$$

$$(B.47)$$

Form the inverse of $[\Delta]$, then the elements of hydrodynamic force and moment matrices can be evaluated from the forces and moments measured by the dynamometer, Eqns. (B.44–45). Then evaluate the steady forces and moments using Eqns. (B.34, 36). Subtract the buoyancy force and moment from F_{ox} and M_{oy}, respectively. The elements are then rotated into the volute reference, Eqns. (B.15–16), and non-dimensionalized, as above.

The effect of stiffness on the hydrodynamic forces and moments is presented for non-cavitating design flow. The components of the steady force and moment over the whirl ratio range $-.3 \leq \Omega/\omega \leq 0.6$ are shown in Fig. B.3. Indicated is the error bar for the infinitely rigid equations representing ± 1 standard deviation including both the wet and the dry runs for 32 cycles each. The full set of instantaneous data of 256 cycles had not been kept. Elements of the hydrodynamic force and moment matrices are shown in Figs. B.4–5. The moments were not particularly changed by including the stiffness. With regard to the forces, the values for reverse whirl, where the magnitude of the unsteady forces are largest, were most affected. These in turn influence the steady force components, Eqn. (B.34). In the region of primary interest, destabilizing forward whirl, the effect was negligible. The above observations cover the other flow coefficients tested and the breakdown tests. The simple model used does not take into account the elastic deflection caused by a moment arising if the axial thrust acts off the impeller center. The finite stiffness of the dynamometer-shaft system was not included in processing the forces and moments presented in the previous chapters.
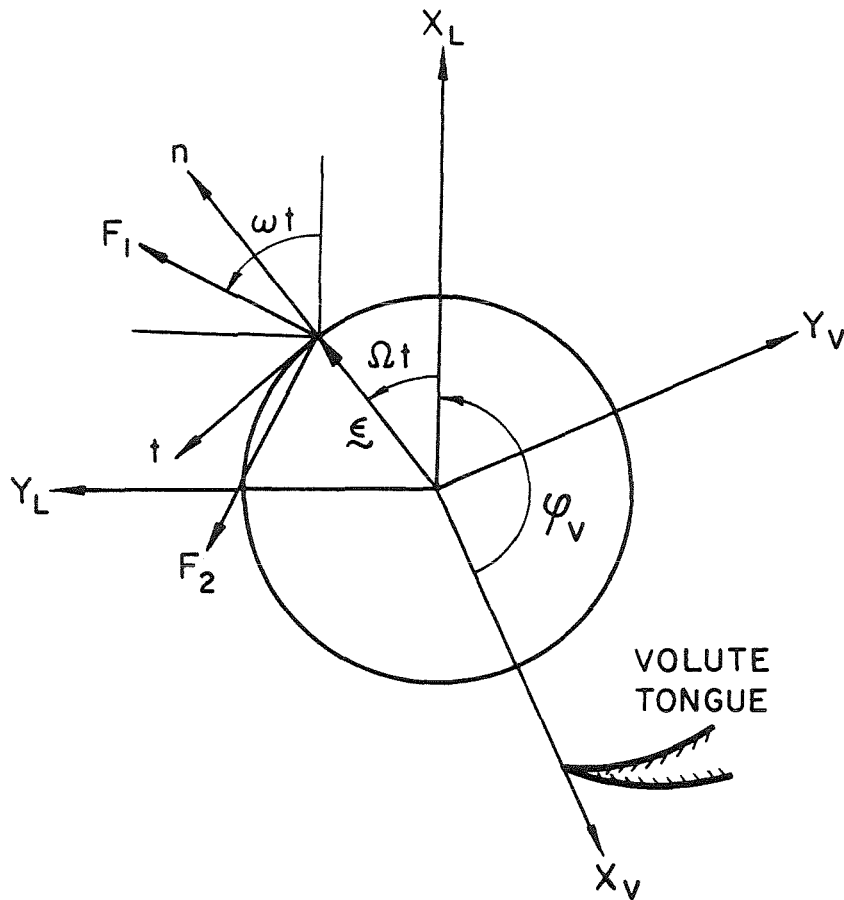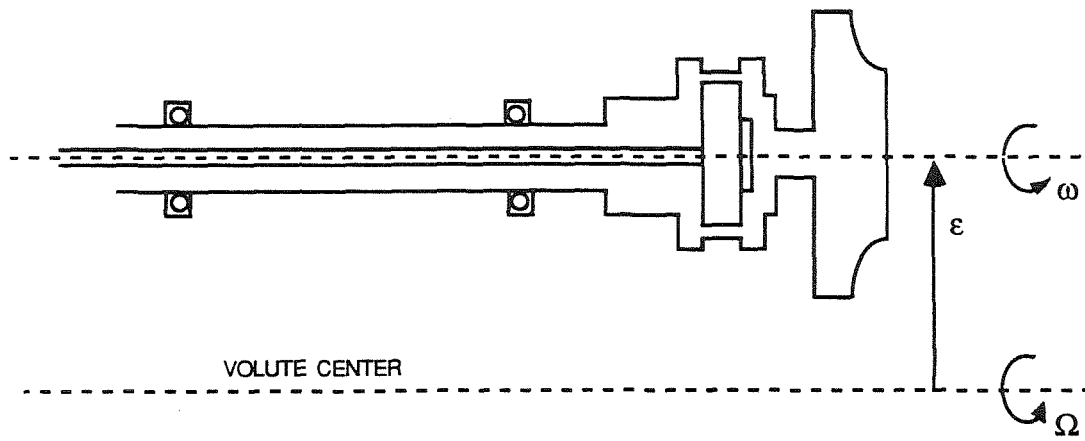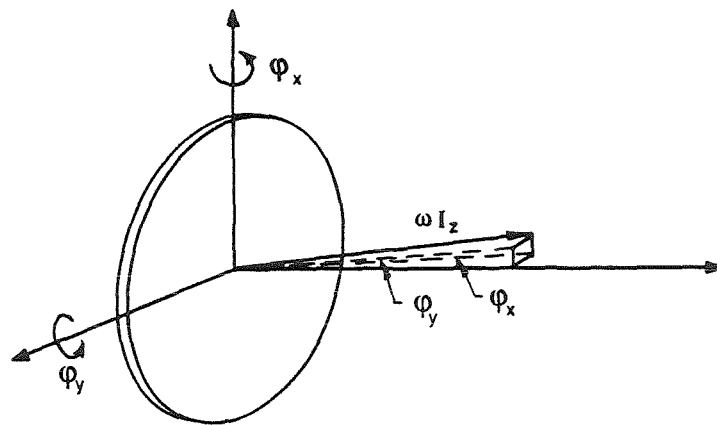
Fig. B.1 Schematic representation of the lateral forces in the rotating dynamometer frame, F_1 and F_2, on an impeller whirling in a circular orbit. X_L and Y_L represent the stationary laboratory frame, X_V and Y_V the stationary volute frame, and n and t the polar coordinate frame, normal to and tangential to the circular whirl orbit.

(a)
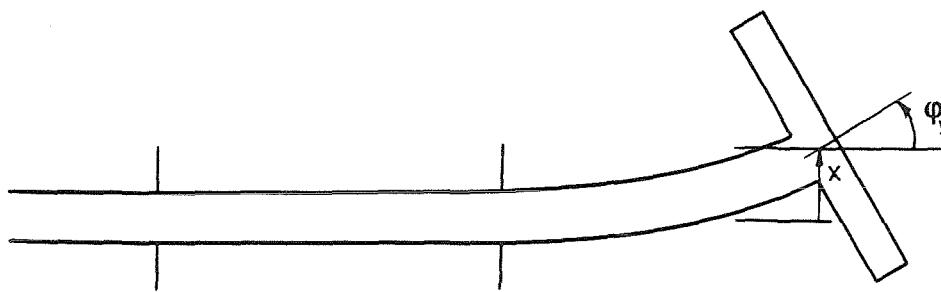
(b)

Fig. B.2   Schematic representation of the overhung impeller mounted on the dynamometer with the shaft supported by two bearings for (a) an infinitely rigid dynamometer–shaft system and (b) an elastic model of the system with the impeller represented as a "disk."
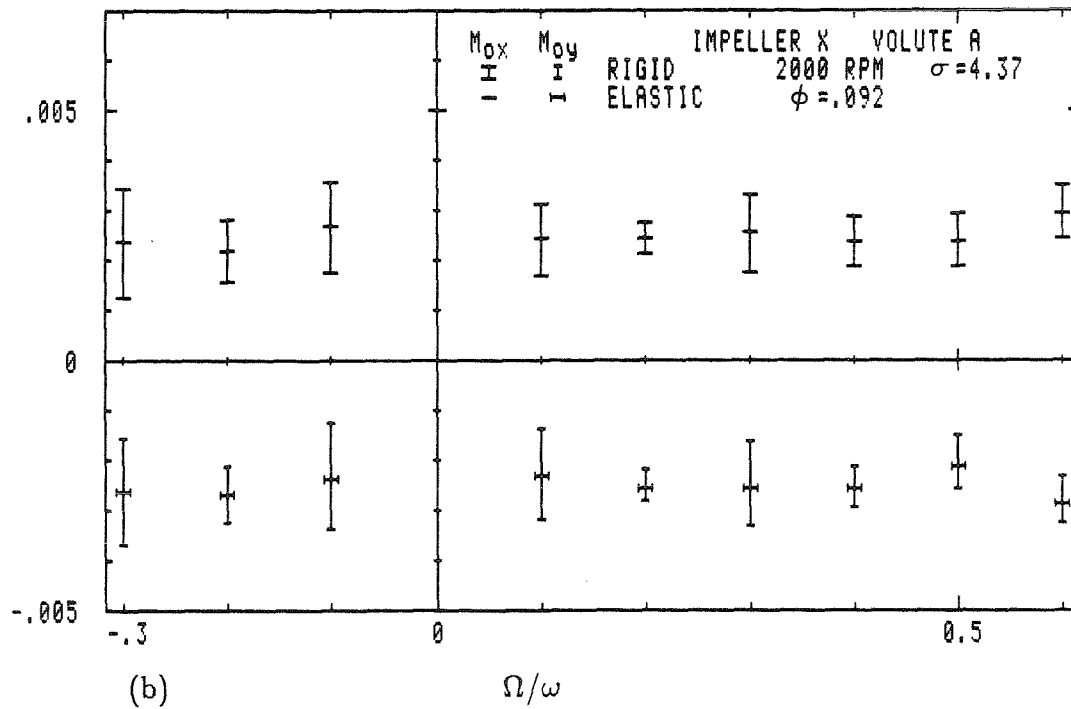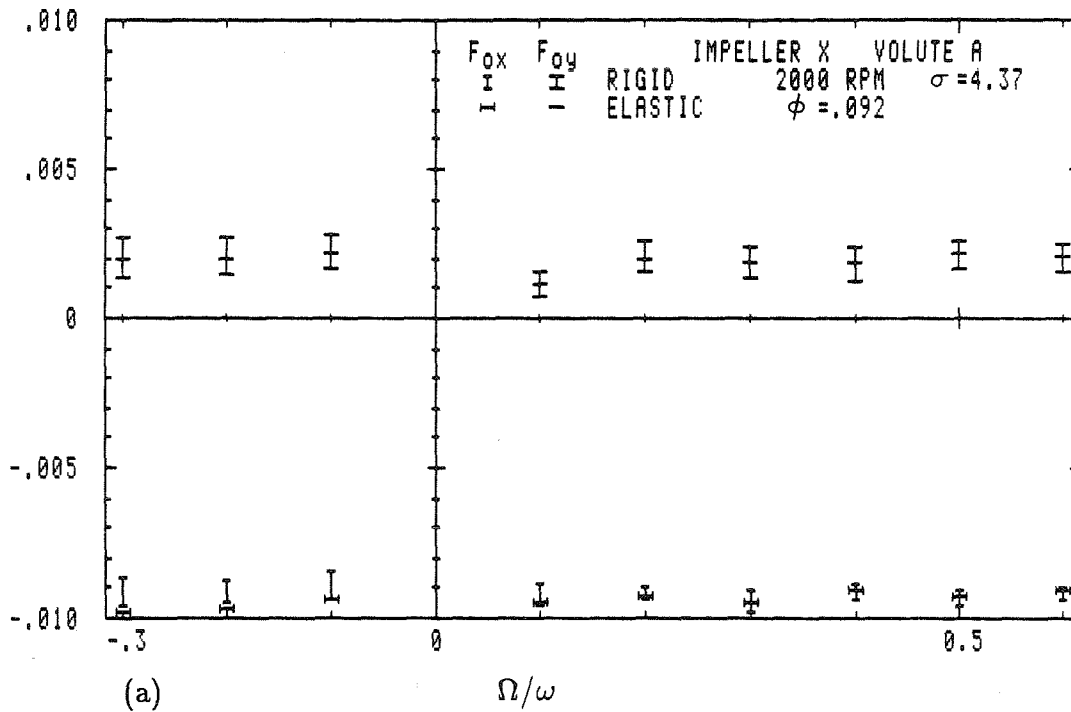
Fig. B.3 The components of (a) the steady force, F_{ox} and F_{oy}, and (b) the steady moment, M_{ox} and M_{oy}, on Impeller X in Volute A showing the effect of the stiffness model for non–cavitating design flow as a function of whirl ratio. The error bars on the "infinitely rigid" values represent ±1 standard deviation.
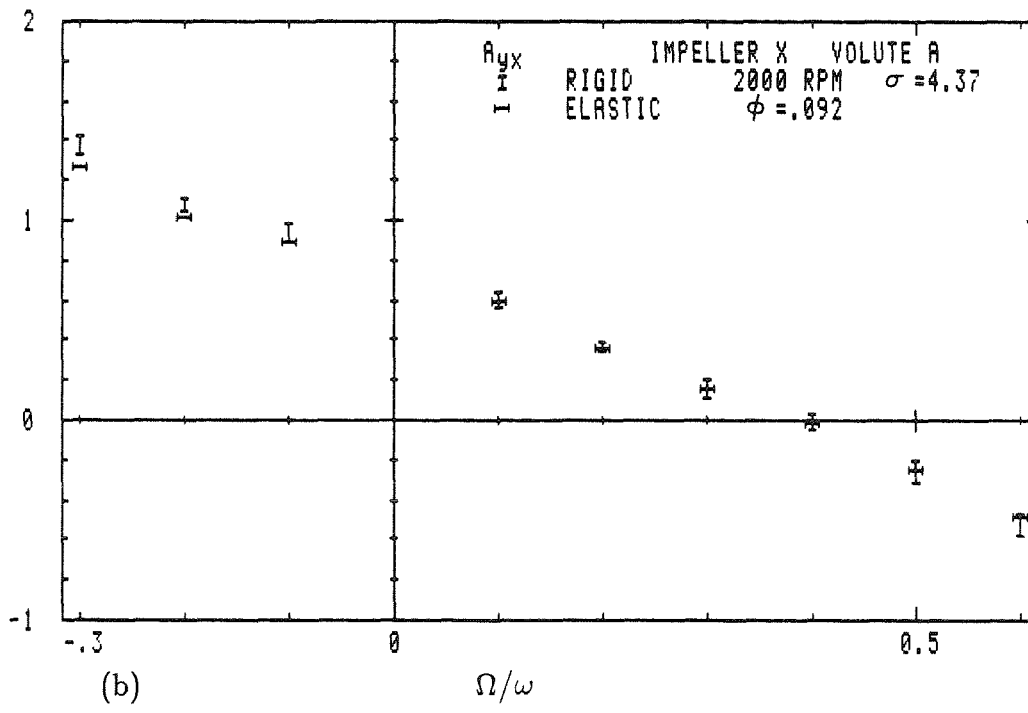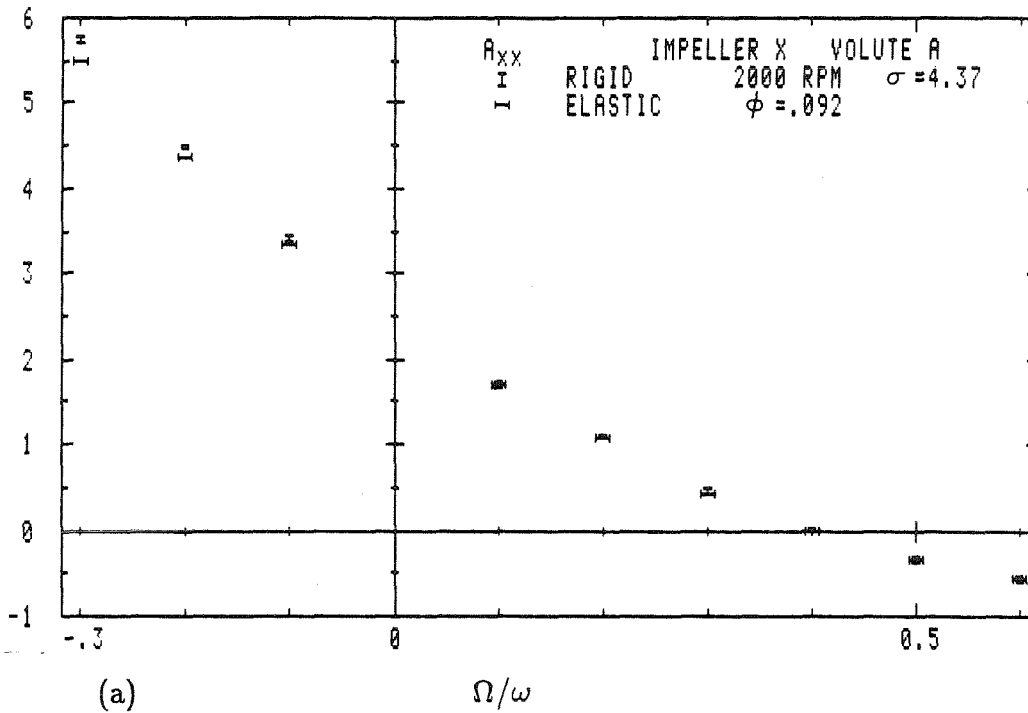
Fig. B.4   Two elements of the hydrodynamic force matrix [A], (a) A_{xx} and (b) A_{yx}, of Impeller X in Volute A showing the effect of the stiffness model for non-cavitating design flow as a function of whirl ratio. The error bars on the "infinitely rigid" values represent ±1 standard deviation.

Fig. B.5 Two elements of the hydrodynamic moment matrix, B_{xx} and B_{yx}, of Impeller X in Volute A showing the effect of the stiffness model for non–cavitating design flow as a function of whirl ratio. The error bars on the "infinitely rigid" values represent ± 1 standard deviation.
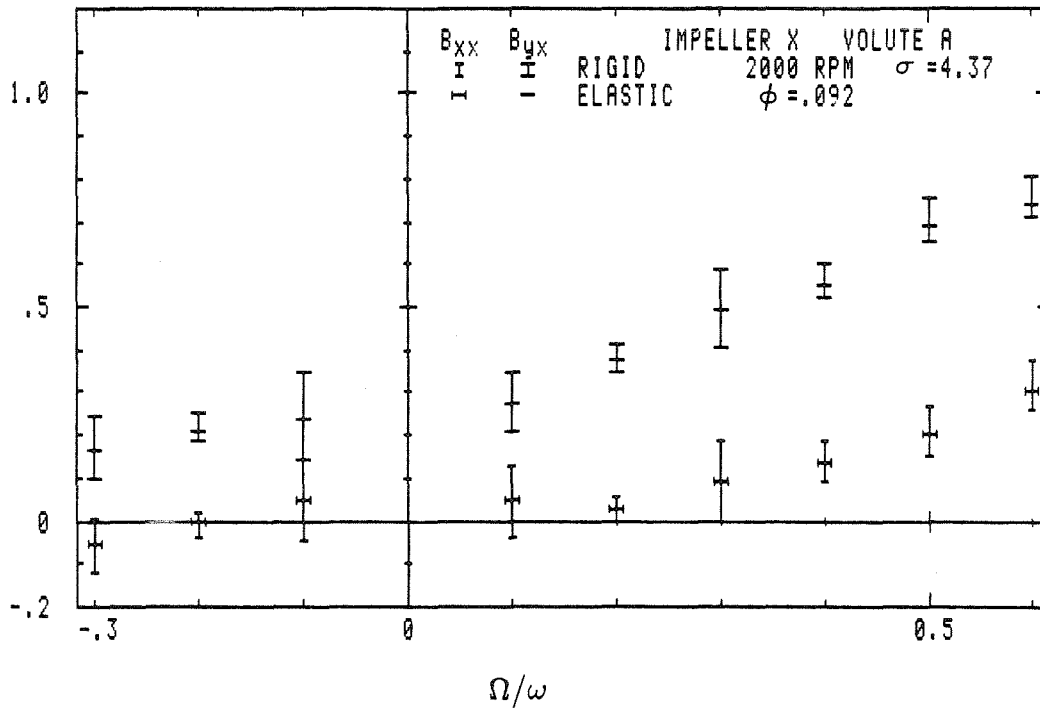
Appendix C

The Data Taker

The data acquisition system consists of the frequency multiplier/divider, two closed-loop motor controls and the data taker. When triggered the data taker converts an analog input signal to a digital word using a 12-bit analog-to-digital converter (ADC). A computer inputs the word and stores it in memory for subsequent processing and storage on a floppy disk.

The data taker was originally designed and built by John Lee. Trigger control circuitry was later added to enable the data taker to be triggered by an external frequency.

Fig. C.1 is a block diagram of the data taker circuitry. Inputs to the external trigger are the reference index and clock, N/J index and clock. The amplified dynamometer bridges, pressure transducers and accelerometers are read by the channel selector of the data taker. The computer communicates with the data taker through I/O ports. The address decoder interface, Fig. C.2, provides access to the data and address buses. Port addresses 20H–3FH have been decoded for use. Table C.1 lists the ports which are actually used.

Fig. C.3 shows the external trigger circuitry. Outputting a byte through port 20H selects the trigger command from among the index, clock or clock divided by 2^n, $n=1$, 4. The divided clock is used when the clock frequency is too high for the channel selector and ADC (25 kHz minimum throughput rate, 30 kHz typical) or for software. The selected trigger goes through two parallel one-shots. A 0.5 μs pulse is sent to the start conversion pin of the ADC. The second one-shot provides a 10 μs pulse long enough to be detected by software through port 28H.

The Analog Input Section (AIS), (channel selector), and ADC from Analog Devices, Norwood, MA, are shown in Fig. C.4. The number of the channel to be sampled is outputted through port 3FH. The AIS points the sample-and-hold at a

particular channel. It typically needs 10 μs to acquire the signal. A convert START pulse to the ADC will freeze the sample-and-hold while the conversion is in progress, typically 22 μs. After the conversion is complete, the sample-and-hold is released to acquire the signal of the channel indicated by the AIS. While the conversion is in progress with the sample-and-hold at hold, the channel that the AIS points to can be altered.

The source of the pulse to start the conversion is selected from software. Besides using an external trigger, two other choices are available. A one-shot loop may be used to start the A/D conversion continually at a preset rate after initially being triggered. Or the external frequency can be inhibited, and an OUT instruction to port 3EH will start the conversion from software.

Fig. C.5 shows the layout of the chips on the S-100 card for the external trigger control and the address decoder interface. The layout of the AIS, ADC and associated chips is shown on Fig. C.6.
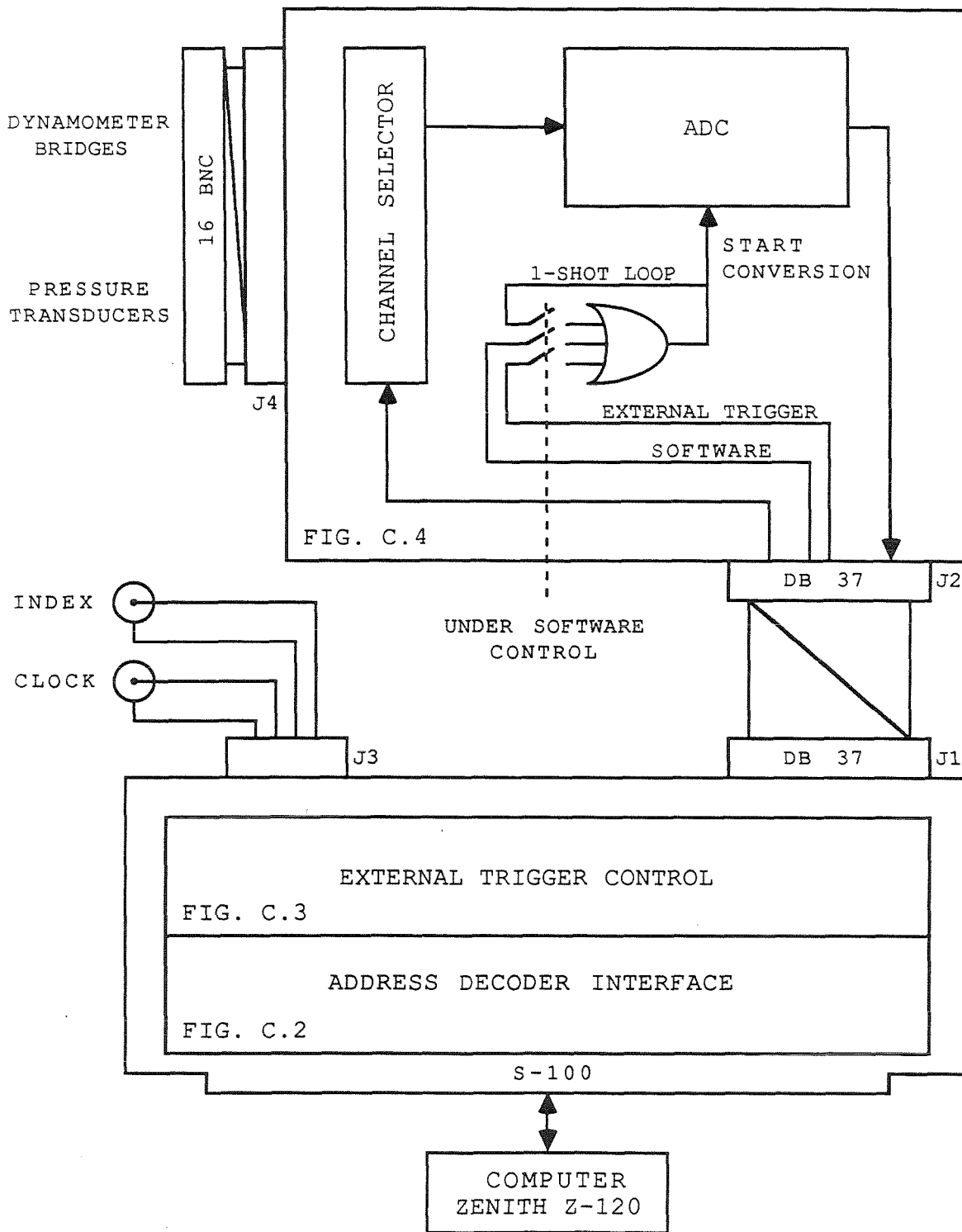
Table C.1 I/O Ports

IN 28H, byte   trigger signal from one-shot (software observed)
               ⊓‾ receive 1 or 0

OUT 28H, byte $- - - D_4 D_3 D_2 D_1 D_0$

D_4 external trigger 1-shot to start A/D   0 enable
                                                     1 inhibit

D_3 $\overline{\text{LOAD}}$ of clock divider   0 load 15 onto output
                                             1 release, to count down

D_2	D_1	D_0	divided signal
0	0	0	CLOCK
0	0	1	CLOCK/2
0	1	0	CLOCK/4
0	1	1	CLOCK/8
1	0	0	CLOCK/16
1	1	1	INDEX

    example: OUT 28H, 00111   enable external trigger one-shot
                                         preset divided signal by loading 15
                                            onto output
                                         pass INDEX
    detect INDEX
    OUT 28H, 01001   pass CLOCK/2 in phase with
                                           INDEX
    take data, when done
    OUT 28H, 1- - - - disable external trigger one-shot

OUT 3DH, byte   0 disable one-shot loop from starting A/D conversion
                 1 enable one-shot loop to start A/D conversion

OUT 3FH, byte   select channel to be sampled (0–15)

OUT 3EH   start A/D conversion from software

IN 3EH, byte   input low-byte of A/D
IN 3FH, byte   input high-byte of A/D with STATUS
             example: IN AX,3EH   AX=STATUS 0 0 0 12-bit data
                                                 1 conversion in progress
                                           0 conversion complete

Fig. C.1 Block diagram of the data taker.
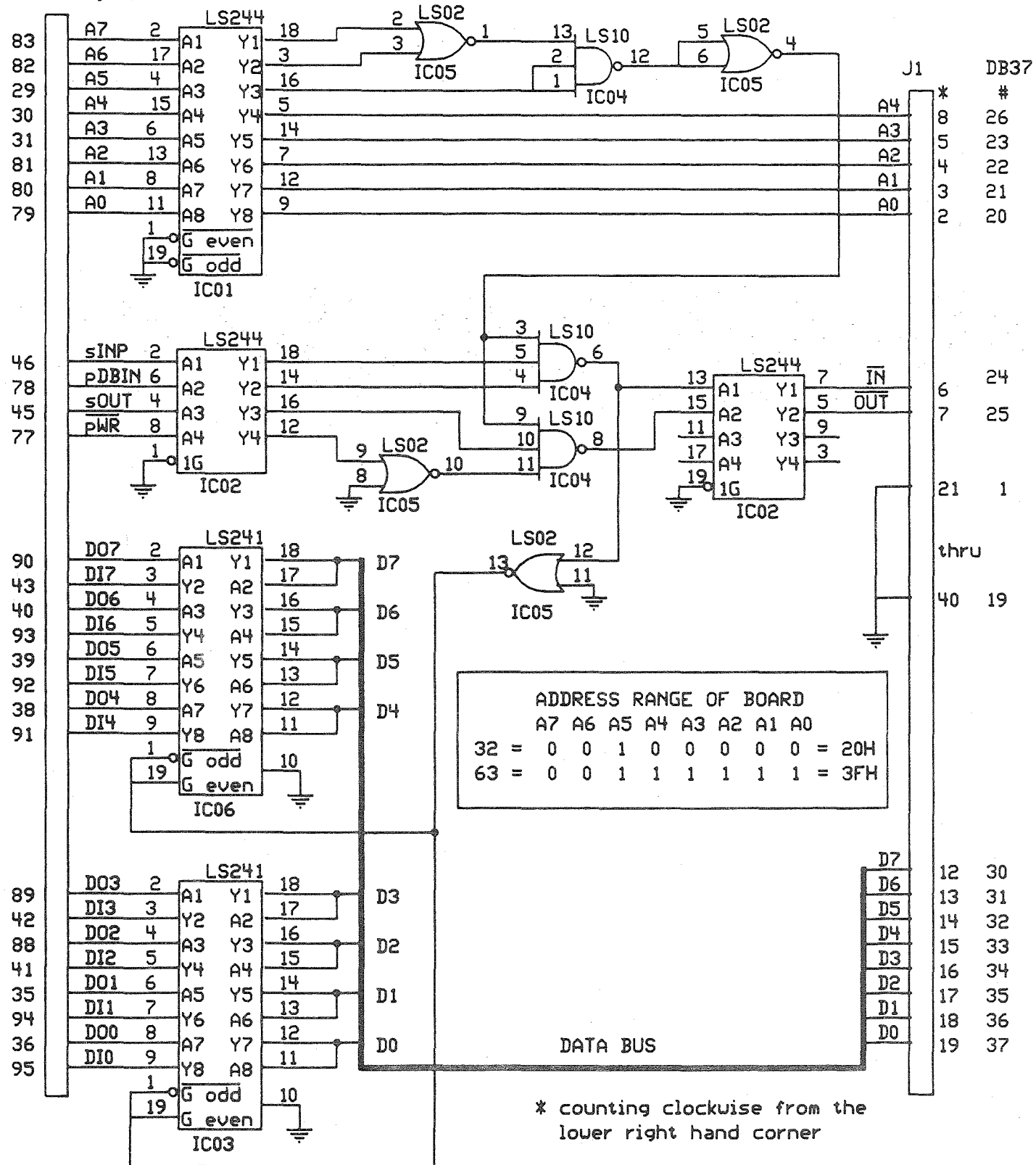
ZENITH 100 SERIES PARALLEL I/O BOARD

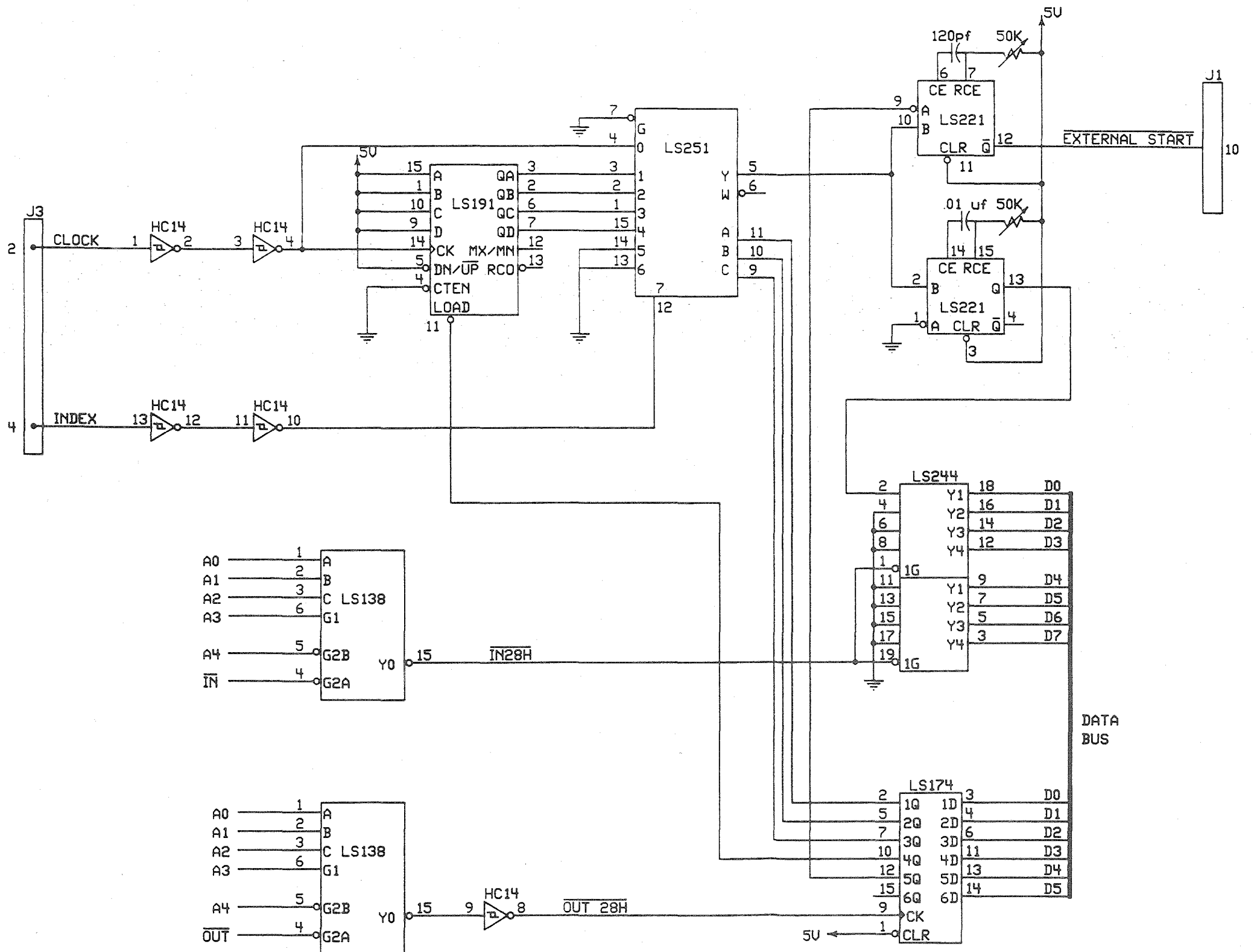Fig. C.2 Circuit drawing of the address decoder interface.

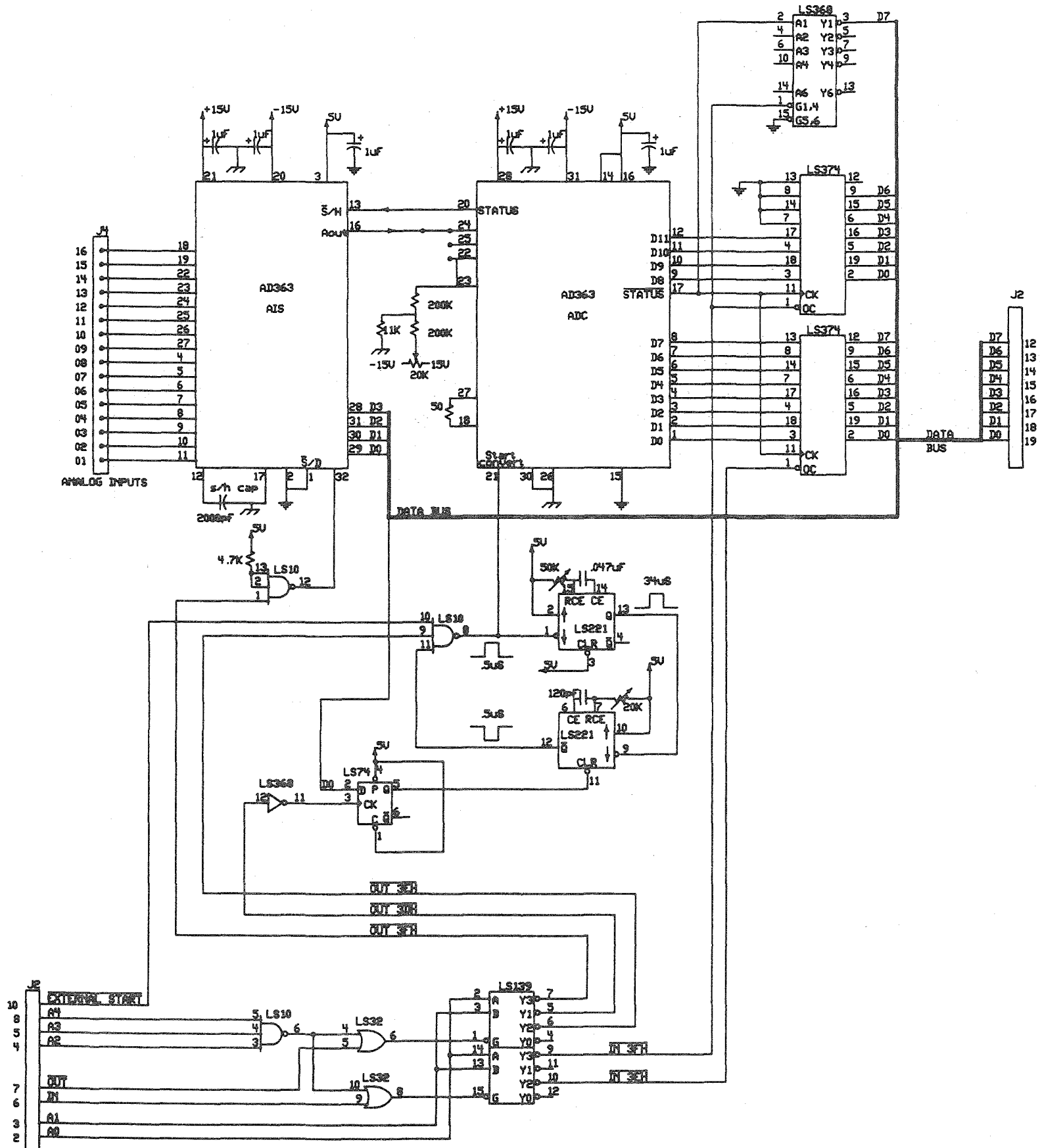Fig. C.3 Circuit drawing of the external trigger control.

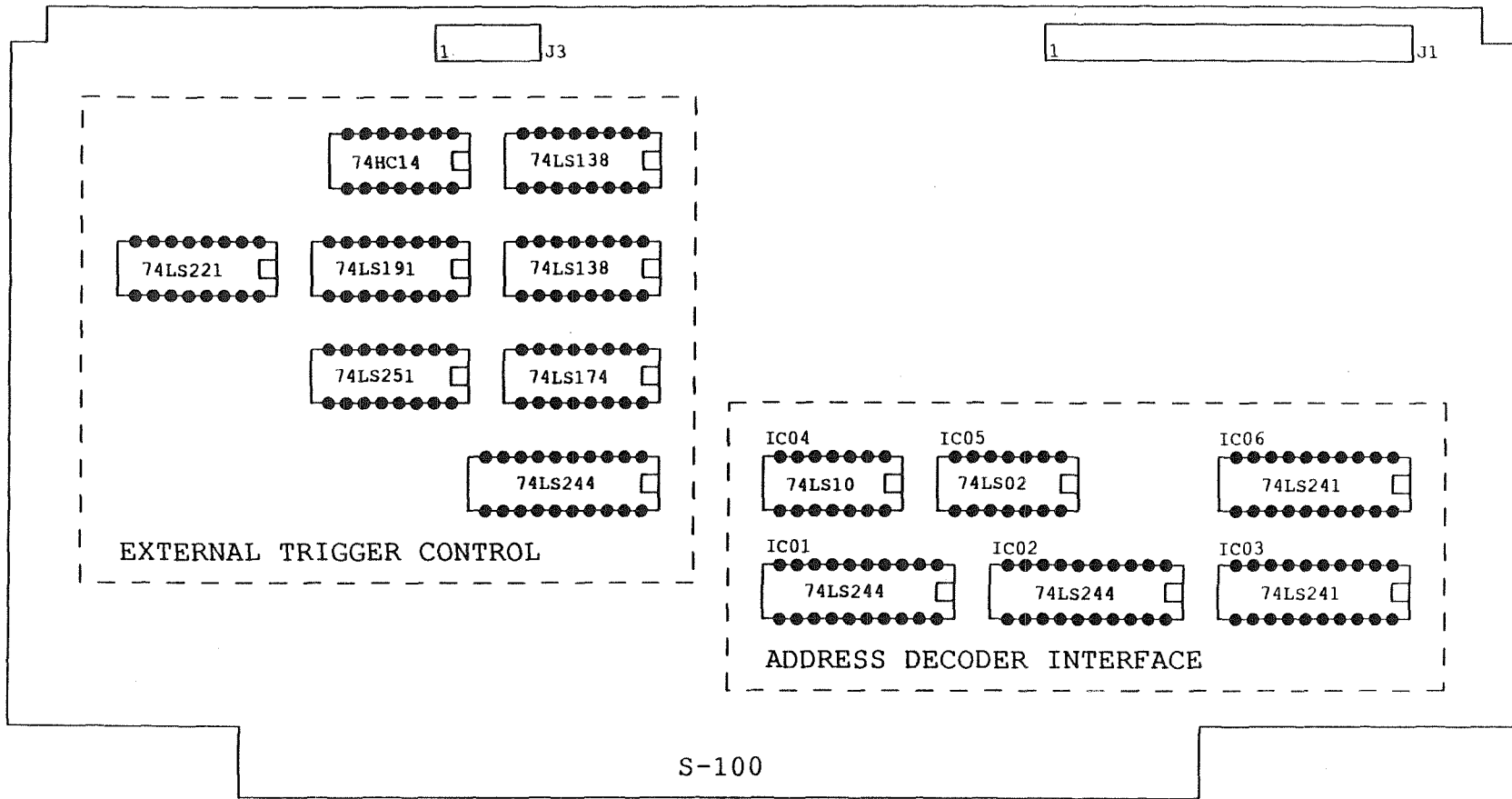Fig. C.4 Circuit drawing of the card with the Analog-to-Digital Converter.

Fig. C.5 Chip layout on the S-100 card of the address decoder interface and the external trigger control.
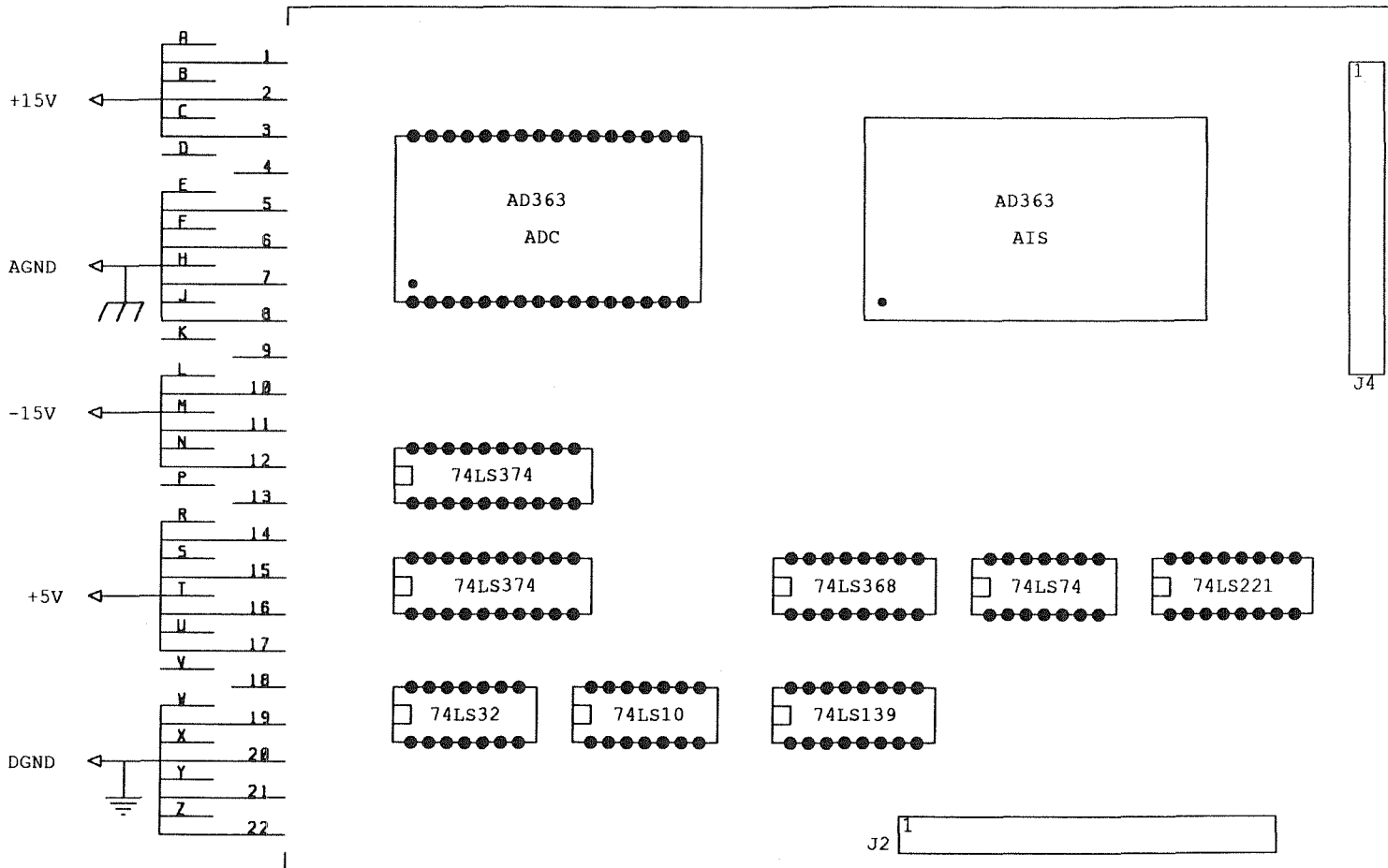
Fig. C.6   Chip layout of the card with the Analog-to-Digital Converter.

Appendix D

The Closed-Loop Motor Control

The two motor closed-loop controls bring the speed and phase of each motor into alignment with the impeller orientation and location on the whirl orbit expected by the data taker. Fig. D.1 is a block diagram of the control system. Drawings of the motor control circuitry are given in Fig. D.2–5. Fig. D.2 shows the connections among the various parts. Fig. D.3–4 are circuit drawings of two wire wrap circuit boards contained within the motor control box. Fig. D.5 shows the isolation amplifier and the stop and start relays of the interface box. From the back panel of the motor control box, two cables go to the interface box, the stop and start relay signals and the control signal with attendant power supply lines. The encoder cable provides power to the optical encoder mounted on the shaft and returns the index and clock signals used for feedback. Fig. D.6–7 shows the layout of the chips on the two wire wrap circuit boards. The block diagram will be discussed and then selected elements of the control system will be discussed further with reference to the circuit drawings.

The closed-loop control uses the optical encoder mounted on each shaft as feedback. It outputs two pulse trains, an index (one per revolution) and a clock (1024 per revolution). These signals are compared to the corresponding command signals. The up/down counter tracks the difference in frequency between the command and encoder clocks. It counts up/down for each command/encoder clock pulse. The anti-coincidence circuitry inhibits the count change if the command and encoder clocks are nearly coincident. The up/down digital-to-analog converter (DAC) reflects the changing counter. The integrator tracks the relative phase between the command index (sync out) and the encoder index. The command index is generated by dividing the command clock by 1024. The N/J index from the frequency multiplier/divider resets the divider, synchronizing motor orientation

with data acquisition. Both the encoder and command indices go to a phase detector. The difference in phase is integrated.

At the summing amplifier, the ramp generator, the up/down DAC, and the phase integrator voltages are weighted and added. The resulting voltage is set across the terminals of the Sabina circuitry instead of the potentiometer for open-loop operation. An isolation amplifier provides the interface between the closed-loop control and the Sabina (open-loop) control.

Initially the up/down counter is set at the middle of its range so that the DAC (± 5V range) outputs zero and the phase integrator is shorted. Pushing the start button releases the ramp counter and passes the pulses of either a fixed oscillator or the command index to the counter. The ramp DAC provides an increasing voltage to the summing amplifier. When the motor is rotating faster than desired, the phase detector will trigger an internal switch which clamps the ramp generator by blocking the counter oscillator and releases the up/down DAC and integrator whose changing voltages reflect speed and phase errors, respectively. Pushing the stop button switches the control system from speed and phase control to the ramp generator. The up/down counter is reset, the phase integrator is reset by shorting the feedback capacitor, and the ramp counters count down.

The input command clock and the reference index (SYNC IN) for resetting the internally derived command index are connected to the front panel of the motor control box, Fig. D.2, using BNC cables. If the speed but not the phase of the shaft is to be controlled then either the SYNC IN BNC should be grounded or the jumper next to the 4040 (U22) on the up/down DAC card should be removed.

From the front panel, the encoder index and clock, ramp DAC, up/down DAC, and integrator outputs are accessible through BNC connectors. A meter is provided to monitor up/down DAC and phase integrator to show that they are still within their effective ranges. The up/down counter can under or overflow and the integrating op amp can saturate. If the up/down DAC nears the limits of the DAC output voltage range (± 5V) the window detector on Fig. D.4 sets the STOP

flip-flop (U6B), as if the STOP button had been pushed, and the motor ramps down. Otherwise, had the up/down counter under or overflowed the DAC output would have switched voltage limits as a saw-tooth wave and the motor attempted to follow the large amplitude change in the control signal.

One half of the 556 (U12a) provides a power up reset pulse to initialize the flip-flops. The other half provides a fixed oscillator for the ramp generator counter. An alternative signal is derived from dividing down the command clock using the 4040 (U22), presently the command clock/1024 (command index) is provided. The jumper near the 556 (U12) of Fig. D.3 selects between the fixed oscillator and the divided command clock. The center pin goes to the clock pin of the ramp counters (U9–U11).

The anti-coincidence section inhibits the up/down counter if the command and encoder clock pulses are nearly coincident. An arriving command or encoder clock pulse triggers its half of a flip-flop (U31a or b). The voltage controlled oscillator (VCO) of the 4046 (U19) is used as a fixed oscillator. The VCO alternatively passes any command or encoder clock pulse that had occurred to a one-shot (U30) which generates a pulse to the corresponding up or down pin of the counter (U25). The one-shot also resets the flip-flops. The VCO frequency should be greater than twice the clock frequency.

The output from the phase detector, 4046 (U19), is low, high or three-state. U18C buffers it before U14C integrates the phase error. U14B subtracts 2.5V to remove the bias of the buffered three-state output for "in-phase" signals.

While the motor is ramping up the phase detector output is high or three-state. When the phase detector first goes low, indicating that the shaft is rotating faster than the command frequency, the voltage comparator LM311 (U16) triggers the SYNC flip-flop (U5b). This switches control from the ramp generator to the the up/down DAC and integrator for speed and phase control.

The resistors at the summing amplifier determine the relative weight given to the ramp DAC, the up/down DAC and the phase integrator. Decreasing the value

of the resistor increases the weighting factor at the output. Select resistances for the up/down DAC and the phase integrator so that the control system behaves as a critically damped system to perturbations in load or speed. The up/down DAC can be isolated by shorting the integrator. Replace the analog switch DG211 (U15) with a component carrier with pins 2 and 3 connected. The behavior of the control system can be monitored by connecting the up/down DAC and integrator outputs accessible from the front panel to a strip chart recorder.

The closed-loop motor control system is similar to the system it replaced, which was designed by Haskell Shapiro. The original design was modified and rebuilt in consultation with John Lee.
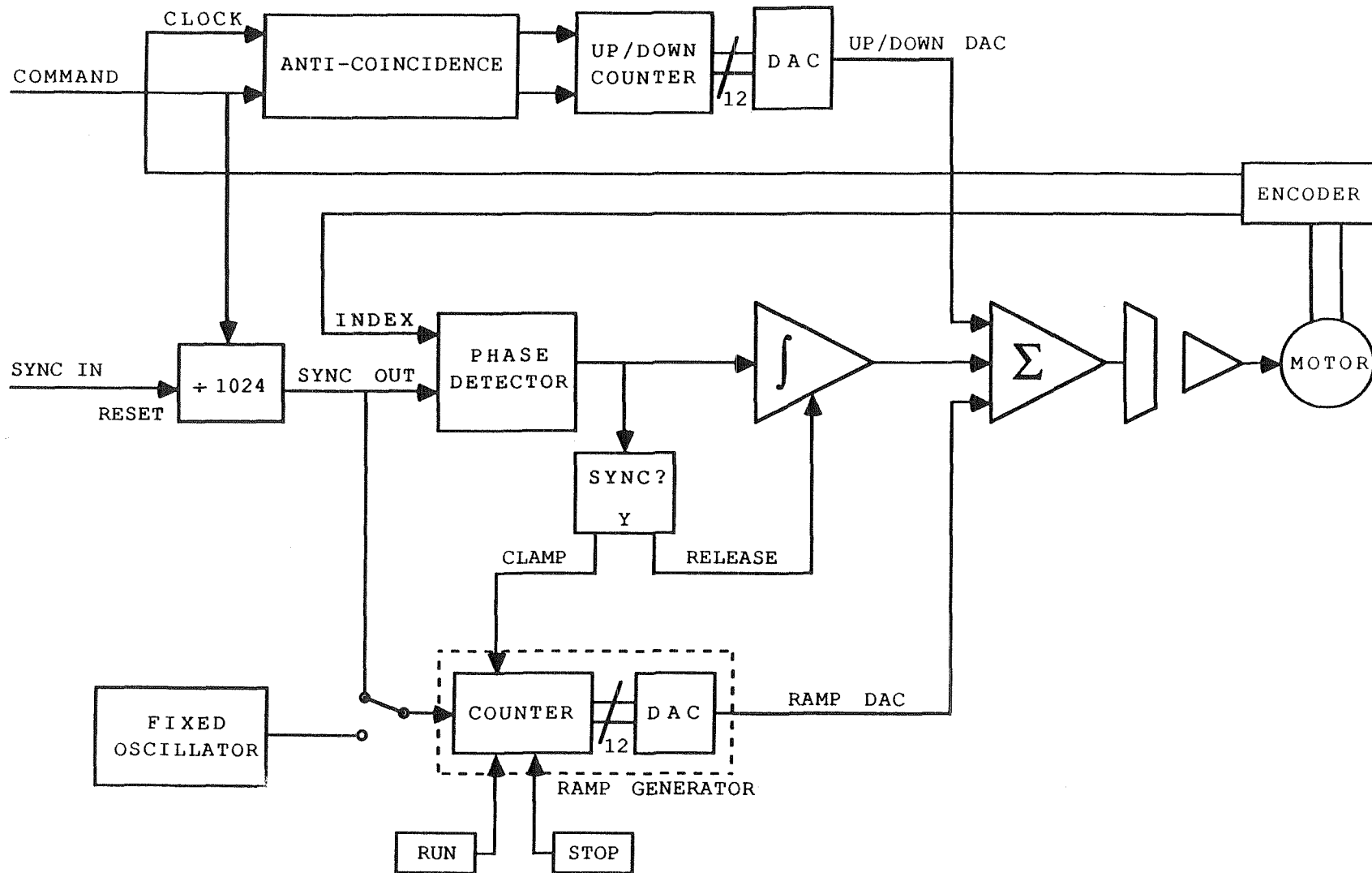
Fig. D.1 Block diagram of the closed–loop motor control system.
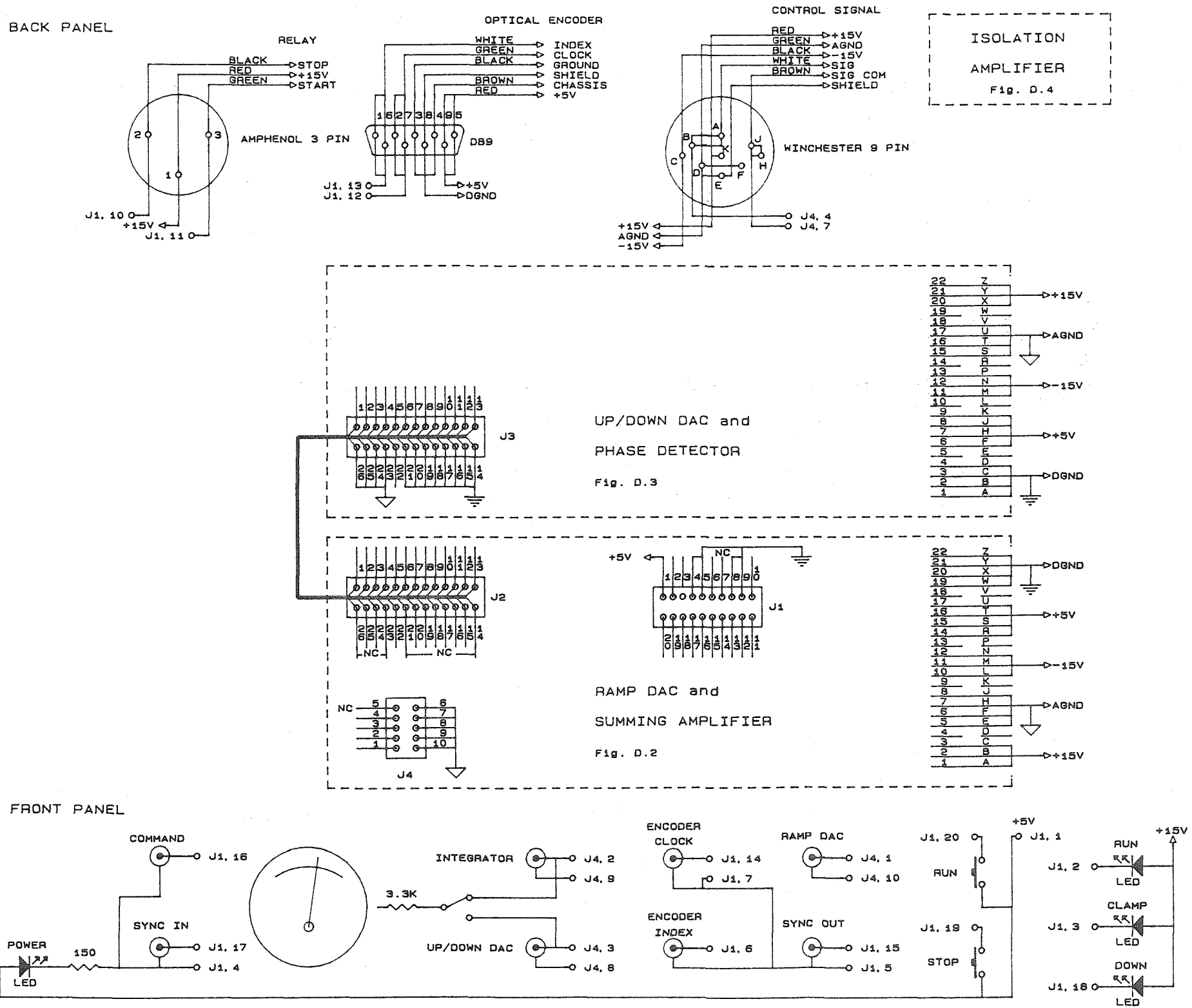
Fig. D.2   Layout diagram of the motor control box.
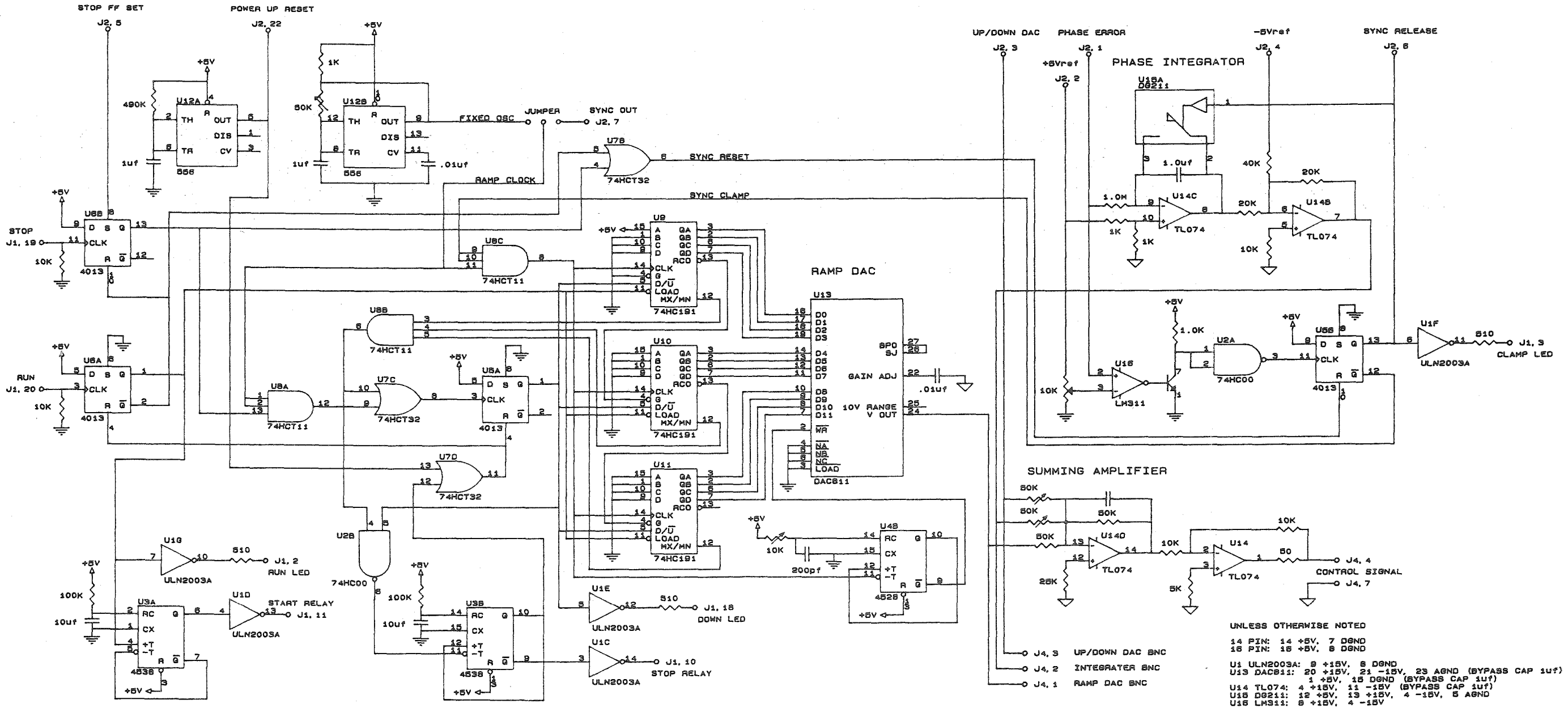
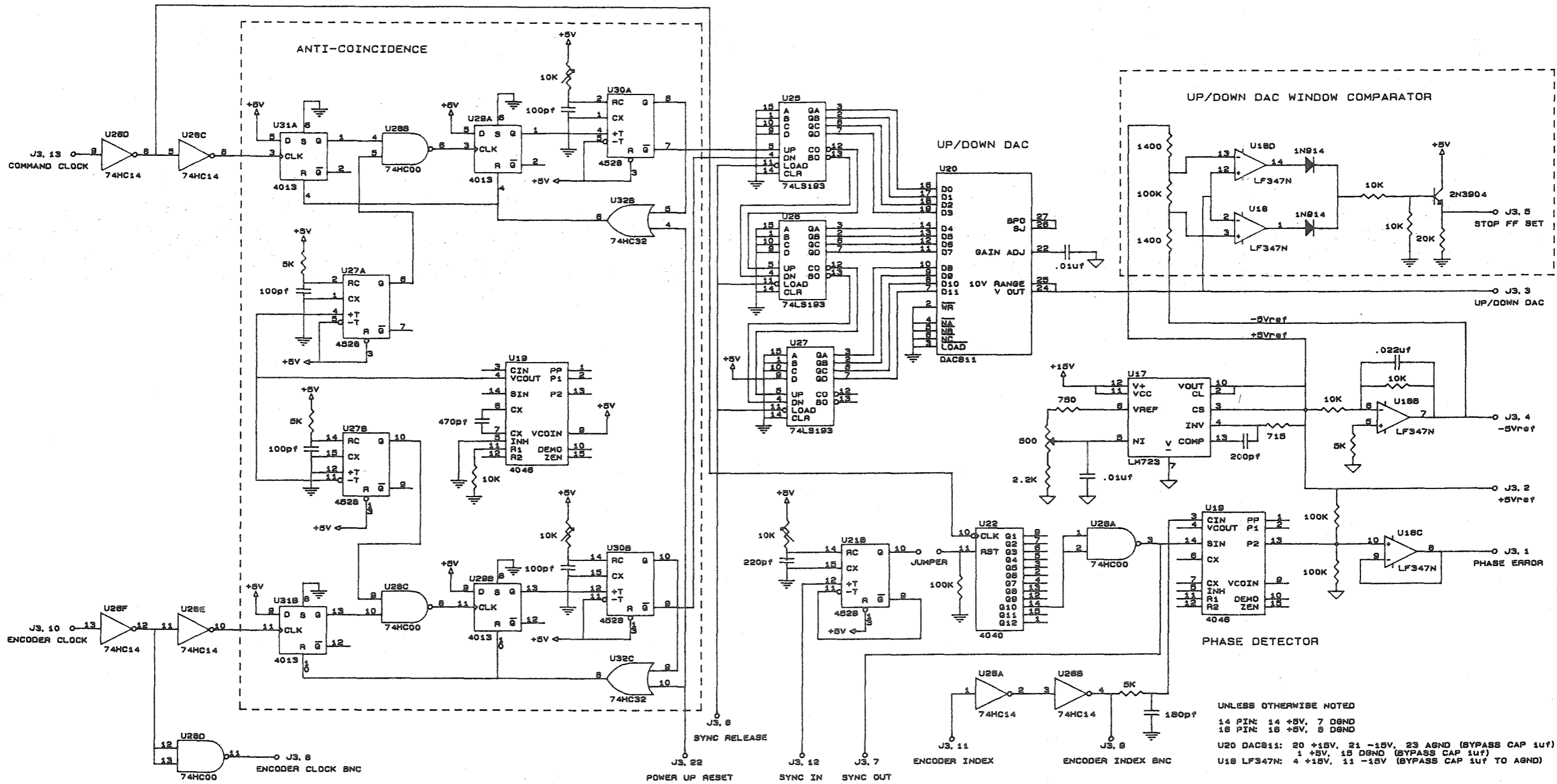Fig. D.3   Circuit drawing of the card with the ramp generator and the summing amplifier.

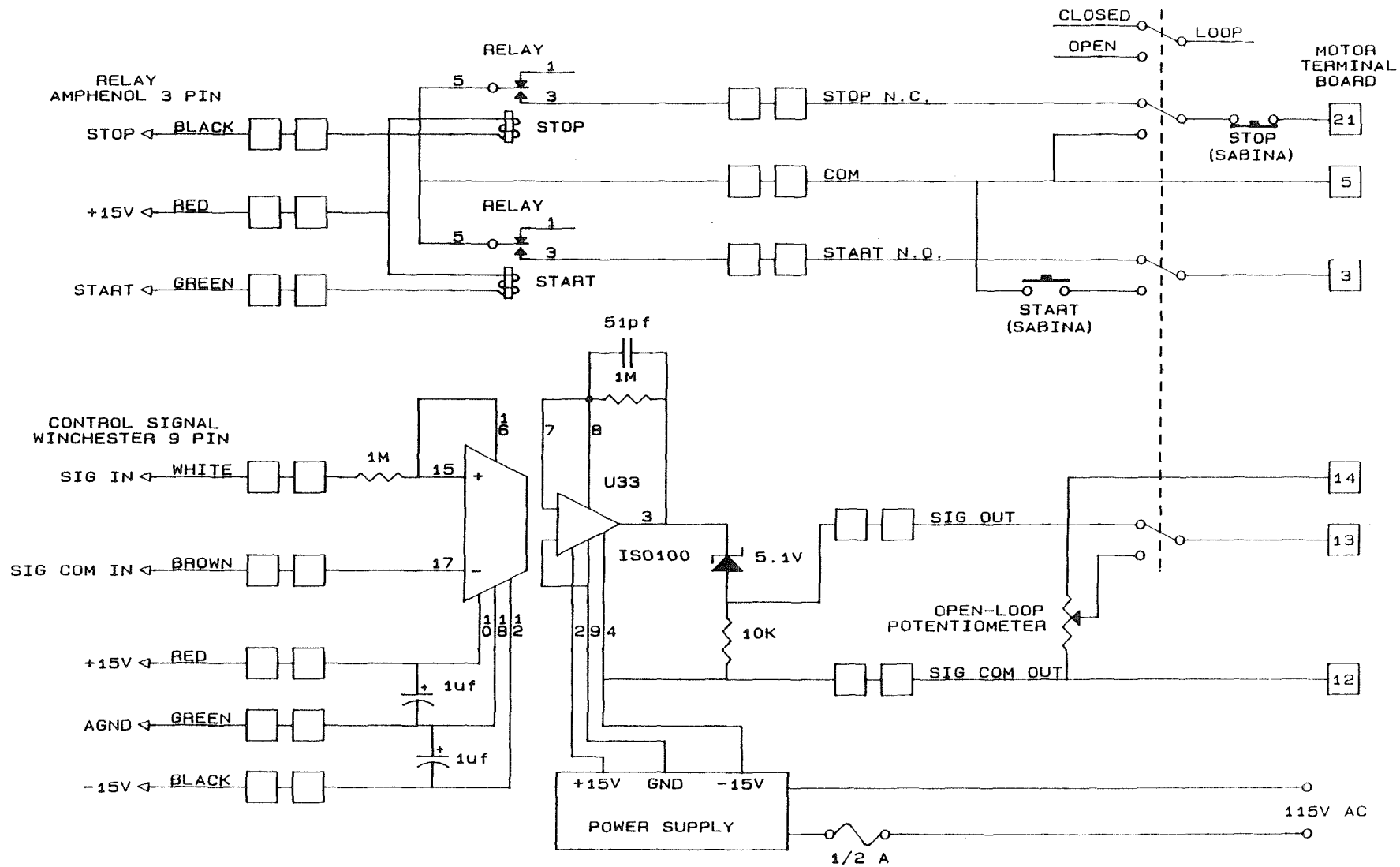Fig. D.4 Circuit drawing of the card with the up/down DAC and the phase detector.

Fig. D.5   Circuit drawing of the interface board with the isolation amplifier and the stop and start relays.
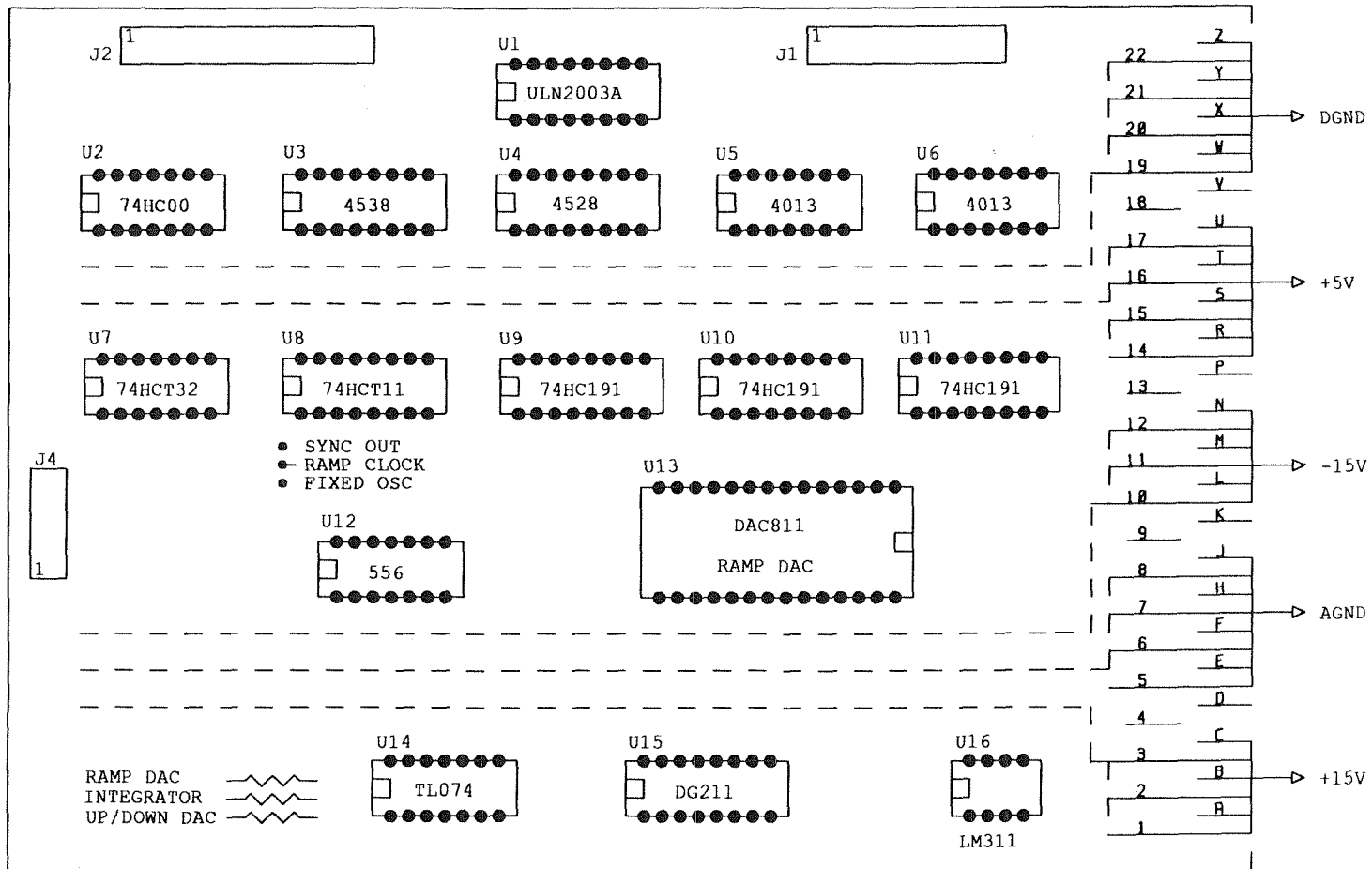
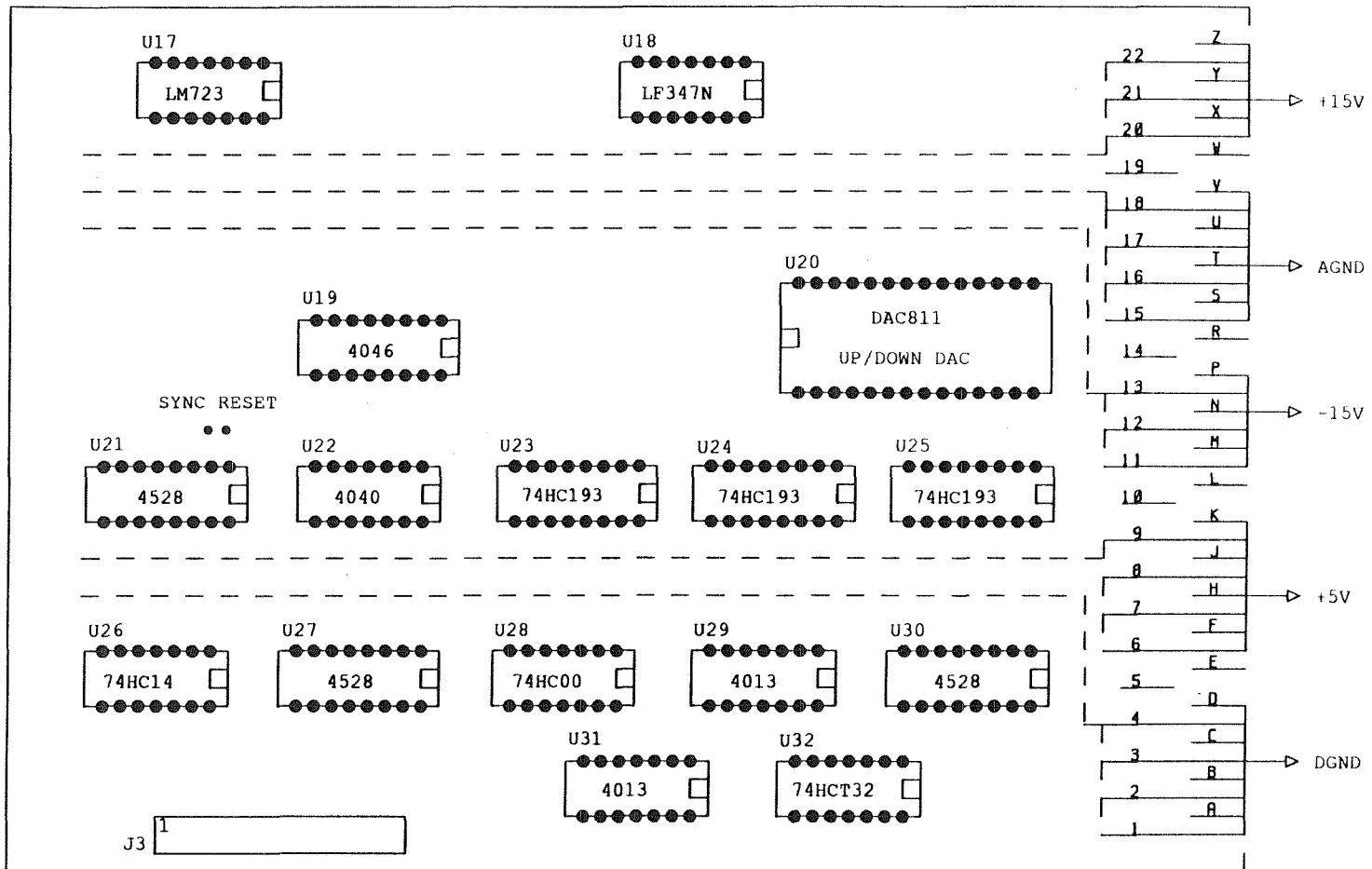Fig. D.6 Chip layout of the card with the ramp generator and the summing amplifier.

Fig. D.7 Chip layout of the card with the up/down DAC and the phase detector.